Technical University of Denmark

DTU

Remote Sensing for Wind Energy

Pena Diaz, Alfredo; Hasager, Charlotte Bay

Publication date:
2010

Document Version
Publisher's PDF, also known as Version of record

Link back to DTU Orbit

DTU Library
Technical Information Center of Denmark

Remote Sensing for Wind Energy

Alfredo Peña and Charlotte B. Hasager (Eds)
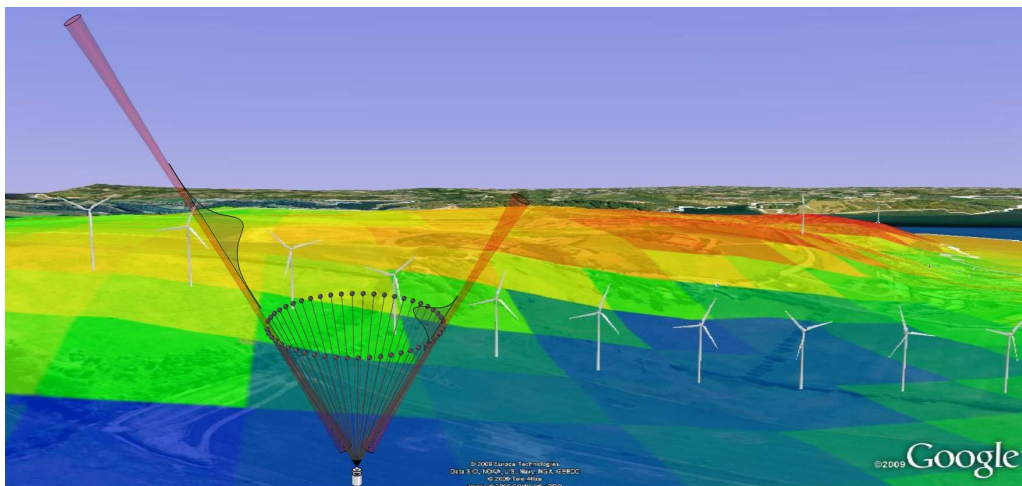
Risø DTU
National Laboratory for Sustainable Energy

DTU

Remote Sensing for Wind Energy

Merete Badger
Rebecca J. Barthelmie
Ferhat Bingöl
Oliver Bischoff
Stefan Emeis
Sten T. Frandsen
Michael Harris
Charlotte B. Hasager
Martin Hofsäß
Martin Kühn
Jakob Mann
Torben Mikkelsen
Frank Monaldo
Alfredo Peña
Sara C. Pryor
Andreas Rettenmeier
Fabio Scanzani
David Schlipf
Donald Thompson
Juan José Trujillo
Rozenn Wagner

Edited by:
Alfredo Peña and Charlotte B. Hasager
Wind Energy Division, Risø DTU, Roskilde, Denmark

Contents

Preface

The Remote Sensing in Wind Energy Compendium provides a description of several topics and it is our hope that students and others interested will learn from it. The idea behind this compendium began in year 2008 at Risø DTU during the first PhD Summer School: Remote Sensing in Wind Energy. Thus it is closely linked to the PhD Summer Schools where state-of-the-art is presented during the lecture sessions. The advantage of the compendium is to supplement with in-depth, article style information. Thus we strive to provide link from the lectures, field demonstrations, and hands-on exercises to theory. The compendium will allow alumni to trace back details after the course and benefit from the collection of information. This is the first edition of the compendium and we warmly acknowledge all the contributing authors for their work in the writing of the compendium and we also acknowledge all our colleagues in the Meteorology and Test and Measurements Programs from the Wind Energy Division at Risø DTU in the PhD Summer Schools. We hope to add more topics in future editions and to update as necessary, to provide a truly state-of-the-art compendium available for people involved in Remote Sensing in Wind Energy.

1   Remote Sensing of Wind

Torben Mikkelsen
Wind Energy Division, Risø DTU, Roskilde, Denmark

1.1   Ground-based remote sensing for today's wind energy research

Wind turbines are being installed at an ever increasing rate today, on and offshore, in hilly and forested areas and in complex mountainous terrain. At the same time, as the wind turbines become bigger and bigger, they reach higher and higher into the atmosphere but also into hitherto unknown wind and turbulence regimes.

The traditional method for accredited measurements for wind energy is to mount calibrated cup anemometers on tall met masts. But as turbines grow in height, high meteorology masts and instrumentation becomes more and more cumbersome and expensive correspondingly. Costs for installation of tall instrumented met towers increase approximately with mast height to the third power and licensing permits can be time consuming to obtain.

With hub heights above 100 m and rotor planes nowadays reaching diameters of 120 m or more on today's 5 MW turbines, the wind speed distribution over the rotor planes will no longer be representatively measured from a single hub height measurement point, but will also require a multi-height measurement strategy with measurements ranging in heights between 50–200 m, for the purpose of capturing the simultaneous wind distribution over the entire wind turbine rotor.

Wind remote sensing (RS) methodologies

A simple way to remotely determine the wind speed is by observing marked cloud drift aloft from the ground on a sunny day. More quantitative and accurate remote sensing measurement techniques for wind energy applications include nowadays sound and light wave propagation and backscatter detection based instruments such as sodar, lidar and satellite-based sea surface wave scatterometry.

Today's quest within RS research for wind energy is to find useful replacement alternatives for expensive and cumbersome meteorology mast erection and installations. However, accuracy is of particular importance for site and resource assessments irrespectively of terrain, on or offshore, and measurement errors much in excess of 1% cannot be tolerated neither by banks nor by project developers, as 1% uncertainty in mean wind speed results in 3% uncertainty in mean wind power.

1.2   Part I: Remote sensing of wind by sound (sodars)

Sodar (sound detection and ranging) is based on probing the atmosphere by sound propagation, lidar (light detection and ranging) is based on probing the atmosphere by electromagnetic radiation (microwaves or laser light) and satellite RS is based on microwave scatterometry on the sea surface and synthetic aperture radar (SAR) methods. The first two (sodar and lidar) are direct measurements of wind speed based on Doppler shift, whereas the satellite scatterometry are based on proxy-empirical calibration methods. First, a description of the background and the state-of-the-art sodar is addressed. Second, the corresponding development and application lidar RS technology is addressed.

Wind turbines operate within the so-called atmospheric boundary layer, which is char-
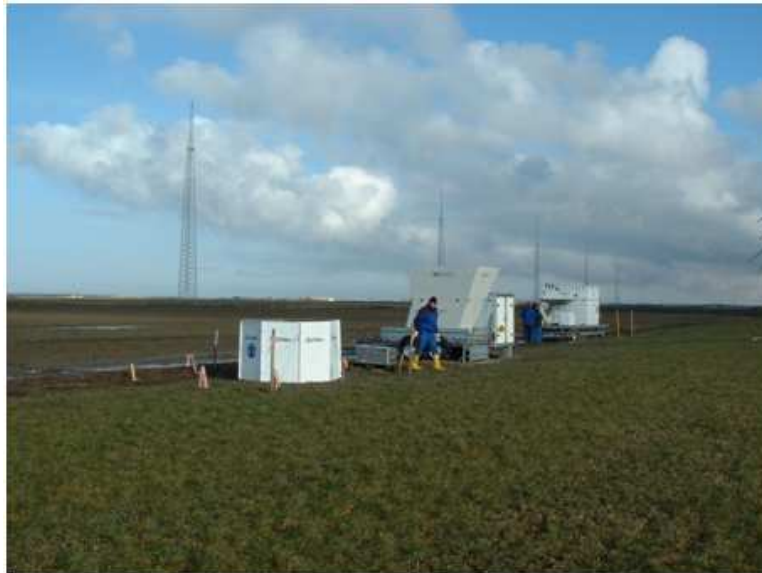
Figure 1. Commercial available sodars being inter-compared during the WISE 2004 experiment: An array of sodars (and one lidar) during inter-comparison and testing against the tall met towers (up to 168 m above ground) equipped with calibrated cup anemometers at several heights. Venue: The Test station for large wind turbines, Høvsøre, Denmark

acterized by relatively high turbulence levels. Turbulence is here created from the strong wind shear due to the proximity of the Earth's surface. The wind speed at the ground is always zero, both on and offshore.

Sodar is a RS methodology for measurements of the wind speed and direction aloft at various heights in the atmosphere. Sodars are ground-based instruments that transmit a sequence of short bursts of sound waves at audible frequencies (2000–4000 Hz) upward in three different inclined directions into the atmosphere.

The sodar measurement technology was well established and in operational use for decades by now, starting in the 1980's where they served environmental protection issues and has been extensively applied to atmospheric research for environmental protection air pollution prediction measures well before the present burst in wind energy research and application. In Germany for example, sodars have been commissioned on several nuclear installations to replaced tall meteorological towers and serve now as operational monitoring devises of the local wind speed, direction and atmospheric stability.

As the sound waves from a sodar propagate forward a small fraction of the transmitted sound energy is scattered and reflected in all directions from temperature differences and turbulence in the atmosphere. A very small fraction of this scattered energy reaches back into the sodar's detector, which in principle is a directional-sensitive microphone.

The height at which the wind speed is measured is usually determined by the time delay in the backscatter from the transmitted pulse. Under standard atmospheric conditions with sound propagation speed of about 340 m s^{-1} backscatter from a sodar measurement at 170 m height above the ground will reach back into the detector after 1 s delay time.

The wind speed component in the transmitted beam direction is subsequently determined from the Doppler shift observed as frequency difference between the transmitted frequency and the frequency of the received backscattered sound wave. By combining the measured wind speed components obtained in this way from three differently inclined sound path directions, e.g. from one vertical and two inclined sound paths, the three-dimensional wind vector including wind speed and direction and tilt can be measured by sodar from preset heights from the ground and up to the limit determined by the sodar's lowest acceptable Carrier-to-Noise (C/N) ratios.
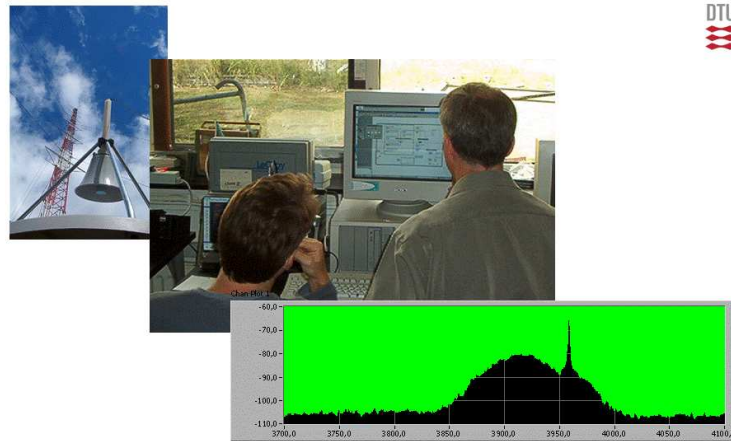
Figure 2. Calibration, laboratory work, and real-time Doppler spectrum obtained at Risø DTU with the experimental bi-static CW sodar "Heimdall" (Mikkelsen et al., 2007). Upper panel: Combined acoustic horn and parabola antenna for high-yield (+30 dB gain) backscatter receiving of sound waves. Middle panel: Two researchers at the Risø DTU Laboratory while testing of the bi-static sodar. Lower panel: A real-time obtainable continuous Doppler spectrum Heimdall bi-static sodar from wind measurements at 60 m above Risø DTU

The above description is for a mono-static system, where transmitter and receivers are co-located on the ground. But alternative configurations, e.g. in the form of so-called bi-static sodar configurations exist as well, where the transmitter and receivers are separated e.g. 100–200 meters on the ground.

Bi-static configurations have significant C/N-ratio advantages over mono-static configurations for wind energy applications. Received backscatter in a bi-static configuration is not limited to direct (180°) backscatter from temperature (density) fluctuations only, but enables also backscatter contributions from the atmospheric turbulence. And the higher the wind speed the more turbulence.

As a consequence significant improvements of the C/N- ratios can be obtained from a so-called "bi-static configuration", in which the transmitter and the receiver are separated from one another on the ground. This becomes in particular relevant during strong wind situations, where the background noise level increases with the wind speed.

A particular configuration considered for wind energy applications is therefore the bi-static continuous wave (CW) sodar configuration. Alternatively to the range gating in a pulsed system, the range to the wind speed measurement in a CW system can be determined by well-defined overlapping transmission and receiving antenna functions. At Risø DTU we have build and investigated such a sodar system for wind energy applications.

RS applications within Wind Energy

Remote sensed wind speed measurements are needed to supplement and extend tall met mast measurements, on and offshore, and within research to evaluate various wind flow models and wind atlases for a number of purposes, including:

1. Wind resource assessments

2. Wind park development projects

3. Power curve measurements

4. Bankability

5. Wind model and wind resource (wind atlas) uncertainty evaluation

The common denominator in most of these issues is high accuracy, and with a demand for reproducible certainty to more than 99% of what can be achieved with a corresponding calibrated cup anemometer. A significant source for uncertainty with RS instrumentation relative to a cup anemometer, and for sodars in particular, is the remote instrument's relative big measurement volumes. A sodar measuring the wind speed from say 100 m height probes a total sampling volume of more than 1000 m^3, whereas a cup anemometer is essentially a point measurement device in this connection. In addition the sodar's measured wind components are displaced in space and time, which makes the interpretation of measured turbulence by a sodar impaired. In addition the huge sampling volumes will be putting restrictions on measurements in non-uniform flow regimes such as found near forest edges, on offshore platforms, and over hilly or complex terrain.

Sodar's RS is also in demand for direct turbine control integration, wind power optimization and turbine mounted gust warning systems, but here the demand on accuracy and reliability is correspondingly high. Today, sodars are typically used to measure 10-min averaged vertical profiles in the height interval between, say 20 and 200 m above the ground, of the following quantities:

- Mean wind speed

- Mean wind directions (including azimuth and tilt)

- Turbulence (all three wind components: longitudinal, transverse and vertical)

Albeit significant inherent scatter persists in sodar measured mean wind speed and direction data average mean wind speed compare relatively well (in most cases to within $\pm 3\%$) to that of a corresponding cup anemometer measured wind speed, cf. the slopes of the scatter plots in Figure 3.

However, the correlation coefficients between sodar and cup anemometer data is, depending on measurement height and atmospheric stability, relative poor as compared to a cup-to cup anemometer correlation, where the two cups are separated by $\sim$ 100 m (typically less than 0.95) and reflects, among other issues, that a mono-static sodar measures the wind speed over a huge volume whereas the cup anemometer represents a point measurement. In addition, increased scatter will occur as a result of beam-bending due to the relative big wind speed to propagation speed of the sound pulses. Also notable is that sodars are able to make only a single 3D vector speed measurement about once per 6–10 s. A slow sampling rate also makes the mean prediction of a 10-min averaged quantity uncertain, due to limited independent sampling counts. In his note "Statistical analysis of poor sample statistics", Kristiansen (2010) has shown that "counting" uncertainty in terms of relative "standard deviation of the sample variance" in a small sample can give rise to a $\sim$ 10% relative uncertainty when averaged quantities are drawn from a set of only 100 independent samples.

It is also seen from the sodar vs. cup anemometer data in Figure 3 that difficulties with the C/N ratio can occur when wind speeds exceed approximately 15 m s^{-1}, which by the way is a nominal wind speed for a wind turbine. This is due to high background noise and the loss of backscatter in neutrally stratified high wind speed regions.

Recently relative good agreements over forested areas have nevertheless been seen ($< 1\%$ discrepancy) between sodar and cup anemometer mean turbulence intensity has been reported by Gustafsson (2008). However, turbulence intensity, which is the stream wise turbulence component relative to the mean wind speed, is in a 10-min averaged quantity dominated, particularly in forested areas, by the most energy containing eddies, which in this case will be larger than the sodar's sampling volumes and therefore be well represented in the statistics. However, the smaller scales including turbulent eddies with wind gusts must be anticipated to be present also on the scales smaller than a mono-static ground based sodar will be able to capture.

While sodars appears to be able to measure accurately both the mean winds speed and the turbulence intensities at a turbines hub height it was found more difficult to use a
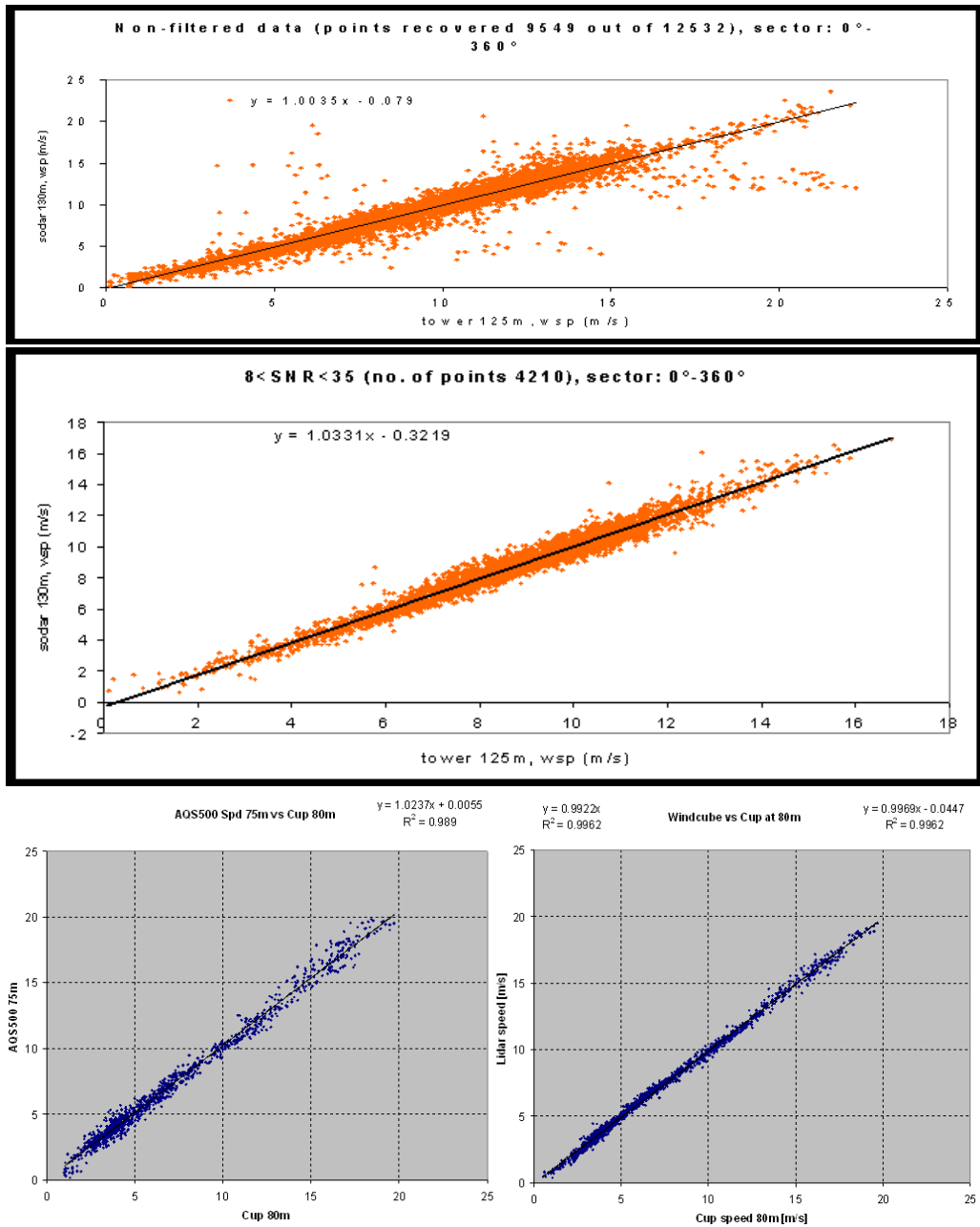
Figure 3. Example of scatter plots from sodar vs. cup anemometer data. The upper graph presents unscreened sodar wind speed data plotted against corresponding high-quality cup anemometer data measured at the Risø DTU met tower at 125 m. A data availability corresponding to 76% (9549 10-min averaged wind speeds) was obtained during this particular sodar vs cup anemometer inter-comparison test of almost three month duration (12532 10-min periods). The middle data graph shows the same data set after screening of the sodar data for high C/N-ratios. The scatter is significantly reduced, but so is also the data availability which with only 4210 data points has been reduced to almost 34%. The bottom panel shows (left) simultaneous measured sodar vs cup scatter plo tat 75 m height (0.989) and (right) lidar vs the same cup for the same data period. The lidar measurements at 80 m are seen to exhibit less scatter and high correlation coefficient (0.996)

sodar for accurate measurements over the entire rotor plane due to low C/N ratio (Wagner et al., 2008). There are several sodar manufactures on the wind RS market today including for example Remtech, Atmospheric Systems Corporation (formerly Aeroviroment), Metek, Scintec, Second Wind Inc. and Swedish AQ System to mention the most dominant. All but one base their sodar technology on mono-static phased array antenna configurations except AQ System sodars which are build on three solid dish parabolas offering a somewhat bigger antenna directivity (12° opening angle). However, only a couple of today's sodar manufacturers address directly the high accuracy demanding wind energy market.

The EU WISE project addressed and evaluated commercial sodars for wind energy (deNoord et al., 2005) and concluded then that neither of the commercial sodars were particularly close to be able to substituting standard measuring masts. In conclusion the WISE project stated that general purpose commercial sodars were unreliable, especially in case of bad weather or high background noise

Recent developments

A few improvements seem to have emerged since 2005. Particularly for the few sodars that addresses the wind energy marked. Replacement of the phased arrays by parabola dish seems to have contributed to the sodars overall C/N performance. Also better and improved signal processing is apparently applied today. However, it is my personal belief that we won't see any significant quantum leap in sodar performance until sodars for wind energy applications are build on bi-static configurations. Research and development along these lines are in progress, and researchers and test engineers at Risø DTU are looking forward to see and to test possible future bi-static configured sodars especially designed to meet the high accuracy demands set within wind energy RS.

Table 1. Pros & Cons of sodars

Pros	Cons
Portable	Low duty cycle (1 pulse transmitted every 3 s, and up to 6–10 s lapse times before all three wind components have been sampled)
Build on well developed and well-proven audio-frequency "low tech" technology	Limited by low S/N- ratio at: 1) high wind speed conditions 2) during neutrally stratified conditions
Sodars are relatively cheap (priced down to some 25% of a corresponding wind lidar)	Prone to solid reflections from the surroundings (including wind turbines)
Low power consumption (one solar powered version uses less than 10 W)	Prone to high background environmental noise
Sound backscatter: Relatively high yield (backscattered power at the detector of the order of 10^{-10} W)	Low wavelength/aperture ratio (1:10) results in undefined broad antenna beams Prone to beam bending with wind speed of the order of 5% or higher of the speed of sound Huge measurement and sample volumes Signal processing limited by pulsed sodars relative long data acquisition times (sampling time per pulse of the order of 1 s)

Table 2. Accuracy with sodars during neutral conditions

Slope mean wind speed vs. calibrated cup anemometers	$\pm 3\%$
Correlation coefficients [at 125 m, neutral stratification]	0.9–0.95
Mean turbulence intensity[at 80 m]	$< 1\%$ error

Summary of sodars

Most of today commercially available sodars are still build on "pre wind energy era" antenna design and processing technology, which do not in particular address nor support the high accuracy demands required within wind energy and resource assessment studies of today. The consequence is that most – if not all – of the available sodars today still exhibit insufficient accuracy to be accepted by the wind energy industry and society as an accurate RS tool for precise and "bankable" wind energy investigations.

Although some improvements seem to have occurred in accuracy since our first 2005 WISE sodar investigation, it is still not this author's belief that sodars as they come will be able to meet the high accuracy demands of the wind energy society in the future unless a major quantum jump can be demonstrated in their overall performance at high wind speed, neutral atmospheric stratification, and at present wind turbine hub heights (> 100 m).

At Risø DTU we see two venues for further research along which improved accuracy of sodars may happen: One is to switch to fully bi-static pulsed or CW based sodar configurations, however cumbersome, and the other is to take advantage of the immense, fast and cheap embeddable processing power set to our disposal from the information technology industry today, and apply these for enhanced on-line real time signal processing.

1.3 Part II: RS of wind by light (lidars)

Introduction to lidars

The motivation and demand in the wind energy market for wind lidars are similar to those of wind sodars. At a continuously increasing rate today wind turbines are being installed on, offshore, in hilly and forested areas, and even in complex or mountainous terrain. At the same time, as the turbines gets bigger and more powerful, they also reach higher and higher into the atmospheric flow, and thereby also into hitherto unknown wind and turbulence regimes – on as well as offshore.

The industry's traditional method for performing accredited and traceable measurements of power performance is to mount a single accurately calibrated cup anemometer at hub height two to four rotor diameters upwind in front of the turbines on a tall meteorological mast. IEC 61400-12-1 describes the accepted standard for power performance verification (power curve measurement) and prescribes measurements of power production correlated with wind speed measurements from a cup anemometer located at hub height in front of the wind turbine 2–4 rotor diameters upstream.

With turbines becoming bigger correspondingly high meteorology masts equipped with wind speed instrumentation becomes progressing more cumbersome and expensive to install, especially in mountainous and complex terrain. As wind turbines rotor planes reaches 120 m in diameter or more it is evident that the incoming wind field over the entire rotor planes is not measured representatively from a single cup anemometer mounted at hub height.

Accurate measurements of the inflow of today's huge wind turbines will require multipoint multi-height wind measurements within the entire rotor plane, to characterize the wind speed and wind shear over the entire rotor plane. Research activities addressing detailed rotor plane inflow and wakes is ongoing at Risø DTU in connection with the
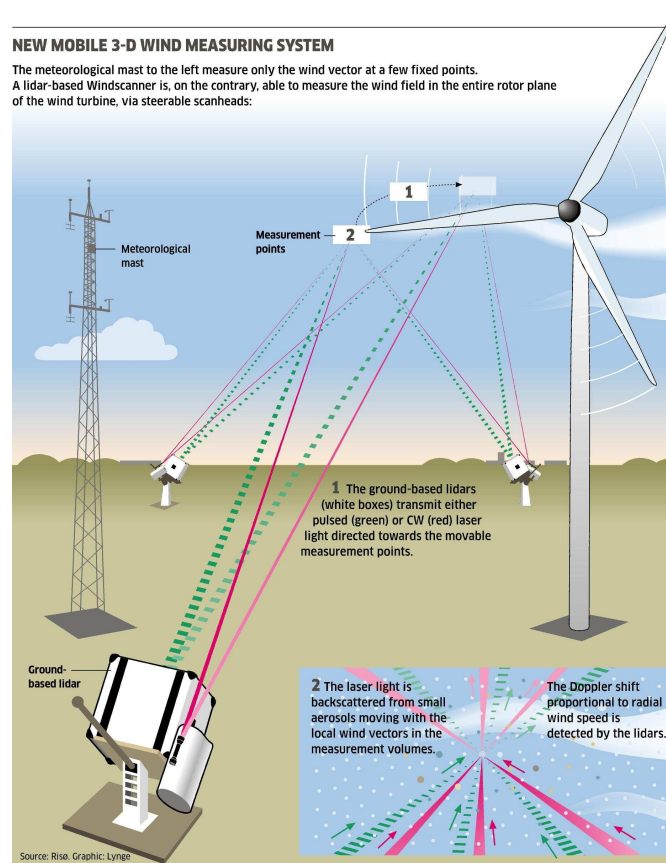
Figure 4. Windscanners in operation – CW and pulsed wind lidars engaged in measurements of the wind and turbulence fields around a spinning wind turbine (See Windscanner.dk for more details)

establishment of new research infrastructure based on wind lidars, see Windscanner.dk and Mikkelsen et al. (2008).

Wind RS methodologies

RS measurement methodologies for wind energy applications are today commercially available and encompass various measurement techniques that include sound based sodars, laser based lidars and satellite borne scatterometry. The application range for wind measurements are also plentiful, and encompass for example:

1. Wind turbine power performance verification – Establishment of new RS based measurement standards for the replacement of in-situ reference met masts. Work within the IEC is at the moment aiming at establishment of a new international IEC-standard for remote sensed wind measurements, as e.g. obtained by lidars, for power curve measurements.

2. Wind energy resource measurements – The global wind resources are now being mapped globally on shore, off shore, over hilly and in mountainous terrain, etc. Here also, high accuracy is of uttermost importance for accurate site and resource assessments. Measurement errors in excess of 1% are unacceptable by project developers and investment banks.

3. Wind turbine control – RS lidar instruments that are directly integrated into the wind turbines hub or spinner or even into the blades are also seen as a forthcoming RS measurement technology that can help improve the wind turbines power performance

and possibly also diminish fatigue wear from extreme gusts and wind shear via active steering the wind turbines individual blade pitch or, to come one day maybe, its trailing edge flaps.

Researchers at Risø DTU have during decades now followed and contributed to the development of improved instrumentation for RS of wind. Starting out already in the 60's with more general boundary-layer meteorological investigations of flow and diffusion our present research and experimental developments within the meteorology and test and measurement programs at Risø DTU has recently become more and more directed towards applications within wind energy. Wind lidars and lidar-based wind profilers, their measurement principles, their measurement performances, and also their possible future integration within wind turbines themselves are here addressed.

Wind lidars

Measuring wind with a wind lidar means to probe the atmospheric flow from the ground by use of light beams. A wind lidar is wind measurement devise able to detect the Doppler shifts in backscattered light. The Doppler shift is proportional to the wind speed in the beam direction in the wind lidar's adjustable measurement volumes.

Lidars, like sodars, provide a ground-based RS measurement methodology for measuring the winds at various ranges, angles and heights aloft. Wind lidars work by transmitting electromagnetic radiation (light) from a laser with a well-defined wavelength in the near infrared band around 1.5 μm. They detect a small frequency shift in the very weak backscattered light, a Doppler shift that results from the backscattering of light from the many small aerosols suspended and moving with the air aloft.

From a meteorological point of view wind turbine are "obstacles" within the lowest part of the atmospheric boundary layer, that is, the part of the atmosphere best characterize by high wind shear, strong wind veers, and with the highest levels of turbulence.

A wind profiler is a ground-based wind lidar transmitting a continuous beam or a sequence of pulsed radiation in three or more different inclined directions. A wind profiler determines the radial wind speeds in multiple directions above its position on the ground. It does so also by determining the Doppler shifts in the detected backscattered radiation along each beam direction. Wind lidars, like sodars, therefore have both transmitting and receiving antennas, which most wind profilers today combine into a single optical telescope. The three-dimensional wind vector as function of height by measuring the radial wind speeds in three or more beam directions above the lidar. In practice, the transmitting and receiving radiation are combined in a single telescope and the beam is then steered in different directions via a rotating wedges or turning mirrors.

Wind lidars in the market for vertical mean and turbulence profile measurements are available based on two different measurement principles:

1. Continuous wave (CW) lidars

2. Pulsed lidars

Several wind lidars addressing the wind energy market are commercial available today. CW-based wind lidars are manufactured by Natural Powers (ZephIR) and OPDI Technologies & DTU Fotonik (WINDAR) while Coherent Technologies Inc. (Wind tracer), Leosphere (WindCube), CatchtheWindInc (Vindicator) and Sgurr Energy (Galion) manufacture pulsed lidars for the time being.

The technology imbedded in today's CW and pulsed wind lidar systems have been spurred from the telecommunication 1.5 μm fiber and laser technology revolution in the 90's. There are however, some principally differences between CW and pulsed lidar's temporal and spatial resolution, properties that have influence on the different lidar types ability to measure and resolve the mean wind and turbulence characteristics of the atmospheric boundary layer wind field.

Figure 5. Two CW wind lidars belonging to the Windscanner.dk research facility being inter-compared and tested up against the tall meteorological masts at Høvsøre, Risø DTU.

The CW lidar focuses a continuous transmitted laser beam at a preset measurement height and there determines, also continuously, the Doppler shift in the detected backscatter also from that particular height. When wind measurements from more than a single height are required, the CW lidar adjusts its telescope to focus on the next measurement height. The measurement ranges (measurement heights) as well as the spatial resolution of a CW lidar measurement is controlled by the focal properties of the telescope. The shorter the measurement distance, and the bigger the aperture (lens), the better defined is a CW lidar's range definition and its radial measurement confinement. A CW lidar resolves the wind profile along its beam in a similar manner as a photographer controls the focal depth in a big sport or bird telescope.

The focal depth of any telescope, however, increases proportional to the square of the distance to the focus or measurement point. This optical property limits a CW lidar build with e.g. standard 3"optics to measurement heights below, say 150 m.

A pulsed lidar on the other hand transmits a sequence of many short pulses, typical 30 m in effective length, and then it detects the Doppler shift in the backscattered light from each pulse as they propagate with the speed of light. While a CW lidar measures from one height at a time a pulsed lidar measures wind speeds from several range-gated distances simultaneously, typically at up to 10 range gates at a time.

The pulsed lidar's spatial resolution, in contrast to the CW lidar, is independent of the measurement range. The pulse width and the distance the pulse travels while the lidar samples the detected backscatter control its resolution. The spatial resolution in the beam direction obtainable with the 1.5 μm wavelength pulsed lidar in the market today are of the order of 30–40 m.

In addition, while a CW lidar's upper measurement distance is limited progressing unconfined measurement volume at long distances, a pulsed lidar's maximum measurement range is limited by deteriorating C/N-ratios in measurements from far distances (height).

Moreover, while a CW lidar equipped with a 1 W 1.5 μm eye-safe laser has been tested able to sample and process up to 500 wind speed measurements per second, a corresponding powered pulsed lidar can handle only 2–4 wind speed samples per second.

Figure 6. CW wind lidars (ZephIRs) under testing at Høvsøre, Risø DTU

Each of these samples, however, then on the contrary contain wind speeds from up to 10 range gates (ranges) measured simultaneously.

CW vs pulsed lidars   Overall, CW lidar features high spatial resolution in the near range and very fast data acquisition rates, features that are well suitable for turbulence measurements. Today's commercial available CW lidar profilers measure radial wind speeds at ranges up to ~ 200 m and wind vectors at heights up to 150 m.

The pulsed lidar configuration on the other hand features lower but always constant spatial resolution properties (30–40 m) at all ranges. They are also inherently slower in their data acquisition rate, but then they measure wind speeds at multiple heights simultaneously, and they hold also potential for reaching longer ranges (heights) than corresponding powered CW lidars. At the test site in Høvsøre Risø DTU, commercial available pulsed wind lidar profiles have regularly measured the wind vector profiles up to 300 m height.

Wind profiling

A wind "profiler" measures 10-min averaged quantities of the vertical wind speed profile, the vertical direction profile, and the vertical turbulence profiles, by combining a series of radial measured wind speed components from several, and at least three, different beam directions, into a three-dimensional wind vector. CW-based wind lidars, e.g. the ZephIR, measure the vertical wind profile at five consecutive heights, selectable in the range from, say 10 to 150 m height. Pulsed lidars, e.g. the WindCube or the Galion, measure correspondingly the vertical wind profile simultaneously at several (of the order of 10) heights, in the height interval from 40–~ 300 m, the upper bound depending on the amount of aerosols in the air.

True for all wind profilers in the wind energy market, however, CW and pulsed lidars irrespectively, is that they rely during combining measured radial wind speeds into a single wind vector on the assumption that the flow over the wind lidar is strictly homogeneous. Homogeneous wind flow means that the air stream is unaffected and not influenced by hills, valleys, other wind turbine wakes, or near-by buildings within their volume of air scanned above the lidar.

Figure 7. Pulsed wind lidars (six WLS7 WindCubes) and one Galion (far back) during testing at Høvsøre, Risø DTU

For this reason, neither lidar nor sodar based wind profilers will be able measure correctly over sites located in hilly or complex terrain where the wind field is affected by the near-presence of hills or upwind turbines. Easily, up to $\sim 10\%$ measurement errors can be observed between wind speeds measured by a lidar and a mast-mounted cup anemometer co-located to take wind profile measurements from the on top of a hill. Research is therefore ongoing in order to correct wind lidar based profile measurements for flow distortion e.g. induced by terrain effects (Bingöl et al., 2008).

Lidar accuracy

Inherently, lidars can remotely measure the wind speeds aloft with much higher accuracy than a sodar. This is due to the nature of light, which propagates ~ 1 million times faster than a sound pulse, and because a lidar's antenna aperture size compared to the wavelength, i.e. "lens diameter-to-wavelength ratio" in a lidar is about 1000 times bigger than practically obtainable with a sodar. This result in superior beam control and also in much higher data sampling rates.

At Risø DTU's test site at Høvsøre, testing and calibration of wind lidar is now daily routine and is performed by inter-comparing and correlating lidar-measured wind speeds with wind speeds from calibrated cup anemometers in our 119-m freely exposed tall reference met mast. During "fair weather conditions", 10-min averaged wind speeds from lidars and the cups are in-situ intercompared and correlated. Linear regression coefficients with both CW and pulsed lidars could be obtained in the range of $\sim 0.99 - 1.00$, and correlation coefficients as high as ~ 0.99 (Wagner et al., 2009).

"Fair weather" means here that lidar data are screened for periods with rain, fog, mist and low-hanging clouds and mist layers. Usually this only removes a few per cent of the data. All lidars, CW and pulsed included, rely during determination of the wind speed from Doppler shift measurements on the assumption that the aerosols in the measurement volumes are homogeneously distributed and follow the mean wind flow.

Sodars for that matter, can under ideal conditions perform almost similarly well with respect to mean wind speed (linear regression coefficients as high as ~ 0.99 has been reported above). The observed scatter, however, as compared to a lidar, is bigger. Correlation coefficients observed while testing of sodars at Risø DTU's 125 m tall met mast

at wind energy relevant neutrally stratified strong wind conditions (> 10 m s^{-1}) has so far not been observed to exceed the 0.90 level.

Wind lidar applications for wind energy

Wind lidar manufactures today address the market for replacement of tall reference meteorology mast installations at the moment required for accredited and bankable wind resource measurements and for ground-based wind turbine performance measurements. Lidar manufactures also offer their wind lidars as instruments for evaluation of model-based wind resource estimation, on and offshore (numerical wind atlases).

Wind lidars in the market today offer the wind energy industry with RS instruments, for:

- Wind speed, wind direction and turbulence profiling.

- Wind resource assessments, on and offshore.

- Wind turbine performance testing (power curves).

- Wind resource assessment via horizontal scanning over complex terrain.

Further developments   Furthermore, new and improved wind lidar data and measurement technologies are under development for RS-based power performance measurements from the ground but also directly from the wind turbines. A conically scanning wind lidar (Control-ZephIR) has during the summer 2009 been tested in a operating NM80 2.3 MW wind turbine located at Tjæreborg Enge, Denmark, with the purpose to investigate the use of wind lidars integrated directly into the wind turbine hubs, blades or spinners. The intention is to improve the wind turbine's performance by use of upstream approaching wind speed measurements from inside the turbines rotor plane as an active input to the wind turbines active control systems. Wind lidars for turbine yaw control are already nowadays on the market (Vindicator) and new and smaller wind lidars are in the near-future envisioned to become integrated as "standard" on wind turbines to provide upstream lead time wind data to the turbines control system, e.g. for:

- Enhanced wind turbine yaw control.

- Lead-time control for individual pitch control.

- Protection against fatigue from extreme wind shear and wind gusts.

- Prolonging the wind turbines longevity.

- Improving the wind turbine productivity.

Summary of lidar

Since the wind lidar era started at Risø DTU in 2004 new wind lidars have emerged on the wind energy market, spurred by the telecom technology revolution of the 90's. Today, wind lidars, continuous and pulsed, and properly calibrated, aligned, installed and maintained, and their volume-averaged wind measurements properly interpreted, are indeed very precise wind measuring devises, capable of matching the wind industry's needs today and in the future for precise and reproducible wind profile measurements and resource assessments.

Before, however, lidar measured wind measurements can become fully certified and accredited to industry standards, new and revised IEC lidar standards have first to be set and come into effect. It is important, however, here also to apprehend the very different nature of the previous standards point measurements as obtained from a mast-mounted cup anemometer and a volume-averaged wind vectors as obtainable from a profiling wind lidar.

Although the first generations of wind lidars, CW and pulsed, indeed had many difficulties with reliability, this era now seems to have been improved beyond their first children growth pains. Today's wind lidars offer realistic and mobile alternatives to the installation of tall meteorological masts for many wind resource estimation assessment studies, on and offshore. The near future will inevitably also show turbine mounted wind lidars fully integrated with the wind turbines control systems for improving the wind turbines productivity and longevity.

Notation

CW	continuous wave
C/N	carrier-to-noise
lidar	light detection and ranging
RS	remote sensing
SAR	synthetic aperture radar
sodar	sound detection and ranging

References

Bingöl F., Mann J., and Foussekis D. (2008) Lidar error estimation with WAsP engineering. *IOP Conf. Series: Earth and Environ. Sci.* **1**:012058

de Noord M. et al. (2005) Sodar power performance measurements, WISE WP5.

Gustafsson D. (2008) Remote wind speed sensing for site assessment and normal year correction – The use of sodar technology, with special focus on forest conditions. Master of Science Thesis in Energy Technology, KTH, Stockholm.

Mikkelsen T., Jørgensen H. E., and Kristiansen L. (2007) The Bi-static sodar "Heimdall" – you blow, I listen. Risø-R-1424(EN), Roskilde

Mikkelsen T., Courtney M., Antoniou I., and Mann J. (2008) Wind scanner: A full-scale laser facility for wind and turbulence measurements around large wind turbines. *Proc. of the European Wind Energy Conf.*, Brussels

Wagner R. and Courtney M. (2009) Multi-MW wind turbine power curve measurements using remote sensing instruments – the first Høvsøre campaign. Risø-R-1679(EN), Roskilde

Wagner R., Jørgensen H. E., Poulsen U., Madsen H. A., Larsen T., Antoniou I., and Thesberg L. (2008) Wind characteristic measurements for large wind turbines power curve. *Proc. of the European Wind Energy Conf.*, Brussels

Kristiansen L. (2010) My own perception of basic statistics. *Available on request from Torben Mikkelsen*, Roskilde

2 Climatological and meteorological aspects of predicting offshore wind energy

Rebecca J. Barthelmie[1,2], Sara C. Pryor[3,2], and Sten T. Frandsen[2]
[1]*Institute for Energy Systems, School of Engineering and Electronics, University of Edinburgh, Scotland*
[2]*Wind Energy Division, Risø DTU, Roskilde, Denmark*
[3]*Atmospheric Science Program, Department of Geography, Indiana University, Bloomington, USA*

2.1 Introduction

Objectives and chapter structure

This chapter reviews climatological and meteorological issues of power output from offshore wind farms. In section 2.1, we introduce the atmospheric structure and variability of wind resource estimation, the short-term fluctuations in the wind energy density and the behaviour of wind turbine wakes. We also describe the existing offshore wind farms from which examples are presented. Section 2.2 concerns the prediction of power output over the lifetime of a wind farm. This assessment of the resource normally occurs at the planning stage and includes lifetime variations in wind speed at hub-height over several decades, which is influenced by climate change. Since climatologically representative measurements of wind speed at hub-height at the location of a proposed wind farm are usually not available, we demonstrate how short-term site measurements may be related to longer-term historical data from a nearby site and how data measured close to the surface may be extrapolated vertically to hub-heights.

Offshore wind farms have regular multiple rows and columns of turbines, so wake effects (i.e. the effects on down-stream rotors of the perturbed wind and turbulence from upstream turbines) are significant and have to be incorporated in the generated power estimate of the entire wind farm. Hence, in section 2.3, we describe tools for evaluating wake behaviour and we illustrate the potential importance of atmospheric boundary-layer phenomena not currently incorporated in standard models used for prediction of wind speeds and wake losses. In section 2.4, we review short-term prediction of power production by offshore wind farms, before providing, in section 2.5, a summary of key points raised in this chapter.

Scales of atmospheric variability

The atmosphere is constantly in motion. It may be characterised by (i) temporal periodicities and (ii) inherent horizontal spatial scales. These range:

- from turbulence (period $\leq$ seconds, spatial scale $\leq$ metre), traditionally referred to as *micro-scale*,

- to local, *meso-scale*, phenomena, such as thunderstorms (period $\sim$ hours, scale hundreds of metres to a few kilometres),

- to synoptic, *macro-scale*), transient weather systems (period $\sim$ days to months, scale continental to global).

The periods and scales are linked by energy exchange and each play a role in dictating the temporal variability of energy density in the wind at a given location.

Atmospheric stability

Atmospheric stability relates to the vertical exchange of momentum and of sensible and latent heat. The stability of the atmosphere indicates whether the atmosphere will develop turbulence or waves of growing amplitude. With stable stratification, the atmospheric flow is laminar (i.e. non-turbulent) because air flow at higher altitude (aloft) is decoupled from surface dissipation of momentum. Unstable conditions are characterised by turbulent mixing between air at different altitudes, with a significant contribution to this mixing from buoyancy forces (i.e. thermally generated eddies). At near-neutral stability conditions, the ambient turbulence is generated principally or solely from mechanical forcing (i.e. vertical wind shear due to surface drag).

So, why should wind turbine designers take atmospheric stability into account?

Under near-neutral atmospheric stability, the average change of wind speed with height has a logarithmic profile:

$$U_z = \frac{u_*}{\kappa} \ln\left(\frac{z}{z_o}\right) \tag{1}$$

where U_z is the wind speed at height z, κ is the dimensionless von Kármán constant (=0.4), z_o is surface roughness, and u_* is the friction velocity. u_* is related to the momentum flux (τ) at the surface by $U_z^2 = \tau/\rho$, where ρ is the air density, and by the dimensionless drag coefficient (C_D) from $U_z^2 = C_D U_{10}^2$, where U_{10} is the wind speed at 10 m above the surface.

Thus the change of wind speed with height is dictated by two time/space variables,

1. surface roughness length z_o, as dictated by the height of roughness elements,

2. the wind speed, U_z

The z_o of land surfaces is documented in the Davenport-Wieringa roughness-length classification (Wieringa, 1992), while water surfaces have a dynamic roughness dictated by the presence of wave-surface features (Charnock, 1955). Generally values of z_o for water surfaces are orders of magnitude less than for land surfaces.

When the atmospheric stability is not near-neutral, the change of wind speed with height is also dependent on the prevailing atmospheric stability. Stability corrections to the logarithmic profile of wind speed are small near the surface, but increase with height (Barthelmie, 1999a; Motta et al., 2005). Hence, as hub-heights of new wind turbines are increased, the role of stability in modifying the wind profile becomes more important, because the correction to the logarithmic profile is height dependent:

$$U_z = \frac{u_*}{\kappa}\left[\ln\frac{z}{z_o} - \Psi_m\left(\frac{z}{L}\right)\right] \tag{2}$$

where the function $\Psi_m\left(\frac{z}{L}\right)$ is dependent on height (z) and the Monin-Obukhov length (L).

The Monin-Obukhov length is a metric of the atmospheric stability and is given by the ratio of mechanically generated to buoyancy generated turbulence (Stull, 1988),

$$L = \frac{-\left(\overline{u'w'}^2 + \overline{v'w'}^2\right)^{3/4}}{\left(\kappa\left(g/\Theta_v\right)\left(\overline{w'\Theta_v'}\right)\right)} \tag{3}$$

$$\text{unit} = [(\text{m}^4\text{s}^{-4})^{3/4}]/[((\text{ms}^{-2})/\text{K})(\text{ms}^{-1})\text{K}] = (\text{ms}^{-1})^3/(\text{m}^2\text{s}^{-3}) = \text{m}$$

where the over-bar indicates a time average. Below S.I. units are given in brackets, g (m s^{-2}) is acceleration due to gravity, Θ_v (K) is the virtual potential temperature $\Theta_v = T(1 + 0.61q)(P_o/P)^{R/c_p}$, where T (K) is temperature, q (kg/m^3) is the specific humidity, P is the atmospheric pressure (mBar), P_o is a standard pressure (1000 mbar), R is the universal gas constant (8.31 J mol^{-1} K^{-1}), c_p is the specific molar heat capacity of air (J mol^{-1} K^{-1}), and $\overline{w'\theta'}$ is the kinematic heat flux (K m s^{-1}). Heat fluxes which are normally expressed as W m^{-2} can be put into kinematic form by dividing by the air density and the specific heat capacity for air (Stull, 2000). u', v', w' (m s^{-1}) are respectively the deviations of the wind speed components from their temporal averages (where u represents the west-east component, v the south-north component and w the vertical component). These components can be used to compute u_*:

$$u_*^2 = \sqrt{\overline{u'w'}^2 + \overline{v'w'}^2}. \tag{4}$$

As $|L|$ goes towards infinity, mechanically driven turbulence dominates and conditions are increasingly near-neutral. Table 1 summarizes the stability classification used herein (Van Wijk et al., 1990).

Table 3. Stability classes defined by Monin-Obukhov length

Monin-Obukhov length (L)	Stability class
$L = 0$ to 200 m	Very stable
$L = 200$ m to 1000 m	Stable
1000 m $> L > -1000$ m	Near-neutral
$L = -200$ m to -1000 m	Unstable
$L = 0$ to -200 m	Very unstable

Note that stability corrections are not equal in magnitude under stable and unstable conditions (i.e. for the same absolute value of the Monin-Obukhov length (Stull, 1988)). They are computed as follows. For $0 < L < 1000$ m (i.e. stable conditions):

$$\Psi_m\left(\frac{z}{L}\right) = \frac{4.7z}{L}. \tag{5}$$

For -1000 m $< L < 0$ (i.e. unstable conditions):

$$\Psi_m\left(\frac{z}{L}\right) = -2\ln\left(\frac{1+x}{2}\right) - \ln\left(\frac{1+x^2}{2}\right) + 2\tan^{-1}x - \frac{\pi}{2} \tag{6}$$

$$\text{where} \quad x = [1 - 15z/L]^{1/4}. \tag{7}$$

The turbulent kinetic energy per unit mass ($\overline{e}$) may be derived from the velocity vector variances:

$$\overline{e} = \frac{1}{2}\left(\overline{u'^2} + \overline{v'^2} + \overline{w'^2}\right). \tag{8}$$

In wind energy applications, the direction of the wind and the vertical components are ignored, so the dimensionless turbulence intensity (I) is computed by aligning the co-ordinates such that $v \to 0$ and hence defined as:

$$I = \frac{\sigma_U}{U} \tag{9}$$

where U is the mean horizontal wind speed and σ_U is the standard deviation of U ($\sigma_U = \sqrt{\overline{U'^2}}$).

Atmospheric turbulence intensity offshore is strongly linked to the dynamic nature of the sea surface, which itself is related to the low-level wind speeds (Barthelmie, 1999b). These wind speeds are dependent on the stability of the atmosphere. At small wind

speeds, turbulence intensity is large on average due to the dominance of thermally generated turbulence. The turbulence intensity decreases to a minimum at wind speeds between 8 and 12 m s^{-1}. At larger wind speeds, the sea surface waves increase in amplitude, and the rougher sea surface increases mechanically generated turbulence intensity of the wind.

The surface roughness of water is generally less than land, so, the offshore value of u_* is small compared with that for most land surfaces. Consequently mechanically generated turbulence over sea waves generally has less impact on stability and on total turbulence intensity than mechanically generated turbulence over land. Conversely stated, the influence of the heat flux (i.e. buoyancy generated turbulence) is generally larger over water surfaces than over land. Hence, the impact of deviations of atmospheric stability from near-neutral is generally more significant for offshore windfarms than for onshore windfarms. Turbine blade stress depends on the wind shear and turbulence, which in turn depend on the atmospheric stability. Consequently, the nature of the vertical wind profile, through which the turbine blades sweep and to which the turbine tower is subject, affects turbine design and performance. It is therefore essential that measurements are made and extrapolated for a resource and performance estimate prior to windfarm design and installation. Moreover, as discussed below, atmospheric stability also substantially impacts the propagation of wakes downstream of the wind turbines.

In addition to its influence on the wind speed profile, atmospheric stability also affects the distance for wind speeds to equilibrate with changed surface conditions and fluxes. This applies as winds pass from land to sea or vice versa. For instance, stable conditions, with reduced vertical momentum transfer, can persist for more than 200 km from the coast-line (Garratt, 1987), so producing very large wind-shear in the atmospheric surface-layer. However, this is only important for windfarms if conditions deviate from near-neutral at approximately $U > 4$ m s^{-1}, relating to turbine cut-in wind speeds (see below). For wind speed > 25 m s^{-1} (typically turbine cut-out wind speed) conditions can be assumed to be neutral. Since L is proportional to u_*^3, conditions tend to become more neutral as wind speed increases. However, stable conditions can persist to $U \sim 15$ m s^{-1} while unstable conditions appear to be less frequent offshore and not to persist at wind speeds more than about 10 m s^{-1} (Motta et al., 2005) (Figure 8).

The division of stability conditions at coastal or sheltered sites between stable/ neutral/unstable conditions is dictated principally by; (i) position of the site with respect to the coast and (ii) the prevailing synoptic meteorology. Offshore sites studied in the north of Europe usually show a large number of stable conditions in Spring, which is related to the lag in sea temperature compared to air temperature (of the order one month) (Figure 8). Similarly unstable conditions are more common in Autumn (Fall) and Winter. Since sea surface temperatures change little over the course of the day, stability offshore does not usually have the pronounced diurnal cycles that are experienced at land sites (Barthelmie et al., 1996).

In addition to the processes presented above, atmospheric stability also influences a number of other coastal phenomena, such as low-level jets which affect wind and turbulence in the Baltic Sea (Smedman et al., 1996) (and possibly other locations where they have been less intensively studied) and sea breezes (Simpson, 1994). Large scale effects, such as channelling, are also related to temperature differences between land and sea (Badger et al., 2006).

Describing wind speed distributions and relating wind speeds to energy density and power production

Although several different probability density functions have been matched to observed wind speed distributions, the two-parameter Weibull probability density function is most frequently applied. This generally gives a good fit to observed wind speed distributions, particularly over water surfaces (Pavia and O'Brien, 1986). The probability distribution, $p(U)$, of wind speed, U, has the following form (Barthelmie and Pryor, 2003a; Pryor et al,
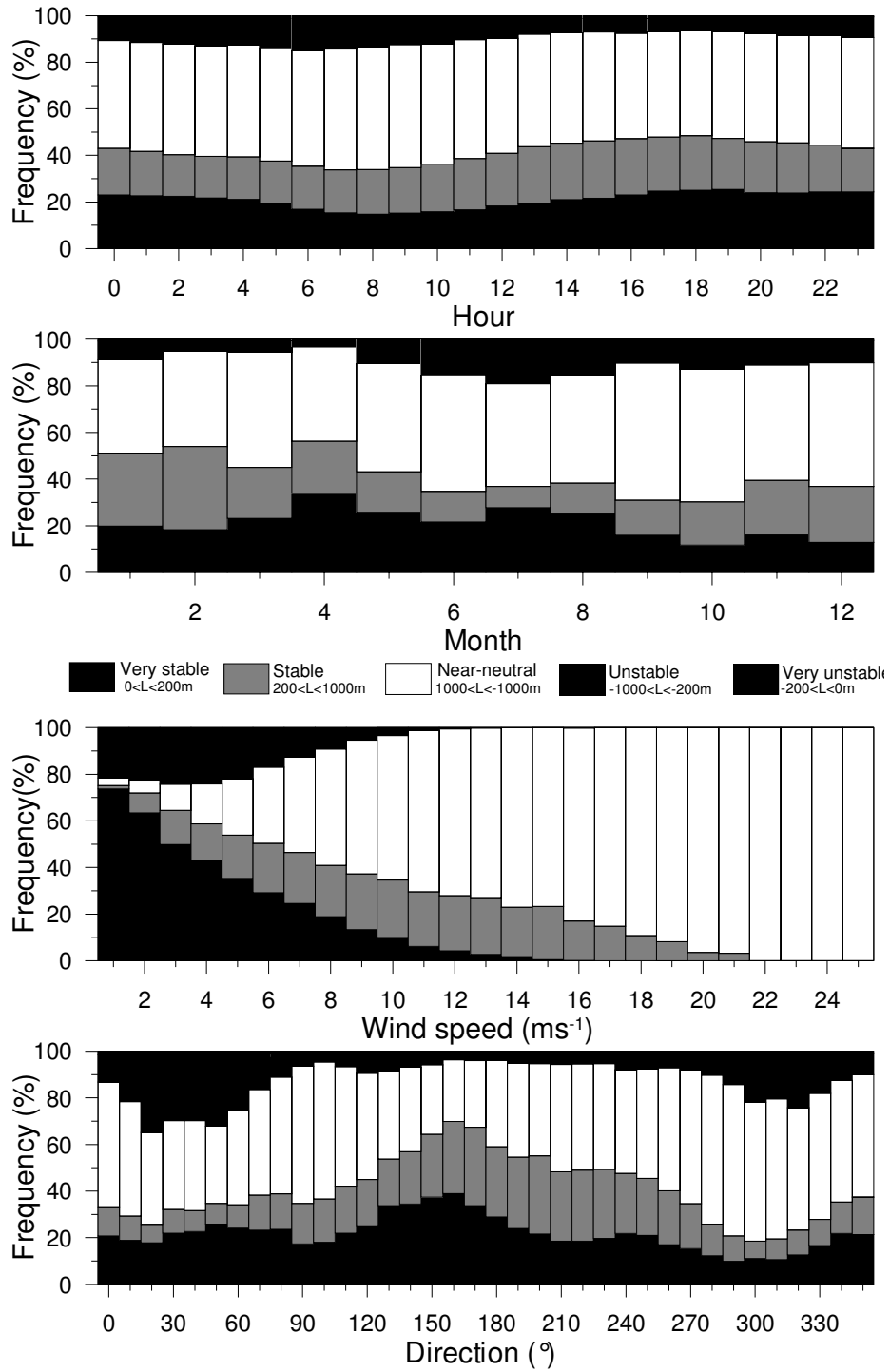
Figure 8. Typical stability climate of an offshore site in Denmark (Vindeby). The four frames show the percent frequency of different stability classes (see Table 3) in terms of the diurnal and seasonal variability (above) and their distribution with wind speed and direction. See the end of this section for a description of this site.

2004):

$$p(U) \equiv \frac{k}{A} \left(\frac{U}{A} \right)^{k-1} \exp \left[- \left(\frac{U}{A} \right)^k \right] \quad \text{for } U \geq 0, A > 0, k > 0. \tag{10}$$

The parameters are the dimensionless shape parameter (k), which describes the 'peaked-ness', of the distribution and the scale parameter (A), which is a measure of the central tendency.

The cumulative probability distribution is given by:

$$P(U) \equiv 1 - \exp\left(\frac{U}{A}\right)^k \tag{11}$$

where $P(U)$ describes the probability that the wind speed has a value less than or equal to U. The Weibull A and k parameters can be used to compute (or can be computed from) the mean wind speed ($\overline{U}$):

$$\overline{U} = A\Gamma\left(1 + \frac{1}{k}\right) \tag{12}$$

where Γ is the gamma function, defined as

$$\Gamma\left(1 + \frac{1}{k}\right) = \int_{v=0}^{\infty} v^{1/k} e^{-v} dv$$

for which standard functions are published in mathematical texts. Also, for percentiles (X^*100) of the wind speed distribution:

$$U_X = A\left(-1 \cdot \ln\left(1 - X\right)\right)^{1/k} \tag{13}$$

The instantaneous wind energy density (i.e. power per unit area of wind front), E is :

$$E = 0.5\rho U^3. \tag{14}$$

Or an "expected" average energy density may be derived from the Weibull distribution parameters:

$$E = \frac{1}{2}\rho A^3 \Gamma\left(1 + \frac{3}{k}\right). \tag{15}$$

The power production of a wind turbine is non-linear with wind speed (Figure 9). Electricity generation begins at the cut-in wind speed (U) of ≈ 4 m s^{-1}, and the power generation increases rapidly to the rated (name plate) power at typical wind speeds of approximately 12 to 15 m s^{-1}. The power production is constant for wind speeds greater than this threshold until cut-out wind speed is reached, the turbine rotation is stopped for safety reasons. The accurate relationship between ambient wind speed and electricity generation is specific to each turbine. Standard power curves are supplied by the manufacturer for each type of turbine and these can be used to predict energy generation from the expected wind speed distribution at the site. Such predictions are in practice approximations, since the exact wind speed distribution at the site is unknown, individual turbines may perform slightly differently from the standard and the structure of the wind (e.g. turbulence) may differ from the standardisation site. For example, at the Middel-grunden offshore wind farm in Copenhagen harbour, measured annual energy output has been 5.7% more than predicted using the manufacturer's power curve (Vikkelsø et al., 2003).

Existing offshore wind farms in Denmark

Global installed wind capacity by the end of 2006 was about 73 GW and the annual average growth rate for installed global capacity is almost 25%/y, including increasing capacity from offshore installations (IEA, 2005). In 2004 wind energy supplied 18.5% of Danish electricity. By 2006 Danish offshore wind farms had a capacity of over 400 MW, relative to a total national wind capacity of over 3000 MW. In this chapter we present specific examples drawn from Danish offshore wind farms, particularly those located at; Vindeby, Horns Rev, and Middelgrunden (Figure 10). The wind farm at Vindeby (Dyre, 1992) was the first offshore wind farm in the world, and this and the other two sites have extensive associated research into resource, wakes and loads (Frandsen et al., 1996; Barthelmie et al., 1996b; Jensen, 2004). Details of the wind farms are given in Table 4.
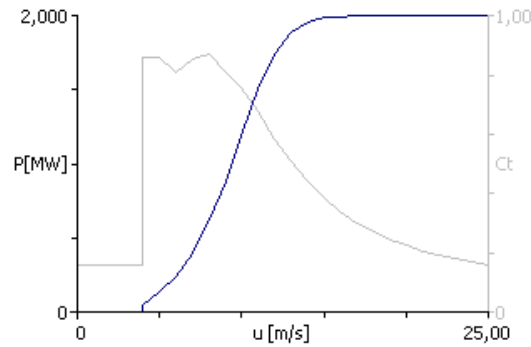
Figure 9. Bonus 2 MW power curve (i.e. power produced by the wind turbine, left ordinate) and thrust coefficient (Ct, right ordinate) as a function of wind speed (U).

Table 4. Offshore wind farms in Denmark operating in 2006

Name	Year of installation	#	Turbine type	Spacing	Hub height (m)	Rotor diameter (m)
Vindeby	1991	11	Bonus 450 kW	8.6D	38	35
Tunø Knøb	1995	10	Vestas 500 kW	5.1D (in row) 10.2D between row	43	39
Horns Rev	2002	80	Vestas 2 MW	7D	60	80
Nysted	2003	72	Bonus 2.3 MW	10.5D (E-W) 5.8D (N-S)	69	82.4
Middel-grunden	2002	20	Bonus 2 MW	2.4D (bow)	64	76
Samsø	2003	23	Bonus 2.3 MW		60	80
Frederiks-havn	2003	5	2 Vestas 3 MW 1 Bonus 2.3 MW 1 Nordex 2.3 MW			

2.2   Resource estimation

Typical wind farms are assumed to have an expected lifetime of 20 to 30 years. To predict the wind resource over the lifetime of a prospective wind farm it is usually assumed that the past wind climate can be used an analogy for the future. Thus the wind resource is implicitly assumed to be stationary (i.e. time invariant at time-scales beyond a few years) and consequently the only requirement for assessing the resource is a historical record of wind speeds at the proposed site. The stationarity of the actual wind resource can be difficult to ascertain; indeed the potential impact of global climate change on renewable energy supplies must be considered, especially the long-term wind climate.
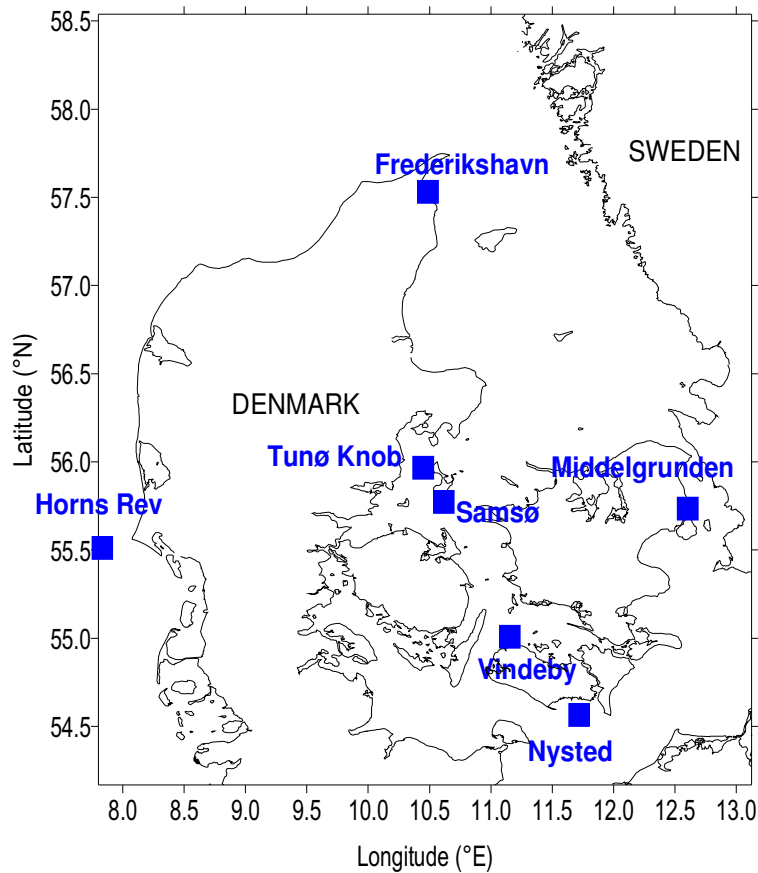
Figure 10. Location of Danish offshore wind farms (2006). See Table 4 for details of these installations.

Prediction of the wind resource on long time scales: impact of climate change

Historic variability It is difficult to characterise long-term variations in wind speeds effectively because, unlike other meteorological variables, such as temperature and precipitation, wind speeds have been measured using different types of instrument and often with poor accuracy and precision. Although innovative and robust measurement methods have been introduced (starting in the 1980's), trend analyses are confounded by the absence of long homogenised records. Additionally, even more than temperature and precipitation, wind speed measurements are strongly influenced by changes in site characteristics, such as the growth of trees or construction of buildings. For this reason there have been only a few studies of historic wind speed trends. These studies have tended to employ reanalysis data sets (Pryor and Barthelmie, 2003), derived using a state-of-the-art analysis/forecast system to model weather using relatively few past data as input. The aim is to generate historic global homogenised records with spatial resolutions of $\approx 2 \times 2°$ and typical temporal resolution of 4 hours (Kistler et al., 2001).

As an example of the potential impact of climate change on wind resource magnitude, we draw on previous research focussed on northern Europe and specifically the Scandinavian countries. This region has a relatively large penetration of carbon-neutral electricity from hydro and wind. For example, in Denmark over 18% of the annual electricity supply is derived from wind farms (IEA, 2005). Many wind energy projects were developed in this region during the 1990's on the basis of wind climates during the mid-1980's onwards. However, average wind speeds over the Baltic significantly increased over the second half of the twentieth century, with the majority of the increase being in the southwest of the region (Pryor and Barthelmie, 2003) (Figure 11) and in the upper quartile of the wind

speed distribution. This "large wind-speed" quartile has the largest impact on the wind energy production.
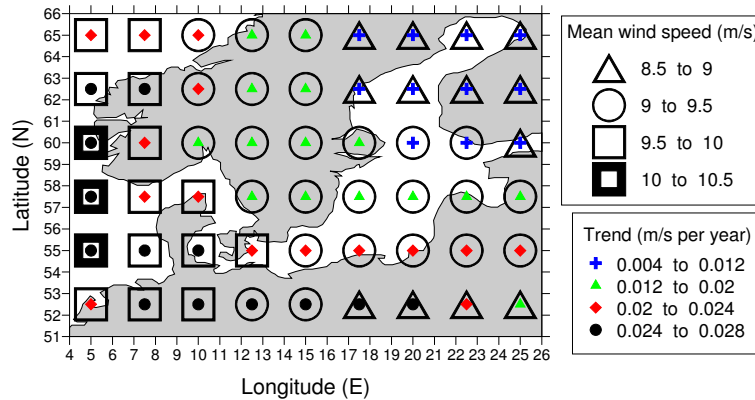
Figure 11. The mean wind speed and temporal trends in the 850 mb (approximately 1.5 km above mean sea-level) wind speed over Scandinavia from 1953–1999 (Pryor and Barthelmie, 2003) based on data from the NCEP reanalysis data set (Kistler et al., 2001; Kalnay et al., 1996).

These changes in wind speed are causally linked to variations in the synoptic scale circulation and the prevalence of a positive phase North Atlantic Oscillation (NAO) (Marshall et al., 2001), which is itself linked to the evolution of the global climate. The NAO index is a teleconnection index (a teleconnection is a link between atmospheric circulation in different parts of the globe) that links to the global scale climate via its dependence on (i) aspects of the primary circulation patterns of the atmosphere, and (ii) the low pressure associated with the polar front. The 10 latter divides the cold polar air from relatively warm mid-latitude air, and the sub-tropical "Azores high" that is a component of the descending limb of the Hadley cell. The NAO is computed from the pressure difference between Iceland and the Azores. It describes, in broad terms, the steering and intensity of low-pressure transient circulation systems into Europe (Hurrell et al., 2003). Positive NAO is associated with low-pressure systems (mid-latitude cyclones) moving northwards into the Baltic and can be characterised by westerly circulation with large wind speeds.

The Baltic region experienced a trend towards increased storminess and wind speeds starting in the 1960's, associated with increased prevalence of positive phase NAO that peaked in 1985–1990 and appears to have been broken in the mid-1990's (Pryor and Barthelmie, 2003; Alexandersson et al., 2000). This example (shown graphically in Figure 12) illustrates that, although wind energy developers frequently use a ten year period to describe the long-term variations in site wind speeds, trends in wind speeds or wind speed cycles can exist on much longer time scales (Pryor and Barthelmie, 2003; Pryor et al., 2005).

Note that local/regional changes in flow regimes need *not* be linked to hemispheric dynamics, changes, but may also occur on more local scales. If areas which currently experience sea ice become ice free, it should be anticipated that changes in the thermal climate will also impact the local wind climate.

Future wind climates Global Climate Models (GCMs) are the principal tools for understanding possible future climate states, and output from a large number of these models are now available with a daily time-step (Meehl et al., 2004). However, GCMs exhibit greatest accuracy at large scales and long averaging periods (IPCC, 2001), while wind speeds exhibit rather low spatial autocorrelation (Pryor et al., 2006; Robesson and Shein, 1997). Accordingly GCMs are unable to replicate the historically observed

magnitude and spatial variability of wind speeds (Pryor et al., 2006; Breslow and Sailor, 2002; Pryor et al., 2005), so alternative techniques are required to quantify the potential climate change impact of the wind energy resource. These include:

1. Use of wind indices, where a normalization is applied to the GCM wind-speed time series to account for bias in the modelled wind speeds (Pryor et al., 2005). This approach has the advantage that it is already used in the wind energy community to quantify interannual variability and hence is well known to the end-user community.

2. Application of dynamical downscaling so a Regional Climate Model (RCM) is nested within a GCM to derive smaller scale climate realizations (Pryor et al., 2005b). This approach has the advantage that it generates wind speeds, and hence wind energy estimates, for the entire area (model domain), regardless of data availability.

3. Application of empirical downscaling approaches where statistical relationships are developed between large-scale predictors of the climate system (derived from the GCM output) and local wind observations (Pryor et al., 2005c). This approach has the advantage that it generates site-specific wind speed and energy density estimates.

We now briefly present the basis for these approaches and some results from research in northern Europe. Note that in these analyses we use daily output from different GCM using the SRES A2 emission scenario (IPCC, 2000). This scenario predicts a moderate to large greenhouse gas global cumulative emission for 1990 to 2100 as a result of projected population growth and fairly slow introduction of carbon-free technologies. The A2 emissions scenario thus provides a reasonable upper bound on likely climate change and hence a strong driving function when comparing current to future wind-flow climates.

Use of wind indices: Wind indices are a normalization tool to quantify variability in wind energy density. Recall that wind power is proportional to the cube of wind speed. A wind index is the average of the cube of the wind speeds in the time window of interest is divided by the average of the cubes of the wind speed during the normalization period. They are computed as follows:

$$\text{Index} = \frac{\overline{U^3_{j...n}}}{\overline{U^3_{i...k}}} \cdot 100 \tag{16}$$

where the bar indicates an average, U are the wind speed observations, $j...n$ denotes the time series of wind speeds in the time window of interest, and $i...k$ denotes the time series wind speeds during the normalization period.

An overview of historical and projected annual wind indices for western Denmark is given in Figures 12a and b (Pryor et al., 2005). The indices were calculated using 10 m wind speed data from the ECMWF reanalysis data set for 1958–2001 and output from a simulation conducted using the HadCM3 GCM for 1990–2100 (Stratton, 1999; Pope, 2000; Johns et al., 1997). Here the grid cell average wind speeds directly from the GCM simulation are used. However, it should be noted that individual simulations conducted with GCM represent one realization of possible future atmospheric composition and climate (IPCC, 2001) and that comprehensive analyses should be based on multiple simulations and ensembling techniques to produce more robust results (Giorgi and Mearns, 2003).

Fig 12a and b (i) demonstrate significant variability on time scales longer than a decade, (ii) show that the inter-annual variability of wind indices over western Denmark (like much of Scandinavia) often exceeds 30%, and hence individual years may deviate by 30% from the long term average wind energy density.

Country specific wind indices, computed using the same HadCM3 simulations as in Figure 12a and b, are shown in Table 5. These simulations predict that the next 30 years will exhibit similar wind energy densities to those experienced during 1990–2001. However in all countries, except Finland, wind indices from this simulation of HadCM3
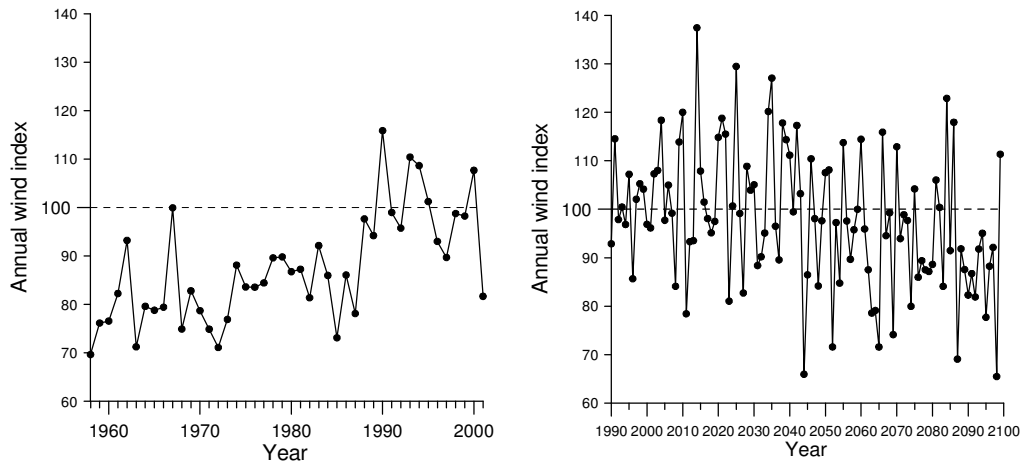
Figure 12. Annual wind indices. (a) for a grid cell located over western Denmark derived for 1958–2001 using data from the ECMWF reanalysis data set. (b) for 1990–2100 using output from HadCM3. For both sets of calculation, a normalization period of 1990–2001 was used to compute the wind indices.

are projected to be substantially smaller at the end of the 21st century than during 1990–2001 or 2005–2034 and the decline in wind indices is most marked in Iceland (Pryor et al., 2006b).

Table 5. Country-wide annual wind indices from HadCM3 output calculated for 2005–2034, 2035–2064, and 2065–2094 with a normalization period 1990–2001. "Mean" is the mean annual wind index. "Std. Dev." is the standard deviation of the annual wind indices

Country	2005–2034	2035–2064	2065–2094
Denmark (Mean)	94	97	95
(Std. Dev.)	14	11	11
Norway (Mean)	100	100	99
(Std. Dev.)	10	10	8
Sweden (Mean)	100	99	98
(Std. Dev.)	8	9	7
Finland (Mean)	100	101	101
(Std. Dev.)	10	11	9
Baltic states (Mean)	101	98	98
(Std. Dev.)	10	10	8
Island (Mean)	96	91	87
(Std. Dev.)	10	8	8

Dynamical downscaling: In dynamical downscaling, RCMs use results of GCMs (or observations) as lateral boundary conditions and simulate (by use of essentially the same procedures as global models) scenario climates that are dynamically consistent with these lateral boundary conditions. Typical resolutions of these RCM simulations are $\approx 50 \times 50$ km.

Example results from analyses of wind speeds and energy density conducted using RCM simulations over the Baltic region (Pryor et al., 2005b) are shown in Figures 13a, b, c, and d. These indicate:

- The Rossby Centre coupled Regional Climate Model (RCAO) simulations with boundary conditions derived from the ECHAM4/OPYC3 and HadAM3H GCMs exhibit realistic wind climates during the control period (1961–1990).

- Simulations conducted for climate projection periods in the twenty-first century (C21st) show important variations in the simulated changes when the GCM is used to supply the lateral boundary conditions:
  - Simulations conducted using boundary conditions from the ECHAM4/OPYC3 GCM indicate increases in virtually all descriptive parameters of the wind speed distribution and energy density in the projected climate change simulations for C21st.
  - RCAO simulations of wind speeds and energy density over the Baltic region, (conducted using boundary conditions supplied from HadAM3H) indicate more spatially heterogeneous changes between the control run simulations and projected climates for 2071–2100.

The changes in wind speeds in the simulations conducted using boundary conditions supplied from the ECHAM4/OPYC3 GCM are linked to the modelled increase in north-south pressure gradient over the North Atlantic during the winter (the NAO). This feature is not present in the HadAM3H simulations, and accordingly the wind climate exhibits a much greater degree of consistency between the control run and the climate projections.
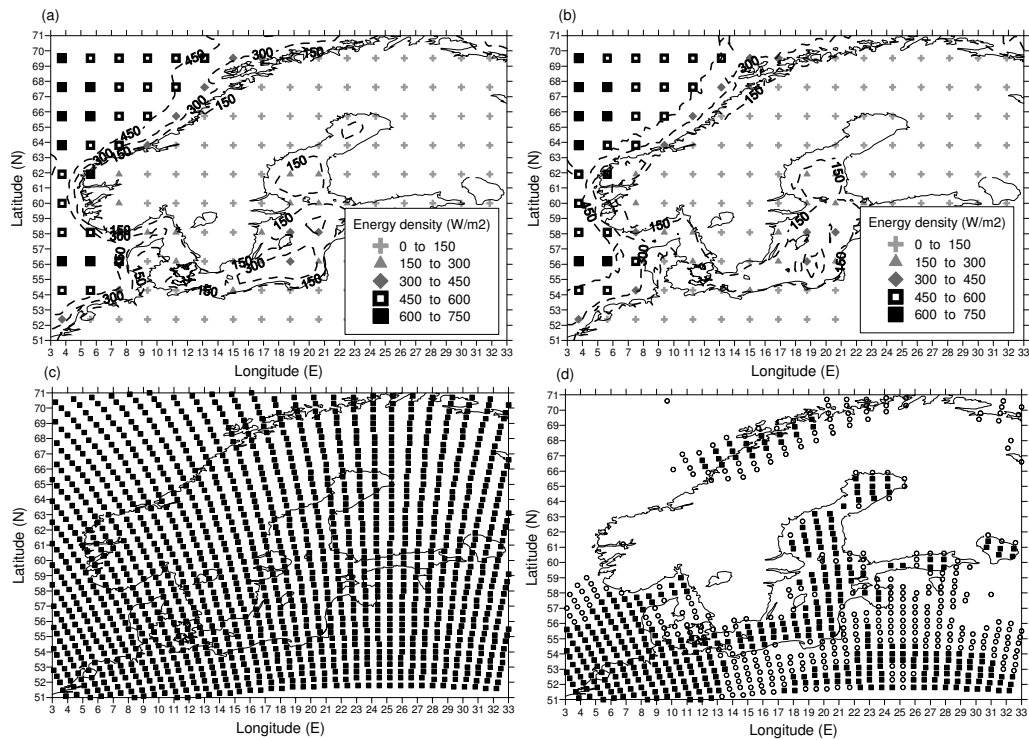
Figure 13. (a) and (b) show (in the contours) the energy density (at 10 m) from the RCAO simulations for 1961–1990 derived using lateral boundary conditions from (a) ECHAM4/OPYC3 and (b) HadAM3H. Symbols depict energy density derived from the NCEP reanalysis data. Frames (c) and (d) show the change in energy density by RCAO grid cell in 2071–2100 relative to 1961–1990 for simulations conducted using the A2 emission scenario for (c) ECHAM4/OPYC3 and (d) HadAM3H. A solid black square indicates that the mean from 2071–2100 is larger than the 97.5th percentile in the control period. If the grid cell is blank, the mean from 2071–2100 is less than the 2.5th percentile in the control period. If the symbol is an open circle, the mean of the future period is within the 95% confidence intervals for the control period (1961–1990) (Pryor et al., 2005b).

Empirical downscaling: Empirical downscaling methods generally use GCM simulations of large-scale variables and atmospheric conditions. They relate those variables statistically

to historical observations of the surface parameter of interest (temperature, precipitation, wind speed, etc.). The required transfer function can be developed using a range of statistical methods, ranging in sophistication from linear regression to highly non-linear techniques, such as neural networks (Giorgi et al., 2001). Once the transfer function is determined, it is assumed to remain invariant under climate change, so it may be applied to the large scale parameters from a GCM climate change scenario.

Recent research has developed an innovative approach to downscaling, focussed on wind speeds and energy density (Pryor et al., 2005c,d). This approach starts with GCM projections of mean sea-level pressure and of the mean and standard deviation of vorticity. These projected values are compared to the Weibull parameters of the wind speed probability distribution (see section 2.1). This empirical downscaling approach has been demonstrated to capture the observed variability of 10 m wind speeds and energy density. At all but one of 46 observing stations across northern Europe, (i) the downscaled mean wind speed is within $\pm 5\%$ of the independent observations, and (ii) energy density is within $\pm 20\%$ of that calculated from observations (Figure 14a, b, and c). When applied to output from ten GCMs, the downscaling results indicate the range of percent changes in the mean and 90th percentile. Wind speed change is $\leq 20\%$ for 2046–2065 and $\leq 35\%$ during 2081–2100 at all stations. As with the changes in downscaled mean and 90th percentile wind speed, the results for energy density at 14 each of the stations tend to span zero, with the downscaled results from some GCMs showing both increases and decreases (Figure 13).
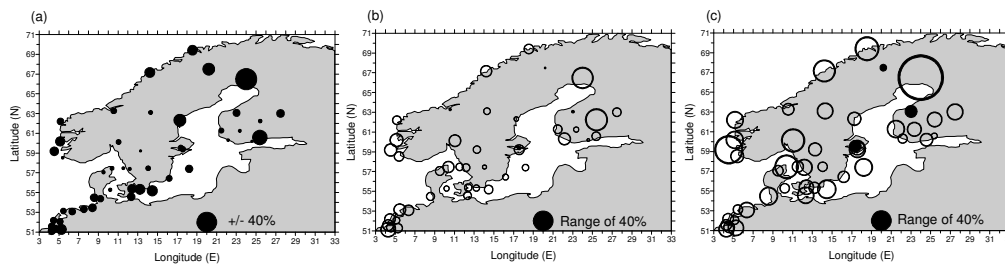
Figure 14. (a) The range of downscaled energy density from ten GCMs relative to independent observations during 1982–2000. A value of $\pm 40\%$ means downscaled energy density from all ten GCMs lie within $\pm 40\%$ of the observed values. Frames (b) and (c) show the change in energy density presented in terms of the range of changes from downscaling of the ten GCMs; (b) for 2046–2065 (i.e. ((2046–2065) — (1961– 1990))/(2046–2065)) and (c) for 2081–2100 relative to 1961–1990. If all the downscaled values indicated decline in the specified parameter, the symbol is solid. If the results from the downscaling of different GCMs span zero, the symbol is an open circle. No stations exhibited consistent increases in downscaled values from each of the ten GCMs. The diameter of the symbol used in each frame is linearly related to the data range.

Synthesis of research over the Baltic region: The various methods described above generate wind energy projections across the Baltic region under climate change scenarios. Comparing results, there are some commonalities and also some discrepancies. The major conclusions are:

1. The late 1980's and early 1990's seem to be somewhat atypical of the second half of the 20th century and of the likely climate states within the 21st century. According to reanalysis data sets, the mean wind energy density in the 1960's and 1970's was approximately 20% less than that of the 1990's. Wind speeds and energy density have generally declined since the peak in the early 1990's. Hence future resource assessments for this region should not rely solely on data from the 1990's in quantifying the available wind resource.

2. The modelling is inconsistent regarding an increase or decrease of the mean wind speed and energy density over the Baltic during C21st relative to the end of C20th. This uncertainty in decadal average wind energy density is mostly due to variations between simulations from different GCMs and is of comparable magnitude to historical estimates of inter-annual variability. Also downscaling results from different GCMs exhibit increased diversity at the end of C21st, which reduces confidence in the projections for the end of C21st relative to the middle of this century.

Prediction of the wind resource over the lifetime of a wind farm assuming a stationary climate

Sources of wind speed observations   In order to predict the wind resource over the lifetime of a wind farm, it is usually assumed that the past wind climate will continue into the future. Nevertheless, even with stationary climate inter-annual variability (Figure 12) and with seasonal fluctuations, there will be uncertainties in the projected wind climate. These uncertainties relate to the length of reference period. A long record of at least 30 years can be assumed to have an uncertainty of at least ±5%, whereas a reference period of one year has an uncertainty of at least ±15% (Barthelmie et al., 1999c). These uncertainties relate solely to the climatological variability and not to any uncertainty introduced by the measurement techniques or to long-terms trends in the climate system.

Because offshore atmospheric stability varies seasonally offshore, rather than diurnally as over land surfaces, the importance of making at least one year of measurements to avoid 15 seasonal bias has to be emphasised. If no site measurements are available, predicting the offshore wind resource becomes difficult and the resulting estimates are highly uncertain. Although large spatial scale datasets, such as the NCEP-NCAR data (Kalnay et al., 1996) and the POWER data set (Watson et al., 2000), are available, the major uncertainty lies in predicting the change of the resource at distances less than 50 km from the coast, where the majority of existing and planned wind farms are located. Since the large-scale datasets have spatial resolutions of 0.5° to 2° these can only be used as a general guide. In addition, these datasets have much reduced accuracy compared with onsite measurements.

An alternative technique to in situ measurements for resource assessment is application of remotely sensed data (Wu, 1995). Scatterometer produced (Liu, 2002) wind speed datasets, such as QuikSCAT, are available with good time resolution worldwide, however the spatial resolution is relatively poor and wind speeds close to the coast are not well resolved. Synthetic Aperture Radar (SAR) data have better accuracy and resolution relative to Scatterometers, especially close to the coast, but poor time resolution, due to infrequent satellite over-passes (Hasager et al., 2005). Winds-peed accuracy in a single image for SAR is given as ± 2 m s^{-1} in the range 2 to 24 m s^{-1} (Hasager et al., 2006) at a spatial resolution of $\sim$ 300 by 300 m (Kerbaol et al., 1998). In general, comparison of satellite-derived windspeeds from different sources, models and measurements give good results in case study analyses (Hasager et al., 2006). However, a relatively large number of satellite images is required to develop robust estimation of the entire wind-speed probability distribution which may prove prohibitively expensive in terms of analysis time and/or may be limited by availability of suitable images (Barthelmie and Pryor, 2003a; Pryor et al, 2004). A further drawback of large scale and satellite derived wind-speed data is that they are wind speeds at heights at, or below, 10 m above the sea surface. The same is true of course for data from buoys (Kerbaol et al., 1998). As discussed in the next section, extrapolation of wind speeds to hub-heights from near-surface measurements is a major source of uncertainty, particularly in the coastal zone. Hence, although remote sensing data can be employed for initial site exploration, they are not yet adequate for resource estimation.

By far the most accurate method of measuring site wind-speeds is to use standard equipment (i.e. good quality, individually calibrated, anemometers) at hub-height on a

slim meteorological mast fixed to the seabed. Low-power instrumentation and satellite transmission of the resulting data means that accurate and reliable measurements for wind resource prediction or wind profile characterisation can be made even at remote offshore sites (Barthelmie et al, 2005). The height above water of a bottom-fixed mast is a compromise between: (i) uncertainty in the power prediction from extrapolating to hub-height, and (ii) the non-linear expense of increasing mast height to hub height above about 50 m. Care should be taken to avoid mast shadow effects, either by measuring on two sides of the mast or by using a slim open mast structure which is not cluttered by obstacles close to the anemometers.

Climatologically robust estimates of wind speeds and energy densities

Assuming one year of in situ meteorological data are available, there are essentially two methods of relating on-site measurements to a longer term reference data set to derive a climatologically adjusted resource estimate. One is to use a physical model and the other is to use *statistical analysis*. These alternatives are described below.

Physical models range in complexity from: (i) *mesoscale models* which attempt to incorporate physical processes across a range of scales in the atmosphere and are based on primitive equations (Bergström, 2002; Bergström and Barthelmie, 2002), to (ii) *linearised models*, such as the Wind Analysis and Application Program (WAsP), which employ certain semi-analytical approximations (Mortensen et al., 1993, 2000) and have been designed specifically for wind energy.

While the sophistication of *mesoscale models* has many advantages in terms of the complexity of flow modelled, they are much more demanding in terms of input and computing resources. Mesoscale models are rarely run in "time-series" mode for wind energy; instead a number of climatologically representative simulations are made, for example wind speed and wind direction classes, and then weighted according to the specific climate of the area. A further major advantage is that no site-specific data are required, although clearly the whole area must be described in adequate detail (orography, roughness, etc). Mesoscale models have also been used to demonstrate the importance of coastal roughness, temperature and topography in dictating offshore wind speeds up to 200 km from the coastline (Bergström, 2002; Kallstrand et al., 2000).

Linearised models require only wind speed and direction time series as input. Local effects such as obstacles, roughness changes and topography can be modelled. However neither type of model gives adequate results if flow separation occurs (such as wind flow over a cliff). As discussed above, wind flow in coastal areas tends to be non-equilibrium and to be affected by horizontal and vertical temperature gradients. These are not modelled specifically by linearised models. In WAsP, a mean stability correction is added to the vertical profile of wind speeds, but temporal or specific site variations in atmospheric stability are not taken into account. Also linearised models cannot capture mesoscale thermal circulations like low-level jets or wind channelling. WAsP predictions for offshore are mainly related to the roughness change at the coastline. This occurs in conditions which are close to near-neutral within about 20 km of the coast. The clear implication is that if WAsP is initialised using wind speeds from a land site, it will not determine further change in wind speed beyond about 20 km from the coast, depending on the height under consideration. The major advantages of use of the WAsP model is the computational efficiency (a site assessment can be generated in a few minutes) and the ability of the model to determine the uncertainty in the resource estimate based on the input data.

The most common statistical method for a climatological wind speed and energy density prediction for a potential windfarm site is "measure-correlate-predict" (MCP). MCP uses a short-term wind dataset from the site itself and relates this to a longer time series from a relatively nearby location. There are a number of variations of MCP (Bunn and Watson, 1996; Rogers, 2005) but all derive a statistical relationship between wind speeds at both the prediction site and the longer-term site, using data from the overlap

period. This relationship is then used to derive the wind speed/direction statistics at the site for the longer period, assuming the relationship between the two sites remains consistent. The two sites should therefore be under the same synoptic influence and, as a rule-of-thumb, not be separated by more than about 50 km. MCP may under-predict wind resources at offshore sites if predictions are made from land-based observations and if the change in the wind speed distribution (not just the mean wind speed) are not accounted for.

Comparisons of these techniques for developing a site-specific wind resource assessment have been made for a number of offshore sites (Barthelmie et al., 1999c). The results indicate merit in both statistical and modelling approaches. For instance, a study of wind-speed prediction over the Baltic compared model results from WAsP and from the Uppsala University mesoscale model (MIUU). As shown in Figure 15, wind speeds derived from the two methods are in good agreement in the central Baltic, but in coastal areas the differences between the wind-speeds derived from the two methods can be substantial. This is probably due to air-sea temperature differences (atmospheric stability variations) close to the coastline.
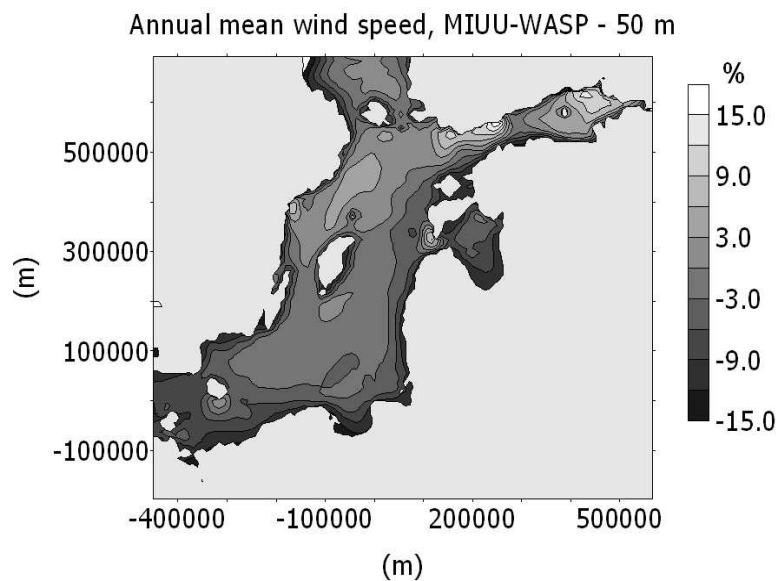
Figure 15. A comparison of 50 m wind speeds predicted by WAsP and the MIUU mesoscale meteorological model for the Baltic (Bergström and Barthelmie, 2002).

Extrapolation of vertical wind speed profiles

The extrapolation of measured wind speeds to turbine hub-heights involves significant uncertainty for wind energy prediction. Ideally, measurements would be at hub-height and clearly the shorter the extrapolation distance, the less the error. If extrapolation is required, a simple model is usually used, such as the power law (Hsu, 1988) or logarithmic wind profile (with stability corrections) (Hsu, 1994; Motta et al., 2005). Figure 16 shows the difference between the logarithmic and stability-corrected profile at a height of 100 m for different values of the Monin-Obukhov length, which relate to the stability (see Eq. 2).

Figure 17 shows predicted wind speed profiles for different stabilities defined according to the Monin-Obukhov length. The central thick solid line is the logarithmic profile prediction from an initial wind speed of 8 m s^{-1} at 10 m height. It is important to note that corrections under stable conditions (0 m $< L <$ 1000 m) are typically larger than for negative L in unstable conditions (0 m $> L > -1000$ m).
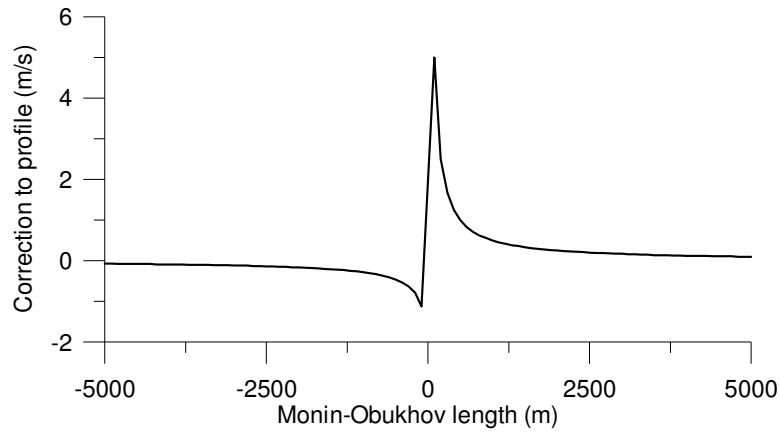
Figure 16. Corrections to the logarithmic wind speed at 100 m height for different values of the Monin-Obukhov length.
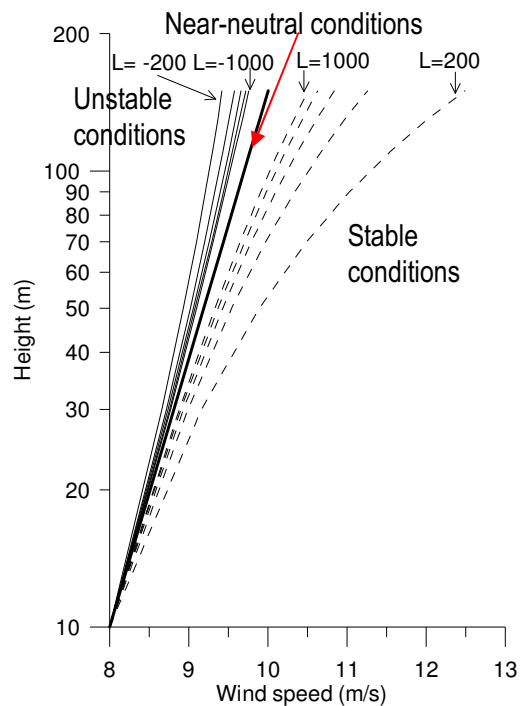
Figure 17. Example of wind speed profiles under different stability conditions with different values of the Monin-Obukhov length. The central thick solid line represents near-neutral conditions, the dashed lines represent stable conditions and the thin solid lines, unstable conditions.

Recently both *sodar* and *Doppler lidar* anemometry have been used on a fixed platform to investigate wind speed profiles up to about 200 m close to the Nysted offshore wind farm (see Table 4 for a description of this wind farm) (Antoniou et al., 2006). Deploying these usually ground-based remote sensing technologies on a boat or moored-buoy is possible (Barthelmie and Pryor, 2003a), although corrections for yaw and tilt are complex, especially in strong wind.

The varying roughness of the sea surface does not affect resource predictions significantly if the lowest height from which the extrapolation to hub-height wind speeds is above 10 m. However, for measurements from a buoy or using an anemometer at less than 10 m height, the extrapolation factor is large and subject to large uncertainties

(Barthelmie, 2001).

As explained in section 2.1, atmospheric stability has a major impact of wind speed profiles and corrections to the profile (Van Wijk et al., 1990). On average, a correction assuming "slightly stable" conditions to the logarithmic profile (as is applied in the WAsP model) has been found to give a good fit to offshore observations in northern Europe, but the majority of these are at less than 70 m height (Barthelmie et al., 1999c). However, Tambke et al. (2005) and Larsen et al. (2005) indicate (i) that similarity theory (used to compute L and relying on a constant flux layer assumption) is not valid above about 50 m from the sea surface, and (ii) that above this height the wind-speed profile becomes linear, which is why the stable correction gives a reasonable fit. The suggestion is that the atmospheric Ekman layer begins at 15 to 45 m, and that below this height, theory linking the atmosphere and the wave surface is required (Bye, 2002). This tendency towards linear profiles at greater heights has also been advanced for land surfaces (Larsen et al., 2005). If the constant flux layer theory does not apply, an additional scaling parameter may be required, such as the boundary-layer height.

2.3 From resource to wind energy: Impacts of wakes

Wind turbine wakes

As energy is extracted by a wind turbine rotor, previously unperturbed air passing through the rotor plane has its speed reduced and its turbulence increased. In a wind-farm, the separation between otherwise identical turbines is seldom large enough for the airflow to return fully to its unperturbed state, i.e. for the wake to "recover" and disappear. So assuming flat terrain, the wind speed at the first downwind turbine will be less than for the initial turbine, so its energy production will be less. The reduced wind speed and enhanced turbulence region of the airflow is known as the *wind turbine wake*. Smoke injected as a tracer, also shows that the wake has angular momentum, which helps define the region. Energy losses of otherwise potential energy relate to the properties of oncoming wakes and the design characteristics of specific wind turbines. In effect, these losses are inversely proportional to the power-extraction efficiency of the turbine, known as the *power coefficient C_p*, which itself is a function of the tip-speed ratio (speed of blade tip divided by speed of oncoming wind). In essence therefore, the more that is understood about wakes, the greater the opportunity for wind turbine and windfarm designers to improve energy capture. Wake recovery depends on both ambient turbulence intensity and wake-generated turbulence intensity. Under conditions of small ambient turbulence intensity, i.e. very stable conditions when vertical energy transfer is limited, wake recovery requires longer distances than in near-neutral conditions when there is vertical mixing with the higher, less perturbed, airflow. In unstable conditions, wake recovery occurs over shorter distances than for near-neutral conditions, due to increased momentum transfer with the higher airflow. Analysis of wake losses by simulation, is usually limited to near-neutral conditions, since most wake models cannot (yet) account for stability variations.

Introduction to wake models

Given the trend towards large offshore wind farms, accurate prediction and analysis of wind farm wakes is a major issue in determining power output. As indicated above, wake losses are more important offshore than onshore because turbulence in the airflow is less and wake recovery longer. The corollary is that the transfer of energy from higher unperturbed airflow into the reduced-energy wake is reduced compared to identical turbines on land sites, so allowing wakes offshore to propagate further downstream than onshore. Wake models extend in complexity from (a) engineering solutions which approximate physical processes and are very fast to run (e.g. WAsP (Mortensen et al., 2000)), to (b) a

number of models based on the Ainslie solution (Ainslie, 1988) to the Navier Stokes equations (Lange et al., 2003), to (c) computational fluid dynamics models (Schepers, 2003). For a detailed description of wind turbine wakes and wake models see Crespo et al. (1999). For the influence of wakes on turbulence and loads within wind farms see Frandsen (2005).

(a) *Engineering models.* The fundamental basis for most engineering models is the wake expansion model (Schlichting, 1968; Pope et al., 2000):

$$D_w \quad \propto \quad X^{1/3}, \tag{17}$$

$$D_w \quad = \quad D\left(\beta + \alpha s\right)^{1/2} \tag{18}$$

where X is the downwind distance in rotor diameters (D), D_w is the wake diameter, α is the wake decay constant (engineering model), β is a constant related to the initial wake diameter and to α, and $s = X/D$ is the non-dimensional distance from the first wind turbine.

This general approach is followed in Risø's WAsP which is widely used by the wind energy community. The wake model in WAsP (Mortensen et al., 1993) is based on a mathematical model of the wake behind a wind turbine (Jensen, 1983; Katic et al., 1986) (Figure 18). The wake is assumed to have a "top hat" form, and the spread of the wake (D_w) is assumed to be symmetric in the vertical and lateral directions, as in Figure 18:

$$D_w = D + 2kX \tag{19}$$

where k is the wake decay coefficient (WAsP definition). The velocity deficit at hub-height, ΔU is calculated:

$$\Delta U = U_{freestream} - U_{wake} \tag{20}$$

and the wind speed in the wake U_{wake} is:

$$U_{wake} = U_{freestream} \left[1 - \left(1 - \sqrt{1 - C_t} \right) \left(\frac{D}{D + 2kX} \right)^2 \right] \tag{21}$$

where C_t is the thrust coefficient (see Fig. 9).
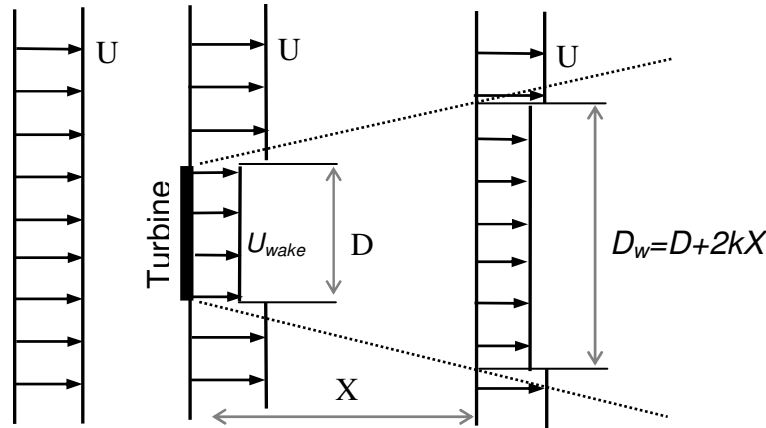
Figure 18. Schematic of the wake model used in WAsP.

In the WAsP model the suggested wake decay coefficients (see Eq. 20) are $k = 0.075$ for land sites and $k = 0.04$ for small offshore wind farms. Current research suggests that for large offshore wind farms (more than 2 rows) the WAsP wake decay coefficient (k) should be less, corresponding to increased wake losses for the same turbine separation with identical turbines.

In WAsP, the model assumes the centre-line of the expanding wake follows the terrain (flat for offshore), and the different hub heights and rotor diameters are taken into account

by the overlapping fraction of a wake with a down-wind rotor plane. Since the near-wake is not modelled specifically, the algorithms for WAsP wakes are valid only for distances in excess of $3D$ to $4D$, which, as shown below, have been evaluated over the entire range of downwind distances.

Evaluation of the wake magnitude and wake models in single wake cases

The performances of state-of-the-art wake models for offshore, including WAsP, have been compared and evaluated (Rados et al., 2002; Schlez et al., 2002) using data from the Vindeby wind farm, principally for single wake conditions (Barthelmie et al, 2003). The first study used results from a sodar experiment at Vindeby (Barthelmie et al, 2003) (Table 6). The second study used a set of systematic scenarios developed for the full-scale evaluation of wake models within the ENDOW project (Rados et al., 2002; Schlez et al., 2002). The former represents the wake behaviour at a range of downwind distances, and the latter allows a more comprehensive representation of ambient conditions.

Figure 19 shows predictions of the wake magnitude from the WAsP wake-algorithm along with the sodar-measured free-stream and wake profiles. As shown in Figure 19 and Table 6, the direct calculation of U_{wake} gives good results for distances $2D$ to $4D$ but under-predicts the wake wind-speed in the near and far wake. The direct U_{wake} calculations have a Root Mean Square Error (RMSE) from measurement of 0.7 m s^{-1}. However, these results are broadly comparable with those from a range of wake models (Pryor et al., 2005d).

Table 6. Measured and modelled velocity deficit from the sodar experiment conducted at the Vindeby offshore wind farm and computed using WAsP. The experiment numbers are as shown in Figure 19.

Experiment #	Freestream U (m s^{-1}) at 48 m	D	ΔU (m s^{-1}) Sodar (measured)	ΔU (m s^{-1}) WAsP (modelled)
4	6.90 ± 0.59	1.7 ± 0.3	4.26	2.71
7	5.74 ± 0.20	2.8 ± 0.3	2.28	2.28
9	7.54 ± 0.45	2.9 ± 0.5	2.57	2.01
10	6.37 ± 0.25	3.4 ± 0.5	1.48	2.11
11	8.19 ± 0.46	3.4 ± 0.3	2.28	1.98
12	6.12 ± 0.74	7.4 ± 0.5	0.61	1.21

A limitation of this comparison is that only a few observational conditions are presented. In a second evaluation of the WAsP wake algorithms, data from a fixed mast were used, and hence the comparison focussed on a fixed distance downstream of a turbine with different flow conditions. Data from the meteorological masts at Vindeby were selected only for when the upstream-turbine to met mast direction was $\pm 5°$ of the direct wake direction. For single wakes, wind speed profiles in the wake were determined from the sea mast (south) while free-stream wind profiles were taken from simultaneous observations at the near-shore land mast. As shown in Table 7, predicted wind speeds at hub-height are approximately equal to those observed. The RMSE was 0.37 m s^{-1} in the three smallest wind-speed scenarios (up to 10 m s^{-1}) at a distance of $9.6D$. However, the WAsP wake-algorithms underpredict the wake horizontal speed magnitude at large wind-speeds, possibly indicating that the calculated wake recovery of the algorithms is too rapid, although this discrepancy may also relate to the influence of stability on turbulence profiles and hence on wake decay.
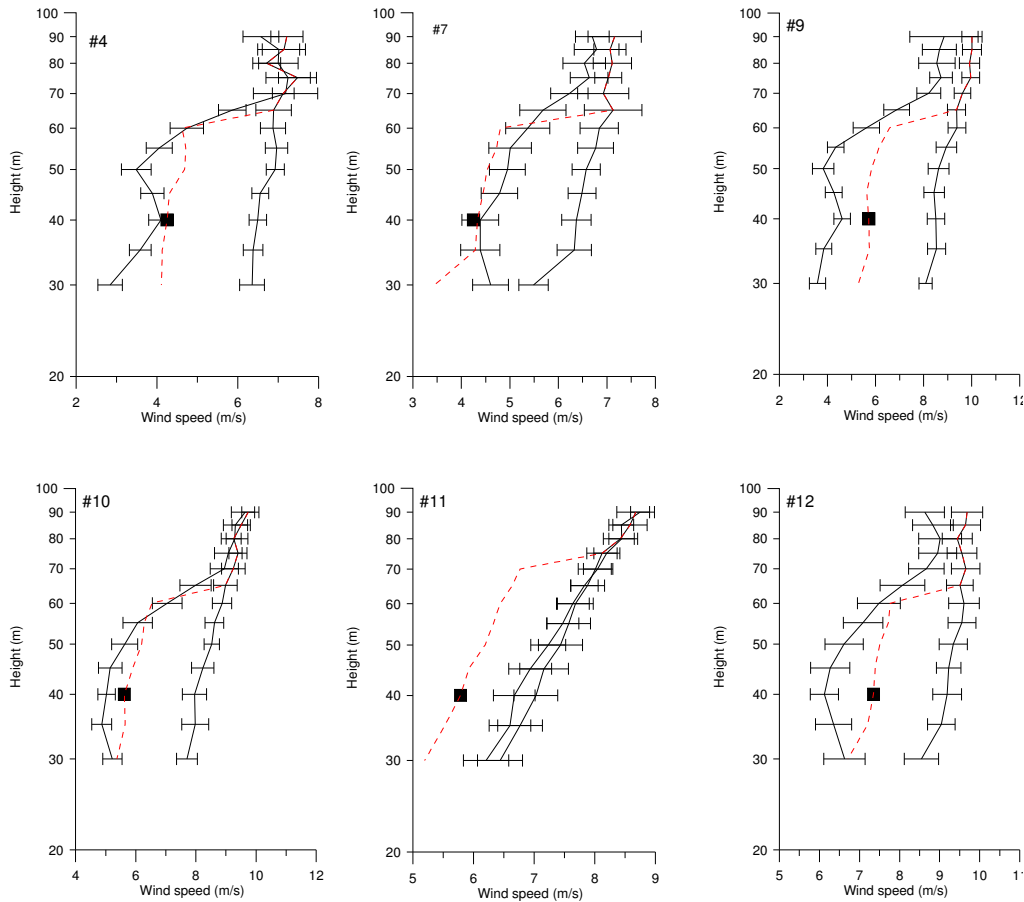
Figure 19. Comparison of sodar wake and free-stream wind speeds (full lines) and WAsP algorithm predicted wake wind speeds at hub-height (square symbol). Error bars calculated from the sodar data are ±0.5 standard deviation. The dashed line shows the wake profile predicted assuming the velocity deficit is applied to the free-stream wind profile within a vertical/horizontal spread calculated from Eq. 10 (a top-hat profile).

Quantifying multiple wakes

A major requirement in the development of large offshore windfarms is design for wake effects within the particular windfarm and the propagation of total windfarm wakes between adjacent windfarms. Hence there is a need to predict multiple wakes both within and downwind of large offshore windfarms. A first order approach for the integrated downwind impact of a large windfarm is to treat the windfarm as a "topographical" element of large roughness (Crespo et al., 1996). As shown in Table 8 (rows 1, 2, 3) for calculations using WAsP, the choice of the roughness length (z_o) assigned to the windfarm affects the downwind distance required for the windspeed at hub-height to recover to 98% of its upwind freestream value. It is also possible to use WAsP to predict the same condition using multiple wake superposition; the results are on Table 8, rows 4 and 5. It is clear that the results of the two sets of simulations vary significantly.

One possible reason for the divergent results in Table 8 is that turbulence generated by large windfarms is likely to alter the structure of the atmospheric boundary-layer and so change momentum transfer affecting wake recovery. This effect is not important over small windfarms so is not analysed in most wake models. Note that a relatively new model within WAsP (the analytical model), which integrates the momentum deficit from individual wakes in order to calculate the whole wind farm wake (Frandsen et al., 2006), is now being evaluated (Rathmann et al., 2006).

Table 7. Wake calculations (wind-speed) from the WAsP algorithms at a range of down-stream distances. The wake wind-speed increases as the airflow recovers with downstream distance. Also shown are the wake wind speeds derived from the observations at the meteorological mast at a distance of 9.6 rotor diameters downstream. The wake wind speeds are for the hub-height in m s^{-1}.

Distance as rotor diameters	3 WAsP	5 WAsP	7 WAsP	9.6 WAsP	9.6 observed	Difference at 9.6 $U_{wasp}-$ $U_{freestream}$	10 WAsP
Distance (m)	106.5	177.5	248.5	340.8			355
Freestream wind speed (m s^{-1})							
5.02	2.89	3.42	3.77	4.08	4.33	-0.25	4.12
7.27	5.03	5.59	5.96	6.29	6.42	-0.13	6.32
9.75	7.40	8.02	8.40	8.73	8.80	-0.07	8.78
13.70	11.50	11.96	12.23	12.46	11.74	0.69	12.49

Table 8. Recovery distances behind a large (100 turbine) wind farm, shown as distance (km) after the wind farm at which the hub-height wind speed recovers to 98% of its upwind freestream value.

Table row number	Model	Distance [km]
1	WAsP z_o(block) 0.1 m	6
2	WAsP z_o(block) 0.5 m	7
3	WAsP z_o(block) 1.0 m	8
4	WAsP wake decay 0.075	2
5	WAsP wake decay 0.050	3

2.4 Windfarm power output at short time scales: Is offshore different?

The primary concern of this chapter so far has been the prediction of power output over the lifetime of a wind farm, so long-term effects have been studied. However, wind climates vary over a range of time scales, including scales relevant for turbine control (from milliseconds to seconds), and for the integration of wind power in the electrical grid (from minutes to days). Short-term forecasting involves many of the same issues as long-term forecasting, especially relating larger scale model data to site-specific energy output.

Knowing weather conditions and with previous experience, electricity power demand can be predicted with a high degree of accuracy; usually about $\pm 1.5\%$ for 24 hours ahead and about $\pm 5\%$ for one week ahead (Giebel et al., 2003). Windfarm energy production cannot be forecast with such accuracy, although the greater the number of dispersed turbines, the greater the accuracy of predication for the total output using national meteorological information.

Hence there is considerable emphasis on developing more accurate wind forecasts which can be used to estimate windfarm power output and to bid for a price in the electricity market up to, say, 48 hours ahead. Most methods use Numerical Weather Prediction (NWP) models to predict site specific wind speeds and hence power output, using similar

downscaling methods to those described in section 2.2. The NWP models typically have resolutions of 5 to 55 km in the horizontal, have up to 40 vertical height zones and use a six hour data assimilation cycle. The grid-cell averaged NWP model output is related to small scale variability using physical/dynamical, empirical/statistical or hybrid approaches (Giebel et al., 2003) to generate location specific power production. For short-term forecasting, statistical methods have some advantages, since in the first six hours persistence-type models give good results. Statistical methods are fast and require limited computing resources and power output can be predicted directly, avoiding the extra step of utilising the turbine power curve (Giebel et al., 2003) to relate the predicted wind speed at hub-height to the power produced by the turbine. As described in section 2.1, use of a manufacturer's standard power curve gives uncertainty in power predictions. Nevertheless in short-term prediction, the largest error in prediction of short-term fluctuations in power output is due to bias and uncertainties in the NWP model simulations (Giebel et al., 2003).

In general, short-term forecasting should be more straightforward offshore than on-shore. This is because offshore wind-speeds in the power-producing range (i.e. more than cut-in speed) are more persistent, and the duration of calms is less, than for adjacent land sites (Pryor and Barthelmie, 2001). Indeed improved accuracy in offshore wind speed predictions, as compared with nearby onshore, has been obtained (Tambke et al., 2005). A further advantage for offshore sites, in terms of the accuracy of power production, is that the average diurnal variability of wind speeds is of minor importance (Barthelmie and Giebel, 2006), especially in comparison with land sites in the summer. At typical land sites, wind speed maxima are obtained in the early afternoon whereas the maxima appear to occur later at offshore sites which are influenced by nearby land. Minimum wind speeds appear to occur in the early morning at coastal offshore sites. However, this seems to be location dependent and maybe due to advection of stronger wind speeds from land, thermal gradients or interaction with larger scale circulation, e.g. sea breezes. The major issues remaining for offshore short-term forecasting are large horizontal gradients in predicted wind speeds in coastal areas (Barthelmie and Giebel, 2006). For some sites there is relatively little information from upwind locations giving a large range of accuracy of the forecasts. Errors in the predicted wind-speed profiles may be due to use of simple prediction models, e.g. logarithmic or stability corrected profiles. The effects of this will be greatest for large turbines with taller hub-heights and larger rotor diameters. The trend towards larger windfarms means that wake losses have a greater impact on the overall power prediction.

2.5   Summary

Accurate prediction of power output from wind farms requires an assessment of the hub-height wind speed which will be valid for the next 20–30 years. Variability of wind speed is usually assessed based on past climates, where the inter-annual variability has usually been at least $\pm 5\%$ at northern European sites. However, the variability has been as large as $\pm 30\%$ for individual years, especially if sites are positioned in heterogeneous locations (e.g. the coastal zone). For site measurements, in general terms, the shorter the record used to assess the wind climate, the more uncertainty will be associated with it. However, even using 10 years data will not fully capture the total variability, especially under non-stationary climate conditions.

In terms of future wind speeds under climate change, recent modelling with Global Climate Models (GCMs) suggests that, at least in northern Europe, major shifts in the wind climate are not anticipated over the coming decades. However, the range of GCM wind-speed projections remains large (i.e. there is large uncertainty), although this can be reduced with appropriate downscaling techniques. Best available estimates suggest the climate signal is moderate and of the same order as the uncertainty in GCM modelling of the 1961–1990 wind climate.

For site wind speed estimation, use of remote sensing data derived from satellite-borne instrumentation provide a good overview of the likely range and spatial distribution of wind speeds. However, these techniques are not yet fully developed to provide good temporal and spatial resolution data at the required accuracy for site assessment. Mesoscale model data are also becoming available and appear to give a good representation of the wind climate. However, at present, by far the most accurate method of determining the potential power output is to measure site wind speeds at hub-height on a fixed meteorological mast. Assuming these are short-term measurements (of the order of a few years) they can be related to longer-term wind speeds using (i) mesoscale, (ii) linearised models, or (iii) well-known statistical techniques, such as measure-correlate-predict. If extrapolating from onshore to offshore, care needs to be taken that the whole wind speed distribution, and not just the mean wind speeds, are transformed.

If hub-height measurements are not available, wind speeds will need to be extrapolated vertically. Standard methods, e.g. the power law, logarithmic profile and stability corrected profile, all seem to be inadequate offshore at heights above about 50 m. A major issue is the lack of observations at heights above 50 to 70 m, to use for model validation.

Wake effects from large offshore windfarms are expected to cause power reductions in the range 10 to 20%. Present models give acceptable results for single wakes and small windfarms, but none of the state-of-the-art models include feedback to and from the boundary-layer which is probably needed for large windfarms. A new analytical model has been specifically designed to calculate the effect of wakes within and down-wind of large windfarms which requires further evaluation.

For short-term forecasting, errors in wind speeds from Numerical Weather Prediction models are typically the largest source of uncertainty in prediction of power production up to 48 hours ahead. For short-term forecasting offshore, the additional major uncertainties appear to be the strong horizontal gradients of wind speed in coastal areas and the accurate prediction of vertical profiles offshore.

It should be noted that we have focussed exclusively on meteorological and climatological aspects of wind energy developments in offshore environments. Other issues such as losses within the electric cables are also significant and are covered in "Offshore Wind Power".

Acknowledgements

Notation

a'	deviation term of a quantity a
$\overline{a}$	time average of a quantity a
A	scale parameter of the Weibull distribution
c_p	specific molar heat capacity of air
C_D	drag coefficient
C21st	twenty-first century
D	rotor diameter
D_w	wake diameter
$\overline{e}$	turbulent kinetic energy per unit mass
E	instantaneous wind energy density
g	gravitational acceleration
GCM	global climate models
I	turbulence intensity

k	shape parameter of the Weibull distribution
	wake decay coefficient
L	Monin-Obukhov length
MCP	measure-correlate-predict
MIUU	Uppsala Universtity mesoscale model
NAO	North Atlantic Oscillation
NWP	numerical weather prediction
$p(U)$	probability distribution of wind speed
P	atmospheric pressure
P_o	standard pressure
$P(U)$	Cumulative probability distribution of wind speed
q	specific humidity
R	universal gas constant
RCAO	Rossby centre coupled regional climate model
RCM	regional climate model
RMSE	root mean square error
s	non-dimensional distance from the first wind turbine
SAR	synthetic aperture radar
T	temperature
u	west-east component of the wind speed
u_*	friction velocity
U	mean horizontal wind speed
$\overline{U}$	mean wind speed
U_A	wind speed at a height A
$U_{freestream}$	freestream wind speed
U_{wake}	wake wind speed
U_{10}	wind speed at 10 m above the surface
v	south-north component of the wind speed
w	vertical component of the wind speed
$\overline{w'\Theta'}$	kinematic heat flux
WAsP	Wind Analysis and Application Program
x	function for the unstable correction of the wind profile
X	downwind distance in rotor diameters
X^*100	percentiles of the wind speed distribution
z	height above the ground
z_o	surface roughness
θ_v	virtual potential temperature
α	wake decay constant
β	constant related to the initial wake diameter
Γ	Gamma function
ΔU	velocity deficit at hub-height
κ	von Kármán constant
ρ	air density
σ_U	stantard deviation of the wind speed
τ	momentum flux
$\Psi_m\left(\frac{z}{L}\right)$	stability function

References

Ainslie J. F. (1988) Calculating the flow field in the wake of wind turbines. *J. Wind Eng. Ind. Aero.* **27**:213–224

Antoniou I., Jørgensen H. E., Mikkelsen T., Frandsen S., Barthelmie R., Perstrup C., and Hurtig M. (2006) Offshore wind profile measurements from remote sensing instruments. *Proc. of the European Wind Energy Conf.*, Athens

Alexandersson H., Tuomenvirta H., Schmith T., and Iden K. (2000) Trends of storms in NW Europe derived from an updated pressure data set. *Clim. Res.* **14**:71–73

Badger J., Barthelmie R., Frandsen S., and Christiansen M. (2006) Mesoscale modelling for an offshore wind farm. *Proc. of the European Wind Energy Conf.*, Athens

Barthelmie R. J., Grisogono B., and Pryor S. C. (1996) Observations and simulations of diurnal cycles of near-surface wind speeds over land and sea. *J. Geophys. Res. (Atmos.)* **101**(D16):21,327-21,337

Barthelmie R. J., Courtney M. S., Højstrup J., and Larsen S. E. (1996) Meteorological aspects of offshore wind energy - observations from the Vindeby wind farm. *J. Wind Eng. Ind. Aero.* **62**(2-3):191–211

Barthelmie R. J. (1999a) The effects of atmospheric stability on coastal wind climates. *Meteorol. Appl.* **6**(1):39–48

Barthelmie R. J. (1999b) Monitoring offshore wind and turbulence characteristics in Denmark. *Proc. of the 21st British Wind Energy Association Conf.*, Cambridge

Barthelmie R. J., Courtney M., Lange B., Nielsen M., Sempreviva A. M., Svenson J., Olsen F., and Christensen T. (1999) Offshore wind resources at Danish measurement sites. *Proc. of the European Wind Energy Conf.*, Nice

Barthelmie R. J. (2001) Evaluating the impact of wind induced roughness change and tidal range on extrapolation of offshore vertical wind speed profiles. *Wind Energy* **4**:99–105

Barthelmie R. J. and Pryor S. C. (2003) Can satellite sampling of offshore wind speeds realistically represent wind speed distributions? *J. Appl. Meteorol.* **42**:83–94

Barthelmie R. J., Folkerts K., Ormel F. Sanderhoff P., Eecen P., Stobbe O., and Nielsen N. M. (2003) Offshore wind turbine wakes measured by SODAR. *J. Atmos. Ocean. Technol.* **30**:466–477

Barthelmie R. J., Hansen O., Enevoldsen K., Højstrup J., Larsen S., Frandsen S., Pryor S. C., Motta M., and Sanderhoff P. (2005) Ten years of meteorological measurements for offshore wind farms. *J. Solar Energy Eng.* **127**(2):170–176

Barthelmie R. J. and Giebel G. (2006) Prediction of wind speed profiles for short-term forecasting in the offshore environment. *Proc. of the European Wind Energy Conf.*, Athens

Bergström H. (2002) Boundary-layer modelling for wind climate estimates. *Wind Eng.* **25**(5):289–299

Bergström H. and Barthelmie R. J. (2002) Offshore boundary-layer modelling. *Global Windpower*, EWEA, Paris

Breslow P. B. and Sailor D. J. (2002) Vulnerability of wind power resources to climate change in the continental United States. *Renew. Energy* **27**:585–598

Bunn J. C. and Watson S. J. (1996) A new matrix method of predicting long-term wind roses with MCP. *European Union Wind Energy Conf.*, Göteborg

Bye J. (2002) Inertially coupled Ekman layers. *Dyn. Atmos. Oceans.* **35**:27–39

Charnock H. (1955) Wind stress over a water surface. *Quart. J. Roy. Meteorol. Soc.* **81**:639–640

Crespo A., Chacon L., Hernandez J., Manuel F., and Gomez-Elvira R. (1996) Modelization of offshore wind farms. Effect of the surface roughness of the sea. *European Union Wind Energy Conf.*, Göteborg

Crespo A., Hernandez J., and Frandsen S. (1999) Survey and modelling methods for wind turbine wakes and wind farms. *Wind Energy* **2**:1–24

Dyre K. (1992) Vindeby off-shore wind farm - the first experiences. in "The Potential of Wind Farms" *EWEA Special Topic Conference*, Herning

Frandsen S., Chacon L., Crespo A., Enevoldsen P., Gomez-Elvira R., Hernandez J., Højstrup J., Manuel F., Thomsen K., and Sørensen P. (1996) Measurements on and modelling of offshore wind farms. Risø National Laboratory, Roskilde

Frandsen S. (2005) Turbulence and turbulence-generated fatigue loading in wind turbine clusters. Risø National Laboratory, Roskilde

Frandsen S., Barthelmie R., Pryor S., Rathmann O., Larsen S., Højstrup J., and Thøgersen M. (2006) Analytical modelling of wind speed deficit in large offshore wind farms *Wind Energy* **9**(1–2):39–53

Garratt J. R. (1987) The stably stratified internal boundary layer for steady and diurnally varying offshore flow. *Bound.-Layer Meteorol.* **38**(4):369–394

Giebel G., Brownsword R., and Kariniotakis G. (2003) The state-of-the-art in short-term prediction of wind power. A literature overview. http://anemos.cma.fr/download/ANEMOS_D1.1_StateOfTheArt_v1.1.pdf, Roskilde

Giorgi F., Hewitson B., Christensen J., Hulme M., von Storch H., Whetton P., Jones R., Mearns L., and Fu C. (2001) Chapter 10: Regional climate information - Evaluation and projections, in Climate Change 2001: The Scientific Basis, Cambridge University Press:583–638

Giorgi F. and Mearns L. O. (2003) Probability of regional climate change based on the Reliability Ensemble Averaging (REA) method. *Geophys. Res. Lett.* **30**(12):p.1629, doi:10.1029/2003GL017130

Hasager C. B., Nielsen M., Astrup P., Barthelmie R., Dellwik E., Jensen N. O., Jørgensen B., Pryor S., Rathmann O., and Furevik B. (2005) Offshore wind resource assessed from satellite SAR wind field maps. *Wind Energy* **8**:403–419

Hasager C. B., Barthelmie R., Christiansen M., Nielsen M., and Pryor S. (2006) Quantifying offshore wind resources from satellite maps: study area the North Sea. *Wind Energy* **9**:(1–2)63–74

Hurrell J., Kushnir Y., Ottersen G., and Visbeck M. (2003) An overview of the North Atlantic Oscillation., The North Atlantic Oscillation: Climatic Significance and Environmental Impact. Geophysical Monograph 134, American Geophysical Union, 35 pp

Hsu S. A. (1988) Coastal Meteorology, London: Academic Press, 260 pp

Hsu S. A. (1994) Determining the power-law wind-profile exponent under near-neutral stability conditions at sea. *J. Appl. Meteorol.* **33**(6):757–765

IEA (2005) IEA Wind Energy Annual Report 2004. *Kendall Printing Company, USA*. p. 264

IPCC (2001) IPCC Third Assessment Report. Climate Change 2001: The scientific basis. Ed. Houghton et al. Cambridge University Press, 881 pp

IPCC (2000) Emissions scenarios Ed. Nakicenovic and Swart. Cambridge University Press, 570 pp

Jensen N. O. (1983) A note on wind turbine interaction. Risø National Laboratory, Roskilde

Jensen L. (2004) Wake measurements from the Horns Rev wind farm. *Proc. of the European Wind Energy Conf.*, London

Johns T. C., Carnell R. E., Crossley J. F., Gregory J. M., Mitchell J. F. B., Senior C. a., Tett S. F. B., and Wood R. A. (1997) The second Hadley Centre coupled ocean-atmosphere GCM: model description, spinup and validation. *Clima. Dyn.* **13**:103–134

Kallstrand B., Bergström H., Højstrup J., and Smedman A. S. (2000) Mesoscale wind field modifications over the Baltic Sea. *Bound.-Layer Meteorol.* **95**:161–188

Kalnay E., Kanamitsu M., Kistler R., Collins W., Deaven D., Gandin L., Iredell M., Saha S., White G., Woollen J., Chelliah M., Zhu Y., Ebisuzaki W., Higgins W., Janowiak J., Mo K. C., Ropelweski C., Wang J., Leetma A., Reynolds R., Jenne R., and Joseph D. (1996) The NCEP/NCAR 40 reanalysis project. *Bull. Amer. Meteor. Soc.* **77**:437–471

Katic I., Højstrup J., and Jensen N. O. (1986) A simple model for cluster efficiency. *European Wind Energy Conf.*, Rome

Kerbaol V., Chapron B., and Vachon P. W. (1998) Analysis of ERS-1/2 synthetic aperture radar wave mode imagettes. *J. Geophys. Res.: Oceans* **103**:7833–7846

Kistler R., Kalnay E., Collins W., Saha S., White G., Woollen J., Chelliah M., Ebisuzaki W., Kanamitsu M., Kousky V., van den Dool H., Jenne R., and Fiorino M. (2001) The NCEP-NCAR 50 year reanalysis: Monthly mean CD-ROM and documentation. *Bull. Amer. Meteor. Soc.* **82**:247–267

Lange B., Waldl H. P., Guerrero A., and Barthelmie R. (2003) Improvement of the wind farm model FLaP (Farm Layout Program) for offshore applications *Wind Energy* **6**:87–104

Larsen S. E., Gryning S.-E., Jensen N. O., Jørgensen H. E., and Mann J. (2005) Profiles of mean wind and turbulence in the atmospheric boundary layer above the surface layer. *EUROMECH colloquium 464b: Wind Energy. International colloquium on fluid mechanics and mechanics of wind energy conversion*, Oldenburg

Liu W. T. (2002) Progress in scatterometer application. *J. Oceano.* **58**:121–136

Masrshall J., Kushnir Y., Battisti D., Chang P. Czaja A., Dickson R., Hurrell J., McCartney M., Saravanan R., and Visbeck M. (2001) North Atlantic climate variability: Phenomena, impacts and mechanisms. *Int. J. Climatol.* **21**:1863–1898

Meehl G., Covey C., Latif M., McAvaney B., Mitchell J., and Stouffer R. (2004) Soliciting participation in climate model analyses leading to IPCC Fourth Assessment Report. *EOS*. **85**. p. 274

Mortensen N. G., Landberg L., Troen I., and Petersen E. L. (1993) Wind Analysis and Application Program (WASP). Risø National Laboratory, Roskilde

Mortensen N. G., Heathfiled D., Landberg L., Rathmann O., Troen I., and Petersen E. L. (2000) Getting started with WASP 7.0. Risø National Laboratory, Roskilde

Motta M., Barthelmie R. J., and Vølund P. (2005) The influence of non-logarithmic wind speed profiles on potential power output at Danish offshore sites. *Wind Energy* **8**:219–236

Pavia E. G. and O'Brien J. J. (1986) Weibull statistics of wind speed over the ocean. *J. Clim. Appl. Meteorol.* **25**:1324–1332

Pope S. A. (2000) Turbulent flows, Cambridge University Press., 806 pp

Pope V., Gallani M., Rowntree P., and Stratton R. (2000) The impact of new physical parameterizations in the Hadley Centre climate model: HadAM3. *Clima. Dyn.* **16**:123–146

Pryor S. C. and Barthelmie R. J. (2001) Comparison of potential power production at on- and off-shore sites. *Wind Energy* **4**:173–181

Pryor S. C. and Barthelmie R. J. (2003) Long term trends in near surface flow over the Baltic. *J. Climatol.* **23**:271–289

Pryor S. C., Nielsen M., Barthelmie R. J., and Mann J. (2004) Can satellite sampling of offshore wind speeds realistically represent wind speed distributions? Part II: Quantifying uncertainties associated with sampling strategy and distribution fitting methods. *J. Appl. Meteorol.* **43**:739–750

Pryor S. C., Barthelmie R. J., and Schoof J. T. (2005) The impact of non-stationarities in the climate system on the definition of "a normal wind year": A case study from the Baltic. *Int. J. Climatol.* **25**:735–752

Pryor S. C., Barthelmie R. J., and Kjellström E. (2005) Analyses of the potential climate change impact on wind energy resources in northern Europe using output from a Regional Climate Model. *Clima. Dyn.* **25**:815–835

Pryor S. C., Schoof J. T., and Barthelmie R. J. (2005) Empirical downscaling of wind speed probability distributions. *J. Geophys. Res.* **110**(D19109):p. doi:10.1029/2005JD005899.

Pryor S. C., Schoof J. T., and Barthelmie R. J. (2005) Potential climate change impacts on wind speeds and wind energy density in northern Europe: Results from empirical downscaling of multiple AOGCMs. *Clima. Res.* **29**:183–198

Pryor S. C., Schoof J. T., and Barthelmie R. J. (2006) Winds of Change? Projections of near-surface winds under climate change scenarios. *Geophys. Res. Lett.* **33**(L11702):p. doi:10.1029/2006GL026000.

Pryor S. C., Barthelmie R. J., and Schoof J. T. (2006) Inter-annual variability of wind indices over Europe. *Wind Energy* **9**:27–38

Rados K., larsen G., Barthelmie R., Schlez W., Lange B., Shepers G., Hegberg T., and Magnusson M. (2002) Comparison of wake models with data for offshore windfarms. *Wind Eng.* **25**:271–280

Rathmann O., Barthelmie R., and Frandsen S. T. (2006) Wind turbine wake model for wind farm power production. *Proc. of the European Wind Energy Conf.*, Athens

Robeson S. M. and Shein K. A. (1997) Spatial coherence and decay of wind speed and power in the north-central United States. *Phys. Geo.* **18**:479–495

Rogers A., Rogers J., and Marwell J. F. (2005) Comparison of the performance of four measure-correlate-predict algorithms. *J. Wind Eng. Ind. Aero.* **93**:243–264

Schepers J. G. (2003) Validation and improvement of ECN's wake model. ECN, Petten

Schlez W., Umaña A. E., Barthelmie R., Larsen S., Rados K., Lange B., Shepers G., and Hegberg T. (2002) ENDOW: Improvement of wake models within offshore windfarms. *Wind Eng.* **25**:281–287

Schlichting H. (1968) Boundary layer theory, McGraw-Hill, 748 pp

Simpson J. E. (1994) Sea breeze and local winds, Cambridge University Press, 234 pp

Smedman A. S., Högström U., and Bergström H. (1996) Low level jets - a decisive factor for off-shore wind energy siting in the Baltic Sea. *Wind Eng.* **20**(3):137–147

Stratton R. A. (1999) A high resolution AMIP integration using the Hadley Centre model HadAM2b. *Clima. Dyn.* **15**:9–28

Stull R. B. (1988) An introduction to boundary layer meteorology, Kluwer Academic Publishers, 666 pp

Stull R. B. (2000) Meteorology for scientists and engineers, Pacific Grove, CA: Brooks/Cole, 502 pp

Tambke J., Lange M., Focken U., Wolff J., and Bye J. (2005) Forecasting offshore wind speeds above the North Sea. *Wind Energy* **8**:3–16

Van Wijk A. J. M., Beljaars A. C. M., Holtslag A. A. M., and Turkenburg W. C. (1990) Evaluation of stability corrections in wind speed profiles over the North Sea. *J. Wind Eng. Ind. Aero.* **33**:551–566

Vikkelsø A., Larsen J. H. M., and Sørensen H. C. (2003) The Middelgrunden offshore wind farm. A popular initiative. *Copenhagen Environment and Energy Office CEEO: Copenhagen.* p. 28

Watson G., Halliday J., Palutikof J., Holt T., Barthelmie R., Coelingh J. Folkerts L., Wiegerinck G., van Zuylen E., Clejne J., and Hommerl G. (2000) POWER - A methodology for the prediction of offshore wind energy resources. *Proc. of the Offshore Wind Energy in Mediterranean and Other European Seas conference*, Sicily

Wieringa J. (1992) Updating the Davenport roughness classification. *J. Wind Eng. Ind. Aero.* **41**:357–368

Wu J. (1995) Sea surface winds - a critical input to oceanic models but are they accurately measured? *Bull. Amer. Meteor. Soc.* **76**:13–19

3 Atmospheric turbulence

Jakob Mann
Wind Energy Division, Risø DTU, Roskilde, Denmark

3.1 Introduction

For many civil engineering structures, including wind turbines, dynamic wind loading caused by the atmospheric turbulence is a serious concern for the designer. Gust loading on streamlines bridge decks requires knowledge of the vertical wind field fluctuations not only in one point, but also how the fluctuations are correlated in space Simiu and Scanlan (1996); Larose and Mann (1998). Also the horizontal components may be of importance in bridge aerodynamics. For dynamical load calculations on a wind turbine, for example at an off-shore location knowledge of all three wind components and their spatial correlations are needed because the gusts are 'sampled' in a complicated way by the sweeping blades. Yet other structures such as tension leg platforms used for extracting oil on deep waters are sensitive to slow variation in the direction of the wind. Thus various engineering structures are sensitive to various components of wind fluctuations at a wide range of frequencies and also to the spatial correlations of these fluctuations.

The spatial structure of turbulence is also important in order to understand how remote sensing instruments such as lidars measure in a turbulent flow fields. That is because the lidar's sampling volume is rather extended and thus very far from the almost point-like measurements of a ultra-sonic anemometer. The description of how lidars measure turbulence may be found in Mann et al. (2009) for a pulsed lidar, or in Sjöholm et al. (2009) for a continuous wave (cw) lidar.

The purpose of this contribution is to model the *spectral tensor* of neutral atmospheric surface layer turbulence. The spectral tensor contains all information on spectra, cross-spectra and coherences, which usually are the input requested by wind engineers. We also want to devise a general algorithm to simulate three-dimensional fields of all three components of the wind velocity fluctuations. Such simulations are particular useful for time domain simulations of gust loading of wind turbines and other structures.

In section 3.3 rapid distortion theory (RDT) is used to estimate the tendency of shear to make turbulence anisotropic. RDT is a linearization of the Navier–Stokes equations and has as such limited applicability. The influence of the non-linearity is modeled by postulating some limit as to how much shear is allowed to make the turbulence anisotropic. This modelling uses the concept of eddy lifetime. Despite the various assumptions and postulates the tensor model only contains three adjustable parameters: a length scale describing the size of the energy containing eddies, a non-dimensional number used in the parametrization of eddy lifetime, and the third parameter is a measure of the energy dissipation.

These three parameters are estimated by comparing the model to measurements over the sea in section 3.4. In section 3.5 the model is compared to various widely used wind engineering spectral formulations. Finally, in section 3.7 the spectral tensor is used in a numerical algorithm to simulate three-dimensional fields of all three components of the wind vector. This is done by recasting the Fourier representation of the wind field in the discrete wave-vector space, i.e. as a trigonometric series, where the statistics of the random coefficients are determined by the spectral tensor. The method is considerably simpler, faster and in some aspects more physical than many other currently used simulation algorithms. The method is now used in bridge aerodynamics and in load calculations on wind turbines.

Much of the material presented here has previously been reported in Mann (1994, 1998),

and more details on many aspects may be found in these papers. Newer comparison with neutral atmospheric data taken from Risø's test station Høvsøre may be found in Peña et al. (2010) and comparison under different atmospheric stabilities are under way.

3.2 Definitions

The atmospheric turbulent velocity field is denoted by $\tilde{\boldsymbol{u}}(\boldsymbol{x})$, where $\boldsymbol{x} = (x, y, z)$ is a right-handed coordinate system with the x-axis in the direction of the mean wind field and z as the vertical axis. The fluctuations around the mean wind, $\boldsymbol{u}(\boldsymbol{x}) = (u_1, u_2, u_3) = (u, v, w) = \tilde{\boldsymbol{u}}(\boldsymbol{x}) - (U(z), 0, 0)$, are assumed to be homogeneous in space, which is often the case in the horizontal directions but is only a crude approximation in the vertical. Since turbulence over the sea at high wind speeds is primarily shear-generated, the mean wind field is allowed to vary as a function of z. Because of homogeneity, the covariance tensor

$$R_{ij}(\boldsymbol{r}) = \langle u_i(\boldsymbol{x}) u_j(\boldsymbol{x} + \boldsymbol{r}) \rangle \tag{22}$$

is only a function of the separation vector $\boldsymbol{r}$ ($\langle \ \rangle$ denotes ensemble averaging).

We shall use *Taylor's frozen turbulence hypothesis* to interpret time series as 'space series' and to serve as a 'dispersion relation' between frequency and wave number (Panofsky and Dutton, 1984). Therefore, we can suppress the time argument in $\boldsymbol{u}$.

We only aim at modelling the second order statistics of turbulence, such as variances, cross-spectra, etc. For simulation purposes the velocity field is otherwise assumed to be Gaussian (see section 3.7). It is still not clear how much influence the statistics of third order, such as skewness, has on load calculations.

All second order statistics can be derived from the covariance tensor or its Fourier transform, the spectral tensor:

$$\Phi_{ij}(\boldsymbol{k}) = \frac{1}{(2\pi)^3} \int R_{ij}(\boldsymbol{r}) \exp(-i\boldsymbol{k} \cdot \boldsymbol{r}) d\boldsymbol{r}, \tag{23}$$

where $\int d\boldsymbol{r} \equiv \int_{-\infty}^{\infty} \int_{-\infty}^{\infty} \int_{-\infty}^{\infty} dr_1 dr_2 dr_3$. The spectral tensor is the basis of the Fourier simulation in section 3.7.

The stochastic velocity field can be represented in terms of a generalized stochastic Fourier-Stieltjes integral:

$$\boldsymbol{u}(\boldsymbol{x}) = \int e^{i\boldsymbol{k} \cdot \boldsymbol{x}} d\boldsymbol{Z}(\boldsymbol{k}), \tag{24}$$

where the integration is over all wave number space. The orthogonal process $\boldsymbol{Z}$ is connected to the spectral tensor by

$$\langle dZ_i^*(\boldsymbol{k}) dZ_j(\boldsymbol{k}) \rangle = \Phi_{ij}(\boldsymbol{k}) dk_1 dk_2 dk_3, \tag{25}$$

which is valid for infinitely small dk_i and where * denotes complex conjugation (Batchelor, 1953).

Is it very difficult to measure the spectral tensor directly. Instead cross-spectra, defined as

$$\chi_{ij}(k_1, \Delta y, \Delta z) = \frac{1}{2\pi} \int_{-\infty}^{\infty} R_{ij}(x, \Delta y, \Delta z) e^{-ik_1 x} dx \tag{26}$$

are often measured, say by two instruments separated by Δy in the horizontal direction perpendicular to the wind and Δz in the vertical, and are used in practical applications. The connection between the components of the spectral tensor and the cross-spectra is

$$\chi_{ij}(k_1, \Delta y, \Delta z) = \int_{-\infty}^{\infty} \int_{-\infty}^{\infty} \Phi_{ij}(\boldsymbol{k}) e^{i(k_2 \Delta y + k_3 \Delta z)} dk_2 dk_3. \tag{27}$$

When the two indices i and j are the same and $\Delta y = \Delta z = 0$ Eq. (27) becomes the one-point spectrum $F_i(k_1) = \chi_{ii}(k_1, 0, 0)$. This definition implies that spectra are *two-sided*, i.e. we get the variance by integrating from $-\infty$ to ∞. This convention is used throughout this chapter.

To distinguish between spectra as functions of wave number k_1 ($= 2\pi f/U$) and frequency f we use F for the former and S for the latter, i.e. $S_i(f)\mathrm{d}f = F_i(k)\mathrm{d}k$. The *coherence* is defined as

$$\mathrm{coh}_{ij}(k_1, \Delta y, \Delta x) = \frac{|\chi_{ij}(k_1, \Delta y, \Delta z)|^2}{F_i(k_1)F_j(k_1)}, \tag{28}$$

which can be interpreted as a normalized cross-spectrum.

3.3 Rapid distortion theory

The incompressible Navier-Stokes equation may be written as

$$\frac{\mathrm{D}\boldsymbol{u}}{\mathrm{D}t} + \boldsymbol{u} \cdot \boldsymbol{\nabla}\ \boldsymbol{U} = -\frac{1}{\rho}\boldsymbol{\nabla}\ p + \text{non-lin. and viscous terms}, \tag{29}$$

where p is the pressure, and $\mathrm{D}/\mathrm{D}t \equiv \partial/\partial t + \boldsymbol{U} \cdot \boldsymbol{\nabla}$ is the 'average Lagrangian derivative.' Assuming a linear shear ($\boldsymbol{\nabla}\ \boldsymbol{U}$ constant), taking the curl, and dropping the non-linear and viscous terms we get

$$\frac{\mathrm{D}\boldsymbol{\omega}}{\mathrm{D}t} = \boldsymbol{\Omega} \cdot \boldsymbol{\nabla}\ \boldsymbol{u} + \boldsymbol{\omega} \cdot \boldsymbol{\nabla}\ \boldsymbol{U}, \tag{30}$$

where $\boldsymbol{\Omega}$ and $\boldsymbol{\omega}$ are the mean and the fluctuating part of the vorticity. It is not at all clear that this linearization is permissible. For example, it can be shown that if the curl of Eq. (29) is used to estimate the change in mean square vorticity the non-linear terms will dominate the linear. However, Hunt and Carruthers (1990) argue that when used for the calculation of the response of velocity fluctuations ($\boldsymbol{u}$ or R_{ij}) to a sudden application of a large scale shearing or straining motion the linearization Eq. (30) is valid.
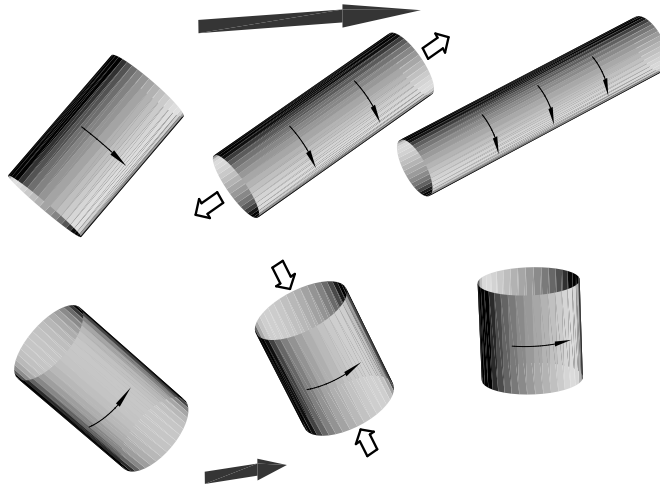
Figure 20. Interpretation of the interplay of shear and turbulence: Two differently oriented eddies are followed over three successive times. Shear stretches (along the axis of rotation) and speeds up the upper eddy while the lower eddy is compressed and slowed down.

Physically, the last term on the right hand side of Eq. (30) may be interpreted as the stretching of vorticity by the mean shear (see Figure 20). The first term is a distortion of the mean vorticity by velocity fluctuations.

In order to solve Eq. (30) we have to Fourier transform the equation. In order to do so, it is important to notice that wave fronts are advected by the mean flow i.e.

$$\frac{\mathrm{d}\boldsymbol{k}}{\mathrm{d}t} = -(\boldsymbol{\nabla}\ \boldsymbol{U})\boldsymbol{k}. \tag{31}$$

The solution to this wave front advection equation is

$$\boldsymbol{k}(t) = \exp(-\boldsymbol{\nabla}\ \boldsymbol{U}t)\boldsymbol{k}_0 \tag{32}$$

where exp means the matrix exponential.

For a general linear $\boldsymbol{U}$ Eq. (30) does not have analytic solution. However, for many simple situations such as unidirectional shear, non-rotational stretching or compression, etc. such solutions exists (Townsend, 1980).

To get the velocity field from the vorticity we shall express $\mathrm{d}Z$ in terms of $\mathrm{d}\boldsymbol{\Omega}$, which is the Fourier transform of $\boldsymbol{\omega}$ defined in parallel to Eq. (24):

$$\boldsymbol{\omega}\ = \boldsymbol{\nabla}\ \times \boldsymbol{u} \Rightarrow \mathrm{d}\boldsymbol{\Omega}\ = \mathrm{i}\boldsymbol{k} \times \mathrm{d}Z \Rightarrow -\mathrm{i}\boldsymbol{k} \times \mathrm{d}\boldsymbol{\Omega}\ = \boldsymbol{k} \times (\boldsymbol{k} \times \mathrm{d}Z). \tag{33}$$

Because of the general identity $\boldsymbol{A} \times (\boldsymbol{B} \times \boldsymbol{C}) = \boldsymbol{B}(\boldsymbol{A} \cdot \boldsymbol{C}) - \boldsymbol{C}(\boldsymbol{A} \cdot \boldsymbol{B})$ and that $\boldsymbol{k} \cdot \mathrm{d}Z = 0$ we get

$$-\mathrm{i}\boldsymbol{k} \times \mathrm{d}\boldsymbol{\Omega}\ = -k^2 \mathrm{d}Z \Rightarrow \mathrm{d}Z = \mathrm{i}\frac{\boldsymbol{k} \times \mathrm{d}\boldsymbol{\Omega}}{k^2}. \tag{34}$$

We shall re-derive (3.11) in Mann (1994), i.e. set up the equations of motion for

$$\boldsymbol{\nabla}\ \boldsymbol{U} = \left(\begin{array}{ccc} 0 & 0 & 0 \\ 0 & 0 & 0 \\ \frac{\mathrm{d}U}{\mathrm{d}z} & 0 & 0 \end{array} \right). \tag{35}$$

In this case

$$\boldsymbol{k}(t) = \exp(-\boldsymbol{\nabla}\ \boldsymbol{U}t)\boldsymbol{k}_0 = \left(\begin{array}{ccc} 1 & 0 & 0 \\ 0 & 1 & 0 \\ -\frac{\mathrm{d}U}{\mathrm{d}z}t & 0 & 1 \end{array} \right)\boldsymbol{k}_0, \tag{36}$$

in accordance with (3.13) of Mann (1994), and $\boldsymbol{\Omega}\ = (0, \mathrm{d}U/\mathrm{d}z, 0)$. The equations of motion Eq. (30) becomes

$$\frac{\mathrm{D}\boldsymbol{k} \times \mathrm{d}Z}{\mathrm{D}\beta} = k_2 \mathrm{d}Z + \left(\begin{array}{c} \mathrm{d}\Omega_3 \\ 0 \\ 0 \end{array} \right). \tag{37}$$

Taking the cross product with $\boldsymbol{k}$ and adding $\dot{\boldsymbol{k}} \times (\boldsymbol{k} \times \mathrm{d}Z)$ on both sides we get

$$-\frac{\mathrm{D}k^2 \mathrm{d}Z}{\mathrm{D}\beta} = \frac{\mathrm{D}\boldsymbol{k}}{\mathrm{D}\beta} \times (\boldsymbol{k} \times \mathrm{d}Z) + \boldsymbol{k} \times \frac{\mathrm{D}\boldsymbol{k} \times \mathrm{d}Z}{\mathrm{D}\beta}$$

$$= \frac{\mathrm{D}\boldsymbol{k}}{\mathrm{D}\beta} \times (\boldsymbol{k} \times \mathrm{d}Z) + k_2 \boldsymbol{k} \times \mathrm{d}Z + \left(\begin{array}{c} 0 \\ k_3 \\ -k_2 \end{array} \right) \mathrm{d}\Omega_3. \tag{38}$$

Writing this more explicitly we get

$$\frac{\mathrm{D}k^2 \mathrm{d}Z}{\mathrm{D}\beta} = \left(\begin{array}{c} (k_1^2 - k_2^2 - k_3^2)\mathrm{d}Z_3 - 2k_1 k_3 \mathrm{d}Z_1 \\ 2k_1(k_2 \mathrm{d}Z_3 - k_3 \mathrm{d}Z_2) \\ 0 \end{array} \right) \tag{39}$$

and using $\mathrm{D}k^2/\mathrm{D}\beta = -2k_1 k_3$ from Eq. (36) this can be shown to be equivalent to (3.11) in Mann (1994).

The differential equations Eq. (39) are easily solved given the initial conditions $\boldsymbol{k}(0) = \boldsymbol{k}_0 = (k_1, k_2, k_{30})$ and $\mathrm{d}\boldsymbol{Z}(\boldsymbol{k}_0, 0)$. Instead of time, t, we shall use the non-dimensional time, β, defined as

$$\beta = \frac{\mathrm{d}U}{\mathrm{d}z}t. \tag{40}$$

The solution to Eq. (39) is

$$d\mathbf{Z}(\mathbf{k}, \beta) = \begin{bmatrix} 1 & 0 & \zeta_1 \\ 0 & 1 & \zeta_2 \\ 0 & 0 & k_0^2/k^2 \end{bmatrix} d\mathbf{Z}(\mathbf{k}_0, 0), \tag{41}$$

where

$$\zeta_1 = \left[C_1 - \frac{k_2}{k_1} C_2 \right] \quad , \quad \zeta_2 = \left[\frac{k_2}{k_1} C_1 + C_2 \right] \tag{42}$$

with

$$C_1 = \frac{\beta k_1^2 (k_0^2 - 2k_{30}^2 + \beta k_1 k_{30})}{k^2 (k_1^2 + k_2^2)} \tag{43}$$

and

$$C_2 = \frac{k_2 k_0^2}{(k_1^2 + k_2^2)^{\frac{3}{2}}} \arctan \left[\frac{\beta k_1 (k_1^2 + k_2^2)^{\frac{1}{2}}}{k_0^2 - k_{30} k_1 \beta} \right]. \tag{44}$$

Eqs. (36) and (41) give the temporal evolution of individual Fourier modes.

RDT and surface layer turbulence

In this section we first discuss the connection between RDT and stationary surface-layer turbulence, then the key concept of eddy lifetime, and finally we combine the different parts to obtain the spectral tensor model. The theory in the previous section describes how turbulence react to a sudden and fast application of a linear shear. It is natural to ask what this has to do with turbulence in the surface layer over the ocean.

If the initial conditions can be represented by the isotropic von Kármán tensor,

$$\Phi_{ij}(\mathbf{k}) = \frac{E(k)}{4\pi k^4} \left(\delta_{ij} k^2 - k_i k_j \right), \tag{45}$$

with the energy spectrum

$$E(k) = \alpha \varepsilon^{\frac{2}{3}} L^{\frac{5}{3}} \frac{(Lk)^4}{(1 + (Lk)^2)^{\frac{17}{6}}}, \tag{46}$$

then the tensor $\Phi_{ij}(\mathbf{k}, t)$ will become more and more 'anisotropic' with time.

The linearization implied by RDT is unrealistic, and at some point (in time) the stretched eddies will break up. We postulate that eddies of linear dimension $\approx |\mathbf{k}|^{-1}$ (or more precisely the Fourier modes) are stretched by the shear over a time which is proportional to their lifetime. The lifetime τ is

$$\tau(k) \propto \varepsilon^{-\frac{1}{3}} k^{-\frac{2}{3}} \tag{47}$$

pertaining, at least in the inertial subrange, to eddies with wave vector magnitude $k = |\mathbf{k}|$ (Landau & Lifshitz 1987, § 33).

The basic *postulate* is that the *stationary* spectral tensor

$$\Phi_{ij}(\mathbf{k}) \equiv \Phi_{ij}(\mathbf{k}, \tau(k)) \tag{48}$$

describes the surface layer turbulence well. The combination of RDT and scale dependent eddy lifetimes has previously been used by Derbyshire and Hunt (1993).

Maxey (1982) has described a similar model with the exception that the lifetime τ was assumed to be constant for all wavevectors. ($\tau \, dU/dz$ is called 'the equilibrium value of the effective distortion strain' by Maxey.) Maxey's model gives a reasonable, but not perfect, description of the ratios between σ_u^2, σ_v^2, σ_w^2 and $\langle uw \rangle$ for turbulent shear flows. There are, however, two grave drawbacks when the model of Maxey (1982) is used to calculate spectra:

1. The *uw*-cross-spectrum in the inertial subrange decays as $k_1^{-\frac{5}{3}}$ whereas Wyngaard & Coté (1972) observe and give scaling arguments for $k_1^{-\frac{7}{3}}$.

2. For typical values of the effective distortion strain the model predicts $F_u/F_w \approx 7$ in the inertial subrange whereas it should be $F_u/F_w = \frac{3}{4}$.

The models presented here do not suffer from these shortcomings.
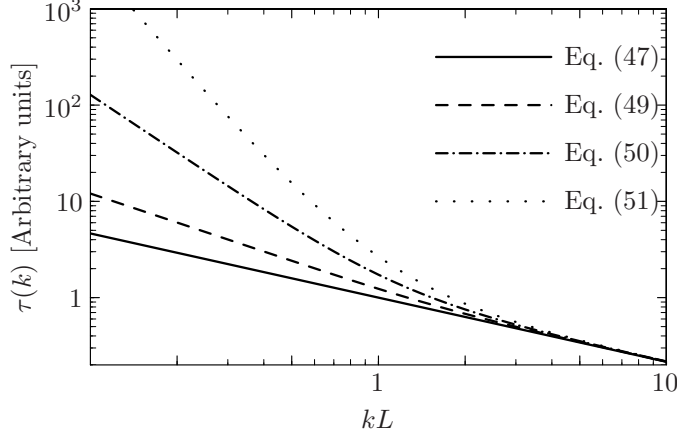
Eddy lifetimes

Figure 21. Eddy lifetimes as functions of the magnitude of the wave vector. The lifetimes given by Eq. (49) give the most realistic results.

At scales larger than the inertial subrange Eq. (47) is not necessarily valid. We construct an alternative model for the 'eddy lifetime' assuming that the destruction of an eddy with size k^{-1} is mainly due to eddies comparable to or smaller than k^{-1}. The characteristic velocity of these eddies may be written as $\left(\int_k^\infty E(p)\mathrm{d}p\right)^{\frac{1}{2}}$, and we simply assume the lifetime to be proportional to the size k^{-1} divided by this velocity:

$$
\begin{aligned}
\tau(k) &\propto k^{-1}\left(\int_k^\infty E(p)\mathrm{d}p\right)^{-\frac{1}{2}} \\
&\propto k^{-\frac{2}{3}}\left[{}_2F_1\left(\frac{1}{3},\frac{17}{6};\frac{4}{3};-(kL)^{-2}\right)\right]^{-\frac{1}{2}} \propto \begin{cases} k^{-\frac{2}{3}} & \text{for } k\to\infty \\ k^{-1} & \text{for } k\to 0 \end{cases}
\end{aligned}
\tag{49}
$$

where we have chosen E as the von Kármán energy spectrum Eq. (46) and where ${}_2F_1$ is the hypergeometric function.

Comte-Bellot and Corrsin (1971) give another lifetime model which has the right asymptotic behaviour for $k\to\infty$, the 'coherence-destroying diffusion time' :

$$
\begin{aligned}
\tau_D(k) &\propto k^{-2}\left[\int_k^\infty p^{-2}E(p)\mathrm{d}p\right]^{-\frac{1}{2}} \\
&\propto k^{-\frac{2}{3}}\left[{}_2F_1\left(\frac{4}{3},\frac{17}{6};\frac{7}{3};-(kL)^{-2}\right)\right]^{-\frac{1}{2}} \propto \begin{cases} k^{-\frac{2}{3}} & \text{for } k\to\infty \\ k^{-2} & \text{for } k\to 0 \end{cases}
\end{aligned}
\tag{50}
$$

which was constructed as the square of the eddy size divided by a k-dependent 'turbulent viscosity'.

Further, the inverse 'eddy-damping rate'

$$
\tau_E(k) \propto \left(k^3 E(k)\right)^{-\frac{1}{2}} \propto \begin{cases} k^{-\frac{2}{3}} & \text{for } k\to\infty \\ k^{-\frac{7}{2}} & \text{for } k\to 0 \end{cases}
\tag{51}
$$

is used by Lesieur (1987) in eddy-damped quasi-normal theories of turbulence as a characteristic non-linear relaxation time.

All lifetime models are shown in Figure 21 normalized such that they coincide in the inertial subrange. It turns out that σ_u^2 becomes infinite using Eq. (50) or (51), while Eq.

(47) and (49) give reasonable results. It also turns out that the spectra calculated from Eq. (49) fit the data better than Eq. (47) for which reason Eq. (49) is used in the rest of this chapter. Some support for Eq. (49) may be found in Panofsky, Larko, Lipschutz, Stone, Bradley, Bowen and Højstrup (1982) who measured eddy 'response times' of eddies in the neutral atmospheric surface-layer. Also Kristensen and Kirkegaard (1987) were in their theoretical model of the growth of a puff in a turbulent fluid compelled to use Eq. (49) rather than Eq. (50) or (51).

It is convenient to write Eq. (49) as

$$\tau(k) = \Gamma \left(\frac{\mathrm{d}U}{\mathrm{d}z}\right)^{-1} (kL)^{-\frac{2}{3}} \left[{}_2F_1\left(\frac{1}{3}, \frac{17}{6}; \frac{4}{3}; -(kL)^{-2}\right)\right]^{-\frac{1}{2}}, \tag{52}$$

where Γ is a parameter to be determined. [1]

It should be emphasized that at low wave numbers the assumptions made so far are not valid. F.ex. the assumptions of linear shear is only valid over small distances, i.e. for large k. Similarly, homogeneity is a dubious assumption for large vertical separations. Finally, despite talking about eddy lifetimes, there is no real modelling of the decay process, because there is no equation describing the non-linear transfer of energy among various wave vectors.

In an attempt to relax the assumption of vertical homogeneity Mann (1994) modelled the influence of the blocking of the surface in addition to shear. This gave slightly better coherence predictions than the present model, but greatly complicated the mathematics and had also other negative consequences.

The uniform shear model

To make a stationary model we use Eqs. (52) and (48) discussed in the beginning of this section, i.e. we substitute t with τ given by Eq. (52). For the 33-component we get

$$\Phi_{33}(\boldsymbol{k}) = \Phi_{33}^{\mathrm{iso}}(\boldsymbol{k}_0)\frac{k_0^4}{k^4} = \frac{E(k_0)}{4\pi k^4}(k_1^2 + k_2^2), \tag{53}$$

where Φ_{33}^{iso} refers to the isotropic von Kármán tensor and E to the energy spectrum Eq. (46). The other components become

$$\Phi_{11}(\boldsymbol{k}) = \frac{E(k_0)}{4\pi k_0^4}\left(k_0^2 - k_1^2 - 2k_1 k_{30}\zeta_1 + (k_1^2 + k_2^2)\zeta_1^2\right) \tag{54}$$

$$\Phi_{22}(\boldsymbol{k}) = \frac{E(k_0)}{4\pi k_0^4}\left(k_0^2 - k_2^2 - 2k_2 k_{30}\zeta_2 + (k_1^2 + k_2^2)\zeta_2^2\right) \tag{55}$$

$$\Phi_{12}(\boldsymbol{k}) = \frac{E(k_0)}{4\pi k_0^4}\left(-k_1 k_2 - k_1 k_{30}\zeta_2 - k_2 k_{30}\zeta_1 + (k_1^2 + k_2^2)\zeta_1\zeta_2\right) \tag{56}$$

$$\Phi_{13}(\boldsymbol{k}) = \frac{E(k_0)}{4\pi k_0^2 k^2}\left(-k_1 k_{30} + (k_1^2 + k_2^2)\zeta_1\right) \tag{57}$$

and

$$\Phi_{23}(\boldsymbol{k}) = \frac{E(k_0)}{4\pi k_0^2 k^2}\left(-k_2 k_{30} + (k_1^2 + k_2^2)\zeta_2\right). \tag{58}$$

Eqs. (53)–(58) with Eq. (52) constitute the uniform shear model (US).

These equations have two differences from the expressions of Townsend (1976) for plane shearing of homogeneous turbulence. The first is the elimination of time by Eq. (52) and the second and related difference is that we do not use the turbulent viscosity of Townsend, which would make the decay time for all eddies equal, independent of their sizes.

---

[1]Keith Wilson has reformulated this expression in terms of the incomplete beta function.

3.4 Fitting spectra to observations

First the uncertainties on estimated spectra are discussed. Theses are either caused by variations in atmospheric stability, which persists even at high wind speeds (> 16 m s^{-1}) over water, or by statistical variations. Secondly, the measured neutral spectra are fitted to the spectral tensor model. Based on this fit the coherences are finally predicted and compared to the measurements.

Uncertainties on spectra

Often spectra are averaged over, say, n consecutive frequencies or wave numbers to decrease the random error of the estimate. Alternatively, the time series could be divided into n segments of equal duration. Each segment is then Fourier transformed and the spectrum determined as the average of the absolute square of these Fourier transforms. For either definition the statistical uncertainty on spectral density F calculated from a stationary time series is (under the assumption that the time series is long compared to the time scale of the process)

$$\frac{\sigma(F)}{\langle F \rangle} = \frac{1}{n^{\frac{1}{2}}} \tag{59}$$

(Koopmans, 1974; Bendat and Piersol, 1986).

Figure 22 shows the result of an analysis of 14 two-hour time series from the Great Belt. The series have mean speeds U between 16 and 20 m s^{-1} and the mean directions are within a narrow range around south where there is an uninterrupted fetch over water for at least 20 km.

Assuming the stability to be neutral, the variation of spectral densities should obey Eq. (59) and the standard deviation at the lowest wavenumbers should be around 25% and 5% at $k_1 = 0.1$ m^{-1}. The observed rms variations are clearly larger, at least 50% at the lowest frequencies and maybe 20% at higher frequencies. Most noticeably, there are spectra with only 10% of the spectral density of the others.

This variation is due to the stability of the atmosphere not being neutral. The case with suppressed turbulence is slightly stable and has $U = 16$ m s^{-1}. From the point of view of aerodynamic loads this may imply enhanced loads on a bridge deck. While the buffeting loads are smaller the loads from vortex shedding can be much larger. Usually vortex shedding from a bridge deck is suppressed or even destroyed by the turbulence in the atmosphere, but if turbulence is absent as in a stably stratified atmosphere (e.g. warm air flowing out over a cold sea) the vortex shedding might be strong. Stable stratification might also alter loads on off-shore wind turbines because of increased shear.

Unstable stratification also alters the spectrum. Though none of the spectra from the Great Belt are obtained under very unstable situations, an analysis of unstable, high-wind spectra on the west coast of Norway indicate that the spectra are mainly enhanced (by more than 100%) at *very* low frequencies ($f < 0.02$ Hz). These might be relevant for various off-shore production units (Mann, 1992).

Spectral fitting and prediction of coherences

In order to conduct simultaneous measurements of spectra and coherence over the sea a 70 m high mast was erected 40 m from an existing mast on the easterly spit of Sprogø, an island in the midst of the Great Belt separating the two Danish islands Funen and Zealand. A 15 m long horizontal boom was mounted symmetrically at the top of the new mast so that the whole construction has the form of a letter "T". A Kaijo-Denki DAT-300 omni-directional sonic anemometer was installed at each end of the boom and at the top of the old mast, providing 15.0, 32.5 and 47.5 m horizontal separations between the three co-linear instruments. The mast array is shown in Figure 24. More details about
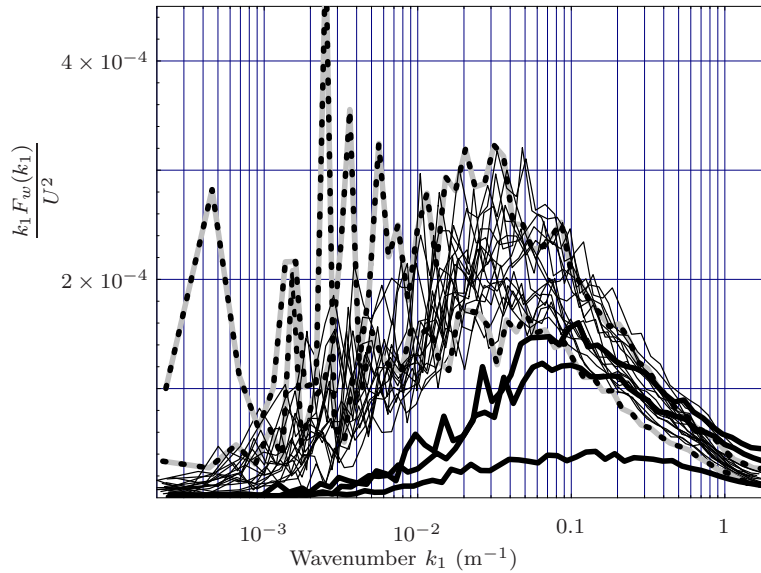
Figure 22. Spectra of w from the Great Belt Coherence Experiment. Mean wind speeds are between 16 and 20 m s^{-1} and directions are in a narrow interval around the South. Dashed spectra have slightly unstable stratification, gray have stable, and the thin have neutral.
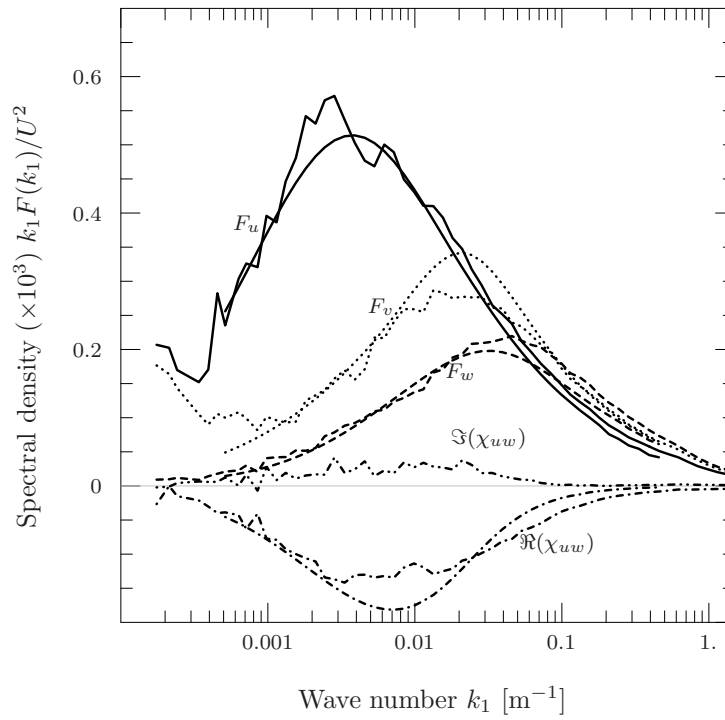
Figure 23. Average u-, v-, w-, and cross-spectra of all the neutral *runs present in Figure 22. The ragged curves are measurements while the smooth are the model spectra. The model has zero imaginary part of the cross-spectrum (quadrature spectrum).*

the experiment including correction for flow distortion by the sonic anemometers may be found in Mann et al. (1991).

The measured spectra shown in Figure 23 are an average of 16 *neutral* two hour runs with wind speeds between 16 and 20 m s^{-1}. The smooth curves are model spectra derived
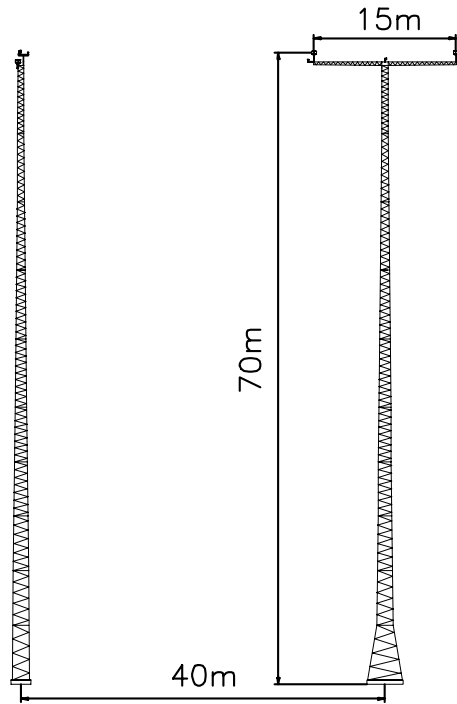
Figure 24. The mast array on Sprogø viewed from SSE. The tiny dots at the top of the masts are the omni-directional sonic anemometers.

from the spectral tensor model with the parameters $\Gamma = 3.2$, $L = 61$ m, and $\alpha\varepsilon^{2/3}/U^2 = 1.810^{-4}$ m$^{-2/3}$, which are taken from Mann (1994), who used fewer two hour runs but slightly higher wind speeds.

Figure 25. The dots are measured coherences from the same set of data as used for Figure 23 for various horizontal separations Δy and for all three velocity components. The lines are the coherences predicted by the model.

These parameters are in turn used to predict the coherences as shown in Figure 25. As seen from this figure the predictions agree well with the measurements except for the w

coherence, especially at the largest separation.

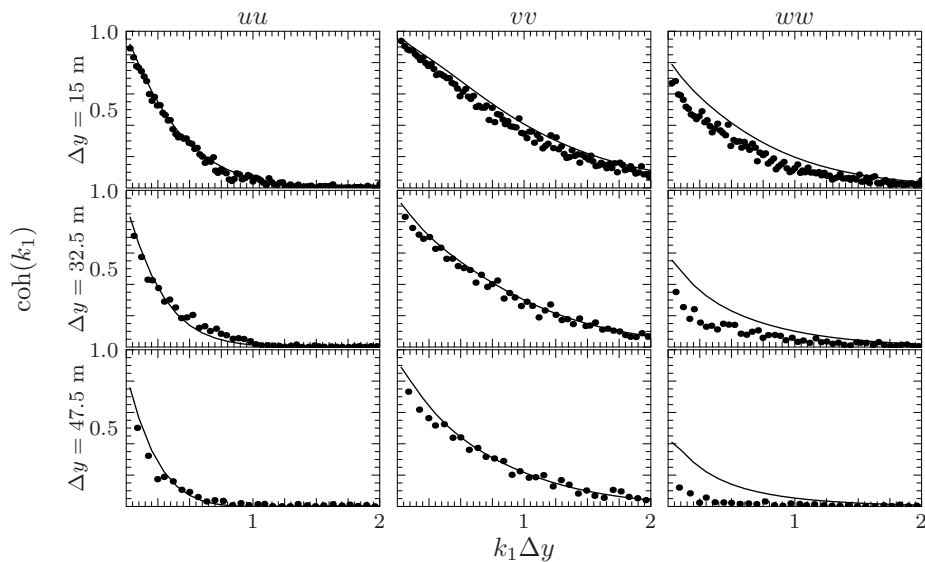## 3.5 Model spectra over the ocean and flat land

Here we compare the tensor model of section 3.3 to spectra and coherences from the literature. We will not give an exhaustive review of spectral models but select a few modern models which the author believes is used in wind engineering. The purpose is to estimate the parameters Γ, L and $\alpha\varepsilon^{2/3}$ for a given mean wind speed U and height above the water surface z.
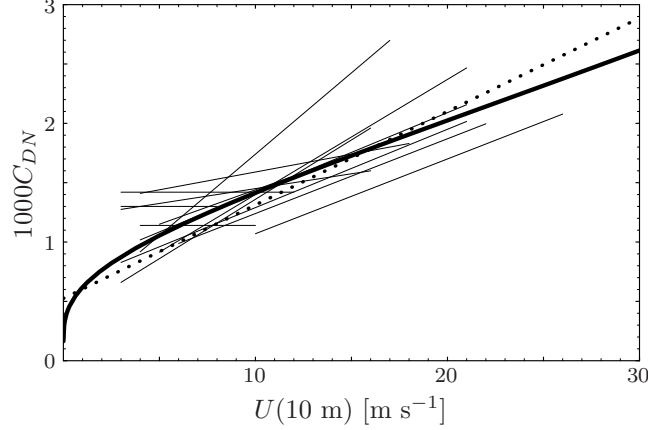

Figure 26. The neutral drag coefficient C_{DN} as a function of mean wind speed at $z = 10$ m. The broad line is from Charnock's relation Eqs. (62) and (60). The thin lines are empirical relations from Geernaert (1987) and the dotted line is from NDP (1998), see Eq. (71).

The logarithmic mean wind profile defines the roughness length:

$$U(z) = \frac{u_*}{\kappa} \ln(z/z_0), \tag{60}$$

where $u_* \equiv (- \langle uw \rangle)^{1/2}_{z \to 0}$ is the friction velocity and $\kappa = 0.40$ the von Kármán constant (Landau and Lifshitz, 1987; Panofsky and Dutton, 1984).

ESDU International (1982) gives a slightly more accurate wind profile:

$$U(z) = \frac{u_*}{\kappa} \left(\ln(z/z_0) + 34.5 f z/u_* \right) \tag{61}$$

with the Coriolis parameter $f \equiv 2\Omega \sin \phi$, where Ω is the angular velocity in $\mathrm{rad\,s^{-1}}$ of the Earth and ϕ the geographical latitude. The profile Eq. (61) is valid up to $z = 300$ m, below 30 m Eq. (60) is a good approximation to Eq. (61). Throughout this comparison we use $f = 10^{-4}$ s^{-1}.

Charnock (1955) argued that over the sea the roughness length is related to $g = 9.8$ m s^{-2} the acceleration due to gravity and the friction velocity by

$$z_0 = A \frac{u_*^2}{g} \tag{62}$$

where A, the Charnock constant, must be determined experimentally. On basis of an extensive literature study of ocean data Garratt (1977) found that the best fit of Eq. (62) is $A = 0.0144$. A slightly newer value is given by ESDU International (1982):

$$A = 0.0167, \tag{63}$$

which will be used here. Over the ocean the neutral drag coefficient

$$C_{DN} = \left(\frac{u_*}{U(10 \text{ m})} \right)^2 \tag{64}$$

increases monotonicly with U as can be seen by solving Eqs. (62) and (60). This is shown in Figure 26 as a broad line together with several recent empirical relations. The figure gives a good impression of the uncertainty in estimates of drag coefficients. Among the various reasons for this variability are atmospheric stability, surface currents, 'wave age', length of the fetch over water, and water depth (Garratt, 1977; Geernaert, 1987; Brown and Swail, 1991). The spectral density of velocity fluctuations is in general proportional to the drag coefficient so the uncertainty of the former is probably of the same order of the latter.

Code and textbook spectra

Surface layer scaling is used in many spectral models, implying that length scales are proportional to z and that variances are proportional to u_*^2. Therefore, it is convenient to normalize the spectra with u_*^2 and present them as functions of either $n \equiv fz/U$ or $k_1 z$. All spectra in this paper are 'two-sided' implying $\int_\infty^{-\infty} S(f)\mathrm{d}f$ is equal to the variance[2].

The spectra of Kaimal are (Kaimal et al., 1972; Kaimal and Finnigan, 1994)

$$\frac{fS_u(f)}{u_*^2} = \frac{k_1 F_u(k_1)}{u_*^2} = \frac{52.5n}{(1+33n)^{5/3}}, \tag{65}$$

$$\frac{fS_v(f)}{u_*^2} = \frac{8.5n}{(1+9.5n)^{5/3}}, \tag{66}$$

and

$$\frac{fS_w(f)}{u_*^2} = \frac{1.05n}{1+5.3n^{5/3}}. \tag{67}$$

Kaimal's spectra are based on measurements over flat homogeneous terrain in Kansas.

The spectra of Simiu and Scanlan (1996) have the same functional shapes as Kaimal's but the numerical constants are different:

$$\frac{fS_u(f)}{u_*^2} = \frac{100n}{(1+50n)^{5/3}}, \tag{68}$$

$$\frac{fS_v(f)}{u_*^2} = \frac{7.5n}{(1+9.5n)^{5/3}}, \tag{69}$$

and

$$\frac{fS_w(f)}{u_*^2} = \frac{1.68n}{1+10n^{5/3}}. \tag{70}$$

Deviations from surface layer scaling are found in the model spectra from ESDU International (1985). Also the spectra of Norwegian Petroleum Directorate NDP (1998) and Højstrup, Larsen and Madsen (1990) do not obey surface layer scaling, but they are only limited to u-spectra.

The Engineering Science Data Unit (ESDU) wind profile, spectra and coherences (ESDU International, 1982, 1985 and 1986) are derived from many sources from all over the world during several decades. ESDU proposes that the turbulence intensities and length scales in the surface layer are dependent on mean wind speed. The argument is that the boundary layer depth increases with increasing wind speed implying larger scales of the turbulence. The other models, relying on surface layer scaling do not contain any information on the boundary layer depth and they contain no explicit reference to the mean wind speed. The equations of ESDU are, compared to all other spectral models discussed here, by far the most complicated. Therefore we shall not cite them explicitly. The most important input parameters are, as for the other spectral models, the height above the surface z, and the mean wind speed at some height. Of less important input is the Coriolis parameter which, as mentioned previously, is taken to be $f = 10^{-4} \mathrm{s}^{-1}$. The models we use are valid for the neutral atmosphere.

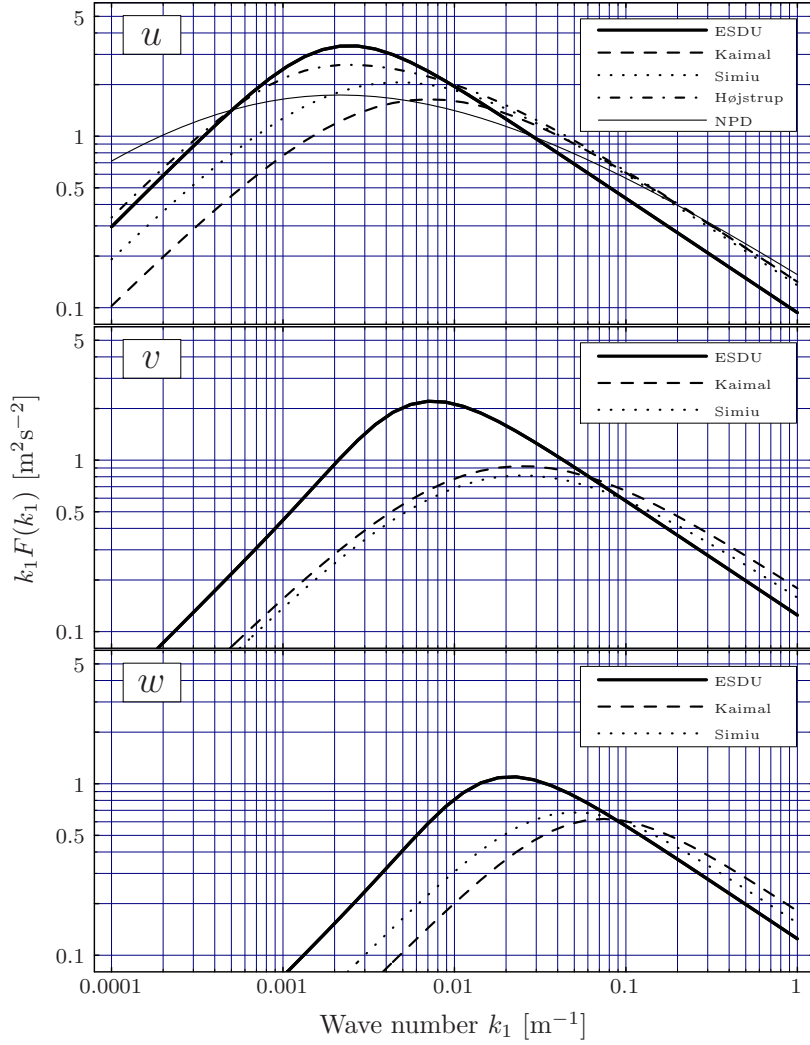[2]The so-called 'one-sided' spectra, where $\int_0^\infty S(f)\mathrm{d}f$ is equal to the variance, are probably more commonly used.

Figure 27. Comparison of spectral models. For the comparison $z = 40$ m and $U = 40$ m s^{-1} (over the sea) is chosen. For u (ESDU International, 1985), Eqs. (65), (68), (78), (74) are used. For v and w (ESDU International, 1985), Eqs. (66) and (69), and (ESDU International, 1985), Eqs. (67) and (70), respectively. Eq. (61) together with Eq. (62) gives $u_* = 1.78$ m s^{-1} and $z_0 = 0.0054$ m.

The u-spectrum of NDP (1998) applies to winds over oceans and assumes the drag coefficient to be

$$C_{DN} = 0.525 \times 10^{-3}(1 + 0.15U_{10}), \tag{71}$$

see Figure 26. Integrating $\mathrm{d}U/\mathrm{d}z = u_*/(\kappa z) = \sqrt{C_{DN}}U_{10}/(\kappa z)$ Eq. (71) implies that

$$U(z) = U_{10}\left(1 + C\ln\frac{z}{10\ \mathrm{m}}\right) \tag{72}$$

with

$$C = 0.0573(1 + 0.15U_{10})^{1/2} \tag{73}$$

where U_{10} has to be measured in meters per second. While discussing the NPD spectrum we also assume the unit of z to be meter, f is Hz and S_u is m^2 s^{-2} Hz^{-1}. The spectral density of the longitudinal wind component is

$$S_u(f) = \frac{160\left(\dfrac{U_{10}}{10}\right)^2\left(\dfrac{z}{10}\right)^{0.45}}{\left(1 + \tilde{f}^n\right)^{\frac{5}{3n}}} \tag{74}$$
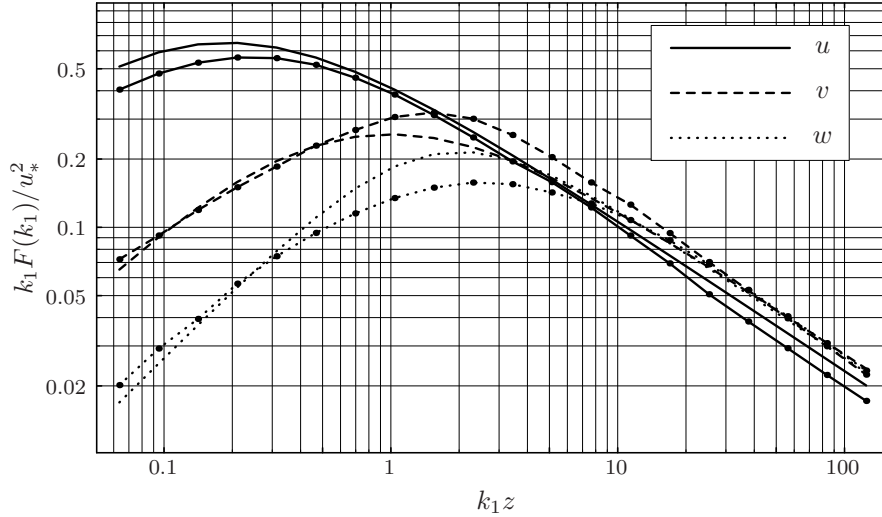
Figure 28. The 'sheared spectral tensor' of section 3.3 (curves with dots) fitted to the models by Simiu and Scanlan Eqs. (68)–(70). The result is given by Eq. (81).

with

$$\tilde{f} = 172 f \left(\frac{z}{10}\right)^{2/3} \left(\frac{U_{10}}{10}\right)^{-3/4} \tag{75}$$

and $n = 0.468$. This spectrum implies that the variance

$$\sigma_u^2 = 0.00309 \frac{U_{10}^{2.75}}{z^{0.217}} \tag{76}$$

will decrease with height and not constant as implied by surface layer scaling. Furthermore, the integral length scale

$$\text{length scale} \propto z^{2/3} U_{10}^{1/4} \tag{77}$$

will not be proportional with height but will grow somewhat slower and it will also increase a little with wind speed. This is not consistent with surface layer scaling where it under neutral conditions is constant with wind speed.

Højstrup et al. (1990) suggested that spectra at low frequencies do not obey surface layer scaling because the low frequency part scales with the height of the boundary layer, not z. To verify their model they used data selected for neutrality and high wind speeds ($11 < U < 23$ m s^{-1}) from both over sea and land sites in Denmark. The u-model is[3]

$$\frac{f S_u(f)}{u_*^2} = \left(\frac{2.5 n_t}{1 + 2.2 n_t^{5/3}} + \frac{52.5 n}{(1 + 33 n)^{5/3}}\right) \frac{1}{1 + 7.4 (z/A)^{2/3}} \tag{78}$$

where the 'neutral length scale' $A = 3000$ m and $n_t = f A / U$. The second term in the parenthesis is the Kaimal spectrum Eq. (65).

All spectral models are compared in Figure 27 for a specific choice of U and z. Generally, ESDU has larger length scales compared to those by Kaimal and by Simiu & Scanlan, which are similar. NPD and Højstrup support ESDU's large u-scale. ESDU, though, has the most peaked spectra and, at high wave numbers, slightly lower spectral densities. All spectra agree fairly well at high wave numbers but have substantial scatter at low wave numbers.

3.6   Comparison with the spectral tensor model

Here we fit the spectral tensor of section 3.3 to models that describe all three component spectra, namely the ones by Kaimal, Simiu & Scanlan and ESDU.

---

[3]Højstrup, Larsen and Madsen (1990) also gives a model for the v spectrum, but it was never compared with data, so it will not be discussed here.
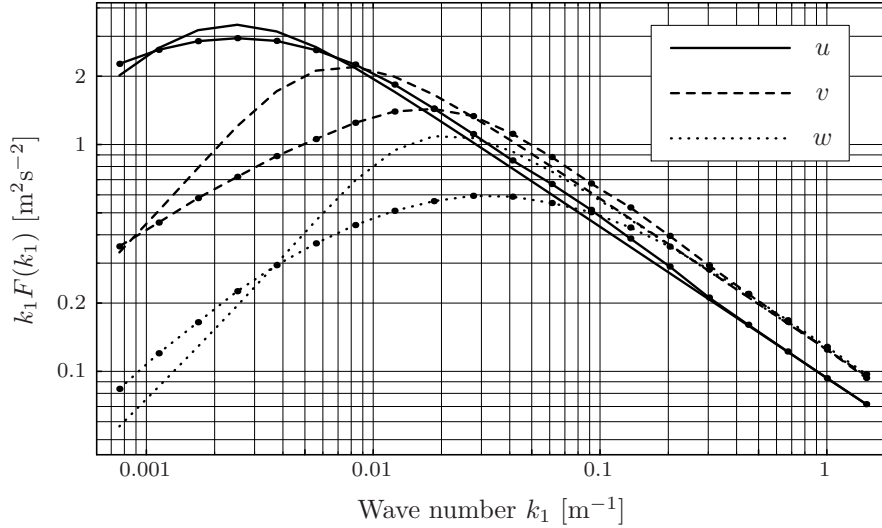
Figure 29. Example with $z = 40$ m and $U = 40$ m s^{-1} of the fit of the spectral tensor model (curves with dots) to the ESDU models.

We obtain the parameters Γ, L and $\alpha\varepsilon^{2/3}$ by making a simultaneous least squares fit to the u-, v- and w-model spectra for wave numbers in the range $0.05 < k_1 L < 100$. For the Kaimal spectra we get

$$
\begin{aligned}
\Gamma &= 3.9 \\
L &= 0.59z \\
\alpha\varepsilon^{2/3} &= 3.2\frac{u_*^2}{z^{2/3}},
\end{aligned}
\tag{79}
$$

where the dependence on z is a consequence of surface layer scaling. For the Simiu & Scanlan spectra, where the fit is shown in Figure 28, we get

$$
\begin{aligned}
\Gamma &= 3.8 \\
L &= 0.79z \\
\alpha\varepsilon^{2/3} &= 2.8\frac{u_*^2}{z^{2/3}}
\end{aligned}
\tag{80}
$$

and for both models u_* can be obtained from Figure 26.

It is more complicated to get the parameters from the ESDU models because the spectra no longer depend on U and z in a simple way. For each set $\{U, z\}$, a fit to the tensor model has to be calculated. We do that on a mesh limited by $10 < U < 80$ m s^{-1}, $5 < z < 300$ m over the sea. The result is shown in Figure 30. As an example of use of these graphs, suppose that the parameters for $U(z = 80$ m$) = 20$ m s^{-1} are wanted. From the upper plot of Figure 30 we get $L = 33$ m and $\alpha\varepsilon^{2/3} = 0.1$ m$^{4/3}$ s^{-2}. The lower plot gives $\Gamma = 4.5$.

Table 9. Parameters of the spectral tensor derived from different sources for $U(40$ m$) = 40$ m s^{-1} at sea.

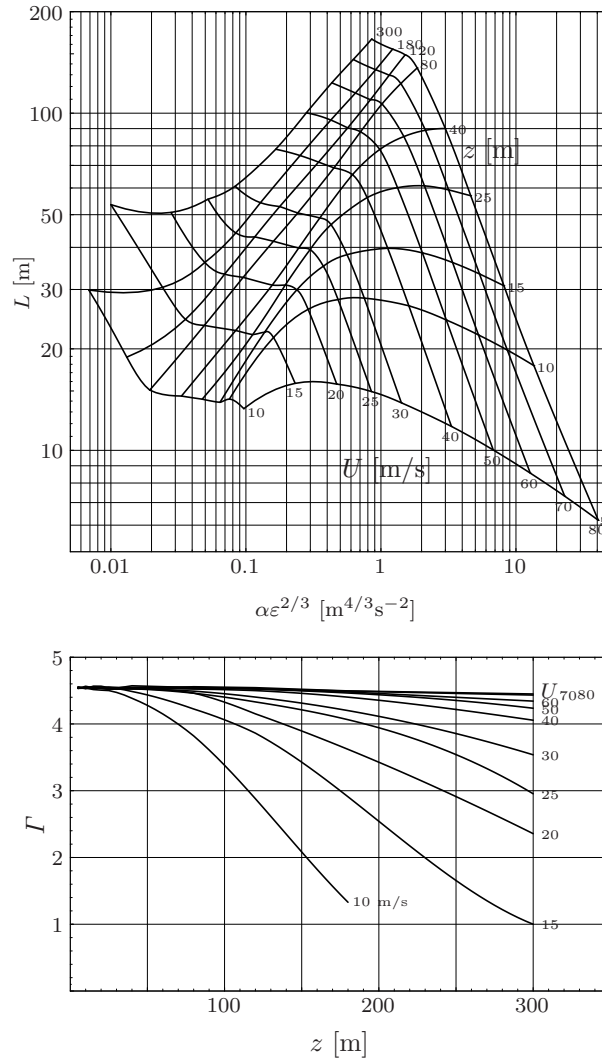|	Γ	L [m]	$\alpha\varepsilon^{2/3}$ [m$^{4/3}$ s^{-2}]
Great Belt	3.2	35	0.79
Kaimal	3.9	24	0.86
Simiu	3.8	31	0.76
ESDU	4.5	66	0.62

Figure 30. The parameters of the spectral tensor model derived from fits to the ESDU model spectra for turbulence over the sea. Given U and z, all three parameters can be extracted from these plots.

Another example is shown in Table 9 where the Great Belt data from Mann (1994) are extrapolated using neutral surface layer scaling to $U(40 \text{ m}) = 40 \text{ m s}^{-1}$. The spectral fit for these values of U and z is shown in Figure 29.

Literature coherences and coherences derived from the spectral tensor by Eqs. (27) and (28) are compared in Mann (1998). Generally, the agreement is good.

3.7 Wind field simulation

Having discussed the spectral tensor in relation to commonly used literature spectra we now describe how to simulate a velocity field $\boldsymbol{u}(\boldsymbol{x})$, which can be used for calculating loads on engineering structures. We approximate the integral Eq. (24) by a discrete Fourier series:

$$u_i(\boldsymbol{x}) = \sum_{\boldsymbol{k}} \text{e}^{\text{i}\boldsymbol{k}\cdot\boldsymbol{x}} C_{ij}(\boldsymbol{k}) n_j(\boldsymbol{k}), \tag{81}$$

where the l'th component of $\boldsymbol{x}$ is $x_l = n\Delta L_l$ with $n = 1, ..., N_l$. The symbol $\sum_{\boldsymbol{k}}$ denotes the sum over all wave vectors $\boldsymbol{k}$ with components $k_i = m2\pi/L_i$, with the integer $m = -N_i/2, ..., N_i/2$, $n_j(\boldsymbol{k})$ are independent Gaussian stochastic complex variables with unit variance and $C_{ij}(\boldsymbol{k})$ are coefficients to be determined. The great advantage of Eq. (81)

is that, once the coefficients are known, it can be evaluated very fast by the fast Fourier transform (FFT) (Shinozuka and Deodatis, 1991).

Solving Eq. (81) we get approximately (Mann, 1998)

$$C_{ij}(\boldsymbol{k})n_j(\boldsymbol{k}) = \frac{1}{V(B)} \int_B u_i(\boldsymbol{x})\mathrm{e}^{-i\boldsymbol{k}\cdot\boldsymbol{x}}\mathrm{d}\boldsymbol{x}, \tag{82}$$

where $V(B) = L_1 L_2 L_3$ is the volume of B and $\int_B \mathrm{d}\boldsymbol{x}$ means integration over the box B. From Eq. (82) it is easy to see that $n_j(\boldsymbol{k})$ *have* to be Gaussian when $u_i(\boldsymbol{x})$ is a Gaussian field. Many authors relax this constraint and let $n_j(\boldsymbol{k})$ have random phase but a fixed absolute value (Shinozuka and Jan, 1972; Shinozuka and Deodatis, 1991, 1996). Using this approach every sample will get exactly the same variance and, given a wavenumber (or vector), the estimated power spectral density at this wavenumber will be the same for all realizations of the same process. This might be advantageous in some situations, but it is in contrast to power spectral density estimates of stationary time series which have 100% rms (Press et al., 1992; Bendat and Piersol, 1986). The difference between the two approaches is discussed in detail in Grigoriu (1993). In practice there is little difference and both models could be used. However, the Gaussian approach is usually easier to analyze theoretically and we shall stick to that here.

To find the coefficients $C_{ij}(\boldsymbol{k})$ we calculate the covariance tensor of Eq. (82) obtaining

$$
\begin{aligned}
C_{ik}^*&(\boldsymbol{k})C_{jk}(\boldsymbol{k}) \\
&= \frac{1}{V^2(B)} \int_B \int_B \langle u_i(\boldsymbol{x})u_j(\boldsymbol{x}')\rangle \, \mathrm{e}^{i\boldsymbol{k}\cdot\boldsymbol{x}}\mathrm{e}^{-i\boldsymbol{k}\cdot\boldsymbol{x}'}\mathrm{d}\boldsymbol{x}\mathrm{d}\boldsymbol{x}' \\
&= \frac{1}{V^2(B)} \int \int R_{ij}(\boldsymbol{x}-\boldsymbol{x}')1_B(\boldsymbol{x})1_B(\boldsymbol{x}')\mathrm{e}^{i\boldsymbol{k}\cdot(\boldsymbol{x}-\boldsymbol{x}')}\mathrm{d}\boldsymbol{x}\mathrm{d}\boldsymbol{x}',
\end{aligned}
\tag{83}
$$

where $1_B(\boldsymbol{x}) = 1$ if $\boldsymbol{x} \in B$ and 0 otherwise. Using the change of variables $\boldsymbol{r} = \boldsymbol{x} - \boldsymbol{x}'$ and $\boldsymbol{s} = \boldsymbol{x} + \boldsymbol{x}'$ having the Jacobian $|\partial(\boldsymbol{r},\boldsymbol{s})/\partial(\boldsymbol{x},\boldsymbol{x}')| = 8$ we get

$$C_{ik}(\boldsymbol{k})C_{kj}(\boldsymbol{k}) = \frac{1}{8V^2(B)} \int R_{ij}(\boldsymbol{r})\mathrm{e}^{-i\boldsymbol{k}\cdot\boldsymbol{r}} \int 1_B\left(\frac{\boldsymbol{s}+\boldsymbol{r}}{2}\right)1_B\left(\frac{\boldsymbol{s}-\boldsymbol{r}}{2}\right)\mathrm{d}\boldsymbol{s}\mathrm{d}\boldsymbol{r} \tag{84}$$

The inner integration can be carried out according to

$$\int 1_B\left(\frac{\boldsymbol{s}+\boldsymbol{r}}{2}\right)1_B\left(\frac{\boldsymbol{s}-\boldsymbol{r}}{2}\right)\mathrm{d}\boldsymbol{s} = \begin{cases} \prod_{l=1}^3 2(L_l - |r_l|) & \text{for } |r_l| < L_l \text{ for all } l \\ 0 & \text{otherwise} \end{cases} \tag{85}$$

so, using the convolution theorem and noting that the Fourier transform of $L - |r|$ (for $|r| < L$ and else 0) is $L^2 \operatorname{sinc}^2(kL/2)$, we get

$$C_{ik}^*(\boldsymbol{k})C_{jk}(\boldsymbol{k}) = \int \Phi_{ij}(\boldsymbol{k}')\prod_{l=1}^3 \operatorname{sinc}^2\left(\frac{(k_l - k_l')L_l}{2}\right)\mathrm{d}\boldsymbol{k}', \tag{86}$$

where $\operatorname{sinc} x \equiv (\sin x)/x$. For $L_l \gg L$, the sinc^2-function is 'delta-function-like', in the sense that it vanishes away from k_l much faster than any change in Φ_{ij}, and the area beneath the sinc^2-curve is $2\pi/L_l$. Therefore, we get

$$C_{ik}^*(\boldsymbol{k})C_{jk}(\boldsymbol{k}) = \frac{(2\pi)^3}{V(B)}\Phi_{ij}(\boldsymbol{k}). \tag{87}$$

The solution to Eq. (87) is

$$C_{ij}(\boldsymbol{k}) = \frac{(2\pi)^{3/2}}{V(B)^{1/2}}A_{ij}(\boldsymbol{k}) = (\Delta k_1 \Delta k_2 \Delta k_3)^{1/2} A_{ij}(\boldsymbol{k}) \tag{88}$$

with $A_{ik}^* A_{jk} = \Phi_{ij}$ and $\Delta k_l = 2\pi/L_l$. This result should be expected when comparing Eq. (24) to (81).

Two problems occur by simulating a field by the Fourier series Eq. (81) with the coefficients Eq. (88). The first is that for many applications the dimensions of the simulated

box of turbulence need *not* to be much larger than the length scale of the turbulence model L. Therefore Eq. (87) may not be a good approximation to Eq. (86). The second problem is that the simulated velocity field Eq. (81) is periodic in all three directions. Both problems have been addressed in Mann (1998).

The algorithms above simulate a three-dimensional vector field on a three-dimensional domain, but it can easily be modified to simulate one- or two-dimensional vectors in a 2- or 3-D domain (Mann, 1998). The algorithms are not needed for a one-dimensional domain, i.e. simulation of wind fluctuations in one point as a function of time.

The implementation of the model includes three steps:

1. Evaluate the coefficients $C_{ij}(\boldsymbol{k})$, either by Eq. (88) or a modification of this (Mann, 1998).

2. Simulate the Gaussian variable $n_j(\boldsymbol{k})$ and multiply.

3. Calculate $u_i(\boldsymbol{x})$ from Eq. (81) by FFT.

The time consumption in the first step is proportional to the total number of points $N = N_1 N_2 N_3$ in the simulation. The required time to perform the FFT is $O(N \log_2 N)$ (Press et al., 1992). In practice, simulating a three-dimensional field, used for load calculations on wind turbines, with millions of velocity vectors takes of the order of a few minutes on a modern pc.

Notation

A	Charnock constant
	neutral length scale
B	box of e.g. turbulence
coh_{ij}	coherence or normalized cross-spectrum
cw	continuous wave
C_{ij}	coefficients for a discrete Fourier series
C_{DN}	neutral drag coefficient
$E(k)$	energy spectrum
ESDU	engineering science data unit
f	frequency
	Coriolis parameter
F	spectrum (function of wave number)
FFT	fast Fourier transform
g	gravitational acceleration
i	tensor index
j	tensor index
k	wave number/component
$\mathbf{k}$	wave vector
L	turbulence length scale or length of a volume
m	integer number
n	number of segments
	normalized frequency
$n_j(\mathbf{k})$	Gaussian variable
n_t	normalized neutral frequency
N	number of points
NPD	Norwegian Petroleum Directorate
p	pressure
$\mathbf{r}$	separation vector
$R_{ij}(r)$	covariance tensor
RDT	rapid distortion theory
S	spectrum (function of frequency)
t	time
u	longitudinal wind component
$\tilde{\boldsymbol{u}}(\boldsymbol{x})$	turbulent velocity field
u_*	friction velocity
U	mean wind speed

U	mean flow
US	uniform shear model
v	transversal wind component
$V(B)$	volume of the box B
w	vertical wind component
x	direction of the mean wind field
$\boldsymbol{x}$	coordinate system
y	transversal direction
z	vertical axis direction or height
z_0	roughness length
Z	orthogonal process
$\alpha\varepsilon$	energy dissipation measure
β	non-dimensional time
Γ	anisotropy parameter
δ	Kronecker delta
κ	von Kármán constant
σ_X	standard deviation of a variable X
τ	eddy lifetime
τ_D	coherence-destroying diffusion time
τ_E	eddy-damping rate
ϕ	geographical latitude
$\Phi_{ij}(\mathbf{k})$	spectral tensor
χ_{ij}	cross-spectra
ω	fluctuating part of the vorticity
Ω	angular velocity
$\boldsymbol{\Omega}$	mean part of the vorticity
∂	partial derivate
∇	vector differential operator
$\langle X \rangle$	ensemble average of the variable X

References

Batchelor G. K. (1953) The theory of homogeneous turbulence, Cambridge University

Bendat J. S. and Piersol A. G. (1986) Random data: Analysis and Measurement Procedures, 2 edn, Wiley-Interscience

Brown R. D. and Swail, V. R. (1991) Over-water gust factors. *Ocean Engng.* **18**(4):363–394

Charnock H. (1955) Wind stress on a water surface. *Q. J. Royal Meteorol. Soc.* **81**:639–640

Comte-Bellot G. and Corrsin S. (1971) Simple Eulerian time correlation of full- and narrow-band velocity signals in grid generated, 'isotropic' turbulence. *J. Fluid Mech.* **48**:273–337

Derbyshire S. H. and Hunt J. C. R. (1993) Structure of turbulence in stably stratified atmospheric boundary layers; comparison of large eddy simulations and theoretical models. *in* S. D. Moobs and J. C. King (eds), Waves and Turbulence in Stably Stratified Flows, Clarendon, Oxford, 23–59 pp

ESDU International (1982) Characteristics of wind speed in the lower layers of the atmosphere near the ground: strong winds (neutral atmosphere), ESDU International, London

ESDU International (1985) Characteristics of atmospheric turbulence near the ground. Part II: single point data for strong winds (neutral atmosphere), ESDU International, London

Garratt J. R. (1977) Review of drag coefficients over oceans and continents, *Mon. Wea. Rev.* **105**:915–929

Geernaert G. L. (1987) On the importance of the drag coefficient in air-sea interactions. *Dynamics Atmos. Oceans* **11**:19–38

Grigoriu M. (1993) On the spectral representation method in simulation. *Prob. Eng. Mech.* **8**:75–90

Højstrup J., Larsen S. E. and Madsen P. H. (1990) Power spectra of horizontal wind components in the neutral atmospheric boundary layer. *in* N. O. Jensen, L. Kristensen and S. E. Larsen (eds), Ninth Symposium on Turbulence and Diffusion, American Meteorological Society, 305–308 pp

Hunt J. C. R. and Carruthers D. J. (1990) Rapid distortion theory and the 'problems' of turbulence. *J. Fluid Mech.* **212**:497–532

Kaimal J. C. and Finnigan J. J. (1994) Atmospheric Boundary Layer Flows, Their Structure and Measurement, Oxford University Press, New York

Kaimal J. C., Wyngaard J. C., Izumi Y. and Coté O. R. (1972) Spectral charcteristics of surface-layer turbulence, *Q. J. R. Meteorol. Soc.* **98**:563–589

Koopmans L. H. (1974) The Spectral Analysis of Time Series, Academic Press

Kristensen L. and Kirkegaard P. (1987) Puff kinematics, Technical Report R–548, Risø National Laboratory

Landau L. D. and Lifshitz E. M. (1987) Fluid Mechanics, Pergamon Press

Larose G. L. and Mann J. (1998) Gust loading on streamlined bridge decks, *J. Fluids Structures* **12**(5):511–536

Lesieur M. (1987) Turbulence in fluids, Martinus Nijhoff Publishers

Mann J. (1992) Investigation of atmospheric low-frequency turbulence over the ocean, Technical Report I–634(EN), Risø National Laboratoty, Roskilde

Mann J. (1994) The spatial structure of neutral atmospheric surface-layer turbulence. *J. Fluid Mech.* **273**:141–168

Mann J. (1998) Wind field simulation, *Prob. Engng. Mech.* **13**(4):269–282

Mann J., Cariou J.-P., Courtney M. S., Parmentier R., Mikkelsen T., Wagner R., Lindelöw P., Sjöholm M. and Enevoldsen K. (2009) Comparison of 3D turbulence measurements using three staring wind lidars and a sonic anemometer. *Meteorol. Z.* **18**(2):135–140

Mann J., Kristensen L. and Courtney M. S. (1991) The great belt coherence experiment – a study of atmospheric turbulence over water, Technical Report R–596, Risø National Laboratory, Roskilde

Maxey M. R. (1982) Distortion of turbulence in flows with parallel streamlines. *J. Fluid Mech.* **124**:261–282

NDP (1998) Acts, regulations and provisions for the petroleum activities, Vol. 2,, Norwegian Petroleum Directorate

Panofsky H. A. and Dutton J. A. (1984) Atmospheric Turbulence, John Wiley & Sons, New York

Panofsky H. A., Larko D., Lipschutz R., Stone G., Bradley E. F., Bowen A. J. and Højstrup J. (1982) Spectra of velocity components over complex terrain. *Q. J. R. Meteorol. Soc.* **108**:215–230

Peña A., Gryning S.-E., Mann J. and Hasager C. B. (2010) Length scales of the netural wind profile over homogeneous terrain *J. Appl. Meteor. Climat.* **49**:792–806

Press W. H., Flannery B. P., Teukolsky S. A. and Vetterling W. T. (1992) Numerical Recipes, 2nd edn, Cambridge University Press

Shinozuka M. and Deodatis G. (1991) Simulation of stochastic processes by spectral representation, *Appl. Mech. Rev.* **44**(4):191–203

Shinozuka M. and Deodatis G. (1996) Simulation of multi-dimensional gaussian stochastic fields by spectral representation. *Appl. Mech. Rev.* **49**(1):29–53

Shinozuka M. and Jan C.-M. (1972) Digital simulation of random processes and its applications. *J. Sound Vibration* **25**(1):111–128

Simiu E. and Scanlan R. H. (1996) Wind Effects on Structures, 3. ed., John Wiley & Sons

Sjöholm M., Mikkelsen T., Mann J., Enevoldsen K. and Courtney M. (2009) Time series analysis of continuous-wave coherent Doppler lidar wind measurements. *Meteorol. Z* **18**(3):281–287

Townsend A. A. (1976) The Structure of Turbulent Shear Flow, 2nd edn, Cambridge University Press

Townsend, A. A. (1980) The response of sheared turbulence to additional distortion. *J. Fluid Mech.* **98**:171–191

4 Introduction to continuous-wave Doppler lidar

Michael Harris
Natural Power, The Old Barns, Fairoaks Farm,
Hollybush, Nr. Ledbury HR8 1EU, U.K.

4.1 Introduction

Remote sensing offers the wind industry an attractive alternative or complement to the traditional methods for obtaining accurate wind measurements that involve the siting of tall masts. Laser anemometry (lidar) is now demonstrating its potential for resource assessment, power curve measurement, and turbine mounted deployment for advance wind speed detection. Widespread acceptance of lidar by the industry requires that this technique be extensively validated, aiming towards a certifiable and traceable measurement standard and formal accreditation of lidar methods for different applications in a range of terrain types. This chapter outlines the lidar measurement process and capabilities specifically for the case of continuous wave (CW) systems.

Wind lidar systems were first demonstrated in the 1970's (Jelalian, 1992) and have since been applied to a wide variety of applications including aviation and meteorology. Although applications to wind energy were explored in the 1980's (Hardesty and Weber, 1987; Vaughan and Forrester, 1989), the lidar systems that existed at that time were too large and expensive to achieve serious acceptance in the industry. The situation has now changed dramatically, with rapid growth of the wind industry coinciding with development of a new generation of lidars based on optical fibre and other components that emerged from the telecommunications boom of the 1990's. The first all-fibre lidars were demonstrated in the late 1990's, and a commercial prototype unit (ZephIR) was mounted on a turbine to demonstrate wind speed detection in front of the rotor plane in early 2003. A demonstration of ground-based wind profiling followed shortly afterwards. ZephIR is a CW coherent lidar system, and this approach was selected as a means to combine simplicity with high sensitivity at ranges relevant to wind energy, and hence achieve a robust, reliable system at relatively low cost. Following this pioneering work the pace of development has accelerated, with lidar increasingly becoming an established tool in the wind industry.

Section 4.2 provides an overview of lidar techniques and technology. Different types of lidar system are surveyed, and the generic physical principles underlying their operation are reviewed. The specific case examined in detail here is that of wind profiling by a ground-based conically-scanned continuous-wave (CW) lidar, rapidly becoming established as a powerful tool in the wind energy industry, and exemplified by the ZephIR lidar, developed by QinetiQ and Natural Power. A number of assumptions must be made in order to extract values of wind speed from raw lidar data; these are reviewed in section 4.3. The different steps that are required during the end-to-end measurement process in order to arrive at a value of wind speed are detailed in section 4.4. It is important to understand the potential sources of error and uncertainty, and these are reviewed and analysed in section 4.5. Section 4.6 examines the important requirement for lidar calibration and traceability. Finally, section 4.7 draws together some conclusions and a summary of the future outlook for lidar in wind energy.

4.2 Basic principles of lidar operation and system description

Brief survey of lidar types

There are many different types of lidar (Jelalian, 1992) and these are capable of performing a diverse range of tasks (e.g. 3D imaging and range finding, gas species detection, remote measurement of vibrations). We concern ourselves here specifically with systems for the measurement of wind speed in the atmosphere (Zak, 2003). Such systems fall into two broad categories: coherent lidar and direct detection lidar. Coherent lidar measures Doppler shifts by comparing the frequency of backscattered radiation to that of a reference beam via a light beating process, whereas direct detection lidar (Chanin et al., 1989) performs its frequency-shift measurements by passing the light through an optical filter, such as a Fabry-Perot etalon. By operating in the ultra-violet, direct detection lidars can exploit molecular scattering processes, guaranteeing signal returns even in very clean air where there is an absence of scattering particles.

Coherent wind lidar systems can be categorised according to their emission waveform (pulsed or continuous), waveband (visible, near-IR, far-IR), and their transmit/receive geometry (monostatic or bistatic). These notes concentrate specifically on CW coherent monostatic lidar systems that operate in the telecommunications near-IR band around 1.55 μm (Karlsson et al., 2000); at this wavelength reliable components including optical fibre are readily available. Such systems can route the light within the lidar via fibre cables (creating an "all-fibre lidar"), rather than use mirrors to direct the beams in free space. This confers an enormous design advantage, simplifying alignment and improving robustness. Pulsed all-fibre lidar has also been developed as reported in Pearson et al. (2002).

Principles underlying anemometry by coherent laser radar (CLR)

The principle by which coherent lidar measures the velocity of a target is simple: a beam of coherent radiation illuminates the target, and a small fraction of the light is backscattered into a receiver. Motion of the target along the beam direction leads to a change in the light's frequency via the Doppler shift: motion towards the lidar brings about a compression of the wave and an increase in its frequency (a "blue shift"), while movement away stretches the wave reducing its frequency (a red shift). This frequency shift is accurately measured by mixing the return signal with a portion of the original beam, and sensing the resulting beats at the difference frequency on a photodetector. Like the Doppler effect, the beat phenomenon is perhaps most familiar in the context of acoustics as, for example, when two closely (but not identically) tuned guitar strings are simultaneously plucked.

The essential features are readily seen in the simplified generic CLR depicted in Figure 31. In order to illustrate the concept this is drawn as a bistatic system, in which the transmit and receive optics are separate and distinct. In practice a monostatic geometry is more usual, in which the transmit and receive paths share common optics.

Role of local oscillator and range selection by focus

The reference beam, or local oscillator (LO) plays a crucial role in the operation of a CLR (Sonnenschein and Horrigan, 1971). Firstly, it defines the region of space from which light must be scattered for detection of the beat signal; radiation from other sources (e.g. sunlight) is rejected both spatially and spectrally, so that CLR systems are usually completely immune to the effect of background light. The LO also provides a stable reference frequency to allow very precise velocity determination; as a consequence the Doppler shift measurement by a CLR system is inherently calibrated. Finally, the LO amplifies
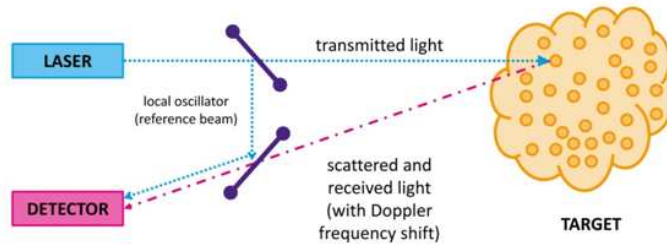
Figure 31. Generic bistatic lidar system. A small fraction of the transmitted light is tapped off by a beamsplitter to form a reference beam. This is superimposed at a second beamsplitter with the weak return scattered from moving particles. The detector picks up the resulting beat signal; this undergoes spectral analysis to determine particle velocity.

the signal via the beating process to allow operation at a sensitivity that approaches the shot-noise (or quantum) limit. This very high sensitivity permits the operation of CLR systems in an unseeded atmosphere, relying only on detection of weak backscattering from natural aerosols.

CW systems are the simplest form of lidar possessing the advantage of reduced complexity, and their performance can be tailored closely to the wind industry's requirements. However, the overall trade-off between the pulsed and CW options for each specific application must take into account a number of factors including sensitivity, cost, velocity resolution, and maximum and minimum ranges. Unlike pulsed lidar systems, which use time of flight to discriminate between returns from different ranges, a CW lidar achieves operation at a given range by beam focusing. Wind profiling is achieved by focusing at a number of chosen ranges in turn; the rapid data rate permits 1 s "snapshots" of the flow across the scan disk at each measurement height. Focusing of the lidar beam brings about a Lorentzian spatial weighting function along the beam axis, with its peak located at the beam waist (Sonnenschein and Horrigan, 1971; Karlsson et al., 2000). This function has a half-width given by the Rayleigh range (the distance from the waist at which the beam area has doubled).

The beam diameter at the waist increases linearly with range while the Rayleigh range increases roughly as the square. Hence the effective probe volume varies as the 4th power of the focus range, and this strong dependence has some implications for the signal statistics at shorter ranges (Harris et al., 2001b). The minimum range for a CW lidar is very short with detection possible in principle at zero range, whereas a pulsed system is blinded while the pulse is leaving the transmitter leading to a minimum range of 10's of metres, typically around 40–50 m.

Doppler frequency analysis and signal processing

The stages of signal processing required for CLR wind signals are discussed in section 4.4. The detector output, containing the beat signal information embedded in broadband noise, is typically digitised by an analogue-to-digital converter (ADC). Spectral analysis (e.g. by fast Fourier transform methods) leads to the generation of Doppler spectra. It is usually necessary to average a number of these spectra in order to improve the signal-to-noise ratio (SNR), after which the Doppler peak stands clearly above a flat shot-noise floor. A value for the line-of-sight wind speed can then be computed via a velocity estimation algorithm. This might calculate, for example, the peak or centroid value of the Doppler signal.

Wind profiling in conical scan mode

Since a single lidar measurement only provides the component of wind speed along the beam direction, it is necessary to scan the direction of the beam in order to generate a measurement of the wind speed vector. A conical or VAD (velocity-azimuth-display) scan pattern has been widely used (Banakh et al, 1993), see Figure 32; as the beam moves, it intercepts the wind at different angles, thereby building up a series of measurements around a disk of air from which the wind speed vector can be derived. In uniform flow, a plot of the measured line-of-sight wind speed (V_{LOS}) versus scan azimuth angle (ϕ) takes the form of a cosine wave (rectified for a lidar system that cannot distinguish the sign of the Doppler shift). The peak Doppler shifts correspond to measurements when the azimuth scan angle aligns with the upwind and downwind directions. Doppler shifts close to zero are obtained when the azimuth angle is perpendicular to the flow.
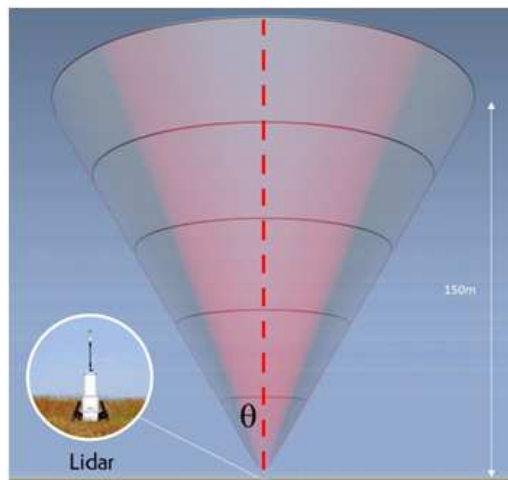

Figure 32. Conical scan pattern as used for lidar wind profiling. The cone half-angle (θ) is typically of order 30°. The lidar can operate successfully even when part of its scan is obscured, e.g. by an adjacent met mast. In order to build up a wind profile, the lidar operates in a repeating sequence during which all the heights are interrogated in series

Pioneering a revolution: QinetiQ/Natural Power ZephIR lidar

Many different research groups have built and successfully deployed wind lidars over the past 30 years. However, commercial lidar products have until very recently been available from only a few companies. In 2003 the UK company QinetiQ (formerly the government-funded establishment RSRE, later DRA then DERA), launched the first commercial all-fibre lidar ("ZephIR^{TM}") which exploits decades of research in the coherent lidar area. QinetiQ began a programme to develop a commercial fibre-based lidar in 2001; its ZephIR product is now an established tool for wind profiling in the wind energy industry. Systems have been deployed successfully around the world in several demanding applications that illustrate the flexibility and robustness of the solution. Initial deployment of the ZephIR lidar (March 2003) was on the nacelle of a large (2.3 MW) wind turbine (Figure 33-left frame), remotely measuring for the first time the wind speed up to 200 m in front of the blades (Harris et al., 2006, 2007). The lidar consisted of a 19" rack unit containing laser source, detector and signal processing computer, situated in the base of the tower, connected via over 100 m of electrical and optical fibre cable to the transceiver head mounted on the top of the nacelle. The lidar system was installed and was fully operational after just a few hours, thus allowing a demonstration of advance warning of oncoming gusts and providing valuable experience in practical deployment issues.

Figure 33. Stages of evolution of the ZephIR lidar. The left-hand picture shows the lidar head mounted on the nacelle of a Nordex N-90 wind turbine (March 2003). The central picture shows prototype ground-based wind profiler at Risø wind energy test site, Høvsøre, Denmark. The right-hand picture shows a ZephIR production model deployed in the field

The system returned to QinetiQ Malvern having achieved several weeks of successful operation. It was then converted into a ground-based scanning unit for wind profiling (Figure 33-middle frame). The system was first trialled in December 2003, and soon after was used in numerous campaigns in the UK, Europe, and other parts of the world. Notably the system is still operational 7 years later! The experience gained through these trials has built confidence in the robustness and reliability of the core ZephIR design. In late 2004, work started on a production instrument (Figure 33-right frame), designed to perform autonomous wind profiling measurements at heights up to 200m (Smith et al., 2006), primarily for site surveys at proposed wind farm sites. Over eighty of these systems (February 2010) have performed more than 200 deployments in 25 countries in a wide variety of locations, including offshore. ZephIR is now marketed and developed for the wind industry by Natural Power, and its basic specifications are available via the web: http://www.naturalpower.com/zephir-laser-anemometer

4.3 Lidar measurement process: Assumptions

The following sections discuss generic CW lidar considerations (most of which apply equally to pulsed systems). Where appropriate, application to the ZephIR lidar is used to provide an illustrative example.

Behaviour of scattering particles

The lidar signals from which wind speeds are derived originate via backscattering of the beam by particles in the atmosphere. The constitution of these particles is generally unknown, but they are normally assumed to consist of dust, organic matter (e.g. pollen), soot, or water droplets. Knowledge of the particles' make-up is not a requirement for lidar wind speed measurement. The particles must provide sufficient signal for Doppler analysis and their motion must faithfully follow that of the wind flow. This latter assumption is very good, since viscous forces are dominant for such small particles. Larger particles for which this does not apply will rapidly fall to ground. Raindrops or snowflakes provide a strong contribution to the lidar signal. Their downward motion can lead to an error in the vertical component of wind speed (a parameter usually of lesser interest; such data can be easily identified and filtered), but the important horizontal component will be correct.

A further excellent assumption is that the return signal is dominated by light generated by single-scattering events. While it is possible for light to suffer multiple scattering in dense fog, it is assumed that any effect on the Doppler spectrum is negligible.

Uniformity of flow and backscatter

A least-squares fitting to the azimuthal variation of line-of-sight wind speed allows the derivation of wind parameters from conical scan data. These parameters pertain to a significant volume of atmosphere – the signal originates from a disk whose diameter commonly exceeds 100 m, and whose depth along the beam direction can be over 10 m. Except in situations of strong shear, turbulence or highly complex terrain the wind speed is reasonably uniform throughout this sampled volume, and the best fit wind parameters are used to indicate the average values over the volume. In fact, ZephIR data itself can provide a straightforward check on wind field uniformity since conical scanning provides measurements at many different azimuth angles; where the assumptions have broken down, measurements with less certainty can be flagged.

The contribution to the lidar signal from different regions of the lidar probe volume is weighted by the value of the atmospheric backscatter coefficient $\beta(\pi)$ at each point. The value of $\beta(\pi)$ is typically constant to $\sim 10\%$ throughout the probe volume (Banakh et al., 1993) except in conditions that lead to stable mist layers, or when the lidar beam intersects a low cloud base.

Beam positional accuracy

Lidar scan angle and focus calibration are performed in the laboratory, and these must be correctly maintained throughout a period of deployment in the field. Obviously errors in the focus setting would result in wind speed measurement at the wrong height. Careful design eliminates the risk of uncertainty in the beam focus: thermal expansion, which could change the length of the transceiver telescope, can be compensated and the position of the focus mechanism can be automatically checked to provide information on any malfunction.

The lidar must be correctly set up, with the vertical and azimuthal orientation adjusted appropriately during installation. External to the lidar, it has been established that small-scale refractive-index atmospheric fluctuations will have negligible effect on the propagation of the lidar beam (Clifford and Wandzura, 1981; Lading et al., 1984).

Optical and electrical interference sources

The lidar identifies the presence of a wind signal when the power density in the Doppler spectrum exceeds a threshold level. In the absence of any significant source of spurious signal, the only mechanism that can lead to such detection events is the backscatter of Doppler-shifted light into the lidar receiver. Optical interference is highly unlikely – even when the lidar points directly at the sun the spectral power density is insufficient to cause a problem, and interaction between two lidars placed side-by-side can be neglected including the possibility of interference from the beam emitted by an adjacent lidar. Careful screening eliminates the risk of spurious spectral features caused by electrical interference for any normal deployment.

Time-of-flight considerations

The round-trip time for light interrogating the atmosphere at a height of 100 m is less than 1 μs. On this timescale the ZephIR scanner moves the focused beam a distance of only 300 μm, and the laser phase drifts by an insignificant amount. The polarisation state of the lidar output is similarly frozen on this timescale.

4.4 End-to-end measurement process for CW Doppler lidar

Introduction

The measurement process can be split into a number of steps. This section describes these steps in turn, arriving at an overall end-to-end description of the wind speed measurement process for a CW coherent Doppler lidar wind profiler. Again, where appropriate, the ZephIR lidar is used as an example.

Transmitter optics

The role of the transmitter is to provide a focused beam at a desired location. This location can be moved around in space with a combination of (i) changing the focus range and (ii) passing the beam through a scanning element such as a rotating prism (wedge). Wind profiling lidars conveniently employ a conical scan with its axis aligned vertically; the cone half-angle is commonly of order $30°$ (i.e. the beam elevation angle is $\sim 60°$).

In a monostatic CW system, a Doppler-shifted contribution to the signal is generated via light scattering from any moving part of the atmosphere that the beam illuminates. The contribution from any point is weighted by the square of the beam's intensity at that point (Harris et al., 2001a). Hence it can be shown that focusing of an ideal Gaussian beam (Siegman, 1986) gives rise to a spatial sensitivity along the beam direction that depends on the inverse of beam area; it follows that the sensitivity rises to a peak at the beam waist, and falls symmetrically on either side. There is also a spatial dependence of sensitivity transverse to the beam, but because the beam is very narrow this is of little interest and can be ignored. To a good approximation the axial weighting function for a CW monostatic coherent lidar is given by a Lorentzian function (Sonnenschein and Horrigan, 1971; Karlsson et al., 2000):

$$F = \frac{\Gamma/\pi}{\Delta^2 + \Gamma^2}, \tag{89}$$

where Δ is the distance from the focus position along the beam direction, and Γ is the half-width of the weighting function to the -3 dB point, i.e. 50% of peak sensitivity. Note that F has been normalised such that its integral from $-\infty$ to ∞ gives unity. To another good approximation, Γ is given by:

$$\Gamma = \frac{\lambda R^2}{\pi A^2}, \tag{90}$$

where λ is the laser wavelength, here assumed to be the telecommunications wavelength $\lambda \sim 1.55 \times 10^{-6}$ m, R is the distance of the beam focus from the lidar output lens, and A is the beam radius at the output lens. The beam intensity profile is assumed to be an axially-symmetric 2D Gaussian; A is calculated for the point at which the intensity has dropped to $1/e^2$ of its value at the beam centre. For example, if A takes the value 20 mm then, at a focus range R of 100 m, Γ has a value of ~ 11 m, or a probe length (to -3 dB points) of ~ 22 m. For $A = 28$ mm, Γ drops by a factor of ~ 2 to give $\Gamma \sim 5.5$ m. At a range R of 50 m, the width drops by a factor 4 ($\Gamma = 2.7$ m for $A = 20$ mm).

Figure 34 shows the behaviour of the theoretical sensitivity curves for the two example cases ($A = 20$ mm, 28 mm) at several focus heights above ground level. In addition the theoretical curve corresponding to one of the calibration ranges has been plotted, with experimental calibration data for comparison. Section 4.6 contains more detail of the calibration processes. The minimum range is determined by the focusing capability of the transceiver optics, and for ZephIR it takes the value 10 m.
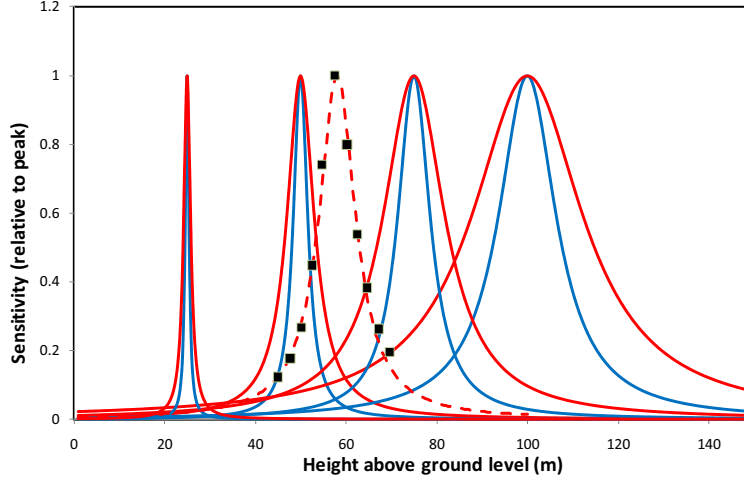
Figure 34. Theoretical lidar sensitivity curves at focus heights 25, 50, 75 and 100 m for the two cases listed above with $A = 20$ mm and 28 mm, corresponding to respectively the original (red curve) and current (blue curve) ZephIR design. The peak is normalised to unity in each case; the absolute peak value decreases as the inverse of height squared, so that the area under each curve (representing the overall sensitivity) is always the same. This illustrates a useful feature of focused CW coherent lidar that in uniform scattering, the signal-to-noise ratio is independent of focus height. Data obtained in calibration measurements (black squares) at a calibration range $R = 68$ m are in close agreement with the corresponding theoretical values (dashed curve) at the equivalent height 58 m ($=68$ m$\times \cos 30°$)

Light scattering by aerosols

Coherent lidar measures the Doppler shift resulting from the component of target velocity along the beam (or line-of-sight) direction. Motion of the target transverse to the beam direction produces no net Doppler shift. Hence, for a lidar at (0,0,0) measuring at a specific location (x, y, z) where wind components are (u, v, w), the lidar will detect a line-of-sight velocity given by the dot product of the wind vector (u, v, w) and the unit vector along the beam direction:

$$V_{\text{LOS}} = \left| (\mathbf{u} + \mathbf{v} + \mathbf{w}) \cdot \left(\frac{\mathbf{x} + \mathbf{y} + \mathbf{z}}{\sqrt{x^2 + y^2 + z^2}} \right) \right|, \tag{91}$$

where the modulus applies to systems that cannot distinguish the sign of the Doppler shift.

In the backscattering geometry considered here, the scattered light experiences a Doppler shift in frequency given by:

$$\delta\nu = \frac{2V_{\text{LOS}}\nu}{c} = \frac{2V_{\text{LOS}}}{\lambda}, \tag{92}$$

where c is the speed of light (2.998×10^8 m s^{-1}) and ν is the laser frequency.

Since the signal originates from a finite probe length, the overall return exhibits a spectrum of frequencies. This results from the contributions from different velocities (with strengths determined by the weighting function, Eq. 89) over all the space occupied by the lidar beam. Note that in the absence of additional information it is not possible to identify from what range each component of the spectrum has originated. Section 4.5 will outline how information from additional focus heights is used to identify and reject spectral components originating from strongly-scattering objects (e.g. clouds) situated well outside the probe length.

For a CW coherent system, the time-averaged optical signal power P_s backscattered

by the aerosols into the receiver is given to a good approximation by:

$$P_s = \pi P_T \beta(\pi) \lambda, \tag{93}$$

where P_T is the transmitted laser power. It is notable that Eq. (93) contains no dependence on either the focus range or the system aperture size. With a value of 10^{-8} (m srad)$^{-1}$ for $\beta(\pi)$ in clear boundary-layer air, a transmitted power $P_T \sim 1$ W and $\lambda \sim 1.5$ μm, the received power P_s derived from Eq. (93) is only of order 5×10^{-14} W emphasising the need for high sensitivity.

Receiver optics

In a monostatic system, the backscattered light returns through the transmission optics (the word transceiver is commonly used to denote this dual role). Any motion of the beam due to scanning over the timescale for the radiation to travel to the aerosols and back will result in misalignment of the receiver, but this is insignificant for the range of parameters considered here.

After entering the transceiver, optical means are used to isolate the return light, and this is passed to the next stages of the detection process.

Light beating

In coherent laser radar, the incoming Doppler-shifted radiation is optically mixed with a reference LO beam. The mixing of two waves in this manner leads to the well-known "beat" phenomenon in which the resulting amplitude oscillates at the difference frequency. In lidar, the process conveniently "downmixes" the optical frequency of the Doppler shifted return at $\sim 2 \times 10^{14}$ Hz to a more manageable signal in the MHz range. The efficiency of the beating process is optimised when the signal and LO beams overlap perfectly in space (i.e. they occupy identical spatial "modes"). This condition is ensured when both beams propagate in the same single-mode optical fibre, assuming that they share the same polarisation state.

It is instructive to consider a simple classical description of the light beating process. Superposition of a LO field $E_{\mathrm{LO}} \cos(\omega_{\mathrm{LO}} t)$ and a stable signal field $E_{\mathrm{s}} \cos(\omega_{\mathrm{s}} t)$ results in a fluctuating detector output:

$$i(t) \propto \left(E_{\mathrm{LO}} \cos(\omega_{\mathrm{LO}} t) + E_{\mathrm{s}} \cos(\omega_{\mathrm{s}} t) \right)^2. \tag{94}$$

This is conveniently separated into a "constant" term and a cross term oscillating at the difference frequency:

$$i(t) \propto \left(E_{\mathrm{LO}}^2 + E_{\mathrm{s}}^2 \right) + 2 E_{\mathrm{LO}} E_{\mathrm{s}} \cos |\omega_{\mathrm{s}} - \omega_{\mathrm{LO}}| \, t. \tag{95}$$

Since the optical power of the local oscillator beam typically exceeds that of the signal beam by many orders of magnitude, the first term is given by E_{LO}^2 to a very good approximation, quantum fluctuations on which give rise to the shot noise floor of the instrument (section 4.6). For a system for which there is no frequency shift between the LO and transmitted beams, the measured Doppler shift is given simply by:

$$\delta\nu = 2\pi \, |\omega_{\mathrm{s}} - \omega_{\mathrm{LO}}| \tag{96}$$

from which the value of V_{LOS} is derived via Eq. (92). In practice a signal field originating from atmospheric scattering exhibits fluctuations in both its amplitude and phase (or frequency). The coherent detection process ensures that these properties are reproduced in the detector output so that, in the limit of high SNR, its spectral analysis gives a correct representation of the scattered light's spectrum (Harris et al., 1994).

The coherent detection process described above is also commonly referred to as homodyne or heterodyne detection. A rigorous quantum-mechanical theoretical treatment of the detection process is given in Loudon (2000). Note that although the detection process is described as coherent, the backscattered radiation itself is incoherent in nature,

meaning that its phase is uncorrelated with that of either the transmitted beam or the local oscillator. The phase and intensity are typically subject to random fluctuations on a timescale that is related to the inverse of the signal bandwidth (see section 4.7).

Photodetection

The beat signal is detected by directing the optically-mixed beam onto a photodetector which measures fluctuations in the light's intensity. In the telecommunications wavelength band around 1.55 μm, reliable photodiodes are readily available that are well suited to this purpose. The photodiode converts the incident photons into photoelectrons, which generate a measurable current (or voltage) that is normally passed through further stages of amplification before digitisation. There are generally four contributions to the output of the photodetector module:

- Dark noise – this is the intrinsic wideband noise floor generated by the detector and amplifier combination in the absence of any incident light.

- Photon shot noise (Bleaney and Bleaney, 1976) (sometimes called quantum noise) – the random generation of photoelectrons by the incident LO beam leads to a wideband, spectrally flat (white) Gaussian noise source. The shot noise power spectral density increases in proportion to the optical power of the LO beam.

- Laser relative intensity noise (RIN) – intensity fluctuations that are in excess of shot noise, caused for example by relaxation oscillation (Siegman, 1986) of the laser output. For a RIN-dominated noise floor, the power spectral density increases as the square of LO power. Such oscillation is typically at relatively low frequency, peaking below 1 MHz, and hence only affects the sensitivity of the lidar at low line-of-sight wind speeds around 1 m s^{-1}. In some systems it is possible to cancel the RIN by use of a dual-channel balanced detector.

- Beat term resulting from the wind signal – this is the contribution that contains the information on Doppler shifts from which the wind speed is derived. Its power spectral density increases in proportion both to the LO power and the signal power.

The requirements for the detector are high quantum efficiency, sufficient bandwidth to cope with the maximum Doppler frequencies of interest, and for the shot noise contribution to significantly exceed that of dark noise. This latter requirement depends on a combination of the detector's intrinsic noise floor and the optical saturation threshold.

Fourier analysis and lidar sensitivity

In order to extract the Doppler frequency information, it is necessary to perform a spectral analysis of the detector output. This is conveniently done digitally; an example of a typical signal processing procedure is described below and illustrated in Figure 35. An ADC with a sampling rate of 100 MHz permits spectral analysis up to a maximum frequency of 50 MHz, corresponding to a wind speed V_{LOS} of $\sim$ 38.8 m s^{-1} (Eq. (93), with $\lambda = 1.55$ μm). A hardware low-pass filter with a cut-off frequency of 50 MHz, inserted between the detector and ADC, eliminates aliasing problems. Spectra are calculated by digital Fourier transform (DFT) methods; a 512 point DFT gives rise to 256 points in the output spectrum with a bin width of $\sim$ 200 kHz, corresponding to a line-of-sight velocity range of $\sim$ 0.15 m s^{-1}. Each DFT represents $\sim$ 5 μs of data; successive DFTs are then calculated, and the resulting "voltage" spectra are squared in order to generate a power spectrum. These power spectra are then averaged to find a mean spectrum for the averaging period. The random fluctuation in the shot noise floor of the spectrum reduces as the square root of the number of averages: the sensitivity increases by this same factor. For 4000 averages, the measurement time amounts to $\sim$ 20 ms (or a data rate of $\sim$ 50 Hz). This requires

that the processing is capable of 100% duty cycle, which is achieved in ZephIR with a fast Fourier transform (FFT) block within a field-programmable gate array (FPGA). It has been shown that a standard fast PC with no additional duties to perform can achieve a similar performance. It is possible to accommodate reasonable variations in any of the above parameters (sample rate, DFT size, number of averages) and maintain the 100% duty cycle.
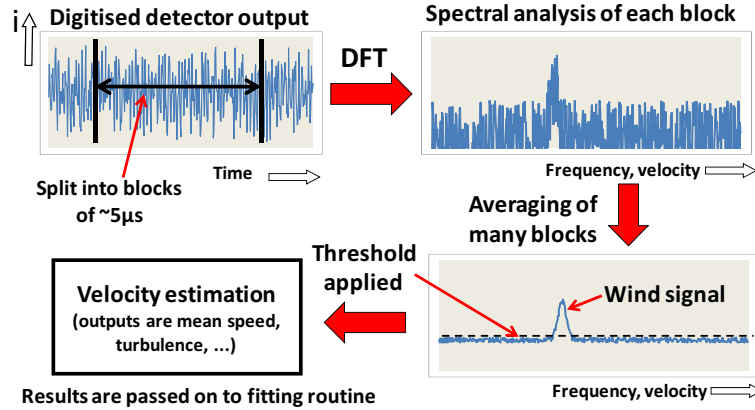

Figure 35. Stages in typical lidar signal processing: DFT analysis is carried out by a computer integrated into the lidar system. As an example, 4000 individual spectra might be averaged to achieve high sensitivity and measurable returns even in very clear air. This entire process takes only 20 ms, giving ∼ 50 measurements per second of line-of-sight wind velocity

The width of the Doppler spectrum is determined by three elements:

- Instrumental width: this corresponds closely to the ∼ 200 kHz bin width mentioned above.

- Transit-time broadening: during the conical scan, the beam passes through the aerosol particles in a timescale of ∼ 10 − 15 μs, independent of the lidar focus setting. The corresponding broadening is again of order 200 kHz.

- Turbulence broadening: the probing of a significant volume results in a range of Doppler shifts from parts of the atmosphere that are moving at different speeds (see section 4.3). In general, this contribution increases with turbulence and shear, and occasionally there is more than one peak in the spectrum as a result.

The last of these usually dominates except under conditions of very uniform airflow. High system sensitivity is of crucial importance for a wind lidar reliant on weak backscatter from the atmosphere. The SNR[4] for a wind speed measurement by a CW CLR is given by:

$$\text{SNR} = \frac{\eta P_s}{(hc/\lambda) \, \Delta\nu \, [1 + D(\nu) + R(\nu)]}. \tag{97}$$

Here η is an efficiency term incorporating optical losses and photodetector sensitivity (typically $\eta \sim 0.5$, approaching the value 1.0 only for a "perfect" system), P_s is the input signal power, as defined in Eq. (93) and hc/λ is the light quantum energy, of order 1.3×10^{-19} J. The signal bandwidth $\Delta\nu$ is determined by the three contributions listed above, and the term inside the square brackets denotes the various noise sources listed in section 4.6. $D(\nu)$ and $R(\nu)$ represent the power spectral density (at frequency ν) from dark noise and RIN respectively in units of the power spectral density of the

---

[4]In the lidar community, this is commonly, and more properly, referred to as the carrier-to-noise ratio (CNR)

local oscillator shot noise. Ideally $D(\nu)$ and $R(\nu)$ should both be $\ll 1$ over the range of Doppler frequencies of principal interest, so that the shot noise is the dominant noise source.

The SNR as defined here is the power spectral density at the Doppler peak divided by that in the surrounding noise floor. The averaging of many spectra (described in the following sections) ensures that good performance can be obtained even when the SNR is well below unity. For example, an SNR of 0.1 will easily exceed a 5σ threshold level (see next section) for an average of 4000 spectra. From the above it is possible to derive an approximate value of $\beta(\pi)_{\text{min}} \sim 10^{-9}$ (m srad)$^{-1}$ for the minimum detectable backscatter, assuming a transmitted intensity 1 W and a 20 ms measurement time.

Velocity estimation

From the preceding sections it is apparent that each measurement of line-of-sight wind speed, obtained over a timescale of ~ 20 ms, generates a Doppler spectrum consisting of one or more peaks of variable width, superimposed on a noise floor that is predominantly white, but which may have spectral features originating from RIN and dark noise sources. This section outlines steps that can be followed to derive an appropriate estimate of the wind speed.

First, the noise floor is "whitened" so that each spectral bin contains the same mean noise level, achieved by dividing the power value in each bin of the spectrum by a previously-measured value for the same bin obtained with the shutter closed. A flat threshold is then applied at a pre-determined level above the mean noise; see Figure 35. A suitable and conservative choice for the threshold is 5 standard deviations (5σ) above the mean noise level. In the absence of any wind signal (e.g. with the output of the lidar blocked) such a setting will give rise to negligible occurrences in which the noise alone exceeds threshold. It follows that any bin whose level exceeds the threshold is deemed to contain a valid contribution to the wind signal. For each 20 ms measurement, the wind spectrum is reconstructed by subtracting the mean noise contribution from the contents of each bin that exceeds threshold, and applying a small re-correction for any distortion resulting from the noise whitening. In order to proceed to the next stage, a single velocity value is derived from the resulting spectrum. A number of options are available, including peak and median values; a common solution is to calculate the mean (or centroid) value $\langle V_{\text{LOS}} \rangle$.

A series of these values of mean line-of-sight wind speed is generated as the ZephIR lidar performs a conical scan. Wind parameters are usually calculated from data obtained from three revolutions of the scanner. With a rotation time of ~ 1 s, up to 150 line-of-sight values are available for the next stage, in which a least-squares fitting algorithm is applied. Data can also be generated for a 1 s, single scan rotation (based on a 50-point fit), as required by the user.

Least-squares fitting routine

The data that are fed to the fitting routine consist of up to 150 pairs of values of $\langle V_{\text{LOS}} \rangle$ and azimuth angle ϕ. In conditions of uniform wind flow, this gives rise to a rectified cosine wave of the form:

$$\langle V_{\text{LOS}} \rangle = |a\cos(\phi - b) + c|. \tag{98}$$

The derivation of this function is straightforward and can be found in a number of publications, e.g. Banakh et al. (1993). The peaks of the function correspond to the azimuth angle aligned parallel or anti-parallel to the wind direction. The function passes through zero when the azimuth angle is perpendicular to wind bearing since there is no component of velocity along the line of sight. The data are also conveniently displayed on a polar plot (Figure 36), which provides information at a glance on the speed, direction

and vertical wind component. A standard least-squares fitting routine provides the best estimates of the values of the three floating parameters (a, b and c).
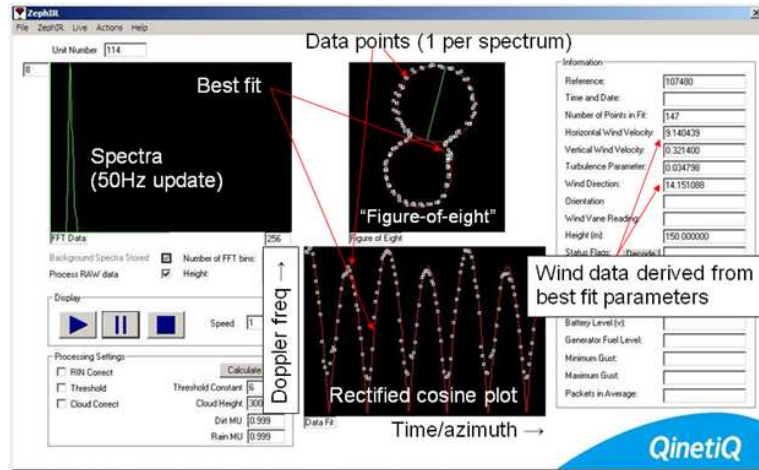

Figure 36. Wind lidar output screen, illustrating many of the features of a wind profile measurement. This example has been obtained at a height 150 m above ground level, one of several heights being probed in sequence. The lower trace shows 147 individual line-of-sight wind speed values, obtained over a total period of 3 s, plotted as white squares against azimuth scan angle. The same data, along with the least-squares fit in red, are displayed above this in polar coordinates on the figure-of-eight plot showing the wind bearing to lie slightly to the East of North. The wind parameters, derived from the fit, appear in the table on the right; the horizontal wind speed at this height is determined to be 9.1 m s^{-1}. The plot on the left shows just one of the spectra from which each point on the other 2 graphs is derived

The high level of redundancy in the fitting process is advantageous and can be used to identify non-uniform flow. The root mean square deviation of the points from the optimum solution gives an indication of the quality of fit, and this can be related to the value of turbulent kinetic energy (TKE; see Wagner et al. (2009)). More work is needed to establish a full understanding of the turbulence information available from lidar signals (Banakh et al., 1999). Note that information on turbulence is also available from the spectral widths of the individual line-of-sight wind speed measurements, but this is not currently used to evaluate turbulence parameters. Owing to data storage constraints, spectral information is commonly discarded after the velocity estimation process.

Parameter extraction

The wind parameters for each 3 s measurement period are extracted from the best fit as follows ($\theta \approx 30°$):

$$
\begin{aligned}
\text{Horizontal speed} \quad V_H &= a/\sin\theta, \\
\text{Vertical speed} \quad w &= -c/\cos\theta, \\
\text{Bearing} \quad B &= b, \quad \text{or} \quad b \pm 180°.
\end{aligned}
\tag{99}
$$

Where there is an ambiguity in the sign of the Doppler shift, there are two equally valid best-fit solutions corresponding to values of b separated by 180°. The correct choice is usually easily made by choosing the solution that lies closest to a conventional measurement from a met station situated close to ground. Conventionally, a wind profiling lidar incorporates such a station that performs these (and other) measurements and feeds the results to the analysis software.

The 3 s (or alternatively 1 s) wind parameter values are stored internally for subsequent analysis; they can also undergo further processing for extraction of average values.

Data averaging

It is a common requirement to calculate 10 min averaged wind data for compatibility with industry standards. This is most easily achieved by calculation of the arithmetic mean ("scalar average") of the individual values of V_H, w and B that have been obtained during the required period. A vector average is also possible in which the resultant of the individual measurements is calculated over each 10 min period. In practice the results from the two methods differ negligibly in reasonably stable conditions. In accordance with industry standards, ZephIR computes a scalar average for V_H and w, and a vector average for B.

When a CW lidar is operating as a wind profiler it is necessary to measure each height in series. Hence, at any given height the wind is not monitored continuously. Instead, an individual measurement (taking 1 to 3 s to obtain) is followed by a period of order 7–20 s during which the lidar is focused at other heights. Since this sampling is carried out randomly with respect to any behaviour of the wind, this duty cycle of order 15% has negligible impact on the validity of the resulting 10 min averaged values. Also the typically large scan area ensures the beam samples a much higher fraction of the overall turbulent fluctuations.

4.5 Uncertainty analysis

Rain/snow/cloud, solid objects

In general the Doppler shift measured by coherent laser radar is very accurate. This is apparent from Eq. (93) as long as the laser wavelength remains stable and the signal processing has been correctly performed - both good assumptions in practice. The values of $\langle V_{\mathrm{LOS}} \rangle$ that are derived from the centroids of the spectra can be measured to considerably better than a bin width. A greater source of error arises from uncertainty about what provides the scattering from which the Doppler shift is derived. The scattering is assumed to originate from atmospheric particles moving at the same speed as the wind and positioned close to the focus of the lidar beam (section 4.3). An obvious example where this breaks down is when the beam intersects a solid object (e.g. a bird) that is moving at a different speed from the wind giving a measurement which could be in error. However, in such a case the value of $\langle V_{\mathrm{LOS}} \rangle$ so derived will stand out as clearly anomalous on the polar plot (Figure 35). The presence of such points will be diluted by approximately 150 correct values of $\langle V_{\mathrm{LOS}} \rangle$ obtained from uncontaminated parts of the atmosphere, and their inclusion should not introduce any bias. A further safeguard against these erroneous points is provided by a simple "outlier removal" algorithm. This identifies points that lie anomalously far from the best fit solution to Eq. (98) and eliminates them. The least-squares routine is then rerun on this slightly reduced set of $\langle V_{\mathrm{LOS}} \rangle$, data pairs.

The presence of precipitation within the probe volume leads to a different source of uncertainty. The downward motion of rain and snow inevitably leads to some error in the vertical component of wind speed. However, the presence of rain and snow is normally easily identified from the measurement process (for example by detecting activation of a rain sensor), and the resulting values of vertical wind eliminated from the data.

Cloud effects

CW laser wind profilers focus the beam in order to measure wind speed at a given height. This technique has the advantage of uniformly high sensitivity independent of focus

measurement height, and of very small probe lengths at lower heights where detailed investigation of shear is important. However, the signals do require correct processing when the beam impacts a cloud base at higher altitude since the contribution to the Doppler signal from cloud provides an additional contribution to that from the aerosols at the desired height.

A general approach to mitigating this problem needs first to identify the presence of a cloud return and then remove its contribution from the Doppler spectra. Cloud returns have a number of characteristics that allow them to be distinguished from aerosol returns:

- Velocity usually higher

- Spectral width usually narrower

- Power in Doppler peak has clear dependence on lidar focus; the power is maximised when the lidar beam is focused close to the height of the cloud base

- Doppler spectrum is independent of focus range

The latter two characteristics are highly dependable and form the basis for identification and elimination of spurious cloud returns. The general strategy for removal of cloud signals is outlined in the following steps (and illustrated in Figure 37):

1. Routinely run the lidar at an additional greater height (e.g. 800 m - essentially a collimated beam output) immediately before or after the maximum height of interest, say 150 m for the sake of argument.

2. For each azimuth angle around scan at 150 m, identify the 800 m ("cloud") spectrum obtained at the closest value of azimuth angle.

3. Apply test conditions to the 150 m spectra to determine whether any cloud signal is present in the spectral data; apply cloud removal algorithm.

4. Run standard thresholding and centroiding routines on resulting "clean" spectra and fit to the rectified cosine wave (Eq. (98)) as usual to obtain wind parameters.

A cloud removal algorithm based on this approach is implemented in ZephIR; this has been extensively tested in a number of locations, and its effectiveness demonstrated by correlation analysis against calibrated tall masts. During the 800 m ("wind profile") scan, background measurements are taken to quantify the specific cloud return and any cloud effect is then removed from the processed data.

In general, lidars of various types of design will all have difficulty measuring in very low cloud and fog scenarios where the light emitted from the lidar is unable to reach all the heights of interest due to absorption in the atmosphere. While this atmospheric condition mostly occurs during low wind speed periods, it is important that these periods be identified. In the majority of cases they are removed by filtering methods.

Recent trials of a ZephIR unit at Risø DTU's test site at Høvsøre (Courtney and Gottschall, 2010) took place in long periods of low cloud and hence provide a demonstration of the performance in challenging cloud conditions. The data set summarised in Table 10 below was taken during a period of 4 weeks in October and November 2009. Cloud height was measured using a ceilometer; 25% of data was obtained with the cloud base below 300 m, and 43% obtained with the cloud base below 600 m. The results of the trial (Table 10) indicate a good agreement between lidar and mast at all heights from 40 up to 116 m. Filtering has been applied to remove sectors prone to the influence of turbine wakes, and speeds below 4 m s^{-1}.
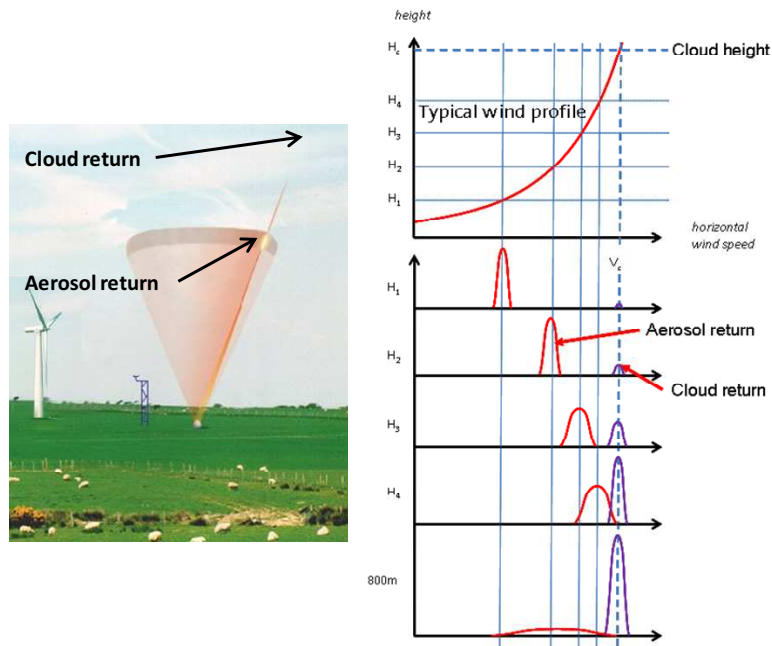
Figure 37. Cloud removal. The left plot shows the lidar conical scan focused at a typical height above ground level. The Lorentzian sensitivity curve is also shown; a spurious return is generated when the far wing of this curve intersects a strongly scattering low cloud layer. The right plot shows the aerosol (red) and cloud (purple) returns as the lidar is focused at various heights - the level of cloud contamination increases with focus height. The cloud signal is easily identified from the 800 m focus, and these data are then used to eliminate the cloud return at the measurement heights

Table 10. Results of correlation analysis (10 min averaged horizontal wind speed) of a ZephIR trial at Høvsøre in late 2009. A gradient m (forced through the origin) and correlation coefficient R^2 both of value 1.00 would imply perfect agreement between lidar and mast-mounted cup anemometer. It should be noted that the slopes very close to 1.0 are slightly fortuitous, since the cup anemometer measurements have uncertainties at least of order $\pm 1\%$, due to calibration and mounting/shadowing effects

Height AGL [m]	Slope m	R^2
116	0.991	0.981
100	0.997	0.978
80	0.999	0.981
60	0.997	0.987
40	0.999	0.985

System positioning accuracy

Correct alignment ensures the risks are low, but errors in aligning the lidar during set-up will have an impact on the measurement of wind bearing (if the lidar is rotated from its correct orientation) and vertical wind speed (if the lidar is tilted, so that the axis of its conical scan is not precisely vertical). For a small tilt angle δ, the error in vertical wind speed w will vary from $\pm V_H \sin \delta$ (if the tilt is towards or away from the direction of the wind) to zero (if the tilt is perpendicular to the wind). Any bias on V_H is negligible to first order.

Probe volume effects and operation at greater heights

As discussed in section 4.2, the lidar samples the motion of air from a finite volume, centred on the beam waist at the focus. Clearly there is minimal risk of bias while all the air within the probe volume moves at the same speed; however, there is usually some degree of shear across the sample region. For a linear shear this leads to spectral broadening of the returns, but no overall bias. A strong non-linear shear profile across the probe volume is required to induce any bias of significance; in practice such conditions will be rare, certainly for measurement heights around hub height and below where the probe length is relatively small.

Most lidar comparisons have taken place beside masts of heights around 100 m or less. However, in early 2009 a study took place in Iowa, USA against a 200 m mast in flat terrain. The results showed high correlation (Table 11, taken from Barker (2009)) even at the greater heights examined (150 and 200 m), which approach the expected maximum operating range for focused CW lidar.

Table 11. Results of a comparative trial of a ZephIR lidar against a very tall mast, equipped with two types of cups at each height. The data indicate that the extended probe length at greater heights did not result in excessive bias or errors. [1]: Forced through the origin; [2]: Only hourly averages containing 6 valid 10 min measurements compared

| | NRG IceFree3 | | | | NRG MAX#40C | | | |
| | Ten min average | | Hourly average[2] | | Ten min average | | Hourly average[2] | |
Height AGL [m]	R^2	Slope[1]	R^2	Slope[1]	R^2	Slope[1]	R^2	Slope[1]
193	0.984	0.987	0.987	0.987	0.982	0.993	0.988	0.992
157	0.982	1.006	0.988	1.005	0.984	1.000	0.989	1.000

Flow uniformity and complex terrain

In complex terrain, the flow undergoes stable and unstable non-uniformities, and the figure-of-eight plot (Figure 36) can distort systematically for a given wind direction, reflecting the speeding up and slowing down in certain regions of the scan. The ZephIR lidar provides some information about the flow non-uniformity, with up to 50 points being interrogated around the scan disk. Because only line-of-sight wind components are measured, a single ground-based lidar unit inevitably provides an incomplete picture of the 3D vector flow, regardless of the scan pattern employed. The full vector at a given point can therefore only be measured by the provision of three (or more) lidar units positioned on the ground at an appropriate separation distance (comparable to the measurement height for best accuracy), such as the Windscanner system under development by Risø DTU (Mikkelsen et al., 2008).

In the presence of non-uniformity in flow (section 4.2), a lidar measurement can indicate a wind speed different to that from a point measurement by a mast-mounted cup anemometer. Work is ongoing to combine lidar data with the output from flow-modelling software, using both linear models (Bingöl et al., 2008, 2009; Bingöl, 2010) and computational fluid dynamics, CFD (Harris et al., 2010). This pragmatic approach generates measurements equivalent to a "point-in-space" sensor by using the results of flow modelling to adjust the lidar wind speed. This topic will be dealt with in detail in Chapter 7, examining possible improvement of lidar resource assessment capability in complex terrain.

Dependence on backscatter level

Under conditions of high backscatter, the spectrum provides an accurate measure of the distribution of line-of-sight velocities within the probe volume, weighted according to Eq. (89). As the backscattering strength drops (usually associated with increased air clarity) this has a similar effect to raising the detection threshold, and will lead to elimination from the spectrum of weaker components of velocity. The impact of the system noise floor on the detailed spectral shape will also be increased. The centroid values $\langle V_{\mathrm{LOS}} \rangle$ will be unbiased and independent of threshold level when the spectrum is symmetrical. However, for a skewed (asymmetric) spectrum the precise value of $\langle V_{\mathrm{LOS}} \rangle$ will be sensitive to the threshold. Hence a small difference in measured wind speed is possible between two measurements under conditions that are identical in every way apart from the level of backscatter. However, there is no evidence from comparisons so far to suggest that this leads in practice to a significant discrepancy.

A further possibility to be considered is the effect of saturation (by very strong scattering returns from thick cloud) of the lidar detector, electronics or signal processing. In the event that the input signal exceeds these limits, the spectrum will become distorted, possibly featuring higher harmonic components of the true Doppler frequencies. In practice, the range of inputs to the ADC can be tailored to accommodate the highest levels of backscatter that will reasonably be encountered, eliminating the risk of bias.

Beam obscuration and attenuation

Lidar can operate successfully even when part of its scan is obscured. This confers great flexibility so that the system can easily be located adjacent to masts, buildings or in forests. Stationary objects pose no major problem other than the loss of wind measurements from the relevant obscured sector of the scan.

In the above cases, the fit to Eq. (98) will no longer contain data over the full 360° range of ϕ. Laboratory experiments on moving belt targets have indicated that accurate measurements are obtained even when over half of the scan is obscured. Catastrophic errors in the least-squares fitting process become possible as the obscuration increases yet further; such conditions are identified and a null result returned.

Wind direction

The two best-fit solutions ZephIR obtains to Eq. (98) give values of wind direction that are 180° apart. Selection between the two options is made with reference to the measurement of wind direction from a ground-based anemometer. This needs to be in disagreement by over 90° with the direction at the chosen height for the incorrect choice to be made. While such a directional shear (veer) is conceivable in highly complex terrain and at very low wind speed, it is much less likely in the reasonably uniform conditions of interest for wind energy applications. In the event of the wrong choice being made, leading to a wind direction that is in error by 180°, the value of vertical component of the wind w will have the wrong sign. In other words, an updraught will be wrongly identified as a down draught (of the same absolute speed) and vice versa.

4.6   Calibration, validation and traceability

Currently, the clearest demonstration of validity is provided by direct side-by-side comparisons between the lidar system and a fully instrumented IEC-compliant meteorological mast of suitable height. Rigorous comparisons must be carried out with great care to avoid a number of problems associated with cup anemometers (Kristensen, 1999). These are well known and include the following:

- Shadowing of the cup anemometer by the mast from certain directions

- Cup overspeeding in turbulence and sensitivity to any vertical wind component

- Cup icing

- Valid cup anemometer calibration

- Topographic effects leading to non-uniform flow across the area occupied by mast and lidar scan (including turbine wakes)

A lidar/mast comparison is commonly used to provide a validation of lidar performance, and examples of such checks were provided by the results in Tables 10 and 11. The lidar can then be used as a traceable reference for comparison with other units.

Lidar systems are normally calibrated in the laboratory before shipping. Routine checks on the calibration of units on their return to base provide confidence of long-term stability. As an example, the calibration process undertaken for a ZephIR lidar is outlined below. This consists of three stages:

1. Velocity and direction check against a calibrated moving belt. The process provides a direct check of laser wavelength and scanner cone angle, each of which affects the velocity calibration (via Eqs. (92) and (98) respectively).

2. A focus range check is carried out with a moving target located at precise distances from the lidar. The closed loop positioning system ensures no drifts over time. An example of the output data from a focus calibration test was plotted in Figure 34 (section 4.4).

3. Finally, each unit undergoes an outdoor test to measure wind speed at several heights side-by-side against a reference unit. The reference unit has been checked against a tall mast to provide traceability. Figure 38 shows an example correlation plot of 10min average horizontal wind speed, obtained over a period of 7 days.

Each of the three tests above gives information on the sensitivity of the unit; for deployments in "clean" air, it is important to ensure this aspect of performance is fully optimised and has not deteriorated, or there is a risk of reduced data availability.

It is important that no adjustments are performed during validation trials, or afterwards for as long as the lidar remains a traceable reference unit. The certification process outlined above has been defined in collaboration with industry experts including Garrad Hassan and provides the traceability that is a key element of formal energy prediction reports used by the financial community.

Lidar offers a potential advantage for accurate shear profiling (both for speed and direction) in that the same instrument is used to make the measurements at all heights. By contrast, a mast relies on consistent calibration of the full set of cups and vanes; any differences in calibration of the individual instruments will lead to uncertainty and error in the shear assessment. There is currently a need for agreement on a unified method to allow meaningful comparison between the performances of different remote sensing systems.

4.7 Summary, state of the art, and future developments

Coherent monostatic CW lidar is a method capable of rapid wind speed measurement at relatively short ranges (all the way from 10 to 200 m) and hence is well suited to several requirements in the field of wind energy. Examination of the measurement process reveals that the basic acquisition of line-of-sight Doppler spectra is a well-established method with little scope for gross errors and miscalibration. The subsequent steps required to convert these spectra into a profile of wind speed are more complex, however, and their
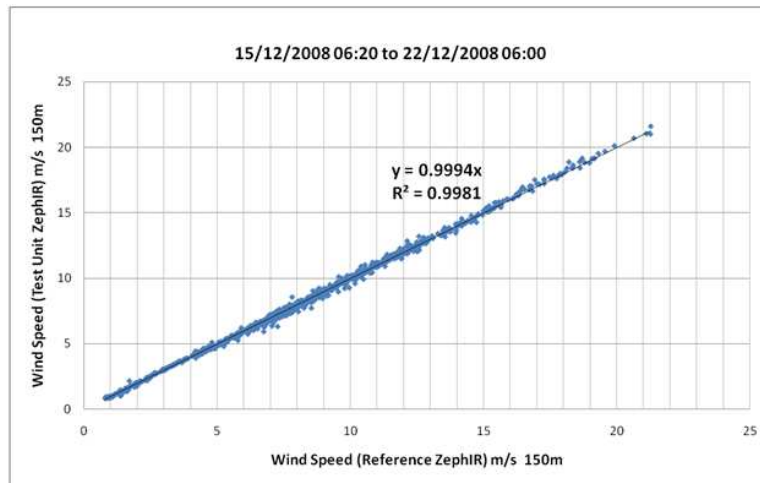
Figure 38. A new ZephIR system is compared to the reference system showing strong correlation and a gradient close to unity. This comparison has been carried out at 150 m height

validity relies on a number of well-established assumptions. Much work has been performed to test the validity of assumptions outlined in section 4.3, and to understand the uncertainties and other issues discussed in section 4.5.

Complex terrain remains a topic of great interest as it becomes increasingly necessary to explore less ideal locations as potential wind farm sites. In such sites the horizontal wind speed deduced by conically-scanned lidar can be subject to differences in comparison to that measured by co-located cup anemometers when the flow is non-uniform across the lidar measurement disk. A method has recently been developed in which the impact of inhomogeneous flow at complex flow sites is examined using computational fluid dynamics (CFD modelling to predict the bias that will be experienced by a lidar in comparison to a conventional met mast equipped with cup anemometers. Similar percentage changes in wind speed as measured by a mast are shown to occur if the mast were to be moved by ±50 m from its original location. This suggests a methodology for resource assessment in complex terrain in which lidar is used in combination with CFD modelling in order to (i) adjust the lidar data for the impact of non-uniform flow and (ii) investigate the wind variations across the site that are a major source of uncertainty for current techniques.

Lidar offers some potential advantages in turbine power curve measurement. The measurement over an extended volume may give a more representative estimate of the wind energy content of the air interacting with the blades, and the ability to re-position the lidar quickly is clearly advantageous. A study reported by Wagner et al. (2008) has shown that exploiting the lidar wind profile data can reduce the scatter of points in a measured power curve. In another recent study (Cayla, 2010) a ZephIR lidar gave an almost identical power curve to an IEC-instrumented power performance mast. The scatter of the points in the power curve obtained using the ZephIR data at hub height was somewhat lower than that for the mast. This result needs further investigation and possibly is a consequence of the more effective sampling of the wind around the scan disk. It follows, interestingly, that remote sensing equipment that agrees perfectly with the mast would therefore have provided higher scatter in the power curve than ZephIR!

The extraction of turbulence data relevant to the wind industry from lidar signals is an area that will benefit from further research and verification through field comparisons. Turbulence can manifest itself as gusts, eddies, and fluctuations in wind speed. It is important in wind energy applications to characterise the levels of turbulence encountered at a specific site location. A commonly-used basic measure of turbulence is turbulence intensity (TI). ZephIR calculates the turbulence intensity that a conventional cup would

have obtained at the same measurement height by analysing the variation in individual wind speed values during a 10 min averaging period. This value of TI is automatically logged in the output data. The calculation takes into account the difference between point measurements obtained from a cup anemometer, and spatially-averaged lidar data where a volume is interrogated. ZephIR's measurements of turbulence have been investigated in a number of independent studies against calibrated met masts in flat, offshore and complex terrain, and at different heights above ground (Wagner et al., 2009).

Resource assessment in maritime locations is becoming increasingly relevant as offshore wind farms assume greater importance. The cost of installing an offshore tall mast is very high, so remote sensing may prove particularly advantageous in such locations. ZephIR lidars have been involved in successful trials on several offshore platforms in the North Sea (e.g. Peña et al. (2009)), the Baltic, and around the lakes and coasts of North America. A floating lidar platform offers an exciting future concept; an early attempt to develop a ZephIR system on a buoy (SeaZephIR) took place in 2004/5. After a redesign, the system took to the water off S Norway in 2009. A world-first demonstration trial took place over a period of several weeks in late 2009, involving one ZephIR unit stationed on land, with the floating SeaZephIR unit positioned 800 m out to sea. The wind speeds measured by the two ZephIR units showed excellent correlation, with differences in mean wind of $\sim 1\%$ or less at all heights over a 3 week test period (see Table 12, from Wiggins (2009)). In this trial there was no attempt to compensate for the platform motion; it may be necessary in very severe conditions to use measurements of the 6 degrees of freedom (3 rotational and 3 translational) that can in principle distort the lidar measurement. The low impact of the motion observed in trials so far may be a consequence of the high stability of the buoy combined with the very fast 50 Hz measurement rate for the ZephIR lidar, which allows a snapshot of the wind around a 360° disk to be obtained in 1 s. Further development of SeaZephIR is ongoing.

Table 12. Correlation analysis from the first SeaZephIR trial in 2009: the table shows m and R^2 for plots of 10 min wind speed for SeaZephIR on a floating platform versus those measured by a second ZephIR unit positioned 800 m away on land

Height AGL [m]	Slope m	R^2
120	0.993	0.972
90	0.998	0.970
60	1.004	0.968
30	0.990	0.954
10	0.984	0.953

Forward-looking turbine mounted lidar, either on the nacelle or in the hub, is another exciting potential future application for advance warning of changes in wind speed. Incorporation of such data into the turbine control system offers possibilities for load reduction and increased energy yield. At the time of writing, it remains to be seen whether lidar will prove sufficiently beneficial to justify the effort of installation; any such system will have to satisfy stringent reliability and cost requirements. Interest in the concept has increased significantly since the world-first proof-of-principle demonstration of turbine-mounted lidar in 2003 (Harris et al., 2006, 2007), with several groups currently working towards evaluating the concept. Recent developments include incorporation of a conical-scanning ZephIR lidar in the spinner of a large turbine (Mikkelsen et al., 2010) giving an unobscured view of the approaching wind.

Acknowledgements

Notation

a	floating parameter for the fit of the line-of-sight velocity
A	beam radius at the output lens
ADC	analogue-to-digital converter
b	floating parameter for the fit of the line-of-sight velocity
B	wind bearing
c	speed of light
	floating parameter for the fit of the line-of-sight velocity
CFD	computational fluid dynamics
CLR	coherent laser radar
CNR	carrier-to-noise ratio
CW	continuous wave
DFT	digital Fourier transform
$D(\nu)$	power spectral density from dark noise
E_{LO}	LO field
E_{s}	stable signal field
FFT	fast Fourier transform
FPGA	field-programmable gate array
h	Planck constant
i	fluctuating detector power output
IR	infrared
LO	local oscillator
m	slope of the linear regression
P_s	time-average optical signal power
P_T	transmitted laser power
R	distance of the beam focus from the lidar output lens
	correlation coefficient
RIN	laser relative intensive noise
$D(\nu$	power spectral density from RIN
SNR	signal-to-noise ratio
t	time variable
TI	turbulence intensity
TKE	turbulent kinetic energy
u	wind speed component in the x-direction
v	wind speed component in the y-direction
VAD	velocity-azimuth-display
V_H	horizontal wind speed
V_{LOS}	line-of-sight wind speed
w	wind speed component in the z-direction
x	horizontal position in longitudinal direction
y	horizontal position in transverse direction
z	position perpendicular to the horizontal plane
β	atmospheric backscatter coefficient
Γ	half-width of the lidar's peak sensitivity
δ	lidar's tilt angle
$\delta\nu$	Doppler shift in frequency
Δ	target distance from the focus position along the beam direction
η	lidar efficiency
θ	lidar's cone half-angle
λ	laser wavelength
ν	laser frequency
ϕ	lidar's azimuth angle
σ	standard deviation
ω_{LO}	local oscillator frequency

ω_s stable signal frequency

$\langle X \rangle$ ensemble average of a variable X

References

Banakh V. A., Smalikho I. N., Köpp F., and Werner C. (1993) Representativeness of wind measurements with a CW Doppler lidar in the atmospheric boundary layer. *Appl. Opt.* **34**:2055–2067

Banakh V. A., Smalikho I. N., Köpp F., and Werner C. (1999) Measurements of turbulent energy dissipation rate with a CW Doppler lidar in the atmospheric boundary layer. *J. Atmos. Oceanic Tech.* **16**:1044–1061

Barker W. (2009) Analysis of ZephIR data from Mason City, Iowa. Natural Power internal report

Bingöl F., Mann J., and Foussekis D. (2008) Lidar error estimation with WAsP engineering. *IOP Conf. Series: Earth and Environ. Sci.* **1**:012058

Bingöl F., Mann J., and Foussekis D. (2009) Conically scanning lidar error in complex terrain. *Meteorol. Z.* **18**:189–195

Bingöl F. (2010) Complex terrain and wind lidars. Risø-PhD-52(EN), Roskilde

Bleaney B. I. and Bleaney B. (1976) Electricity and magnetism, Oxford University Press, Section 23.4

Cayla M. (2010) Comparison of ZephIR measurements against cup anemometry and power curve measurements. Natural Power internal report

Chanin M. L., Gariner A., Hauchecorne A., and Portneuve J. (1989) A Doppler lidar for measuring winds in the middle atmosphere. *Geophys. Res. Lett.* **16**:1273–1276

Clifford S. F. and Wandzura S. (1981) Monostatic heterodyne lidar performance: the effect of the turbulent atmosphere. *Appl. Opt.* **20**:514–516

Courtney M. and Gottschall J. (2010) ZephIR 145 validation test. Risø report for Natural Power

Hardesty R. M. and Weber B. F. (1987) Lidar measurement of turbulence encountered by horizontal-axis wind turbines. *J. Atmos. Oceanic Tech.* **67**:191–203

Harris M., Pearson G. N., Hill C. A., and Vaughan J. M. (1994) Higher moments of scattered light fields by heterodyne analysis. *Appl. Opt.* **33**:7226–7230

Harris M., Constant G., and C Ward (2001) Continuous-wave bistatic laser Doppler wind sensor. *Appl. Opt.* **40**:1501–1506

Harris M., Pearson G. N., Ridley K. D., Karlsson C. J., Olsson F. A., and Letalick D. (2001) Single-particle laser Doppler anemometry at 1.55 μm. *Appl. Opt.* **40**:969–973

Harris M., Hand M., and Wright A. (2006) Lidar for turbine control. Tech. Report NREL/TP-500-39154

Harris M., Bryce D. J., Coffey A. S., Smith D. A., Birkemeyer J., and Knopf U. (2007) Advance measurements of gusts by laser anemometry. *J. Wind Eng. Ind. Aerodyn.* **95**:1637–1647

Harris M., Locker I., Douglas N., Girault R., Abiven C., and Brady O. (2010) Validated adjustment of remote sensing bias in complex terrain using CFD. *European Wind Energy Conf.*, Warsaw

Jelalian A. V. (1992) Laser radar systems, Artech House, Boston

Karlsson C. J., Olsson F. A., Letalick D., and Harris M. (2000) All-fiber multifunction CW 1.55 micron coherent laser radar for range, speed, vibration and wind measurements. *Appl. Opt.* **39**:3716–3726

Kindler D., Oldroyd A., MacAskill A., and Finch D. (2006) An 8 month test campaign of the QinetiQ ZephIR system: preliminary results. *ISARS 13th Conf. Wiss. Ber. FZKA* 7222: 165–167 Garmish-Partenkirchen

Kristensen L. (1999) The perennial cup anemometer. *Wind Energy* **2**:59–75

Lading L., Hanson S., and Skov Jensen A. (1984) Diffraction-limited lidars: the impact of refractive turbulence. *Appl. Opt.* **23**:2492–2497

Loudon R. (2000) The quantum theory of light, Oxford University Press, 3rd edition

Mikkelsen T., Mann J., Courtney M., and Sjöholm M. (2008) Windscanner: 3-D wind and turbulence measurements from three steerable doppler lidars. *IOP Conf. Series: Earth and Environ. Sci.* **1**:012018 (9 pp)

Mikkelsen T., Hansen K., Angelou N., Sjöholm M., Harris M., Hadley P., Scullion R., Ellis G., and Vives G. (2010) Lidar wind speed measurements from a rotating spinner. *European Wind Energy Conf.*, Warsaw

Pearson G. N., Roberts P. J., Eacock J. R., and Harris M (2002) Analysis of the performance of a coherent pulsed fiber lidar for aerosol backscatter applications. *Appl. Opt.* **41**:6442–6450

Peña A., Hasager C. B., Gryning S.-E., Courtney M., Antoniou I., Mikkelsen T. (2009) Offshore wind profiling using light detection and ranging measurements. *Wind Energy* **12**:105–124

Smith D. A., Harris M., Coffey A. S., Mikkelsen T., Jørgensen H. E., and Mann J. (2006) Wind lidar evaluation at the Danish wind test site in Høvsøre. *Wind Energy* **9**:87–93

Sonnenschein C. M. and Horrigan F. A. (1971) Signal-to-noise relationships for coaxial systems that heterodyne backscatter from the atmosphere. *Appl. Opt.* **10**:1600–1604

Siegman A. E. (1986) Lasers, University Science Books, Mill Valley

Vaughan J. M. and Forrester P. A. (1989) Laser Doppler velocimetry applied to the measurement of local and global wind. *Wind Eng.* **13**:1–15

Wagner R., Mikkelsen T., and Courtney M. (2009) Investigation of turbulence measurements with a continuous-wave conically scanning lidar. Risø-R-1682(EN), Roskilde

Wagner R., Jørgensen H. E., Paulsen U. S., Larsen T. J., Antoniou I., and Thesbjerg L. (2008) Remote sensing used for power curves. *IOP Conf. Series: Earth and Environ. Sci.* **1**:012059

Wiggins J. (2009) Unpublished internal report. Natural Power

Zak J. A. (2003) Atmospheric boundary layer sensors for application in a wake vortex advisory system. NASA/CR-2003-212175

5 What can remote sensing contribute to power curve measurements?

Rozenn Wagner
Wind Energy Division, Risø DTU, Roskilde, Denmark

5.1 Introduction

Power performance measurement is central to the wind industry since it forms the basis for the power production warranty of the wind turbine. The power curve measurement has to be realised according to the IEC 61400-12-1 standard. The power curve is obtained with 10-min mean power output from the turbine plotted against simultaneous 10-min average wind speeds. The standard requires the wind speed to be measured by a cup anemometer mounted on top of a mast having the same height as the turbine hub and located at a distance equivalent to 2.5 rotor diameters from the turbine.

Such a plot usually shows a significant spread of values and not a uniquely defined function. The origin of the scatter can mainly be grouped into three categories: the wind turbine components characteristics, sensor error and the wind characteristics. Within the last group, the current standard only requires the wind speed at hub height and the air density measurement. However, other wind characteristics can influence the power production like the variation of the wind speed with height (i.e. wind speed shear). The influence of wind speed shear on the power performance was shown in several studies: some based on aerodynamic simulations (Antoniou, 2009; Wagner et al., 2009) others based on measurements (Elliot and Cadogan, 1990; Sumner an Masson, 2006).

A major issue is to experimentally evaluate the wind speed shear. The wind speed profile is usually assumed to follow one of the standard models such as the logarithmic or power law profiles. However, these models are valid for some particular meteorological conditions, and therefore, cannot represent all the profiles experienced by a wind turbine. Measurements are then a better option but are also challenging. Indeed characterising the wind speed profile in front of the rotor of a multi-MW wind turbine requires measurements of wind speed at several heights, including some above hub height, i.e. typically above 100 m. Remote sensing instruments such as lidar or sodar then appear as a very attractive solution.

This chapter starts with a description of the influence of the wind speed shear on the power performance of a multi-MW turbine. The challenge of describing the wind speed profile is then discussed followed by a description of an experiment using a lidar for its characterisation. This is followed by the introduction of the definition of an equivalent wind speed taking the wind shear into account resulting in an improvement of the power performance measurement. Finally, some recommendations about remote sensing instruments are given to successfully apply this method.

5.2 Power performance and wind shear

Shear and aerodynamics

In order to see the effect of the wind speed shear on a wind turbine, aerodynamic simulations were carried out for two inflow cases:

1. constant wind speed profile (same wind speed everywhere) with 8 m s^{-1}

2. power law profile with 8 m s^{-1} at hub height and a shear exponent of 0.5

The power law profile is defined as:

$$u = u_{hub} \left(\frac{z}{z_{hub}} \right)^{\alpha}, \tag{100}$$

where u is the wind speed at height z, z_{hub} the hub height, u_{hub} the wind speed at that height and α the shear exponent. Both profiles are shown in Figure 39.

The model used was HAWC2Aero. The modeled turbine was a Siemens 3.6 MW with a rotor diameter of 107 m and a hub height of 80 m.The wind speed is assumed horizontally homogeneous (i.e. the wind speed is the same everywhere on each horizontal plane). In order to emphasize the effect of wind speed shear, the simulations were carried out with laminar inflow, the tower shadow was turned off and the tilt angle of the rotor was set to 0°.
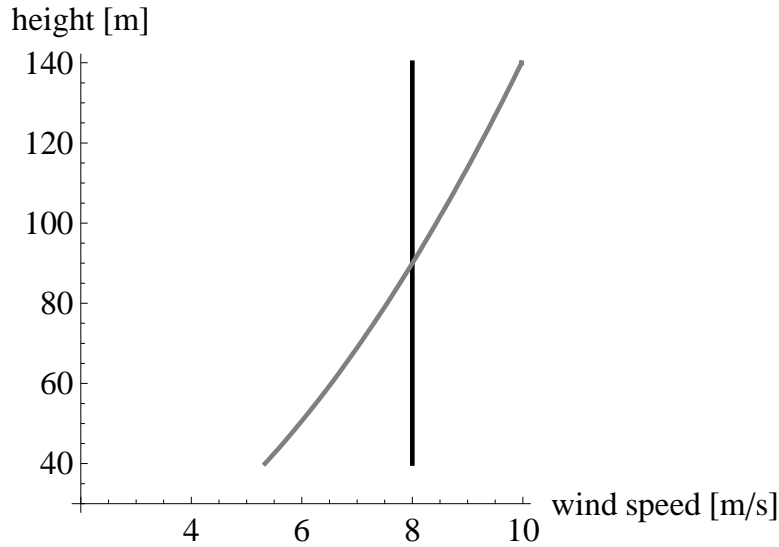
Figure 39. Wind profiles used as input for the wind speed shear aerodynamic investigation. Black curve: no shear; grey curve: power law profile with shear exponent of 0.5. Both profiles have the same wind speed at hub height

Figure 40 shows the free wind speed (i.e. the absolute wind speed in absence of a turbine) seen by a point at a radius of 30 m from the rotor centre, rotating at the same speed as the rotor as a function of time for the 2 inflow cases. Whereas in a uniform flow the blade is subjected to a constant wind speed, in a sheared flow, the point is exposed to large variations of wind speed even though the inflow is laminar. The variation of the wind speed seen by this rotating point in time is only due to the fact that it is rotating within a non uniform flow (wind speed varying with height).

Figure 41 shows the variations of the free wind speed seen by the same rotating point as function of the azimuth position (0° = downwards). The point experiences the hub height wind speed (same as uniform inflow) when it is horizontal (±90°), lower wind speed when it is downward (0°) and higher wind speed when it is upward (180°).

A rotating blade does not experience the free wind speed because of the induction from the drag of the rotor. In reality, a rotating blade is directly subjected to the relative wind speed w (i.e. the speed of the wind passing over the airfoil relative to the rotating blade) and the angle of attack ϕ (i.e. the angle between the blade chord line and the relative wind speed) with the effects of the induced speed included. The variations of these two parameters as function of θ are shown in Figure 42. As these two parameters directly depend on the free wind speed, they vary with the azimuth angle in a sheared inflow, whereas they remain constant in a uniform inflow.
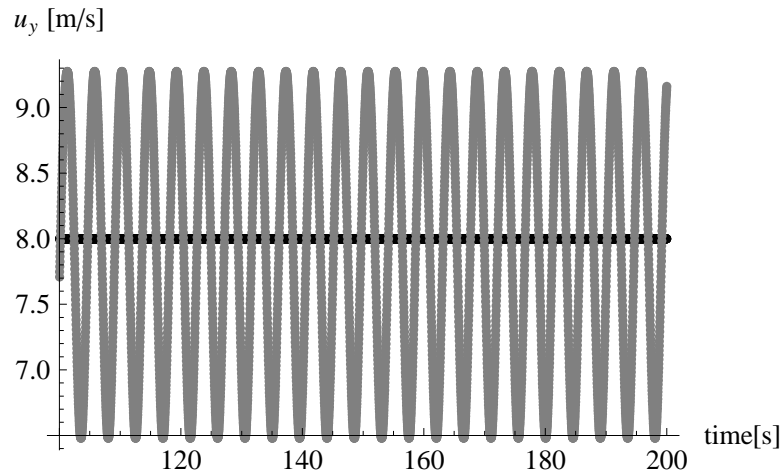
Figure 40. Time series of free wind speed seen from a rotating point, positioned at a radius of 30 m, rotating at rotor rotational speed (no induced velocity). Black curve: no shear; grey curve: power law profile with shear exponent of 0.5
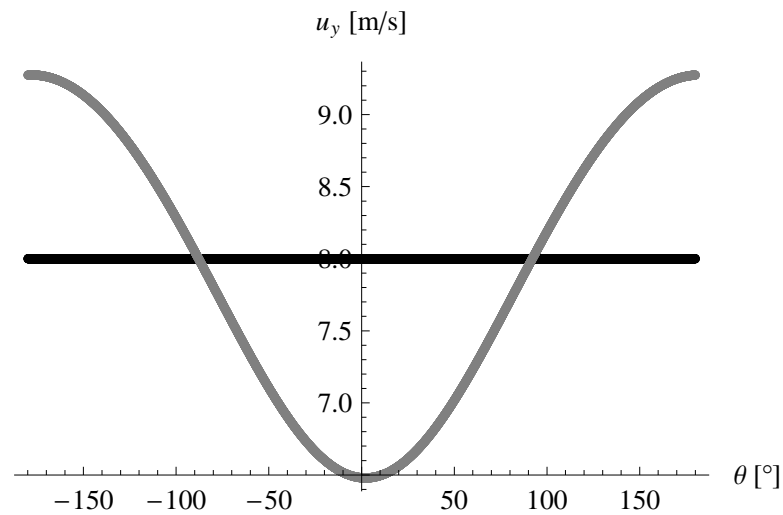

Figure 41. Free wind speed seen from a rotating point, positioned at a radius of 3 0m, rotating at rotor rotational speed, as function of the azimuth angle θ. Black curve: no shear; grey curve: power law profile with shear exponent of 0.5

The relative speed and the angle of attack are derived from the rotor speed and the induced velocity. Therefore, they depend on the way that the induction is modeled and it is difficult to evaluate their variations due to a non uniform flow in a simple way. However, some basic considerations (ignoring the induction) can give a basic insight to the variation of the relative speed and the angle of attack as the blade rotates. In case of uniform inflow, the free wind speed is the same at any point of the swept rotor area. Therefore, the angle of attack and the relative speed are the same at any azimuthal position (see Figure 43).

In case of sheared inflow, the free wind speed depends on the position of the blade. When the blade is horizontal, the free wind speed is the speed at hub height and the speed triangle is the same as in Figure 43. Below hub height, the wind speed is lower than the hub height speed, see Figure 44 (left). Consequently w and ϕ are lower than those at hub height. Above hub height, the wind speed is higher than the hub height wind speed. Consequently w and ϕ are higher than those at hub height, see Figure 44
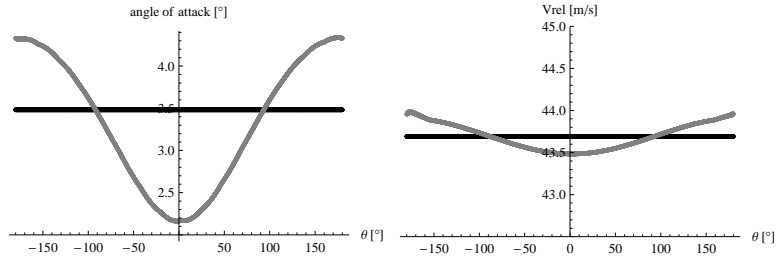
Figure 42. phi (left) and w (including induction) (right) as a function of θ, seen from a point at radius r = 30 m on a rotating blade. Black curve: no shear; grey curve: power law profile with shear exponent of 0.5
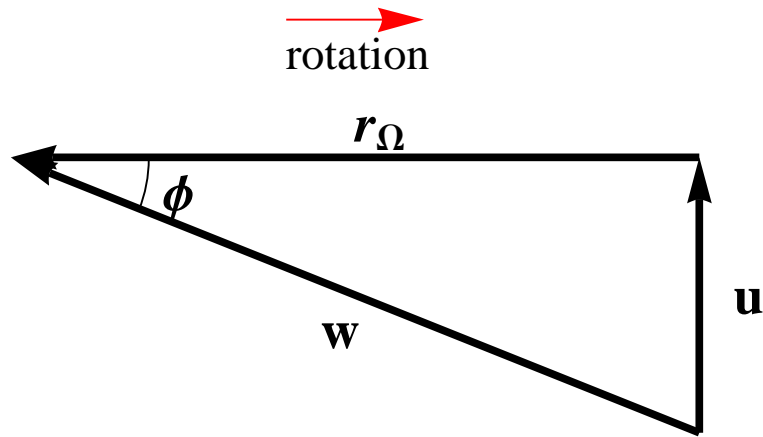

Figure 43. Speed triangle for a blade element at radius r. r_Ω is the blade speed and w corresponds to the sum of the pitch angle, the twist angle and φ. As the twist angle is constant for a given position on the blade and the pitch angle is 0° for wind speeds below rated speed, φ represents the variation of the angle of attack

(right). The variations in φ and w cause a variation of the local lift and drag as the blade rotates, which finally results in the variation of the local tangential force contributing to the wind turbine power (see Figure 45). For a given φ, local lift dF_L and local drag dF_D, the local tangential force dF_T is given by (Manwell et al., 2002):

$$dF_T = dF_L \sin \phi - dF_D \cos \phi. \tag{101}$$

As the wind speed increases with height (e.g. in the case of the power law profile), the amplitude of the variations of the free wind speed seen by a rotating point increases with the radius (not shown here). The local tangential force consequently varies with the radius too. As the torque results from the integral of the tangential force over the whole rotor, it thus depends on the wind speed profile.

Consequences on the power production

A series of cases were simulated with theoretical wind speed shear defined from the power law in Eq. (100), with $-0.1 < \alpha < 0.5$ and 5 m s^{-1} < u_{hub} < 10 m s^{-1}. The relative variations in power (defined as the percentage difference between the power outputs obtained with a shear inflow and an uniform inflow) are shown in Figure 46. According to the simulations results, the power output obtained with shear inflow is generally smaller than the power output obtained with an uniform inflow. Moreover, it decreases as the shear exponent increases except at 5 m s^{-1} where the power output reaches a minimum for $\alpha = 0.2$ and increases for larger shear exponents, even exceeding the power output
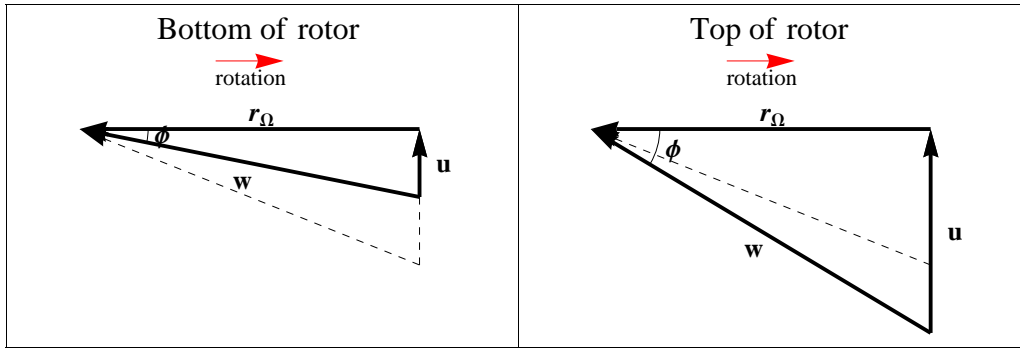
Figure 44. Speed triangles at the top and bottom of the rotor showing the effect of wind speed shear. The speed triangle at hub height is shown with dashed arrows
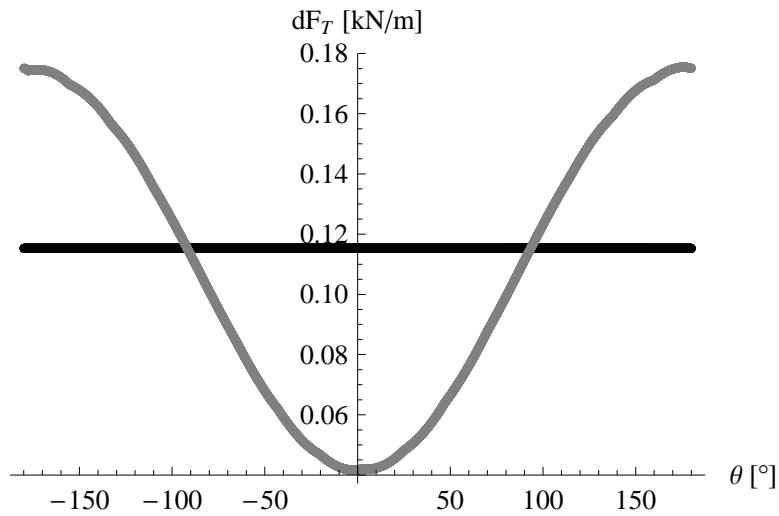

Figure 45. Local tangential force seen from a point $r = 30$ m on a rotating blade as function of θ. Black curve: no shear; Gray curve: power law profile with shear exponent of 0.5

from uniform inflow with $\alpha = 0.5$.

The first difference between a sheared and an uniform inflow is the kinetic energy flux. In case of horizontally homogeneous inflow, the kinetic energy flux can be expressed by:

$$KE_{\text{profile}} = \int_{H-R}^{H+R} 0.5\rho u^3 c\, (z - (z_{hub} - R))\, dz, \tag{102}$$

where ρ is the air density, R the rotor radius and c is the chord (of the circle defined by the rotor swept area) as function of z which varies between the bottom and the top of the rotor:

$$c = 2\sqrt{2Rz - z^2}. \tag{103}$$

In order to compare to the power output variations, Figure 46 also shows the difference between the kinetic energy flux for a power law profile and a constant profile, normalised with the power obtained with a constant profile $KE_{\text{profile}} - KE_{\text{hub}}/KE_{\text{hub}}$ (see gray dashed line) [5]. Figure 46 shows two other interesting results:

1. The kinetic energy flux varies with shear exponent.

2. The power output of the turbine does not follow the same trend as the kinetic energy flux.

---

[5]The kinetic energy flux is not an output of HAWC2Aero, it has been here estimated and for power law profiles, the normalized difference does not depend on the wind speed
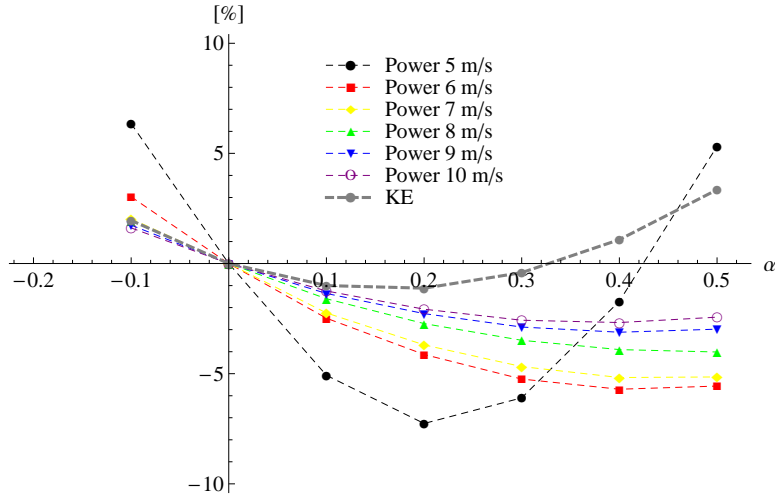
Figure 46. Normalised difference in power output and kinetic energy flux between shear and uniform case as function of the shear exponent, for various wind speed at hub height

Despite the high uncertainty in the modeled power output for a sheared inflow, the results highlight that the influence of the shear on the power performance of a turbine can be seen as the combination of two effects:

- The variation in kinetic energy flux (power input).

- The ability of the turbine to extract the energy from the wind, which depends on the details of the design and the control strategy of the turbine.

These results clearly indicate that wind speed profiles encountered by the turbine during a power performance measurement should be known and taken into account.

5.3 Wind speed profiles

Within the power performance evaluation context, the wind speed shear is often described by α obtained from the assumption of a power law profile (Eq. (100)). This procedure was applied to profiles measured by a high meteorological mast located at the test site for large wind turbines, at Høvsøre, on the west coast of Denmark with $z_{hub} = 80$ m and $z = 40$ m to determine α. For some cases, this model fits the measured profile very well, but it cannot represent all kinds of profiles observed at Høvsøre. Figure 47 shows two examples of measured profiles and their corresponding modelled profiles.

The distribution of the error made by such an approximation is shown in Figure 48. We define the error as the difference between the wind speed at 116.5 m (top of the mast) estimated by the power law model and the speed measured by the cup anemometer. Over a year of measurements, for a large wind sector 60°–300° degrees (with predominant wind from west), 7% of the profiles show a wind speed error at 116.5 m larger than 10%. We should keep in mind that all the anemometers are mounted on a boom except the top anemometer, and this can induce an error in the profile extrapolation to the top (116.5 m).

As shown by the simulations presented in section 5.2, such an error in the wind speed profile can significantly affect the power curve. The shear exponent from wind speed measurements at two heights is not acceptable for this application. Therefore it is important to measure the wind speeds at several heights below and above hub height. For this purpose remote sensing instruments such as lidar and sodar are highly relevant since in many cases they can measure up to 200 m with the required degree of accuracy.

An experimental campaign using a lidar to measure the wind speed profile in front of a multi-MW turbine showed the importance of measuring the complete profile for power
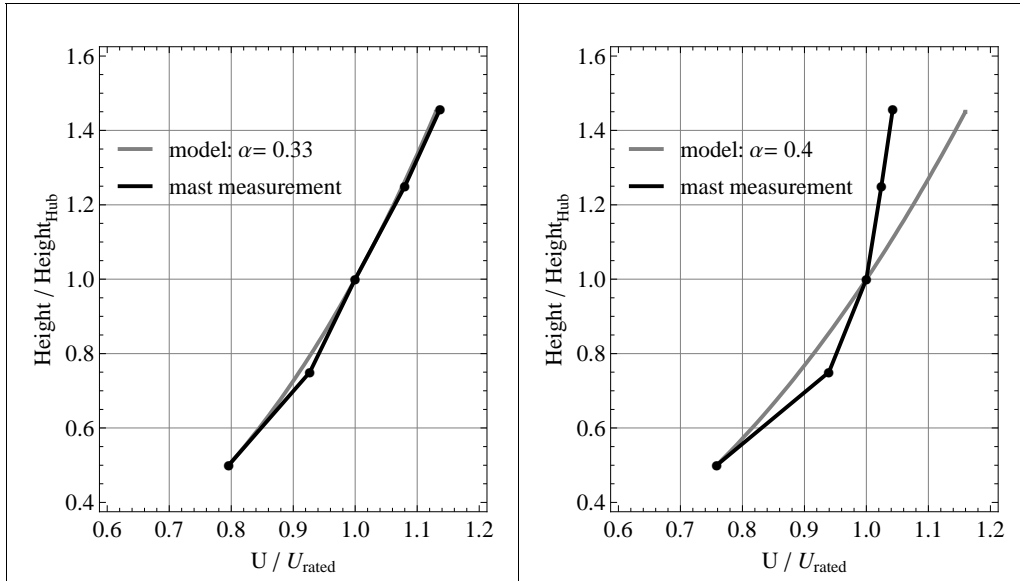
Figure 47. Two examples of profiles and their fit to the power law model (using the wind speed values at 40 and 80 m). The model fits very well the measured profile on the left, but it does not work for the profile on the right
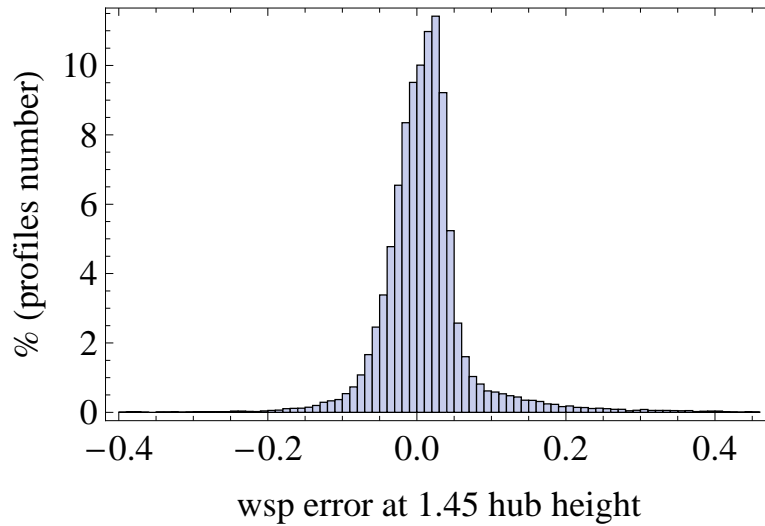

Figure 48. Distribution of the error made on the wind speed at 116.5 m height when assuming a power law profile with a shear exponent estimated with the wind speeds at 40 and 80 m

performance. In our experiment, the lidar measured the wind speed at 9 uniformly distributed heights covering 90% of the vertical rotor diameter. Each wind speed profile measured by the lidar was fitted to a power law profile in order to find the most representative shear exponent for this profile (α_{fit}). The fit is forced through the point of coordinate (u_{hub}, z_{hub}):

$$u_{fit}(z) = u_{hub} \left(\frac{z}{z_{hub}} \right)^{\alpha_{fit}}. \tag{104}$$

In order to separate the profiles for which the power law assumption was acceptable, we evaluated the goodness of fit with the residual sum of squares RSS, defined as:

$$\text{RSS} = \sum_i \left(u_{fit}(z_i) - u_i \right)^2, \tag{105}$$

where u_{fit} is the fit function defined in Eq. (104) and u_i the wind speed measured by the lidar at height z_i ($i = 1$ to 9). Figure 49 shows two examples of measured profiles with their shear exponents and RSSs.
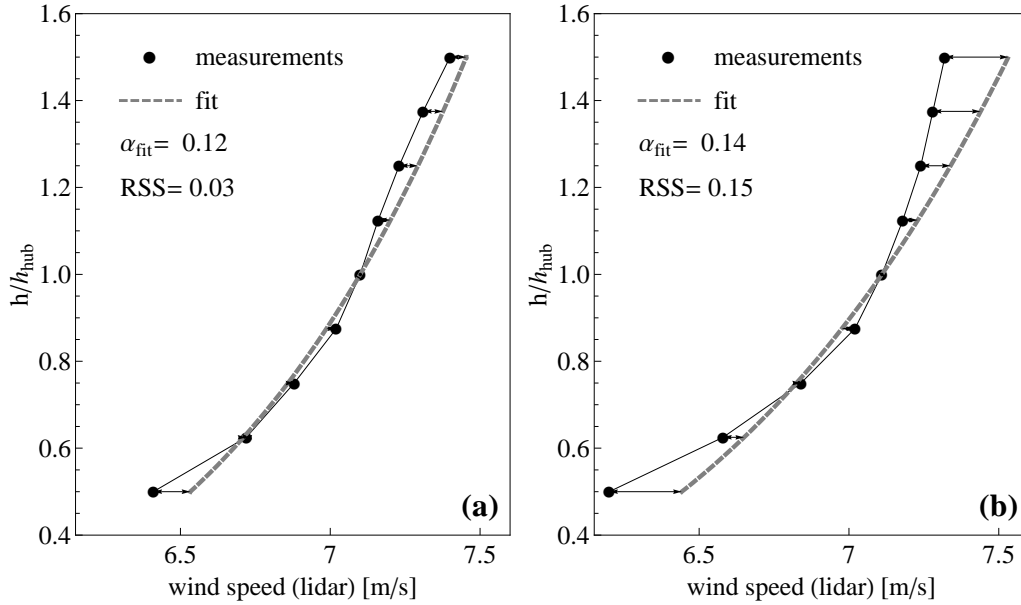

Figure 49. Example of measured wind profiles and their fit to a power law profile. (a) RSS ≤ 0.1, (b) RSS > 0.1

The profiles were then divided into two groups according to the RSS:

- Group 1: RSS ≤ 0.1 – the profiles from this group have a shape close to a power law profile and are referred to as the power law profiles.

- Group 2: RSS > 0.1 – the profiles from this group have a shape that cannot be well represented by a power law profile and are referred to as the non power law profiles.

According to this classification, profile (a) in Figure 49 would be in group 1 and profile (b) in group 2. The value of 0.1 was chosen here as threshold for the RSS, because it gave two groups of data showing two trends (shown below) while being statistically comparable (as they count similar numbers of data: 511 in group 1 and 396 in group 2). It is recognized that this threshold is somewhat arbitrary and should subsequently be "fine-tuned" using a large number of datasets.

5.4 Equivalent wind speed

Standard power curve for the two groups of wind profiles

Figure 50 shows the standard scatter plot of the power (a) and the C_p (b) as function of the wind speed at hub height. C_p is defined as in the current IEC standard 61400-12-1:

$$C_p = \frac{P}{0.5\rho u_{hub}^3 A},\qquad(106)$$

where P is the electrical power output of the turbine and A is the rotor swept area. The two colours represent the two groups of wind profiles: points obtained with the group 1 profiles (RSS ≤ 0.1) are displayed in black and those obtained with group 2 profiles (RSS > 0.1) are displayed in red.

Figures 50(a) and (b) show two trends (one for each group) leading to two mean power curves and C_p curves (obtained after binning the data into 0.5 m s^{-1} wind speed bins

and averaging as required by the IEC 614000-12-1 standard) (Figures 50(c) and (d)). The power output of the turbine for a given wind speed (at hub height) is smaller for data from group 2 (non power-law profiles) than for data from group 1 and the data from group 2 generally give a lower C_p.
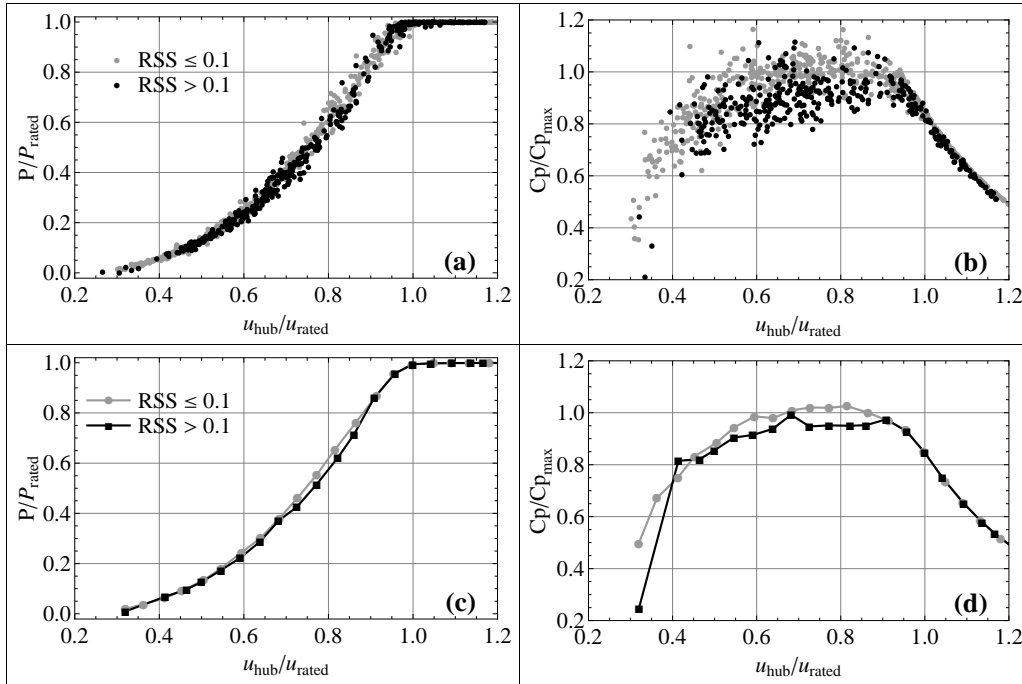

Figure 50. (a) Scatter plot of power curves, (b) Scatter plot of Cp curves, (c) Averaged power curves, (d) Averaged Cp curves. These plots are obtained by using the wind speed at hub height only and Cp calculated as in the IEC standards

What might appear here, for the non-power law profiles, as an underperformance of the wind turbine is an overestimation of the kinetic energy flux of the wind. Indeed, the C_p definition given by Eq. (106) implicitly assumes that the wind speed is constant over the entire rotor swept area:

$$u(z) = u_{hub} \qquad KE_{\text{hub}} = 0.5\rho u_{hub}^3 A, \qquad (107)$$

or, in other words, the wind speed shear is ignored.

A better approximation of the kinetic energy flux

However, as mentioned earlier, the real kinetic energy flux is obtained with Eq. (100). The kinetic energy flux for each profile measured by the lidar can be approximated by:

$$KE_{\text{profile}} = \sum_i 0.5\rho_i u_i^3 A_i, \qquad (108)$$

where u_i is the wind speed measured at the ith height in the profile and corrected for the air density and A_i is the area of the corresponding segment of the rotor swept area (see Figure 51).

The ratio $KE_{\text{profile}}/KE_{\text{hub}}$ is displayed in Figure 45. The profiles from group 1 (black points) follow rather well the analytical results showing a moderate error due to the constant wind profile assumption.

The non power-law profiles (group 2), on the other hand, do not follow the analytical curve and show a much larger difference between the two ways of evaluating the kinetic energy flux. The approximation of a constant wind speed over the whole rotor swept area
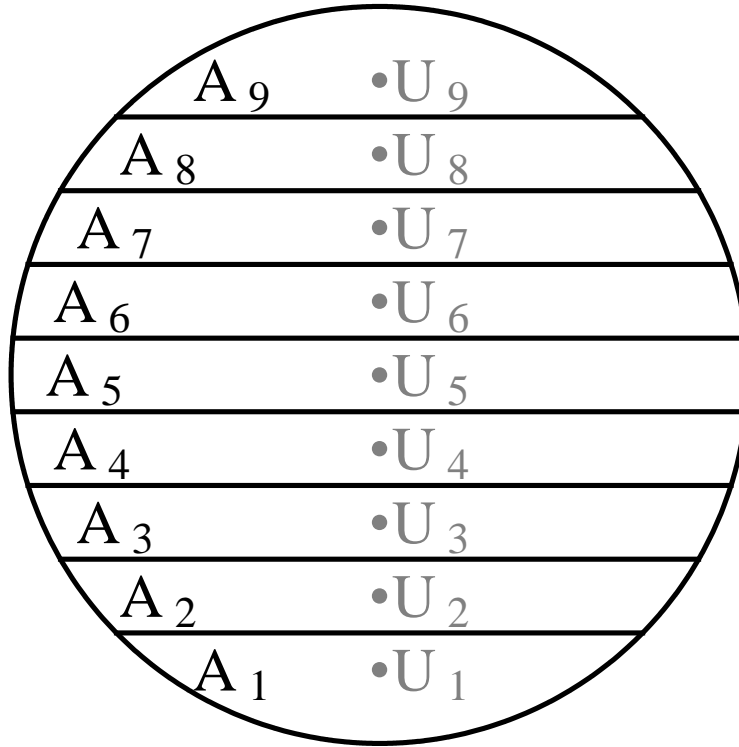
Figure 51. Rotor swept area divided into 9 segments corresponding to the 9 heights where lidar observations are performed. Each wind speed is assumed to be constant in each segment

overestimates the kinetic energy flux for most of the data of group 2 and underestimates it for a few of them.

Two wind speed profiles can have the same wind speed at hub height but different kinetic energy. In a standard power curve, such profiles would have the same abscissa (hub height wind speed), whereas they would almost certainly result in different power outputs. This is partially why the two groups of wind profiles give two different power curves. The kinetic energy flux overestimation has even more impact on C_p, explaining the lower C_p for the group 2 wind profiles compared to that for group 1.

Another contribution to the differences between the power curves in figure 50 can be the influence of the wind speed shear on the power output. Indeed, two wind profiles resulting in the same kinetic energy may give different turbine power output, because for some wind speed shear conditions (e.g a power law profile with a large shear exponent), the turbine is not able to extract as much energy as in other shear conditions (e.g. a constant profile).

Equivalent wind speed definition

Intuitively, the power output of the turbine should be more closely related to the kinetic energy flux derived from the whole profile than that derived from the wind speed at hub height. We should then consider the power output of the turbine as a function of the kinetic energy flux. In order to do so, an equivalent wind speed is suggested:

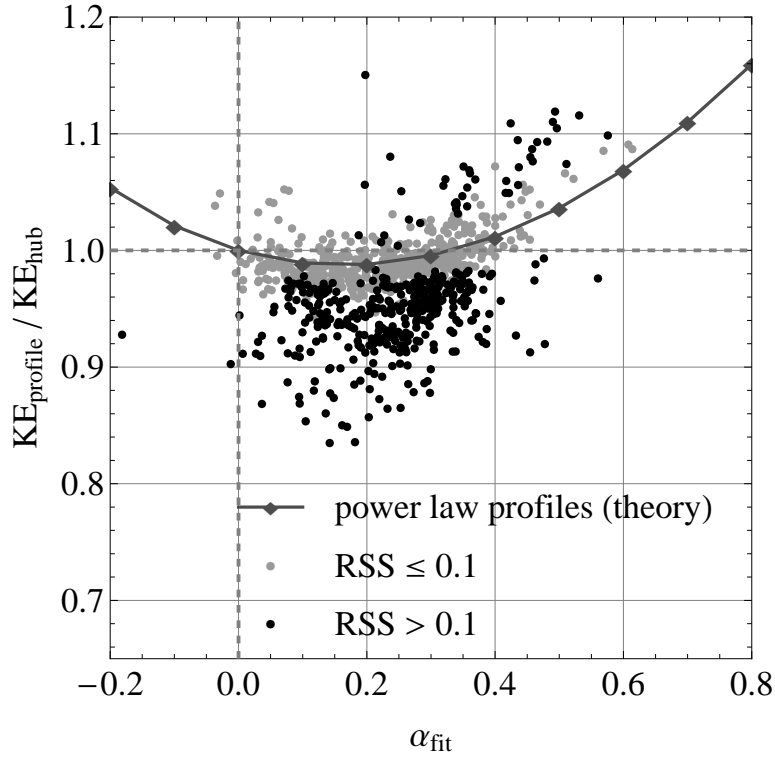$$u_{eq} = \left(\sum_i u_i^3 \frac{A_i}{A} \right)^{1/3}. \tag{109}$$

Figure 52. Ratio between the kinetic energy flux obtained with the wind speed profiles ($KE_{profile}$ for the theoretical and measured profiles) and the kinetic energy assuming a constant wind speed with height equal to the hub height wind speed (KE_{hub})

Then C_p becomes:

$$
\begin{aligned}
C_p &= \frac{P}{0.5\rho_0 u_{eq}^3 A} = \frac{P}{0.5\rho_0 \left(\sum_i \left(\left[\frac{\rho_i}{\rho_0}\right]^{1/3} u_i \right)^3 \frac{A_i}{A} \right) A} \\
&= \frac{P}{\sum_i 0.5\rho_i u_i^3 A_i} = \frac{P}{KE_{\text{profile}}}.
\end{aligned}
\tag{110}
$$

Figure 53 shows plots comparable to the plots in Figure 50: in Figure 53, the power and C_p are plotted as a function of the equivalent wind speed defined in Eq. (109) (instead of the wind speed at hub height in Figure 43) and C_p is calculated according to Eq. (110) (instead of Eq. (106) in Figure 50). In Figure 53, profiles from both groups follow the same trend. The mean power and C_p curves obtained with each group of points overlap each other. This shows that the difference in power curves between the two groups shown in Figure 53 was mainly due to the error in kinetic energy flux.

Choice of instrument

The question now is: can any remote sensing instrument be used to measure a power curve and reduce the scatter with the equivalent wind speed method? Figures 54(a) and (b) show the comparison of the simultaneous 10-min mean wind speed measured by a remote sensing instrument (sodar and lidar respectively), and a cup anemometer at the same height. The lidar and the sodar were placed next to each other but with a lateral distance of 100 m from a mast equipped with a top-mounted cup anemometer used for the comparisons. Both datasets include the same 10-min periods. It can be clearly seen that the sodar data are noisier than the lidar data. There was no indication of any major problem with the sodar during this experiment. The difference in measurements
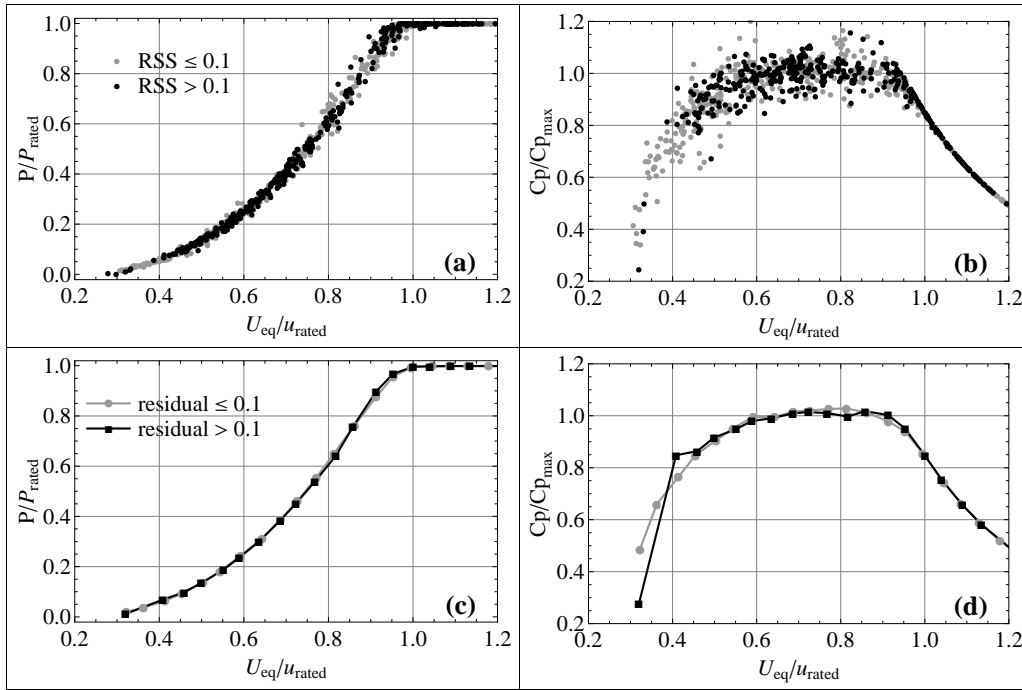
Figure 53. (a) Scatter plot of power curves, (b) Scatter plot of $C:p$ curves, (c) Averaged power curves, (d) Averaged C_p curves. These plots are obtained using the equivalent wind speed Eq. (109) and a C_p definition taking the wind shear into account

from the two instruments can be explained by the difference in the way they operate. Because sodar measurements are based on sound properties, they are sensitive to noise from the surroundings and obstacles (which is not the case for light beams). Moreover, the sampling frequency of a sodar is much smaller than that of a lidar. A sodar measures one wind speed every 10 min, whereas a lidar can measure the wind speed 30 to 100 times during that time.

The power curve obtained with such noisy measurements (at hub height) presents a much larger scatter than the power curve obtained with the cup anemometer (Figure 54(c)), whereas the scatter in power curve obtained with better remote sensing measurements is similar to that obtained with the cup anemometer (Figure 54(d)). If the remote sensing instrument increases the scatter in power curve compared to a cup anemometer, it is very unlikely that the observation of wind speed profiles from that same instrument can help to reduce the scatter. Thus, an instrument presenting noisy measurements is not suitable for power curve measurement and cannot be used to calculate an equivalent wind speed in order to reduce the scatter. This restricts very much the possibility of using sodar because of the inherent noise in the measurements. However, the point here is not to disqualify sodars, but to make the difference between an instrument which is suitable and one which is not suitable for the application of the equivalent wind speed method.

Figure 55 shows a lidar cup comparison for two lidar systems (same brand, same test location). Even though the gain factor and the coefficient of determination (R^2) is good for both instruments, a clear difference appears when we look at the lidar error (i.e. difference between wind speed measured by the lidar and the cup). Lidars are very attractive because of their capacity to measure wind speed and direction profiles with the convenience of a ground based measurement device. However, this is still a new and rather immature technology and it is strongly recommended to verify each instrument against a tall mast (equipped with good wind speed sensors at several heights) in flat terrain. A remote sensing classification and a verification procedure are currently being defined within the standard committee.
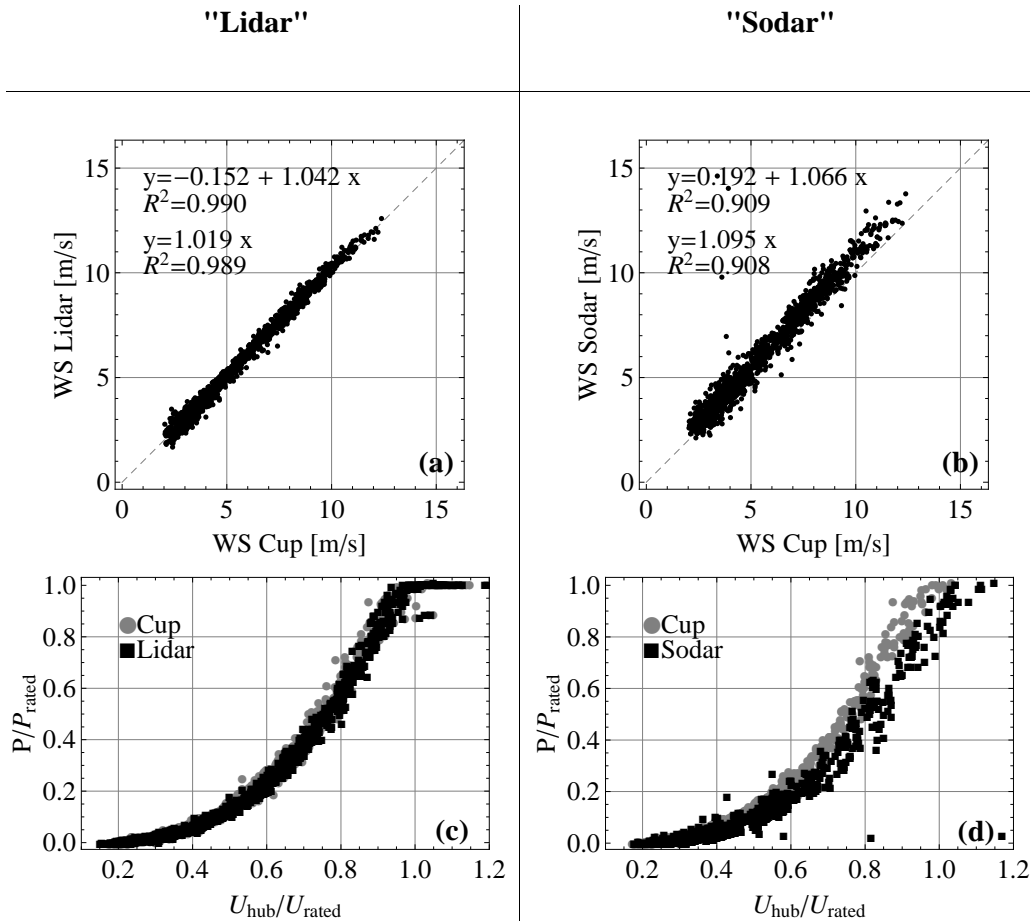
Figure 54. (a) Linear regression of 10-min mean wind speed measured by a lidar and a cup anemometer; (b) Linear regression of 10-min mean wind speed measured by a sodar and the same cup anemometer as in (a) for the same 10-min periods; (c) power curve obtained with wind speed measurement at hub height with a cup and a lidar; (d) power curve obtained with wind speed measurement at hub height with a sodar and the same cup anemometer as in (c) for the same 10-min periods

5.5 Summary

As wind speed shear influences the power performance of multi-MW turbines, it is necessary to characterize the wind speed profile in front of the turbine rotor. Remote sensing instruments are of great interest, since they can measure the wind speed profile over the whole rotor range. Such measurements avoid the use of assumptions about the shape of the wind speed profile. A more accurate kinetic energy flux can then be calculated resulting in a better evaluation of the power performance of the turbine. The use of an equivalent wind speed taking the wind speed shear into account reduces the scatter in the power curve and the uncertainty in power performance measurement. In that sense, the use of remote sensing measurements can improve the power performance measurements. However, this can only be achieved with a good instrument. Finally, the remote sensing instrument should not show more scatter in the power curve than that of a cup at a given height. This requires a verification of the instrument prior to the power performance measurement.
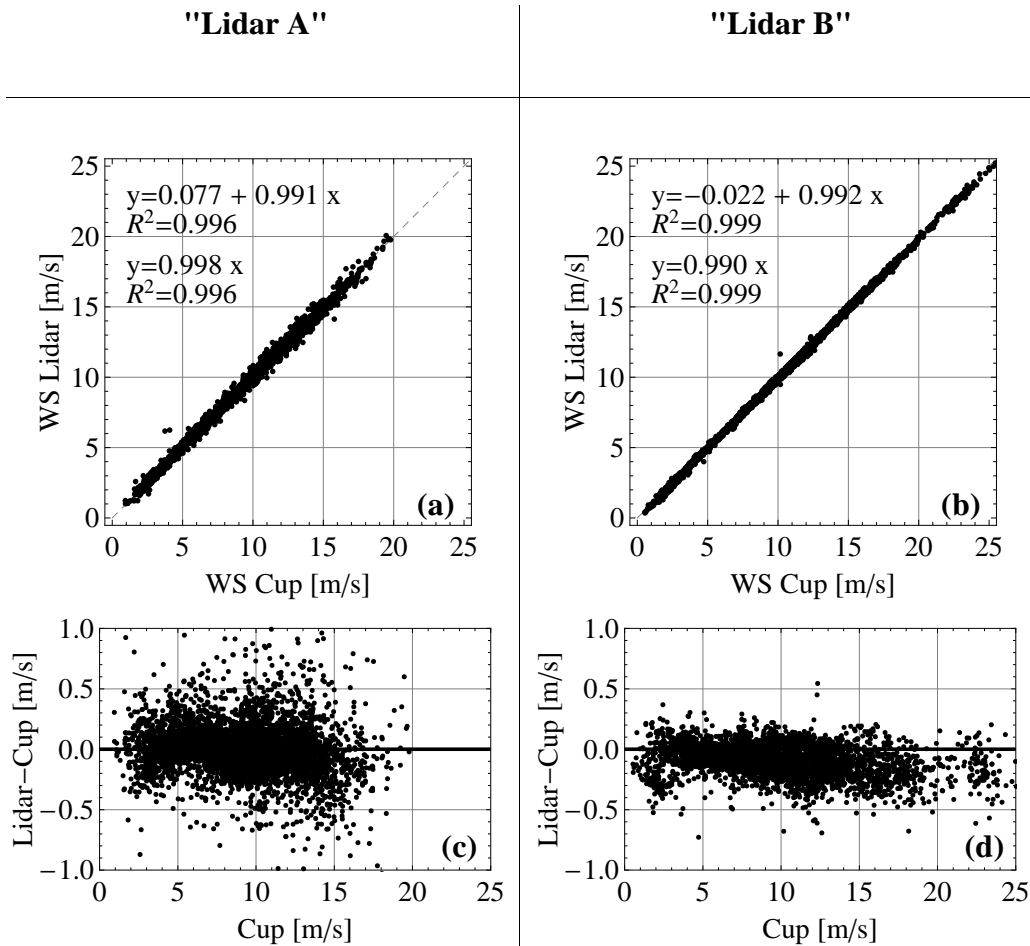
Figure 55. (a and b) Linear regression of 10-min mean wind speeds measured by a lidar and a cup anemometer from two lidar systems; (c and d) lidar error for each system

Notation

A	rotor swept area
A_i	area of the ith element
c	chord defined by the rotor swept area
C_p	power coefficient
dF_D	local drag force
dF_L	local lift force
dF_T	local tangential force
KE_{hub}	kinetic energy flux of a constant wind profile
KE_{profile}	kinetic energy flux of the wind profile
P	electrical power output of the turbine
r	radial position
r_Ω	blade speed
R	coefficient of determination
R	rotor radius
RSS	residual sum of squares
u	wind speed
u_{eq}	equivalent wind speed
u_{fit}	fit wind speed function to the power profile
u_{hub}	hub height wind speed
u_i	wind speed at height z_i
w	relative wind speed
z	height above the ground
z_{hub}	hub height
z_i	lidar height
α	shear exponent of the power law

α_{fit} shear exponent fit
θ azimuth angle
ρ air density
ϕ angle of attack

References

Antoniou I. (2009) Wind shear and uncertainties in power curve measurement and wind resources. *WindPower*

Elliot D. L. and Cadogan J. B. (1990) Effects of wind shear and turbulence on wind turbine power curve. *Proc. of the European Community Wind Energy Conf.*, Madrid

IEC (2005) IEC 61400-12-1 Wind turbines - Power performance measurements of electricity producing wind turbines. Int. Electrotechnical Commission

Manwell J. F., McGowan J. G., and Rogers A. L. (2002) Wind energy explained: Theory, design and application, John Wiley & Sons Ltd, 577 pp

Sumner J. and Masson C. (2006) Influence of atmospheric stability on wind turbine power performace curves. *J. Solar Energy Eng.* **128**:531–538

Wagner R., Antoniou I., Pedersen S. M., Courtney M., and Jørgensen H. E. (2009) The influence of the wind speed profile on wind turbine performance measurements. *Wind Energy* **12**:348–362

6 Lidars and wind profiles

Alfredo Peña
Wind Energy Division, Risø DTU, Roskilde, Denmark

6.1 Introduction

Wind lidars have been able to observe wind profiles since the beginning of their commercialization in 2005.[6] The ZephIR continuous wave (cw) lidar, nowadays manufactured by Natural Power, entered the wind energy community to compete with the traditional instrumentation, such as cup anemometers and wind vanes, offering in advantage the measurement of wind speed and direction profiles up to 200 m above ground level (AGL), avoiding the flow distortion effects that the traditional instruments suffer when they are mounted on structures. The performance of the ZephIR, when compared with cup anemometers at several heights up to about 100 m, showed high agreement from first studies over land (Smith et al., 2006) and over the sea (Kindler et al., 2007).[7]

Later, observations from cup anemometers were combined with ZephIR measurements at the Nysted (Antoniou et al., 2006) and at the Horns Rev (Peña et al., 2009) offshore wind farms to reproduce wind profiles up to about 160 m above mean sea level (AMSL). Although the results from the campaign at Horns Rev showed good agreement with the wind profile theory, limitations on the measurement range were found due to the contamination of the lidar's Doppler spectra by clouds, which gave the opportunity to Natural Power to improve the cloud correction algorithms of the ZephIR.

Since we are interested in wind profile retrieval within 30–200 m where large wind turbines operate, cloud contamination is a serious concern. In fact, when this issue was first addressed, the role of the aerosol profile on the lidar's probe volume (for any kind of lidar) became more important, specially since the expertise on this subject is rather limited. Mist and fog have also been realized as serious hazards for cws lidars (Courtney M., 2009, personal communication), which for wind profile analysis results in high wind shears close to the ground,[8] i.e. that–for example, neutral wind profiles might be interpreted as stable.

Nowadays, the Windcube and Galion pulsed lidars, from the companies LeoSphere and Sgurr Energy, respectively, are also in the market. Both lidars offer instantaneous wind profile observation up to about 2000 m, but the instruments' range actually depends on the atmospheric conditions, namely on the amount of aerosols in the atmosphere, which is proportional to the signal-to-noise ratio (SNR).

As with the ZephIR, a number of campaigns combining observations from cup and sonic anemometers at high meteorological masts and from pulsed lidars have started. Peña et al. (2010b) described the neutral wind profile and Peña et al. (2010a) the diabatic wind profile, both for homogenous and flat terrain up to 300 m AGL, both using the Windcube to extend wind speed observations from traditional meteorological instrumentation at the National Test Station for Large Wind Turbines (NTWT) at Høvsøre, Denmark.

Other meteorological campaigns are envisioned for the description of the wind profile up to 500 m (Gryning S.-E., 2009, personal communication), which will not only help for increasing the accuracy in wind power calculations, but also for the improvement of the parameterizations used in boundary-layer meteorology.

---

[6] By wind profile, it is meant the horizontal wind speed profile

[7] High agreement refers to 1 : 1 comparisons of wind velocity observations with correlation coefficients close to 1

[8] By wind shear, it is meant the vertical wind shear

6.2 Wind profile theory

Mixing-length theory, firstly introduced by Prandtl (1932) for the description of atmospheric flow, is here chosen for the analysis of the wind profile. The local wind shear $\partial U/\partial z$, where U is the mean horizontal wind sped and z the height above the ground, is parameterized as

$$\frac{\partial U}{\partial z} = \frac{u_*}{l} \tag{111}$$

where u_* is the local friction velocity and l is the local mixing length.

Surface layer

In the surface layer, which covers the first 5–10% of the atmospheric boundary layer (ABL), the mixing length l_{SL} is given as

$$l_{SL} = \kappa z \phi_m \tag{112}$$

where κ is the von Kármán constant (≈ 0.4) and ϕ_m the dimensionless wind shear from Monin-Obukhov similarity theory (MOST) (Monin and Obukhov, 1954), which is defined as

$$\phi_m = \frac{\kappa z}{u_{*o}} \frac{\partial U}{\partial z} \tag{113}$$

where u_{*o} is the surface-layer friction velocity (u_* is rather constant in the surface layer). Several experiments have suggested expressions for the behaviour of ϕ_m with stability, which have resulted in the so-called flux-profile relationships. For unstable and stable conditions, respectively, these are given as

$$\phi_m = (1 - az/L)^p \qquad \text{and} \tag{114}$$

$$\phi_m = 1 + bz/L \tag{115}$$

where a, b, and p are empirical constants (Businger et al. 1971; Högström 1988) and L is the Obukhov length estimated as

$$L = -\frac{u_{*o}{}^3 T_o}{\kappa g \overline{w'\Theta_v'}_o} \tag{116}$$

where T_o is the mean surface-layer temperature, g is the gravitational acceleration, and $\overline{w'\Theta_v'}_o$ is the surface-layer kinematic virtual heat flux. Assuming $u_* = u_{*o}$ and $l = l_{SL}$ in Eq. (111), and combining it with Eqs. (112) and (113), the integration with height of Eq. (111) gives the surface-layer wind profile,

$$\frac{U}{u_{*o}} = \frac{1}{\kappa} \left[\ln\left(\frac{z}{z_o}\right) - \psi_m \right] \tag{117}$$

where z_o is the surface roughness length and ψ_m is the diabatic correction of the wind profile, which is derived from the integration with the dimensionless stability parameter z/L of ϕ_m in Eqs. (114) and (115) (Stull, 1988). For neutral conditions, which are favorable for wind energy due to high wind speed characteristics, $\phi_m = 1$ and $\psi_m = 0$, thus resulting in the well-known logarithmic wind profile.

Figure 56 illustrates the average dimensionless wind profiles observed for different stability conditions over flat and homogenous terrain at Høvsøre, Denmark. Each average wind profile is computed by classifying the individual 10-min wind profiles into stability classes, based on the Obukhov length as performed in Gryning et al. (2007) and Peña et al. (2010a). As shown in the figure, Eq. (117) fits well the observations in the surface layer and the observations start to departure from the surface-layer wind profile at about 100 m for near-neutral conditions and 60 m for very stable conditions. The roughness length is estimated fitting Eq. (117) to the first observational height only.

With such dimensionless x-axis, the wind profile is a function of roughness length and stability only. In the surface layer and over flat and homogenous land, Eq. (117)
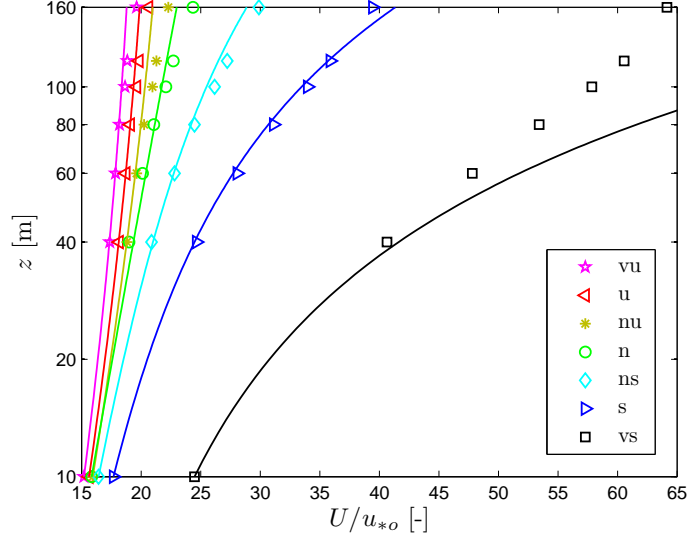
Figure 56. Wind profiles observed for different stability classes at Høvsøre, Denmark. The markers indicate the observations and the solid lines the predictions using Eq. (117). Legend: vu (very unstable), u (unstable), nu (near unstable), n (neutral), ns (near stable), s (stable), and vs (very stable).

generally fits well the average observations and the wind profile can easily be studied using such dimensionless fashion, because z_o does not vary significantly. The standard error for the observations in Fig. 56 increases with height, indicating that other external parameters, such as the boundary-layer height z_i, start to play a more important role for the description of the wind profile. However, even for the observations at 160 m, the highest standard error is 0.35, i.e. the individual wind profiles concentrate close to the average.

Marine surface layer

Over water, the roughness length is not constant and depends, among others, on wind stress, waves, and fetch. The scaling U/u_{*o} is appropriate for the surface-layer wind profile for constant z_o values. Using the simple parameterization of Charnock (1955),

$$z_o = \alpha_c \frac{u_{*o}^2}{g} \tag{118}$$

where α_c is the Charnock's parameter (≈ 0.012), it is straightforward to realize that the scaling U/u_{*o} produces wind profiles that do not converge onto a straight line. Peña and Gryning (2008) analyzed this issue and suggested the following scaling for the marine wind profile,

$$\frac{U}{u_{*o}} + \frac{1}{\kappa} \ln \left[1 + 2\frac{\Delta u_{*o}}{\overline{u_{*o}}} + \left(\frac{\Delta u_{*o}}{\overline{u_{*o}}} \right)^2 \right] = \frac{1}{\kappa} \left[\ln \left(\frac{z}{\overline{z_o}} \right) - \psi_m \right] \tag{119}$$

where $\Delta u_{*o} = u_{*o} - \overline{u_{*o}}$, i.e. Δu_{*o} is a *fluctuating* surface-layer friction velocity equal to the difference between the observation u_{*o} and the ensemble average $\overline{u_{*o}}$. $\overline{z_o}$ is a mean roughness length parameterized as Eq. (118), but replacing u_{*o} with the ensemble average $\overline{u_{*o}}$. Eq. (119) differs from Eq. (117), because it adds a dimensionless wind speed, the left term in square brackets in Eq. (119), which allows the wind profiles to converge onto a straight line for the same stability class. It also uses a mean roughness length, which allows for an empirical estimation of the Charnock's parameter.

Boundary layer

The surface-layer wind profile was previously derived from the assumption that the length scale grows infinitively with height. At about 100 m AGL and neutral conditions–for example, this assumption is not longer valid. The IEC (2005) standard suggests to use surface-layer scaling for the length scale up to 60 m AGL and to assume a constant length scale upwards.

There has been a number of suggestions for the behaviour with height of the mixing length in the ABL, which departure from Eq. (112). Blackadar (1962) and Panofsky (1973) limited the growth of the length scale and proposed neutral mixing-length models, which were used to numerically compute the ABL wind profile. Lettau (1962) proposed a similar model to that of Blackadar (1962), but in which the length scale starts to decrease slowly beyond the surface layer. Gryning et al. (2007) proposed a mixing-length model, which assumes that the top of the boundary layer acts as the ground, and therefore, the length scale has a zero value at the top of the ABL. Based on the length-scale behaviour observed from turbulence measurements far beyond the surface layer, as shown in Caughey and Palmer (1979), and the close relation between the length scale of the wind profile and that derived from turbulence measurements as observed in Peña et al. (2010b), the idea of a decreasing mixing-length with height is rather reasonable.

Simple analytical models for the ABL wind profile can be derived, using such *limiting* mixing-length models and a model for the local friction velocity, by integrating with height Eq. (111). This was performed by Gryning et al. (2007) and Peña et al. (2010a) for the diabatic flow over flat land and homogeneous terrain, Peña et al. (2008) for diabatic flow over the sea, and Peña et al. (2010b) for neutral flow over flat and homogeneous land. The main results of the comparison of these models and wind speed observations at great heights at Høvsøre and at the Horns Rev wind farm are presented in the following section.

6.3 Comparison with observations at great heights

Marine observations

Marine wind speed observations from combined cup anemometer and ZephIR measurements up to 161 m AMSL, within a sector where the upstream flow is free and homogeneous at the Horns Rev wind farm, were compared to wind profile models in Peña et al. (2008) showing good agreement. The neutral and unstable wind profile models are identical to those traditionally used for the surface layer, Eq. (117), although the physics involved in their derivation are different. For the stable wind profile, a correction is applied to the stability parameter to take into account the boundary-layer height, z_i:

$$\frac{U}{u_{*o}} = \frac{1}{\kappa} \left[\ln\left(\frac{z}{z_o}\right) - \psi_m\left(1 - \frac{z}{2z_i}\right) \right].$$ (120)

Figure 57 illustrates the results using the scaling proposed in Peña and Gryning (2008), which can be used for wind profile comparison whenever the wind speed can be scaled with the friction velocity.

The stable boundary-layer height was estimated in Peña et al. (2008) by use of the Rossby and Montgomery (1935) formula,

$$z_i = C\frac{u_{*o}}{|f_c|}$$ (121)

where C is a proportionality parameter (≈ 0.15) and f_c is the Coriolis parameter. Eq. (121) is valid for neutral conditions only, thus, the buoyancy contribution was accounted for in stable conditions by decreasing the value of C.

Neutral observations over flat land

Near-neutral wind speed observations from combined cup anemometer and Windcube measurements up to 300 m AGL, within an homogenous upwind sector at Høvsøre, were
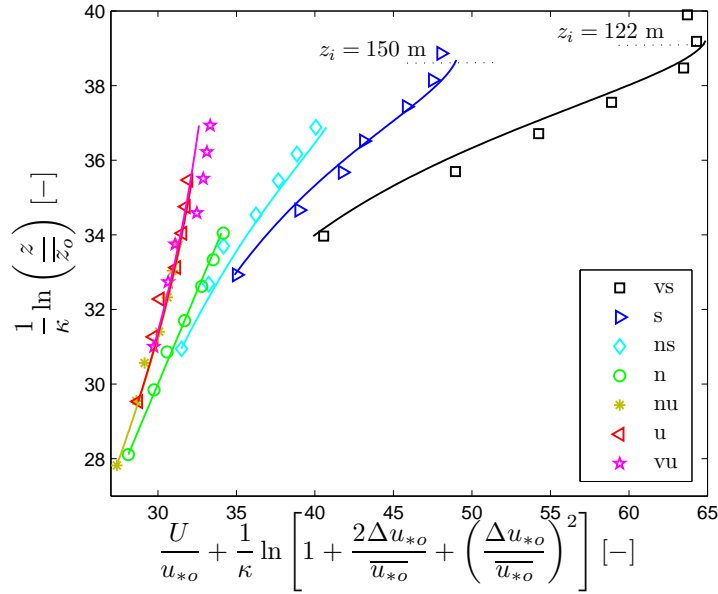
Figure 57. Wind profiles for different stability classes from combined lidar/cup anemome-ter observations at the Horns Rev wind farm in Denmark. The markers indicate the observations and the solid lines the predictions using Eq. (117) for unstable and neu-tral conditions and Eq. (120) for stable conditions. The boundary-layer height z_i is also indicated. Legend as in Fig. (56).

compared in Peña et al. (2010b) to a set of neutral wind profile models:

$$U = \frac{u_{*o}}{\kappa} \ln \left(\frac{z}{z_o} \right), \tag{122}$$

$$U = \frac{u_{*o}}{\kappa} \left[\ln \left(\frac{z}{z_o} \right) + \frac{1}{d} \left(\frac{\kappa z}{\eta} \right)^d - \left(\frac{1}{1+d} \right) \frac{z}{z_i} \left(\frac{\kappa z}{\eta} \right)^d - \frac{z}{z_i} \right], \tag{123}$$

$$U = \frac{u_{*o}}{\kappa} \left[\ln \left(\frac{\sinh \left(\kappa z/\eta \right)}{\sinh \left(\kappa z_o/\eta \right)} \right) - \frac{z}{z_i} \frac{\kappa z}{2\eta} \right], \tag{124}$$

$$U = \frac{u_{*o}}{\kappa} \left[\ln \left(\frac{z}{z_o} \right) + \frac{z}{l_{MBL}} - \frac{z}{z_i} \left(\frac{z}{2l_{MBL}} \right) \right], \tag{125}$$

which correspond to the logarithmic wind profile, a simple analytical solution for the wind profile from the mixing-length model of Blackadar (1962) ($d = 1$) and Lettau (1962) ($d = 5/4$), another simple solution using the mixing-length model of Panofsky (1973), and the wind profile model of Gryning et al. (2007), respectively. d is a parameter that controls the growth of the length scale, η is the limiting value for the length scale in the upper atmosphere, and l_{MBL} is a middle boundary-layer length scale.

η has traditionally been parameterized as,

$$\eta = D \frac{u_{*o}}{|f_c|} \tag{126}$$

where Blackadar (1965) suggested $D = 63 \times 10^{-4}$ and from the analysis of Lettau (1962) and assuming Ro $= 5.13 \times 10^5$, where Ro is the surface Rossby number, $D = 96 \times 10^{-4}$. In this fashion, when combining Eq. (127) with Eqs. (122)–(125), the ratio $u_{*o}/|f_c|$ in can be replaced by z_i/C from Eq. (121). l_{MBL} was parameterized by Gryning et al. (2007) as

$$l_{MBL} = \frac{u_{*o}/|f_c|}{-2 \ln \left(\frac{u_{*o}}{|f_c|z_o} \right) + 55}. \tag{127}$$
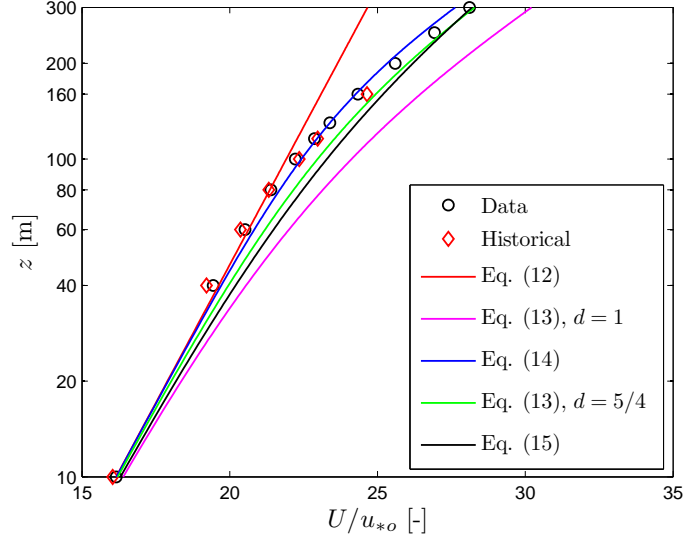
Figure 58. Neutral wind profile observed at Høvsøre, Denmark. The markers indicate combined lidar/cup anemometer observations (Data) and the mean wind profile from about 3 years of cup anemometer observations (Historical). The solid lines indicate the predictions using $C = 0.15$, $D = 73 \times 10^{-4}$, 58×10^{-4}, and 100×10^{-4} for Eq. (123) with $d = 1$, Eq. (124), and Eq. (123) with $d = 5/4$, respectively.

The results of the comparison are illustrated in Figure 58. The models, which limit the growth of the length scale, have a better agreement with the wind speed observations beyond the surface layer (≈ 80 m). The logarithmic wind profile fits well the measurements within the surface layer only.

Diabatic observations over flat land

Wind speed observations from combined cup anemometer and Windcube measurements up to 300 m AGL, within an homogenous upwind sector and for different stability conditions at Høvsøre, were compared in Peña et al. (2010a) to a set of diabatic wind profile models. These models were derived by extending the surface-layer length scale of the mixing-length models of Blackadar (1962), Lettau (1962), and Gryning et al. (2007) to account for atmospheric stability using MOST. For example, using the extended mixing-length models of Blackadar (1962) and Lettau (1962), the wind profile is given as,

$$ U = \frac{u_{*o}}{\kappa} \left[\ln\left(\frac{z}{z_o}\right) - \psi_m + \frac{1}{d}\left(\frac{\kappa z}{\eta}\right)^d - \left(\frac{1}{1+d}\right)\frac{z}{z_i}\left(\frac{\kappa z}{\eta}\right)^d - \frac{z}{z_i} \right], \qquad (128) $$

$$ U = \frac{u_{*o}}{\kappa} \left[\ln\left(\frac{z}{z_o}\right) + b\frac{z}{L}\left(1 - \frac{z}{2z_i}\right) + \frac{1}{d}\left(\frac{\kappa z}{\eta}\right)^d - \left(\frac{1}{1+d}\right)\frac{z}{z_i}\left(\frac{\kappa z}{\eta}\right)^d - \frac{z}{z_i} \right] \qquad (129) $$

for unstable and stable conditions, respectively.

η was parameterized in Peña et al. (2010a) using Rossby-number similarity as,

$$ \eta = \frac{\kappa z_i}{[d(1+d)]^{1/d}} \left[\left(\left[\ln\left(\frac{u_{*o}}{f_c z_o}\right) - A\right]^2 + B^2 \right)^{1/2} + 1 - \ln\left(\frac{z_i}{z_o}\right) \right]^{-1/d} \qquad (130) $$

where A and B are the integration constants for a given stability from the resistant laws. A similar paramaterization is found in Gryning et al. (2007) for l_{MBL}. z_i was estimated from Eq. (121) for neutral and stable conditions, and from observations of the aerosol backscatter coefficient from a Vaisala CL31 ceilometer for unstable conditions. Figure
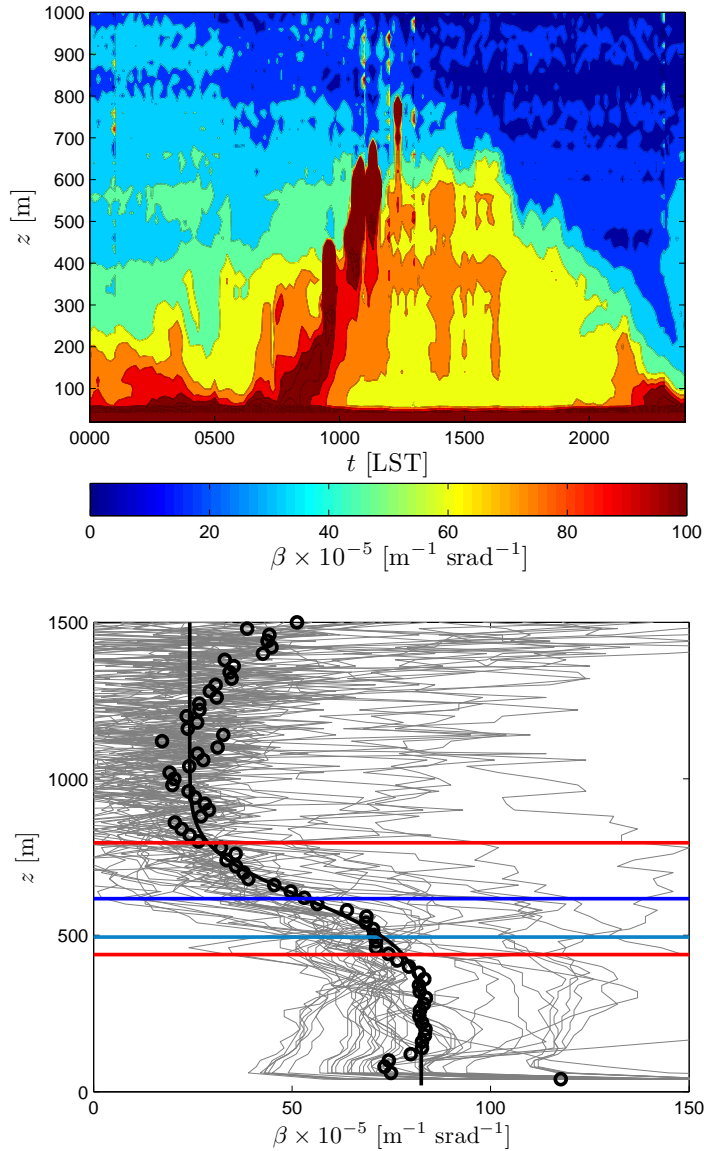
Figure 59. Top frame: Ceilometer observations of the aerosol backscatter coefficient β during a convective day at Høvsøre, Denmark. Bottom frame: Aerosol backscatter profile from ceilometer measurements at Høvsøre for neutral conditions. The gray lines show the aerosol profiles, the markers the average aerosol profile, the black line the fit function from Steyn et al. (1999), and the horizontal lines the estimation of z_i from the fit function (blue), the entrainment zone depth (red lines), and the estimation of z_i from Eq. (121) (cyan).

59 (top frame) illustrates the behaviour of the aerosol backscatter coefficient, β, during a day where most of the unstable profiles were measured. It is observed that during daylight time (1000–1800 LST), the aerosols reached 600–700 m marking the height of the unstable boundary layer. In Peña et al. (2010a), aerosol backscatter profiles observed simultaneously with the wind profiles for each stability class are used to estimate the boundary-layer height. The results for the neutral stability class are illustrated in Figure 59 (bottom frame). z_i is estimated using the modified error function suggested by Steyn et al. (1999) and a good agreement was found when compared to the estimation from Eq. (121) for neutral conditions.

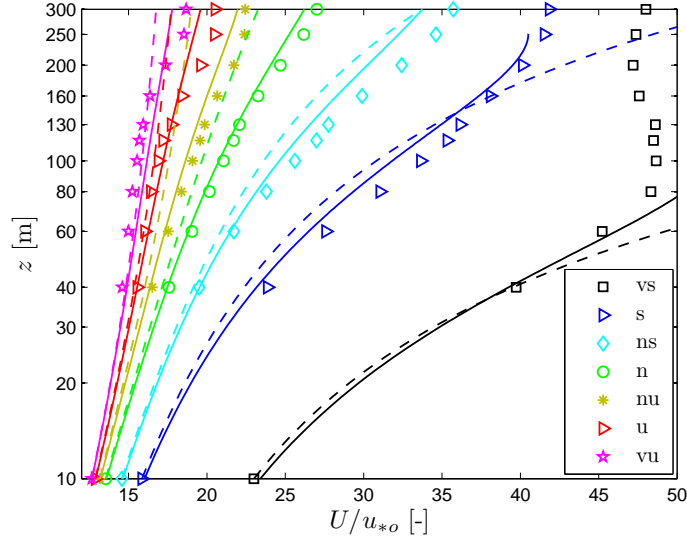Once η and z_i are estimated, the wind speed observations can be compared to the

Figure 60. Wind profiles observed for different stability classes at Høvsøre, Denmark. The markers indicate the combined lidar/cup anemometer observations, the solid lines the predictions using Eqs. (128) and (129) with $d = 5/4$, and the dashed lines the predictions from Eq. (117). Legend as in Fig. 56.

models. Figure 60 illustrates the comparison of the models in Eqs. (128) and (129) with $d = 5/4$, the surface-layer wind profile, Eq. (117), and the wind speed observations for the number of stability classes also used in Figures 56 and 57. As with the neutral observations, surface-layer scaling fits well the observations within the surface layer only. The wind profile model, which limits the value of the length scale, corrects for the departures of the observations beyond the surface layer. Similar results were obtained in Peña et al. (2010a) using Eqs. (128) and (129) with $d = 1$ and the wind profile models in Gryning et al. (2007).

6.4   Summary

- The use of ground-based remote sensing instruments has been useful for the study and description of the wind profile in and beyond the surface layer and for the improvement of the models that are traditionally used in wind power and boundary-layer meteorology.

- Over flat land and homogenous terrain and over the sea, the surface-layer wind profile fits well the observations for a wide range of atmospheric stability conditions within the surface layer only. For the analysis of wind profiles over water, however, a new scaling should be added in order to account for the variable roughness length.

- Wind speed observations from combined lidar/cup anemometer measurements up to 160 m AMSL at the Horns Rev offshore wind farm are well predicted by wind profile models that limit the value of the length scale, as suggested by Gryning et al. (2007), where the boundary-layer height becomes an important parameter, particularly for stable conditions.

- Near-neutral wind speed observations from combined lidar/cup anemometer measurements up to 300 m AGL at Høvsøre, Denmark, departure from the logarithmic wind profile beyond the surface layer. Simple analytical models, which limit the value of the length scale, predict such departure and fit well the observations.

- Wind profile models, extended for diabatic conditions, are compared to wind speed observations from combined lidar/cup anemometer measurements up to 300 m AGL at Høvsøre, Denmark, for a number of stability conditions. The models, which also limit the growth of the length scale, agree better with the observations compared to the surface-layer wind profile, which under- and over-predicts the wind speed beyond the surface layer. The models also depend on the boundary-layer height, which is estimated under neutral and stable conditions using surface-layer turbulence measurements and under unstable conditions using ceilometer observations of the aerosol backscatter profile.

Notation

a	parameter for the convective dimensionless wind shear
A	integration constant for a given stability from the resistant laws
ABL	atmospheric boundary layer
AGL	above ground level
AMSL	above mean sea level
b	parameter for the stable dimensionless wind shear
B	integration constant for a given stability from the resistant laws
cw	continuous wave
C	proportionality constant for the boundary-layer height
d	parameter for the control of the length scale
D	proportionality parameter for the limiting length scale
f_c	Coriolis parameter
g	gravitational acceleration
l	local mixing length
l_{MBL}	middle boundary-layer length scale
l_{SL}	surface-layer mixing length
L	Obukhov length
LST	local standard time
MOST	Monin-Obukhov similarity theory
NTWT	National Test Station for Large Wind Turbines
p	parameter for the convective dimensionless wind shear
Ro	surface Rossby number
SNR	signal-to-noise ratio
T_o	mean surface-layer temperature
u_*	local friction velocity
u_{*o}	surface-layer friction velocity
$\overline{u_{*o}}$	average surface-layer friction velocity
U	horizontal mean wind speed
$\overline{w'\Theta_v'}_o$	surface-layer kinematic virtual heat flux
z	height above the ground or above mean sea level
z_i	boundary-layer height
z_o	surface roughness length
$\overline{z_o}$	mean surface roughness length
α_c	Charnock's parameter
β	aerosol backscatter coefficient
Δu_{*o}	fluctuating surface-layer friction velocity
η	limiting value for the length scale
κ	von Kármán constant
ϕ_m	dimensionless wind shear
ψ_m	diabatic correction of the wind profile
∂	partial derivative

References

Antoniou I., Jørgensen H. E., Mikkelsen T., Frandsen S., Barthelmie R., Perstrup C., and Hurtig M. (2006) Offshore wind profile measurements from remote sensing instruments. *Proc. of the European Wind Energy Conf.*, Athens

Blackadar A. K. (1962) The vertical distribution of wind and turbulent exchange in a neutral atmosphere. *J. Geophys. Res.* **67**:3095–3102

Blackadar A. K. (1965) A Single-layer theory of the vertical distribution of wind in a baroclinic neutral atmospheric boundary layer. In: Flux of heat and momentum in the planetary boundary layer of the atmosphere. AFCRL-65-531, The Pennsylvania State University, 1–22

Businger J. A., Wyngaard J. C., Izumi Y., and Bradley E. F. (1971) Flux-profile relationships in the atmospheric surface layer. *J. Atmos. Sci.* **28**:181–189

Caughey S. J. and Palmer S. G. (1979) Some aspects of turbulence structure through the depth of the convective boundary layer. *Quart. J. Roy. Meteor. Soc.* **105**:811–827

Charnock H. (1955) Wind stress over a water surface. *Quart. J. Roy. Meteorol. Soc.* **81**:639–640

Gryning S.-E., Batchvarova E., Brümmer B., Jørgensen H., and Larsen S. (2007) On the extension of the wind profile over homogeneous terrain beyond the surface layer. *Bound.-Layer Meteorol.* **124**:251–268

Högström U. (1988) Non-dimensional wind and temperature profiles in the atmospheric surface layer: a re-evaluation. *Bound.-Layer Meteorol.* **42**:55–78

IEC (2005) IEC 61400-12-1 Wind turbines - Design requirements. Int. Electrotechnical Commission

Kindler D., Oldroyd A., MacAskill A., and Finch D. (2007) An eight month test campaign of the QinetiQ ZephIR system: Preliminary results. *Meteorol. Z.* **16**:479–489

Lettau H. H. (1962) Theoretical wind spirals in the boundary layer of a barotropic atmosphere. *Beitr. Phys. Atmos.* **35**:195–212

Monin A. S. and Obukhov A. M. (1954) Osnovnye zakonomernosti turbulentnogo peremeshivanija v prizemnom sloe atmosfery (Basic laws of turbulent mixing in the atmosphere near the ground). *Trudy Geofiz. Inst. AN SSSR* **24**(151):163–187

Panofsky H. A. (1973) Tower Micrometeorogy. Haugen D. A. (Ed.) Workshop on Micrometeorolgy. American Meteorology Society, 151–176

Peña A. and Gryning S.-E. (2008) Charnock's roughness length model and non-dimensional wind profiles over the sea. *Bound.-Layer Meteorol.* **128**:191–203

Peña A., Gryning S.-E., and Hasager C. B. (2008) Measurements and modelling of the wind speed profile in the marine atmospheric boundary layer. *Bound.-Layer Meteorol.* **129**:479–495

Peña A., Gryning S.-E., and Hasager C. B. (2010a) Comparing mixing-length models of the diabatic wind profile over homogeneous terrain. *Theor. Appl. Climatol.* **100**:325–335

Peña A., Gryning S.-E., Mann J., and Hasager C. B. (2010b) Length scales of the neutral wind profile over homogeneous terrain. *J. Appl. Meteorol. Climatol.* DOI 10.1175/2009JAMC2148.1

Peña A., Hasager C. B., Gryning S.-E., Courtney M., Antoniou I., Mikkelsen T. (2009) Offshore wind profiling using light detection and ranging measurements. *Wind Energy* **12**:105–124

Prandtl L. (1932) Meteorologische Anwendung der Strömungslehre (Meteorological application of fluid mechanics). *Beitr. Phys. Atmos* **19**:188–202

Rossby C. G. and Montgomery R. B. (1935) The layers of frictional influence in wind and ocean currents. *Pap. Phys. Oceanogr. Meteorol.* **3**(3):101 pp

Smith D. A., Harris M., Coffey A. S., Mikkelsen T., Jørgensen H. E., Mann J., and Danielian R. (2006) Wind lidar evaluation at the Danish wind test site in Høvsøre. *Wind Energy* **9**:87–93

Steyn D. G., Baldi M., and Hoff R. M. (1999) The detection of mixed layer depth and entrainment zone thickness from lidar backscatter profiles. *J. Atmos. Ocean. Technol.* **16**:953–959

Stull R. B. (1988) An introduction to boundary layer meteorology, Kluwer Academic Publishers, 666 pp

7 Complex terrain and lidars

Ferhat Bingöl
Wind Energy Division, Risø DTU, Roskilde, Denmark

7.1 Introduction

The term "complex terrain" can be simply defined as any site where the wind is under effect of the terrain. This general definition includes landscapes with either vegetation or sudden elevation changes. In recent years, the interest of the European wind energy industry for such sites has increased. Formerly, they were considered as suboptimal for investments. This is not a coincidence and there are many reasons for such interest; most importantly the following two. Firstly, most of the suitable flat terrains have already been used. One example to this case is Northern Europe where the installed capacity is reaching its limit on flat terrain and the investors became more interested in complex sites. Secondly, the market is also growing in regions where wind resources are not fully utilized, like Mediterranean countries, where the land surface is dominated by rough terrain in the form of hills, mountains and forests (Figure 61).

In both cases, the terrain poses a challenge for flow modelling because the assumptions of classical boundary-layer theory are violated which which has a great impact on the site assessment. If one has to identify the wind conditions in complex terrain, knowledge beyond the classical site assessment methods would be needed. Hence, procedures are needed for the verification of the power curve for wind turbines erected in complex terrain because the power curve variation is $6 - 8\%$, higher compared to that measured over flat terrain (Pedersen et al., 2002). Therefore, current site assessment techniques are not *generally* reliable in such conditions, which may lead to reduced turbine/wind park lifetime and loss of investment.

In addition to land cover and elevation complexity challenges in the terrain, the wind industry faces another equally important challenge related to the size of the wind turbines. In the last decade, the turbine hub heights have doubled, reaching a minimum of 100 m with 100 m of rotor diameter. The top and bottom edges of the blade of such turbines are typically at 150 and 50 m above ground level (a.g.l.), respectively.

This multitude of factors has created the need for a new generation of measurement devices with certain capabilities. The instruments;

1. should be able to measure up to 200 m to cover the whole rotor swept area,

2. must be able to perform in profile measurement standards (e.g. IEC (2005)),

3. and be easy to install/operate in complex terrains.

The above requirements cannot easily be fulfilled with conventional meteorological masts; installation of a meteorological mast and its maintenance, is a big logistical problem. Furthermore minor adjustments on the position of the meteorological mast entails almost the same amount of work as installing it. A category of instruments which can meet these goals is the wind energy Light Detection and Ranging instruments; mostly known as wind lidars or just lidars in wind energy. In this chapter, we will discuss on using the lidars in complex terrain.

7.2 Lidars

The lidars have become a part of wind energy meteorology after 1997 (Mayor et al., 1997). The capabilities of the instrument were well-known but the necessary investment
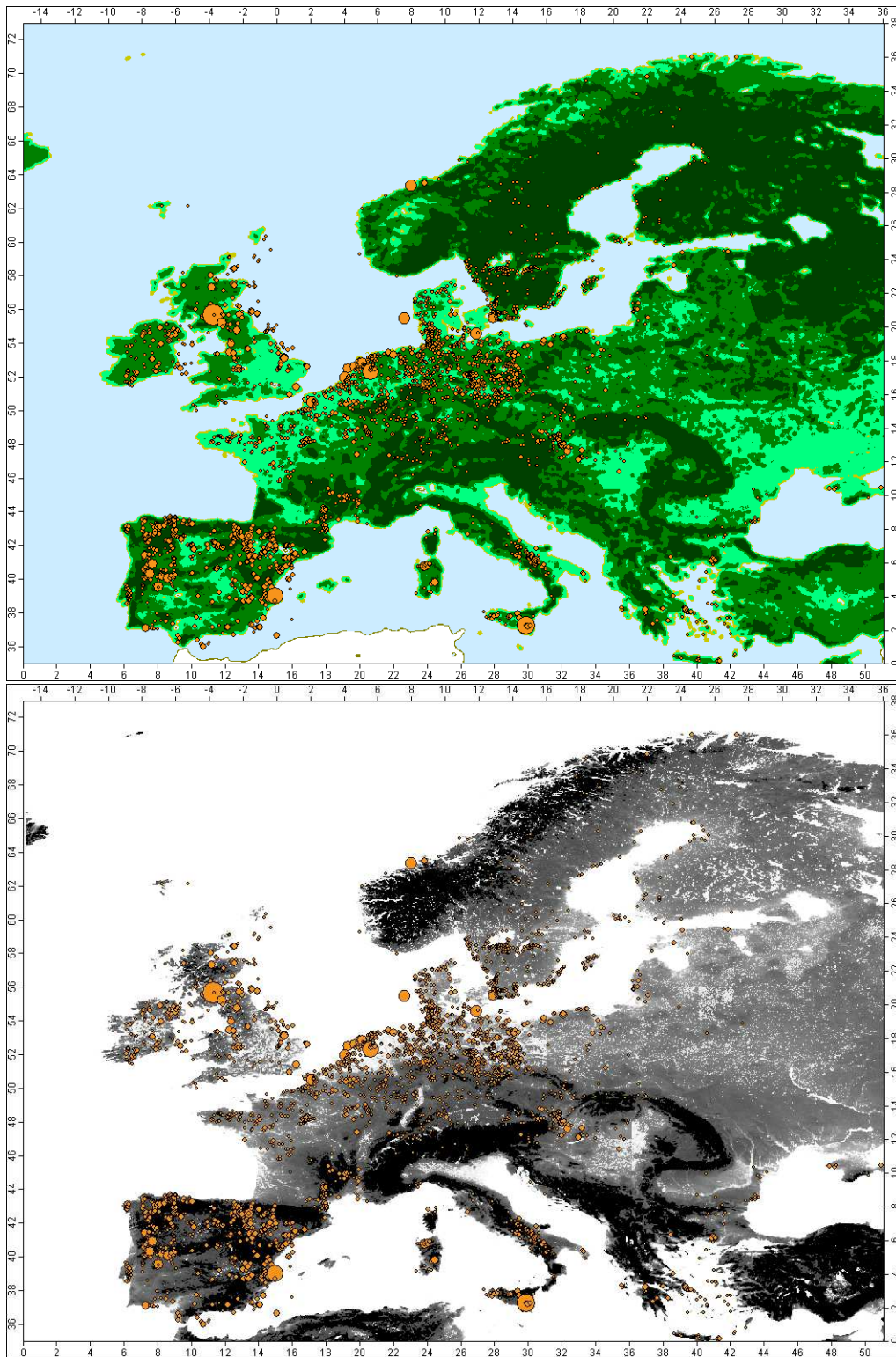
Figure 61. Spatial distribution of land use (top) and terrain slope map (bottom) in Europe derived from an EEA study (JRC, 2006) and grid size map of Hastings et al. (1999), respectively (Bingöl, 2009). Dark green areas are forest; green areas are sparse forest or shrub/herbaceous cover. Light green areas are crop land. The black areas are the regions where the slope is higher than 20°. Wind park locations with capacity between 3 and 322 MW are denoted by orange disks. The diameter of the disk is proportional to the installed capacity (TheWindPower.net, 2009)

was too high for many applications and the operating heights were not relevant to wind energy related studies. Therefore, the usage of them is recent and it has started after the "wind energy lidars" are developed (Jørgensen et al., 2004).

The main drawback of the wind lidars in complex terrain is that the horizontal wind measured from the instruments are based on the assumption that the data are collected on flat homogeneous terrain where the flow is homogeneous. Hence an adaptation to complex terrain is needed. Lidars have been previously adapted to various needs and used out of their designed envelope (Bingöl, 2005; Mikkelsen et al., 2008; Trujillo et al., 2009; Bingöl et al., 2009b). Such adaptations are of interest to wind turbine producers, wind park developers and the boundary layer meteorology community, as well as the lidar producers.

ZephIR

The British company QinetiQ designed a cost effective lidar model, ZephIR, in 2002. Risø DTU bought the first *prototype* (Figure 62-right) in 2004 and the *commercial* version (Figure 62-left) in 2005.

The prototype and the commercial models differ from each other mainly in physical appearance and in minor signal processing capabilities. The prototype is a combination of two parts; an optical head and the laser source/sensor. The parts are separated by means of an optical cable, while in the commercial model the two part have to be assembled directly together with a third containing a battery. For both versions, comparisons with several tall, meteorological masts have already proven the instrument to be accurate over flat homogeneous terrain (Antoniou et al., 2004; Smith et al., 2006) and offshore (Peña et al., 2009). In complex terrain, the interpretation of the lidar data is still under development and Bingöl et al. (2009b) addresses this issue.

The instrument is a scanning tool that focuses the laser beam at different heights between 10 and 180 m and essentially assesses the radial velocity along the beam direction at the point of focus. The laser beam is deflected an angle $\phi \approx 30°$ from the vertical by making use of a prism, which rotates one full revolution every second. The along beam or radial velocity component of the wind is thus measured on a circle as indicated in Figure 63-(left). The ZephIR is a continuous wave lidar, therefore it can only measure at the focus height. For each focus height, the prism rotates three times before the instrument changes focus to the next height. At each full revolution, 49 radial velocities are recorded and a total of 147 measurements in three seconds are used to derive the wind speed. It is possible to change the focus distance in 1 s. The number of prism rotations, the signal processing speed and the recursive focus height change can be adjusted freely for the prototype model (Bingöl, 2005; Bingöl et al., 2010).

In conical scanning mode, the measured radial wind speed, v_r, combined with the scan azimuth angles, θ, are fitted to the function (Harris et al., 2006, 2007):

$$v_r(\theta) = |A\cos(\Theta - \theta) + B| \tag{131}$$

where

$$U = \frac{A}{\sin\phi} \quad w = \frac{B}{\cos\phi} \quad . \tag{132}$$

The instrument can only measure the absolute value of the velocity. Therefore, the wind direction, Θ, is directly taken from the fit with a ambiguity of 180° which can be identified with the wind direction readings from the instrument's built-in mast. If the built-in vane is not present, as in prototype, a wind direction measurement is needed. The instrument records the 3 s statistics as well as the 10 min averages and one can use the raw data, which can be also recorded on demand, to calculate longer period averages or turbulence parameters. In this study, 30 min radial wind speeds are used, if the raw data are present, otherwise 10 min averages are preferred.
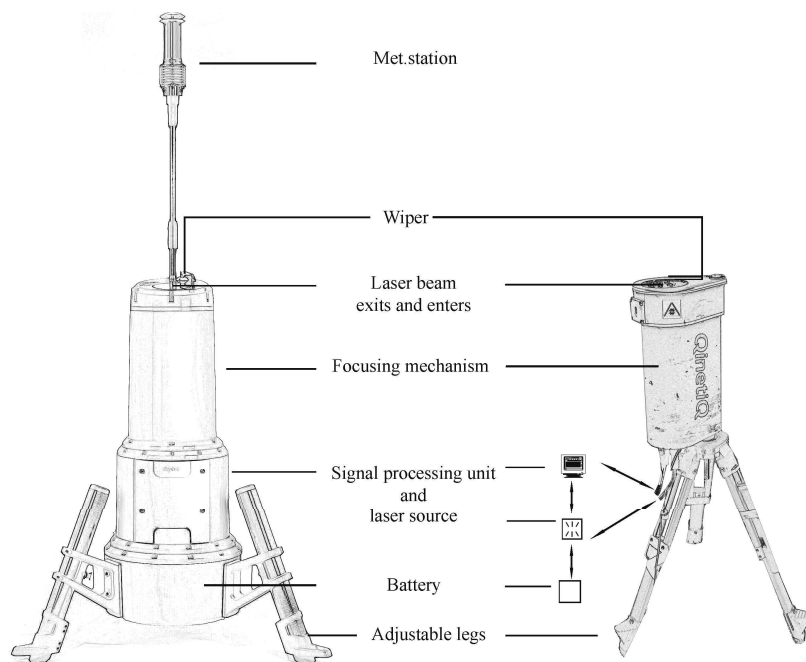
Figure 62. The ZephIR models which are used in the study. (Left) The commercial model which is 1.7 *m tall and* 0.5 *m width. The instrument weights* 100 *kg. (Right) The proto-type which is* 1.5 *m tall with adjustable legs. Including the signal processing unit, laser source/sensor and battery which are separated from the head by means of an optical cable, it weights* 120 *kg.*

It is possible to remove the prism from a lidar and turn it into a "straight shooter" scanner where it measures the wind speed in the direction it is pointed. This working mode is referred as *staring mode* in this study. In staring mode, the beam direction is fixed and the instrument focuses at different distances and measures the component of the wind vector (Figure 63-right). The wind direction cannot be measured. Therefore, the beam direction must be known and the measured data must be used combined with a wind direction measurement instrument.

The staring mode approach was applied for the first time by Harris et al. (2006) with the aim of investigating possibilities for controlling the wind turbine based on upstream wind measurements with the prototype model of the ZephIR lidar. Subsequently, the prototype is used in other experiments in this context, like by mounting on a wind turbine to measure the wake behind (Bingöl et al., 2010; Trujillo et al., 2009), for synchronized multi-lidar field measurements (Mikkelsen et al., 2008) and horizontal wind profile measurements (Bingöl et al., 2009a).

Windcube

The second wind energy lidar that came into the market is the Windcube, developed by the French company LeoSphere. The Windcube lidar is also a vertical profile measurement device and used in more recent studies (e.g. Peña et al. (2010)). Evaluation reports, mostly for the measurements over flat terrain, are also available recently (Albers and Janssen, 2008).

Contrary to the ZephIR, Windcube is a pulse lidar, which measures the wind speed and direction at measurement points 90° apart from each other on the conical scan circle for all chosen heights simultaneously. Each sector is scanned for 1 s and every 6 s (2 extra seconds are used to move the wedge), the values are used to derive wind speed and
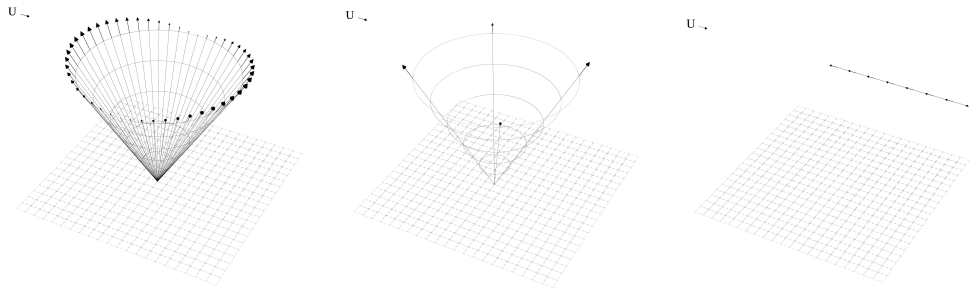
Figure 63. Lidar working modes. The arrows denote the laser beam direction and the measured wind components. (Top) The original conical scanning mode of ZephIR. At upwind and downwind directions the absolute value of the along beam velocity component has the maximum value. When the wind is perpendicular to the beam direction the wind component on the radial vector has a minimum value. (Middle) Conical Scanning Mode of the Windcube lidar. The data is recorded only in four equally separated sectors on the conical circle. (Bottom) Illustration of the Staring Mode. The beam direction is fixed and the instrument focuses at different distances and measures the component of the wind vector indicated by the arrows. In this mode, the lidar data is used combined with separate wind direction measurements

direction profiles; calculated via (Lindelöw, 2007);

$$u = \sqrt{u_1^2 + u_2^2} \tag{133}$$

where u_1 and u_2 are the horizontal plane wind speed components, derived as

$$u_1 = v_r(0) - v_r(\pi), \quad u_2 = v_r(\tfrac{\pi}{2}) - v_r(\tfrac{3\pi}{2}) \tag{134}$$

and

$$w = \frac{v_r(0) + v_r(\pi)}{2\cos\phi} = \frac{v_r(\tfrac{\pi}{2}) + v_r(\tfrac{3\pi}{2})}{2\cos\phi}, \quad \Theta = \arctan(u_1, u_2) \tag{135}$$
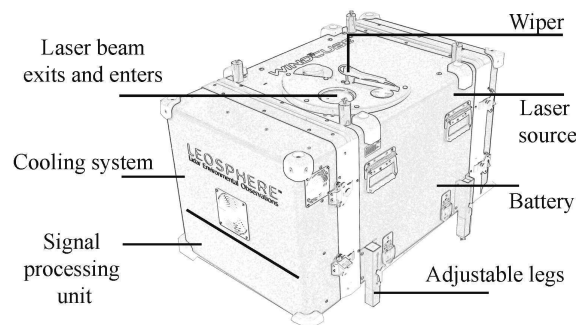

Figure 64. Leosphere Windcube; the laser source is located right on top of the unit and generates the beam in the direction to the the prism located under the beam exit lense where it is tilted to upwards. The dimensions are 0.7 m×0.4 m×0.4 m and the instrument weights ≈ 55 kg.

The Windcube is equally mobile to ZephIR with the added advantage that the wedge opening angle, ϕ, can be adjusted between 15° and 30°. This option is introduced as a "bypass" for complex terrain problems such as inhomogeneous flow. This hypothesis is discussed in the section 7.3. Windcube is also being used in staring mode in recent studies (e.g. Mikkelsen et al. (2008)) but there is no published journal article available on the topic that the author is aware of.

Other lidars

The other lidar instruments like Gallion, by Sgurr Energy, has the classical design of the conical scan as well as the possibility of making any possible pattern between 0° and 0° in pan, between 0° and 0° in tilt. The instrument is new and is not used in any of the experiments related to this chapter. When this chapter is written Gallion was still under tests at Risø Høvsøre Test Site. An early technical report was published (Gottschall et al., 2009).

7.3 Challenges and Known Issues

The conical scanning error in complex terrain

The success of the lidar conical scan operation is limited to flat terrain. In complex terrain, the flow is no longer homogeneous and that can give a large bias on the horizontal wind speed estimated from the lidar up to 10% in horizontal wind speed measurements (Bingöl et al., 2008a). The basic problem also applies to any other conically scanning lidar and sodars as well (Bradley, 2008). Some of the lidar producers present the smaller half opening angle (Leosphere, 2009) or custom scan regimes (SgurrEnergy, 2009) as one of the possible solutions to overcome the problem caused by the inhomogeneous flow.
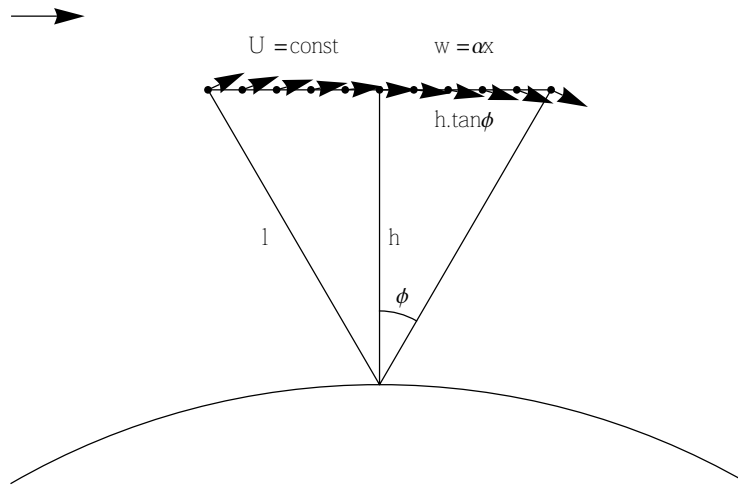

Figure 65. Simplified lidar scanning geometry in a linearly changing mean flow. The lidar is shooting upstream and downstream with a half opening angle ϕ.

The error can be illustrated as in Figure 65 where the horizontal wind speed U is taken constant, but the vertical wind speed w is assumed to change linearly with the downwind position; parametrised with a factor of α. This is similar to the case over a hill. The upstream has positive and the downstream has negative tilt relative to the top of the hill. The projected wind speed on the upwind and downwind beams are

$$v_{up} = -(U + h\alpha)\sin\phi \qquad v_{down} = (U + h\alpha)\sin\phi \quad . \qquad (136)$$

Assuming horizontal inhomogeneity, the horizontal velocity can be calculated as

$$U_{lidar} = \frac{v_{down} - v_{up}}{2\sin\phi} = U + h\alpha, \qquad (137)$$

which shows, in the case of a negative α that the horizontal wind is *underestimated* (Bingöl et al., 2008a). A simplified three dimensional analysis of the error is derived by Bingöl et al. (2008b), where the the mean wind field $\mathbf{U} = (u, v, w)$ is assumed to vary

linearly. In such case, the wind vector estimations become:

$$u_{\text{lidar}} = u + h\frac{\partial w}{\partial x} \tag{138}$$

$$v_{\text{lidar}} = v + h\frac{\partial w}{\partial y} \tag{139}$$

$$w_{\text{lidar}} = w - \frac{l}{2}\tan^2\phi\frac{\partial w}{\partial z} \tag{140}$$

where l is the focus distance $h/\cos\phi$. Eq. 140 shows that the error due to inhomogeneity of the mean flow vanishes for the vertical component as the half opening angle ϕ goes to zero. The errors on the horizontal components are independent of ϕ.

Predicting the error by means of a flow model

Conical scanning mode of the lidar can be simulated in flow models. An automated script for commercial software WAsP Engineering has been written by the author for the ZephIR and Windcube lidars and has been published (Bingöl and Mann, 2009). The method can be simplified as below and can be adapted to different scanning regimes such as different ϕ.

A unit vector in the direction of the laser beam can be written as,

$$\mathbf{n} = (\cos\theta\sin\phi, \sin\theta\sin\phi, \cos\phi) \tag{141}$$

where ϕ is half opening angle and θ is the geographical angle in which the beam is pointing. As it is previously stated, assuming the flow field to be roughly homogeneous over the averaging circle with a mean $U = (u, v, w)$. The radial velocity in the direction of the laser beam, the radial wind speed v_r, calculated at θ azimuth of the prism is the projection of $\mathbf{U}$ onto $\mathbf{n}$:

$$v_r(\theta) = \mathbf{n}(\theta) \cdot \mathbf{U}\left(\mathbf{n}(\theta)l - (0, 0, z')\right), \tag{142}$$

where z' is absolute position of the instrument a.g.l. if it is placed on an artificial elevation (e.g. tower).

For ZephIR lidar, after calculating 60 points on the conical circle, all three velocity components can be obtained through a linear fit to trigonometric series

$$a + b\cos\theta + c\sin\theta, \tag{143}$$

as;

$$u = \frac{b}{\sin\phi} \qquad v = \frac{c}{\sin\phi} \qquad w = \frac{a}{\cos\phi} \qquad \Theta = \arctan\frac{v}{u} \quad . \tag{144}$$

For Windcube, radial wind speed v_r from calculated at four measurement points are used in Eq. (133)–(135) directly to derive wind speed components and direction.

Does smaller cone angle make better measurements?

The standard cone angle, ϕ, for most of the lidars is $30°$ but reducing the cone angle to $15°$ is introduced as a "bypass" for complex terrain problems such as inhomogeneous flow. In section 7.3, we have seen that, theoretically, the error is not dependent on the cone angle. A validation of this theory has been made with a field measurement campaign (Bingöl, 2009) and experimental results are discussed further in section 7.4 of this chapter.

Extracting momentum flux

Momentum flux measurements are important in order to understand the atmospheric flow over the terrain. It is possible to extract the momentum flux from lidars in conical scanning mode. The methods listed in this section describes a general idea of extracting

momentum fluxes from lidar, which would not only be helpful in flat terrain but would be very significant parameter in complex terrain. Although this basic information is given here, the readers are encourage to make further reading about the standard bias of lidars for these methods from the reference Mann et al. (2010). In refereed article it has been shown that the error of calculating the momentum flux with the method below can be between 15% to 60% for ZephIR lidar and around 20% for Windcube lidar at the heights of interest of wind energy developers. Furthermore the paper, includes a section explaining how to avoid this possible error in flat terrain. The method is not tested in complex terrain and readers should be aware of this phenomenon.

From ZephIR lidar The variance of the radial velocity for ZephIR lidar can be calculated as (Eberhard et al., 1989):

$$
\begin{aligned}
\sigma^2\left(v_r(\theta)\right) &= \left\langle \left[\mathbf{n}(\theta)\cdot\mathbf{u}'\left(\mathbf{n}(\theta)l\right)\right]^2\right\rangle \\
&= \sigma_u^2\sin^2\phi\cos^2\theta + \sigma_v^2\sin^2\phi\sin^2\theta + \sigma_w^2\cos^2\phi + \\
&\quad 2\left\langle u'v'\right\rangle\sin^2\phi\cos\theta\sin\theta + \\
&\quad 2\left\langle u'w'\right\rangle\cos\phi\sin\phi\cos\theta + \\
&\quad 2\left\langle v'w'\right\rangle\cos\phi\sin\phi\sin\theta
\end{aligned}
\tag{145}
$$

For the upwind ($\theta = 180°$), and the downwind ($\theta = 0°$) the variances can be extracted as,

$$
\begin{aligned}
\sigma_{\mathrm{up}}^2 \equiv \sigma^2\left(v_{\mathrm{up}}\right) &= \sigma_u^2\sin^2\phi + \sigma_w^2\cos^2\phi \\
&\quad -2\left\langle u'w'\right\rangle\sin\phi\cos\phi
\end{aligned}
\tag{146}
$$

$$
\begin{aligned}
\sigma_{\mathrm{down}}^2 \equiv \sigma^2\left(v_{\mathrm{down}}\right) &= \sigma_u^2\sin^2\phi + \sigma_w^2\cos^2\phi \\
&\quad +2\left\langle u'w'\right\rangle\sin\phi\cos\phi \quad.
\end{aligned}
\tag{147}
$$

The momentum flux is the difference between Eq. (146) and (147):

$$
\left\langle u'w'\right\rangle = \frac{\sigma_{\mathrm{down}}^2 - \sigma_{\mathrm{up}}^2}{4\sin\phi\cos\phi} \quad.
\tag{148}
$$

From Windcube lidar Following the same logic, for Windcube we can derive from four azimuthal positions separated $\pi/2$ around the circle formed by the conical scanning. Therefore, the momentum flux can be defined as;

$$
\begin{pmatrix} \Delta_0 \\ \Delta_{\pi/2} \end{pmatrix} = \begin{pmatrix} \sigma^2\left(v_r(\theta)\right) - \sigma^2\left(v_r(\theta+\pi)\right) \\ \sigma^2\left(v_r(\theta+\pi/2)\right) - \sigma^2\left(v_r(\theta+3\pi/2)\right) \end{pmatrix},
\tag{149}
$$

i.e. the differences in variances in two perpendicular directions. We can then use Eq. (145) to get

$$
\begin{pmatrix} \Delta_0 \\ \Delta_{\pi/2} \end{pmatrix} = 2\sin2\phi \begin{pmatrix} \cos\theta & \sin\theta \\ -\sin\theta & \cos\theta \end{pmatrix} \begin{pmatrix} \left\langle u'w'\right\rangle \\ \left\langle v'w'\right\rangle \end{pmatrix}.
\tag{150}
$$

So knowing the half opening angle ϕ and the angle of the first beam direction relative to the mean wind direction, θ, we can calculate the vertical flux of horizontal momentum in the mean wind direction and perpendicular to that:

$$
\begin{pmatrix} \left\langle u'w'\right\rangle \\ \left\langle v'w'\right\rangle \end{pmatrix} = \frac{1}{2\sin2\phi} \begin{pmatrix} \cos\theta & -\sin\theta \\ \sin\theta & \cos\theta \end{pmatrix} \begin{pmatrix} \Delta_0 \\ \Delta_{\pi/2} \end{pmatrix}.
\tag{151}
$$

7.4 Experimental studies

Conically scanning lidars assume the flow to be homogeneous in order to deduce the horizontal wind speed as it has been described in section 7.3. However, in moderately

complex or complex terrain this assumption is not valid implying a risk that the lidar will derive an erroneous wind speed. The magnitude of this error was measured by collocating a meteorological mast and a lidar at two Greek sites, one hilly and one mountainous. In order to predict the error for various wind directions the flows at both sites were simulated with the linearised flow model LINCOM as described in section 7.3. The measurement data were compared with the model predictions with good results for the hilly site.

In both experiments lidar data are collected by the standard QinetiQ software and synchronized with mast data by the CRES WindRose software. Instruments are calibrated according to the requirements of IEC61400-12-1:2005/Annex F and MEASNET guidelines at CRES Laboratory for Wind Turbine Testing.

Hilly site; Lavrio

The Lavrio site is located 38 km SE of the center of Athens close to the coast of the Aegean Sea. The experiment took place between 2008-Dec-01 and 2008-Jan-15. The highest point is 200 m ASL and main wind direction is 0°. The 100 m triangular lattice reference meteorological mast is equipped with cup anemometers and vanes at five heights (10, 32, 54, 76, and 100 m). Cups are to the east and vanes are to the west. There are also ultrasonic 3D Gill anemometers at three heights (34, 78, and 98 m) which are not used in this study due to problems with icing but this does not influence the used cup anemometers and vanes. Additionally, the temperature profile is measured using differential thermometers, as well as, the atmospheric pressure and the solar radiation. Dedicated instrumentation is used for signal protection, filtering and conditioning. The lidar is located nearly 12 m north of the mast. The measurement heights are 32 and 78 m.

At Lavrio, most of the winds are northerly which means it is blowing from lidar to the mast. The scatter plots (Figure 66-top) show generally 5 to 7% errors in wind speed measurements. For the WAsP Engineering model we have used 3 km×3 km map with 4 m resolution simulating the wind direction from 0° to 360° with 6° bins. We have used all the data from the mast at each height and averaged them according to the wind direction in 10° bins.

The comparison between the model and the measurements is shown in Figure 66 (lower two plots) and shows good correlation in some sectors. The mast is voluminous, thus the selected data must be far from boom direction which is 113°. These sectors are marked with light grey areas in the plots for ±30°. The ideal ratio line of one is also shown and it represents the cases where there is no difference between the lidar and the mast measurements. The black line is the model and the points are the measurement results.

Especially for northerly directions the model predicts the lidar error well for both heights, while for the southerly directions the prediction is not so good. We believe this can be a result of the limitation of WAsP Engineering. In southerly directions very close to the site there are steep slopes. In this sector and height, the flow model has difficulties predicting the tilt angles as compared to sonic measurements for periods with no icing problems.

Mountainous site; Panahaiko

The Panahaiko site is located 165 km northwest of Athens, at Vounogiorgis mountain south east of the village Sella, 14 km south of the Patras Sea. The experiment ran from 2007-Sep-19 to 2007-Oct-11. The terrain in the vicinity of the site is very complex. Highest point is 2000 m in the region where the experiment surrounding is between 1700 and 1750 m ASL. The prevailing wind directions are ENE and SW. The triangular lattice reference meteorological mast has six cup anemometers (10, 20, 30, 40, and 54 m) and two vanes (40 and 54 m). Additionally, there are also air temperature and relative humidity measurements at 54 m. The boom cross-section is 40 mm×40 mm. All wind sensors are mounted at a height of 75 cm above the boom and at a distance of 225 cm from the outer
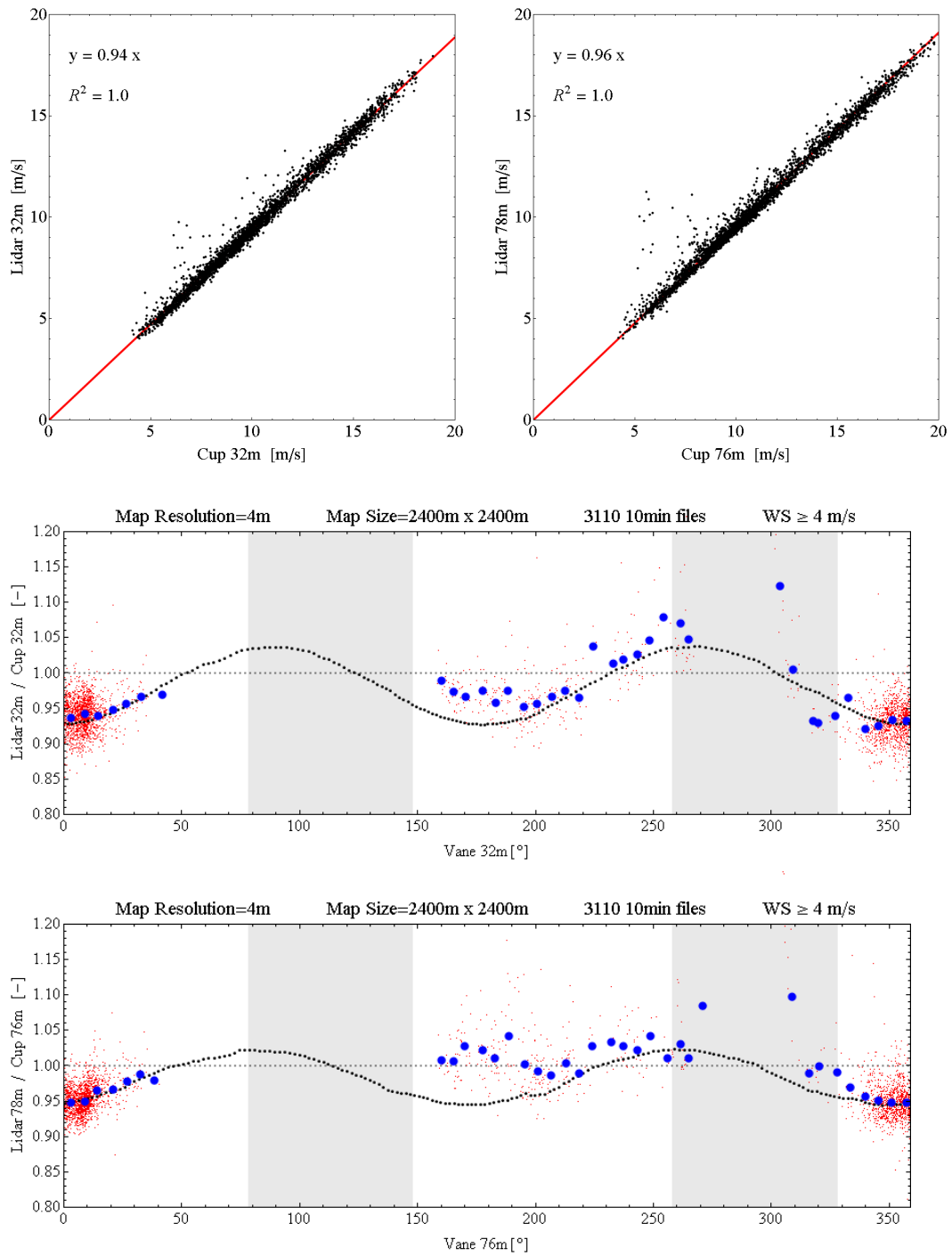
Figure 66. Lavrio: The scatter plots show generally 4% to 6% errors in wind speed measurements (top). Lower two plots are the comparison between the model and the measurement data for two different heights. Small red dots are the error ratio for each 10 min measurement, big blue dots are the averaged 6° bins according to the wind direction and medium black dots are the model results. The mast shadow is marked with grey rectangles. The ideal ratio line of one, dashed blue, is also shown and it represents the cases where there is no difference between the lidar and the mast measurements. Especially for northerly directions the model predicts the lidar error well for both heights, while for the southerly directions the prediction is not so good.

mast leg. The lidar is located nearly 20 m WSW of the mast. The lidar measurement heights are 30 m and 55 m.

The second site, Panahaiko, is much more complex than Lavrio, so there are many sectors which could be problematic for WAsP Engineering to model. The scatter plots in Figure 67 (top) show data for all directions. The mast at Panahaiko is smaller than at Lavrio so the sector with flow distortion is smaller ($\pm25°$) shown in grey in the figure. The boom direction is 210°.

The comparison between the modelled error and the measurements as a function of direction is shown in Figure 67 (lower two plots). It is not a perfect prediction, but the model gives the right order of magnitude for this complex site.

The outliers mainly seen for the larger heights in Figures 66 and 67 are probably due to cloud return as discussed in Courtney et al. (2008).

Validation of cone angle hypothesis

The hypothesis that reducing the cone angle will not change the systematic error on the horizontal wind measured by the lidar (section 7.3) was tested with measurements on a non-forested hilly site in Greece. The experiment was made by CRES and statistical data were shared with the author [9].

One ZephIR and two Windcube lidar units were located next to a tall meteorological mast at Greece Renewable Energy Laboratories test site at Lavrio (Figure 68) which is described in section 7.4. The experiment took place between 2008-Sep-17 and 2009-Jan-17. The measurement location was on a hill with a gentle slope of approximately 10° in the main wind direction sector to both sites. Further away the northerly sector is a flat terrain, southerly sector includes more hill after approximately 150 m (Figure 69).

The 100 m triangular lattice reference meteorological mast was equipped with cup anemometers and vanes at three heights (54, 76 and 100 m). Cups are to the east and vanes are to the west. The lidars were located between 12 and 20 m north of the mast. One of the Windcube units and the ZephIR lidar were in operation with a $\phi = 30°$ prism while the other Windcube operated with $\phi = 15°$. The ZephIR unit measured at 54, 78, 100 and 120 m. Both Windcube units measured at 40, 54, 78, 100, 120, 140 and 160 m.

The data from northerly sector, $0\pm15°$ were selected for comparison. All available data, 1163 of 10 min runs, were used. Initially, the horizontal wind speed, wind direction and standard deviation of the horizontal wind speed were compared with the sonic anemometers at same heights; 54, 78 and 100 m (Figures 70, 71 and 72). The results agreed with a previous experiment at the same site for the same wind sector (Bingöl et al., 2008a). The horizontal wind speed measurements from the lidars were in good correlation but wind direction and the standard deviation of the horizontal wind speed deteriorate for the 15° Windcube.

Subsequently, horizontal wind speed and flow inclination angles were compared between the 30° prism instruments and the 15° Windcube for available common heights (Figures 73 and 74). The results showed that the horizontal wind speed measurements were not effected by the cone angle. However, the flow inclination angles showed less scatter with the lower cone angle as it was expected.

As a conclusion, it can be stated that the lower half opening angle, $\phi = 15°$ do not help in complex terrain on improving the horizontal wind speed measurements. For any other statistical term the $\phi = 15°$ has an even higher bias in measurements. Therefore, the hypothesis described at the beginning of this section agrees with the measurements and the 30° prism is advised by the author instead of 15° prism at such sites.

---

[9] Courtesy of Dimitri Foussekis, The Centre for Renewable Energy Sources (CRES) GREECE
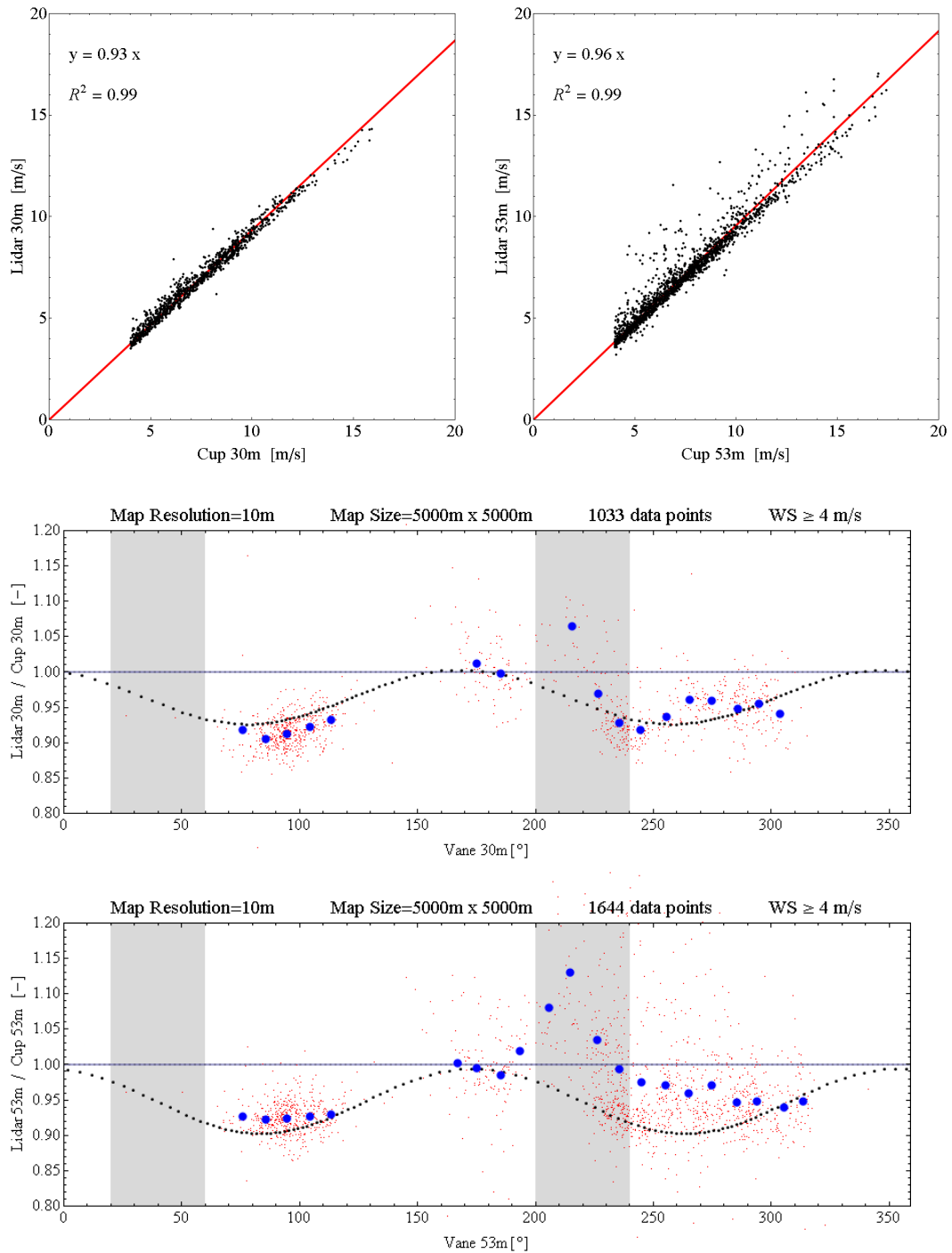
Figure 67. Panahaiko: The scatter plots show generally 4% to 7% errors in wind speed measurements (top). Lower two plots are the comparison between the model and the measurement data for two different heights. Small red dots are the error ratio for each 10 min measurement, big blue dots are the averaged 10° bins according to the wind direction and medium black dots are the model results. The mast shadow is marked with grey rectangles. The ideal ratio line of one, dashed blue, is also shown and it represents the cases where there is no difference between the lidar and the mast measurements. It is not a perfect prediction, but the model gives the right order of magnitude for this complex site.

Figure 68. The experimental set-up at Lavrio, Greece for the comparison of the lidars in different working modes.
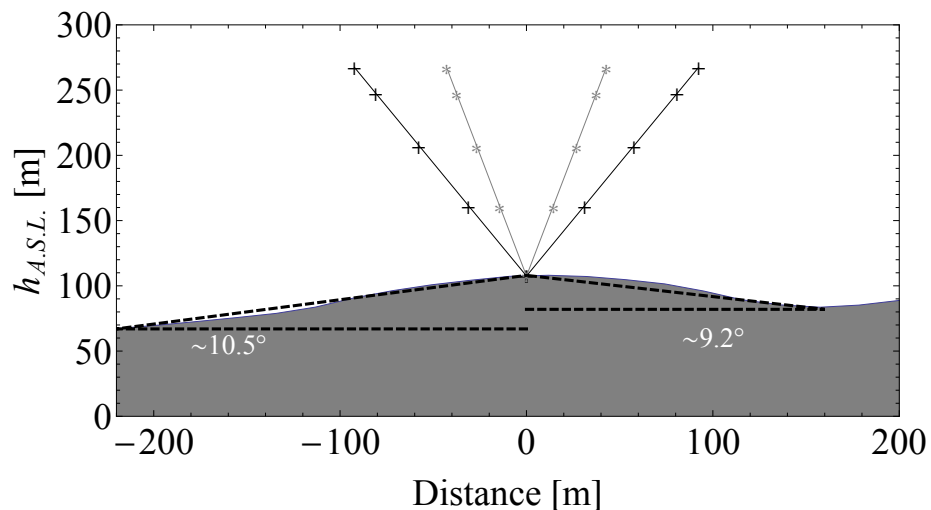

Figure 69. The hill transect at Lavrio. Left is northerly direction which is the dominant wind direction.

7.5 Conclusions

Lidars, used over flat homogeneous terrain, show errors in the mean wind speed of only a few percent. We have shown that in complex terrain of the type commonly used for wind turbine parks, errors in the horizontal wind speed as measured by a conically scanning lidar can be of the order of 10%. This is due to the lack of horizontal homogeneity of the flow, which is assumed in the interpretation of the lidar data. The findings are based on two experiments involving collocated lidars and meteorological masts in complex terrain, together with flow calculations over the same terrains. For that calculation we use WAsP Engineering, and we find that the calculations match the experiment except for some sectors where the terrain is particularly steep. This is not surprising, since the WAsP Engineering is built on a linearized flow model, which is only valid for limited terrain
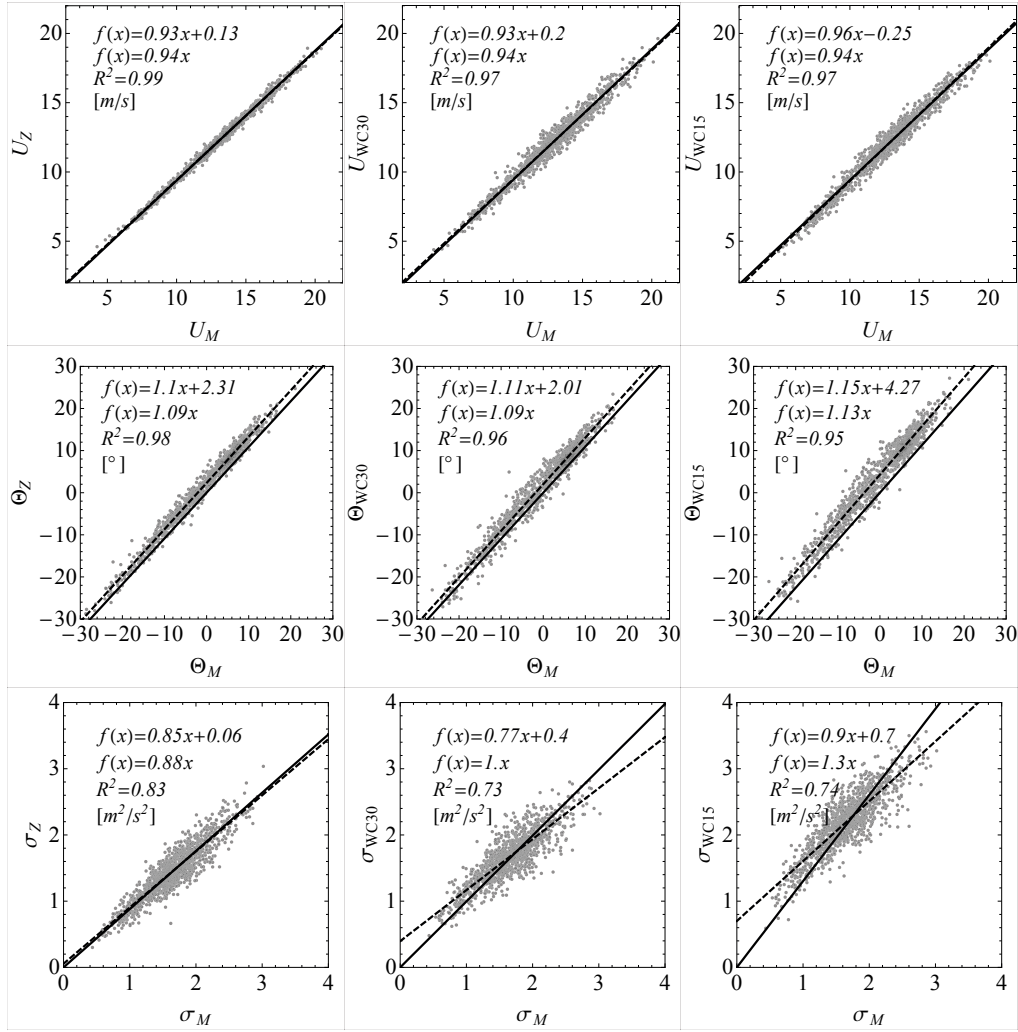
Figure 70. Lidars vs Sonics at 54 m. Top row is the horizontal wind speed, middle row is the wind direction and bottom row is the standard deviation of the horizontal wind speed.

slopes.The model is not for highly complex terrain that can incorporate the stability effect in any reliable way. Furthermore most of the wind speeds analyzed, from both sites, are quite high so it is not unreasonable to assume neutral stratification. That is why there is concluding thoughts about stability. To make more reliable predictions of the error in very steep terrain, other more advanced flow models ((Castro et al., 2003)) must be used.

The hypothesis that the lidar conical scan error due to inhomogeneity of the mean flow is independent of the half opening angle ϕ on the horizontal components has been supported with experimental results from moderately-complex terrain site measurements. The synchronized measurements from the lidars with different half opening angles and meteorological mast instruments reported no positive effect of smaller half opening angle in horizontal wind speed measurements, contrary to what was being suggested by some of the producers and academics. The measurements agreed with the described hypothesis and it can be concluded that smaller half opening angles can only be helpful in sites with the presence of dense canopy or obstacles, in order to measure the desired height easily.

As a general conclusion of this study, lidars can be used in complex terrain with support of flow models which should include well defined flow separation predictions. It is important to note that modelling must be accompanied by flow analysis before and after
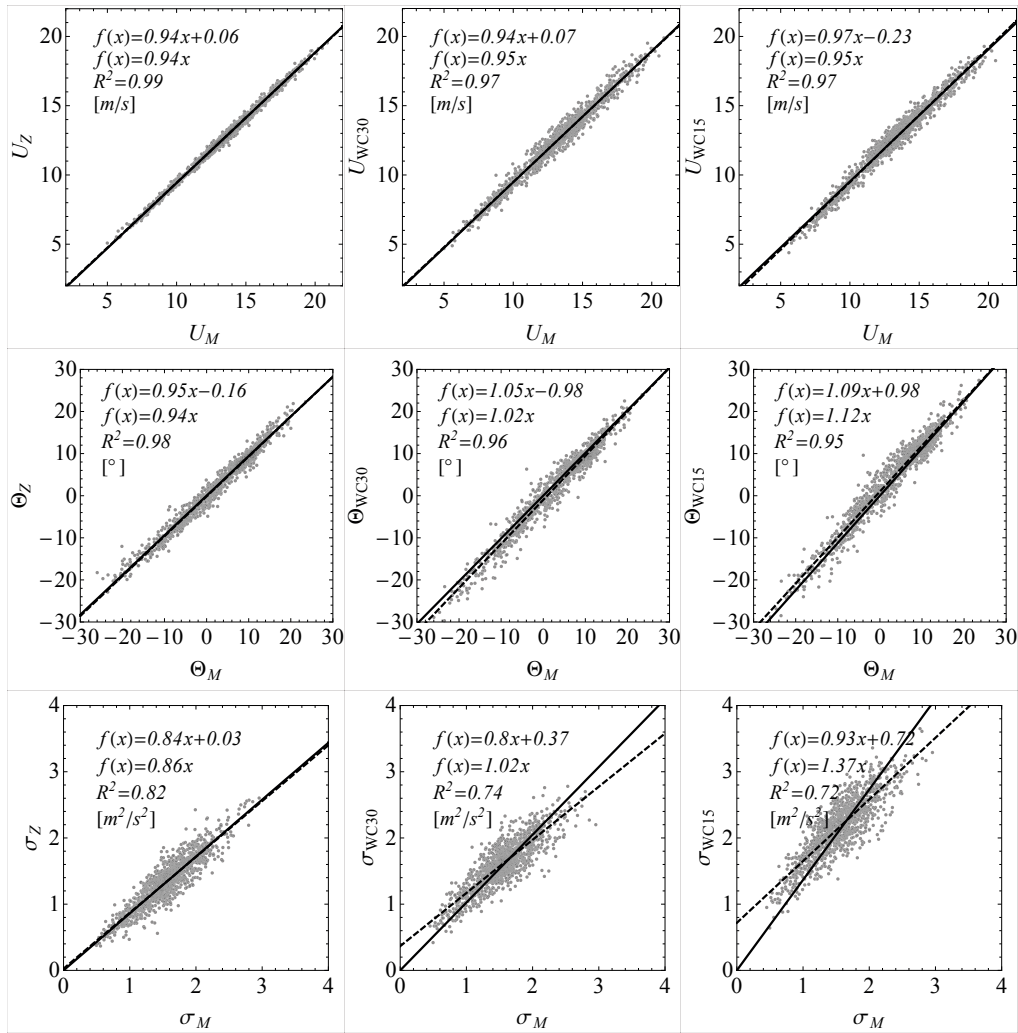
Figure 71. Lidars vs Sonics at 78 m. Top row is the horizontal wind speed, middle row is the wind direction and bottom row is the standard deviation of the horizontal wind speed.

the measurements. Prior to the measurements, models should be used to detect possible suitable locations for lidar placement. This can be done with linearised or advanced CFD models because any of these can perform a simple assessment based on rough calculations of error values. Thus, the majority of sub-optimal locations can be eliminated. Subsequently, any attempt to correct the lidar data must be performed with an advanced flow model, preferably a CFD model that has already been tested in complex terrain with measurements. It is advised that the described modelling steps for lidar data correction should be included in wind turbine and site assessment and implemented in well established international standards (e.g. IEC 61400 series) after further studies.

The author also would like to bring to attention certain shortcomings of the current commercial versions of the lidar instruments. Some of the experiments, which are conducted in this study or cited in the manuscript, would not have been possible without full software and hardware access to the instruments. The re-formulation of signal processing methods and the physical manipulation of instrument parts were essential to achieve the necessary scanning speed and to create custom scan regimes. This underlines the importance of instrument flexibility for a wide range of uses (e.g. in complex terrain). Unfortunately, most of the producers of currently available commercial models are gradually stepping back from such an approach in an effort to create stable, robust instruments.
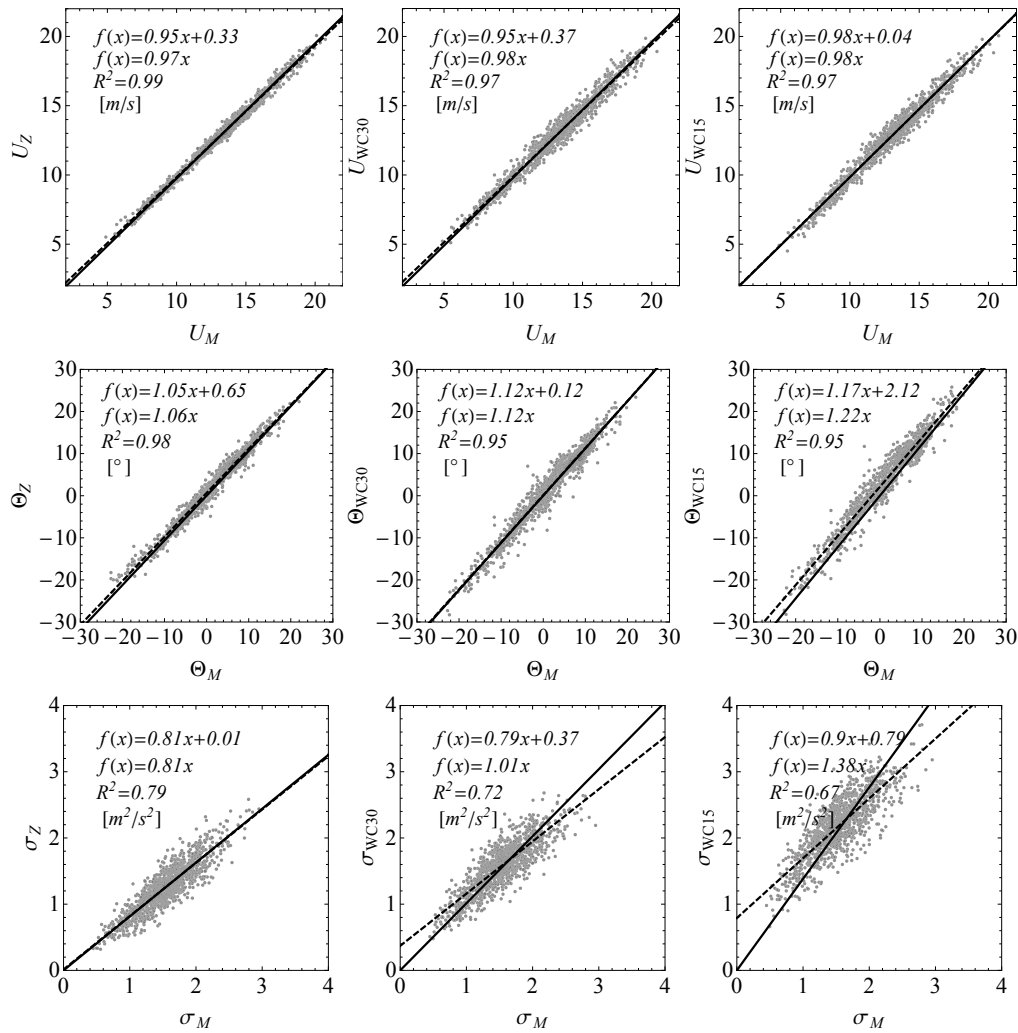
Figure 72. Lidars vs Sonics at 100 m. Top row is the horizontal wind speed, middle row is the wind direction and bottom row is the standard deviation of the horizontal wind speed.

In order to achieve faster development in lidar technology in complex terrain, the author believes that these instruments must be accessible in a software as well as a hardware level, and suggests a more detailed documented developer interface mode.

Concluding, current standards of the instruments are adequate to perform wind measurements over most of the terrain types and it is believed that it is possible for lidars to replace conventional meteorological mast in the future if the data interpretation is improved, particularly.

Notation

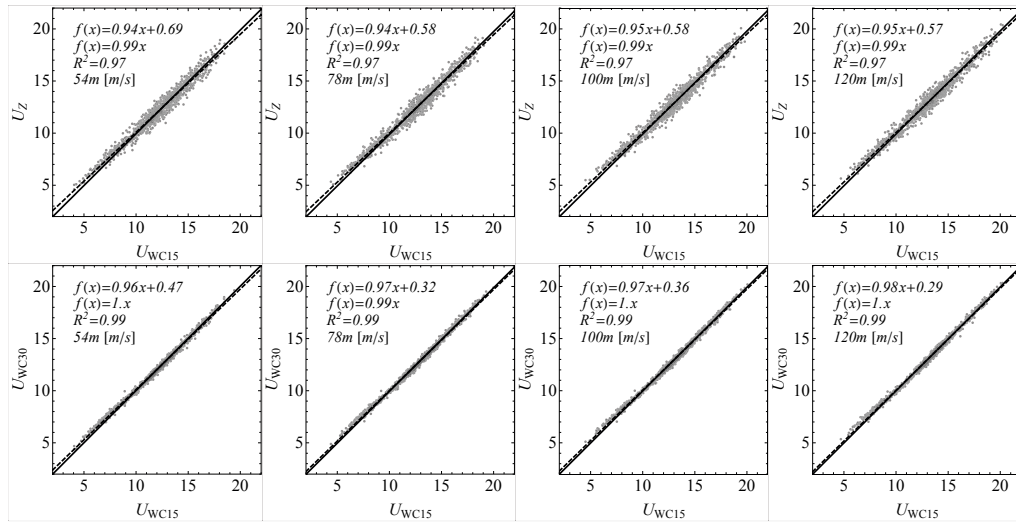|	
a.g.l.	above ground level
h	focusing height
l	focus distance
$\mathbf{n}$	unit vector in the direction of the laser beam
u	longitudinal wind speed component
u_i	wind speed component in the i direction
U	horizontal wind speed
$\mathbf{U}$	mean wind field
v	transversal wind speed component
v_{down}	projected wind speed in the downstream beam

Figure 73. Horizontal wind speed correlation between the 30° prism instruments vs. 15° Windcube for available heights; 54, 78, 100 and 120 m. The ZephIR is at the top
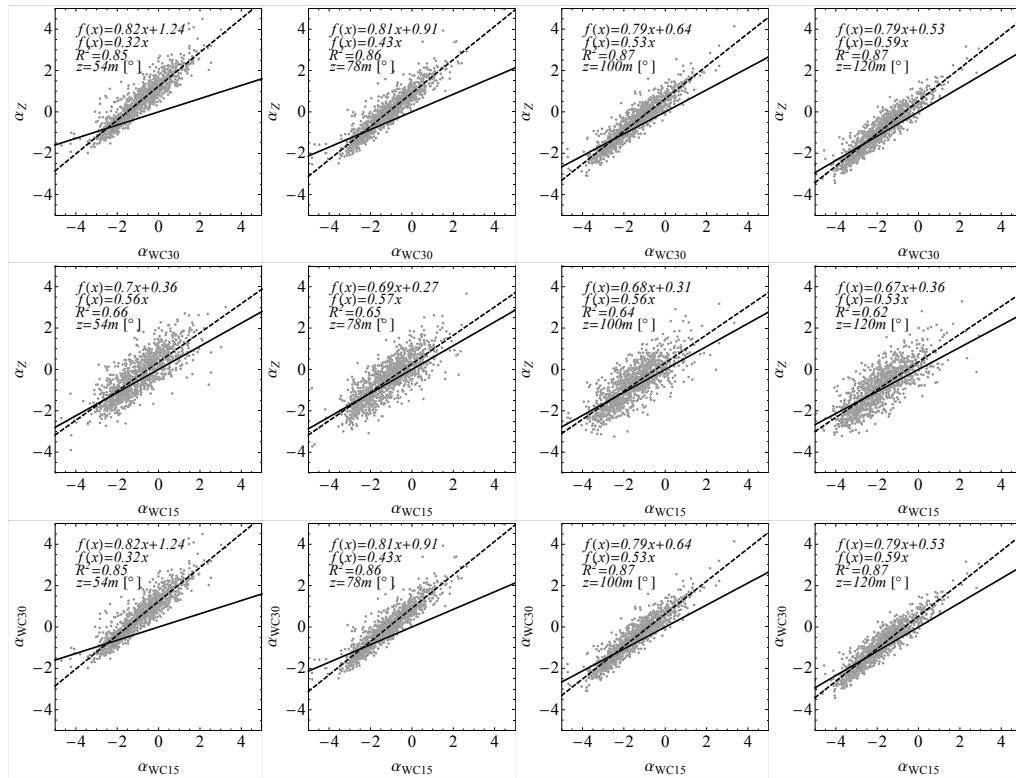

Figure 74. Flow inclination angles correlation between the 30° prism instruments vs 15° Windcube for available heights

v_{up}	projected wind speed in the upstream beam
v_r	radial wind speed
w	vertical wind speed
X'	fluctuation part of a variable X from the mean
z'	absolute position of the instrument a.g.l
α	linear factor for parametrization of the vertical wind speed
θ	scan azimuth lidar angle
Θ	wind direction

σ_X^2 variance of a variable X
ϕ deflection lidar angle from the vertical or wedge angle
$\langle X \rangle$ time average of a variable X

References

Albers A. and Janssen A. (2008) Windcube evaluation report. Technical report, Deutsche WindGuard Consulting GmbH

Antoniou I., Jørgensen H. E., Mikkelsen T., Petersen T. F., Warmbier G, and Smith D. (2004) Comparison of wind speed and power curve measurements using a cup anemometer, a lidar and a sodar. *Proc. of the European Wind Energy Conf.*, London

Bingöl F. (2005) Adapting Laser Doppler Anemometer into Wind Energy. Master's thesis, Technical University of Denmark, Lyngby

Bingöl F. (2009) *Complex Terrain and Wind Lidars*. PhD thesis, Risø DTU, Roskilde

Bingöl F. and Mann J. (2009) Lidar performance estimation script for WAsP Engineering. Technical report, Risø DTU, Roskilde

Bingöl F., Mann J., and Foussekis D. (2008) Lidar error estimation with wasp engineering. *IOP Conf. Series: Earth and Environ. Sci.*, 012058 (9pp)

Bingöl F., Mann J., and Foussekis D. (2008) Modeling conically scanning lidar error in complex terrain with WAsP Engineering. Risø–R–1664(EN), Risø DTU, Roskilde

Bingöl F., Mann J., Dellwik E., Sogachev A., and Rathmann O. (2009) Flow over limited size forest; measurements and modelling. *Wind Energy*, under review.

Bingöl F., Mann J., and Foussekis D. (2009) Conically scanning lidar error in complex terrain. *Meteorologische Z.*, **18**:189–195

Bingöl F., Mann J., and Larsen G.-C. (2010) Lidar measurements of wake dynamics Part I: One Dimensional Scanning. *Wind Energy* **13**:51–61

Bradley S. (2008) Wind speed errors for lidars and sodars in complex terrain. *IOP Conf. Series: Earth and Environ. Sci.* 012061 (7pp)

Castro F., Palma J., and Lopes A. (2003) Simulation of the askervein flow. part 1: Reynolds averaged Navier-Stokes equations (k-epsilon turbulence model). *Bound.-Layer Meteorol.* **107**:501–530

Courtney M., Wagner R., and Lindelöw P. (2008) Testing and comparison of lidars for profile and turbulence measurements in wind energy. *IOP Conf. Series: Earth and Environ. Sci.* 012021 (14pp)

Eberhard W. L., Cupp R. E., and Healy K. R. (1989) Doppler lidar measurement of profiles of turbulence and momentum flux. *J. Atmos. Oceanic Tech.* **6**:809–819

Gottschall J., Lindelöw P., and Courtney M. (2009) Executive summary of key test results for SgurrEnergy galion. Independent test results, Risø DTU, Roskilde

Harris M., Hand M., and Wright A. (2006) Lidar for turbine control. Technical Report NREL/TP-500-39154, NREL

Harris M., Bryce D. J., Coffey A. S., Smith D. A., Birkemeyer J., and Knopf U. (2007) Advance measurement of gusts by laser anemometry. *J. Wind Eng. Ind. Aerodyn.* **95**:1637–1647

Hastings D. A., Dunbar P. K., Elphingstone G. M., Bootz M., Murakami H., Maruyama H., Masaharu H., Holland P., Payne J., Bryant N. A., Logan T. L., Muller J. P., Schreier G., and MacDonald J. S. (1999) he global land one-kilometer base elevation (globe) digital elevation model, version 1.0. Digital data base on the www and cd-roms, National Oceanic and Atmospheric Administration, National Geophysical Data Center, Boulder

IEC (2005) 61400-12-1: Power performance measurements of electricity producing wind turbines. Technical report, International Electrotechnical Commission

JRC (2006) Global land cover 2000 - Europe. Technical report, European Environmental Agency

Jørgensen H., Mikkelsen T., Mann J., Bryce D., Coffey A. S., Harris M., and Smith D. A. (2004) Site wind field determination using a CW Doppler lidar - comparison with cup anemometers at Risø. *Proc. EWEA Special Topic Conference: The Science of Making Torque from Wind* 261–266. Delft University, Delft

Leosphere (2009) Windcube information booklet

Lindelöw P. (2007) Uncertainties in wind assessment with lidar. Risø technical report, Risø-I-1234(EN), Risø DTU, Roskilde

Mann J., Peña A., Bingöl F., Wagner R., and Courtney M. S. (2010) Lidar scanning of momentum flux in and above the surface layer. *J. Atmos. Oceanic Tech.*, in press

Mayor S. D., Lenschow D. H., Schwiesow R. L., Mann J., Frush C. L., and Simon M. K. (1997) Validation of NCAR 10.6-μm CO_2 Doppler lidar radial velocity measurements and comparison with a 915-MHz profiler. *J. Atmos. Oceanic Tech.*, **14**:1110–1126

Mikkelsen T., Mann J., Courtney M., and Sjöholm M. Windscanner: 3-D wind and turbulence measurements from three steerable doppler lidars (2008) *IOP Conf. Series: Earth and Environ. Sci.* 012018 (9pp)

Pedersen T. F., Gjerding S., Ingham P., Enevoldsen P., Hansen J. K., and Jørgensen H. K. (2002) Wind turbine power performance verification in complex terrain and wind farms. Technical report, Risø-R-1330(EN), Risø DTU, Roskilde

Peña A., Gryning S.-E., and Hasager C. B. (2010a) Comparing mixing-length models of the diabatic wind profile over homogeneous terrain. *Theor. Appl. Climatol.* **100**:325–335

Peña A., Hasager C. B., Gryning S.-E., Courtney M., Antoniou I., Mikkelsen T. (2009) Offshore wind profiling using light detection and ranging measurements. *Wind Energy* **12**:105–124

SgurrEnergy (2009) Galion

Smith D. A., Harris M., Coffey A. S., Mikkelsen T., Jørgensen H. E., Mann J., and Danielian R. (2006) Wind lidar evaluation at the Danish wind test site in Høvsøre. *Wind Energy* **9**:87–93

TheWindPower.net (2009) Windparks in Europe. Database, TheWindPower

Trujillo J. J., Bingöl F., Larsen G. C., Mann J., and Kühn M. Lidar measurements of wake dynamics, Part II : Two dimensional scanning. *Wind Energy*, In press

8 Lidars and wind turbine control

David Schlipf, Oliver Bischoff, Martin Hofsäß,
Andreas Rettenmeier, Juan José Trujillo, and Martin Kühn
Endowed Chair of Wind Energy, Institute of Aircraft Design,
Universität Stuttgart, Stuttgart, Germany

8.1 Introduction

Reducing mechanical loads caused by atmospheric turbulence and energy optimization in the presence of varying wind are the key issue for wind turbine control. In terms of control theory changes in the inflowing wind field as gusts, varying shears and directional changes represent unknown disturbances. However, conventional feedback controllers can compensate such excitations only with a delay since the disturbance has to be detected by its effects to the turbine. This usually results in undesired loads and energy losses of wind turbines.

From the control theory point of view disturbance rejection can be improved by a feed-forward control if the disturbance is known. Not fully covered by theory, but used in practice is the further advantage of knowing the disturbance in the future, e.g. in chassis suspension or in daily life when vision is used to circumnavigate obstacles with a bicycle.

In a similar way wind field measurements with remote sensing technologies such as lidar might pave the way for predictive wind turbine control strategies aiming to increase energy yield and reduce excessive loads on turbine components. Remote sensing offers wind speed tracking at various points in space and time in advance of reaching the turbine and before hitting sensors at the blades or nacelle. This provides the control and safety system with sufficient reaction and processing time.

In Figure 75 the different steps for predictive wind turbine control are shown. The objective of the first step is to obtain wind fields in different distances in front of the turbine, e.g. by use of lidar. In the next step, turbulence theory, e.g. the "Taylor's frozen turbulence theorem", is considered when modelling the wind on its way towards the turbine. In the last step, the predicted future wind fields are used to improve wind turbine control by model predictive control strategies.
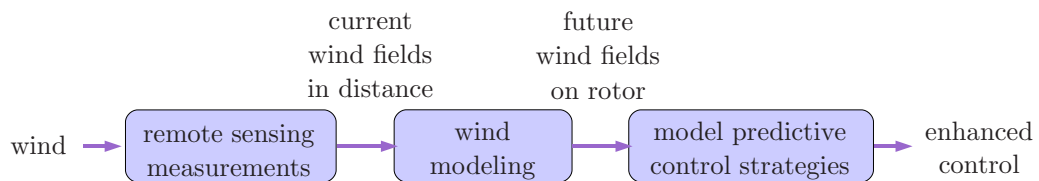

Figure 75. Steps in model predictive wind turbine control assisted by remote sensing

8.2 Measuring wind fields with lidar

Wind fields can be considered as time variant vector fields: one vector $\mathbf{a}$ in each point in space $\mathbf{p}$. Therefore the objective of wind fields assessment is to reconstruct wind fields in discrete space and time points as much as possible.

Commercial lidar systems have the disadvantage that they are not flexible due to measurement in conical domain and normally they are ground based and don't measure

in main wind direction. Thus nacelle based lidar systems with scanner or beam splitter are better suited, but still some issues have to be considered:

- Which points have to be scanned to get best information for control purpose?

- How does the probe volume effect the measurements?

- How can 3D vectors be reconstructed from line-of-sight measurements to obtain information for control? (see section 8.2)

To investigate these effects, a lidar simulator is presented in section 8.2.

The "Cyclops" dilemma

As a Cyclops cannot see three-dimensionally with only one eye, it isn't possible to measure a 3D wind vector with only one lidar system. Three lidar systems focusing in the same point with linearly independent laser beams are needed. With one nacelle mounted lidar system, the two missing systems can be substituted by different assumptions, e.g.:

1. no vertical and no horizontal wind component, or

2. no vertical component and homogenous flow on each height

In Figure 76 the effect of both assumption possibilities is shown. In this case the 3D vectors in p_1 and p_2 (measured in the same height) should be reconstructed from the line-of-sight wind speeds v_{los1} and v_{los2}. The first assumption yield a_{11} and a_{21} representing a horizontal shear. With the second assumption the resulting vectors a_{21} and a_{22} are equal representing a cross-flow, as homogenous flow on each height was assumed.

The dilemma consist, if the lidar measurement should be used for yaw and pitch control at the same time: If the first assumption is used to calculate the inhomogeneous inflow, perfect alignment is assumed. If the second assumption is used to obtain the misalignment, homogeneous flow is assumed.
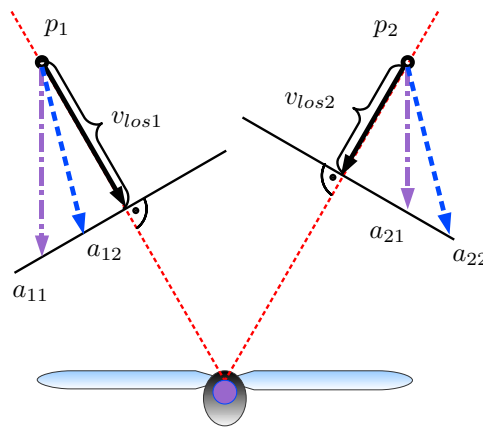

Figure 76. Different possibilities of 3D wind vector reconstruction

WITLIS (WInd Turbine LIdar Simulator)

To understand better the above mentioned effects and to plan measurement campaigns it is helpful to simulate lidar measurements. The main objective of the simulation tool is to reproduce the operation of a nacelle-mounted lidar system. Thus the tool facilitates the evaluation of scanning patterns to find the best hardware and software solution for applications like control, power curve assessment and wake measurements. Wind turbine

control strategies based on lidar can be tested with aeroelastic wind turbine simulation tools in a realistic setup. A modular setup provides software parts that can be used to process measurement data in the same way as simulated data (see Figure 77).

Figure 78 depicts the wind field reconstruction of a simulated measurement: On the left side a generic wind field from TurbSim (Jonkman, 2009) is shown superposed with a wake for better illustration. On the right side the interpolated wind field with WITLIS can be seen. The dots represent a real trajectory as can be done by the adapted Windcube lidar and perfect alignment is assumed. It can be seen that main characteristics can be measured.
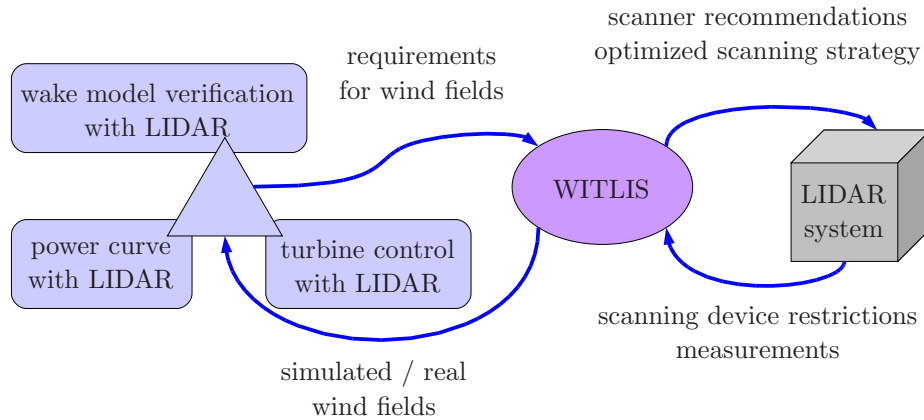

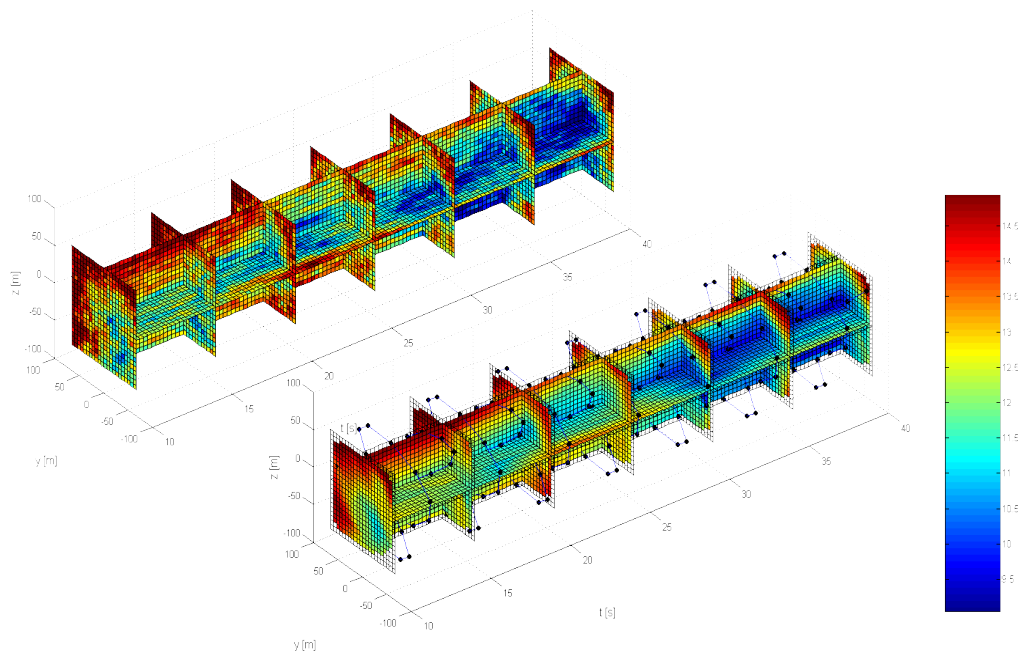Figure 77. Interactions between the applications, the simulator and the lidar system

Figure 78. Simulation of realistic lidar measurements in a turbine wake: Original down-flow wind component (left) and scanned (right) downflow wind component

8.3 Prediction of wind fields

The inflow wind field for control purpose shouldn't be measured in the rotor plane because of several reasons:

- Because of stability and performance reasons the undisturbed wind field should be measured. But wind in rotor plane is affected by the turbine itself.

- It is difficult to perform measurements in the rotor plane, e.g. with pitot tubes or lidar on the blades.

- Measuring in front of the turbine provides the control system more time to react. The easiest way to model the wind on its way towards the turbine is to use "Taylor's frozen turbulence theorem". It assumes that wind characteristics remain the same while being transported through space with the mean wind speed.

8.4 Improving control

The new information of upwind wind speeds obtained by lidar measurements can be used for improving the turbines control systems. Thereby we distinguish between four different control activities: Yaw control, speed control, collective pitch control and individual pitch control. Possible benefit and potential is listed respectively in table 13.

Table 13. Possible application and benefit of lidar based control. Here is assumed that measurements are at least as beneficial as (e)stimation.

	benefit	potential	reference
yaw	more energy	up to 12%	Cath the Wind (2009)
speed	more energy	up to 10%(e)	Boukhezzar and Siguerdidjane (2005)
collective pitch	less loads	up to 20%	Schlipf and Kühn (2008)
individual pitch	less loads	up to 30%(e)	Selvam et al. (2009)

In this paper we will focus on advanced collective pitch control only.

Predictive Disturbance Compensation (PDC)

Fluctuating wind speed causes the speed of rotation to vary, which affects the loads to the turbine. The objective of pitch control in full operating load range is therefore to maintain a constant rotational speed of the rotor. The wind speed data provided by a lidar can be used to compensate wind speed fluctuations. The block diagram in figure 79 illustrates the control schema.
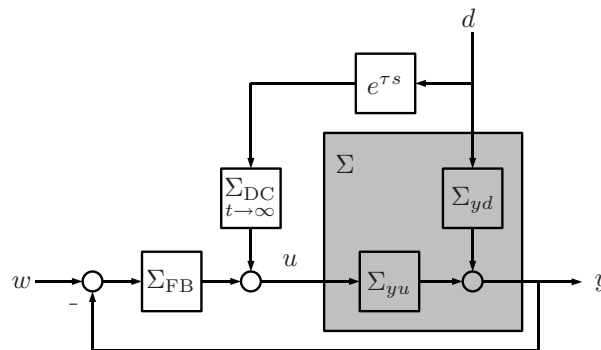

Figure 79. Control loop with predictive disturbance compensation.

The output y (in this case the rotor speed Ω) is influenced by two signals: pitch angle β which is identically equal to the control input u and the effective wind speed v_{eff} which is a disturbance d in terms of control theory. Subsequently the wind turbine system Σ can theoretically be divided into two subsystems, Σ_{yu} and Σ_{yd}. If d is now forwarded by a transfer function Σ_{DC} to the control input u, a compensation of the disturbance can be reached. In this case the feedback controller Σ_{FB} is responsible for reference signal tracking and Σ_{DC} for disturbance rejection.

$\Sigma_{\text{DC}} = -\Sigma_{yu}^{-1}\Sigma_{yd}$ would give a perfect compensation, but in practice the inversion of the nonlinear dynamic turbine model Σ_{yu} cannot be calculated. Therefore a static compensation is proposed

$$\Sigma_{\text{DC}}_{t \to \infty} = u_{\text{ss}}(d_{\text{ss}})$$

which is the static value u_{ss} of the system input subject to the static disturbance d_{ss}. The feedback controller Σ_{FB} then will react during the dynamic transitions.

The time interval of the transition is influenced by the difference in the dynamic orders of Σ_{yd} and Σ_{yu}. In the case of pitch control Σ_{yu} has a higher dynamic order, because pitch angles have a delayed impact on the rotor speed compared to the wind disturbance. Therefore a prediction time τ shifts the disturbance signal in time in the way that the pitch moves earlier. Due to the lidar measurement in front of the rotor plane this prediction is possible.

Stability of the control loop is influenced neither by the added static feed-forward control nor by time shift, because none of the newly implemented blocks is part of the closed control loop and no new poles were introduced.

Simulation

For evaluation of the proposed controller a Simulink implementation of the generic aero-elastic NREL offshore 5-MW baseline wind turbine model (Jonkman et al., 2009) was used (see Table 14).

Table 14. Specification of the generic NREL wind turbine model.

Rotor	upwind, 3 blades
Rated power output	$P_{\text{rated}} = 5$ MW @ $\Omega_{\text{rated}} = 12.1$ rpm
Dimensions	$D = 126$ m, $h = 90$ m
Controller	collective pitch with gain scheduling
Pitch actuator	2nd order
Filter	Ω, β, v_{w} : 1st order

For the PDC implementation the shift time τ is chosen to

$$\tau = T_{63, \text{ filter wind}} + T_{63, \text{ pitch actuator}} = 1 \text{ s}$$

where T_{63} denotes the rise time to 63 % of the filters and actuators final value respectively.

The static pitch over wind speed donated $\beta_{\text{ss}}(v_{w,\text{ss}})$ is given in Jonkman et al. (2009) and shown in Figure 80.

The wind is modeled using the stochastic, full-field, turbulent-wind simulator TurbSim (Jonkman, 2009). The measuring of the full-field wind is simulated using WITLIS, see section 8.2. In order to use the wind data for collective pitch control, it is necessary to reduce it to one effective wind speed v_{eff}. Therefore a weighting function (Figure 81) has been developed Schlipf and Kühn (2008). It takes account of the impact of the wind on the aerodynamic torque with respect to the radius using Prandtl root and tip losses.
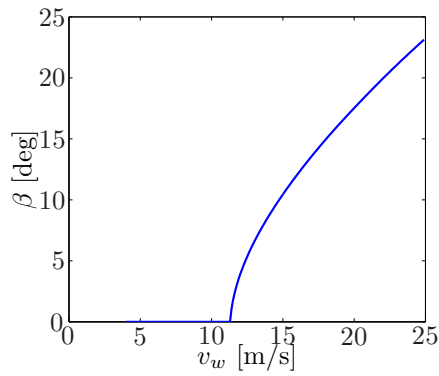
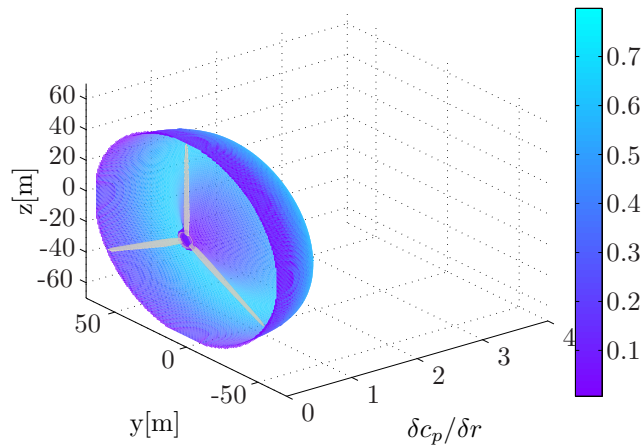*Figure 80. Static pitch over wind speed of the NREL turbine model.*

Figure 81. Weighting function for the calculation of the effective wind speed.

Results

The following simulation results show the impact of the proportional-integral (PI) controller and the PDC on rotor speed and bending moment respectively. In frequency domain for PDC a better disturbance rejection in the frequency range up to 0.3 Hz can be observed (figure 82), in which according to the Kaimal spectrum the wind contains most of its energy.
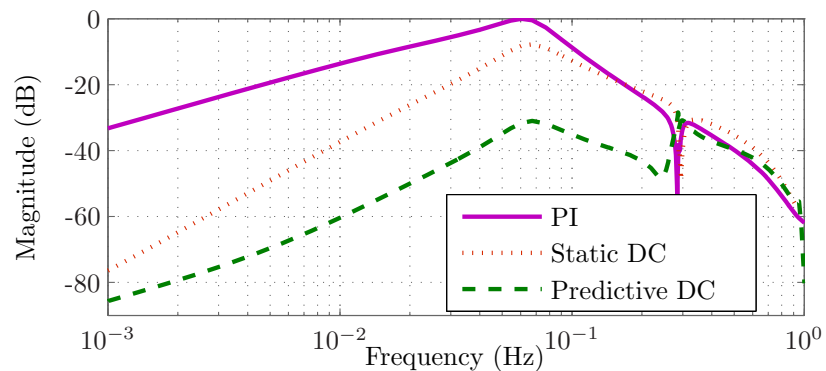

Figure 82. Frequency domain: disturbance rejection of different control strategies.

Extreme Operating Gust (EOG)

Figure 83 shows the results in time domain of simulations of an EOG according to IEC (2005) applied on the NREL wind turbine model. Here, no turbulence occurs and perfect measurement is assumed.
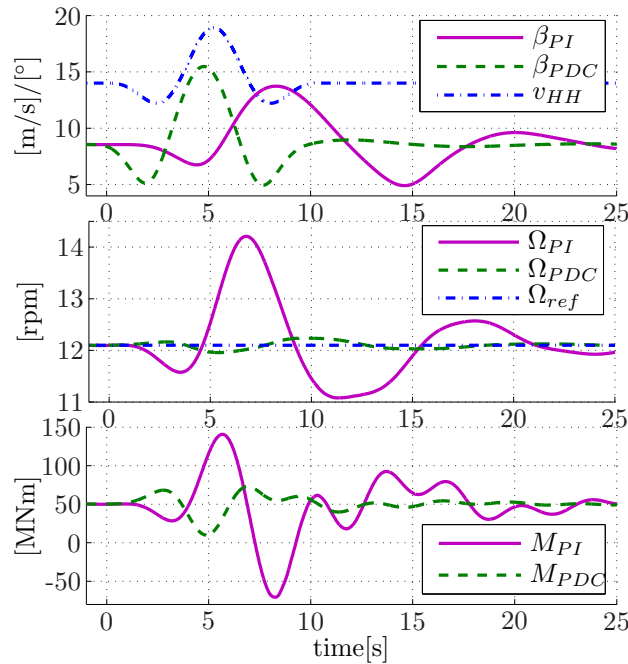

Figure 83. Comparison of conventional and PDC control strategy (EOG). The subscript ref denotes reference

PDC control technique leads to a significantly reduced rotor overspeed. Consequently the fore-aft bending moment M_{yT} at the tower base is decreased by PDC as well, compare table 15.

Table 15. Standard deviation of signals from figure 83

	PI	PDC	PDC/PI
$\sigma(\Omega)$ / [rpm]	0.74	0.08	9%
$\sigma(M_{yT})$ / [MNm]	38.2	11.0	29%

Turbulent Wind Field

Figure 84 and table 16 show the results for simulations with realistic turbulent wind fields with a spatial resolution of 9 m and a time resolution of 0.05 s. It is based on a Kaimal spectrum with a mean wind speed at hub height of $v_H = 18 \text{ m s}^{-1}$ and turbulence intensity of $TI = 16 \%$. Again, perfect measurement is assumed.

PDC reduces rotor speed variation and loads at the tower base despite lower pitch dynamics occur. Simulations also show reduced loads at the blades.

Measurement simulation using WITLIS

In a third simulation the influence of a non-perfect measurement, simulated by WITLIS (see section 8.2) was investigated. From table 17 it can be seen that there is still a remarkable improvement using PDC.
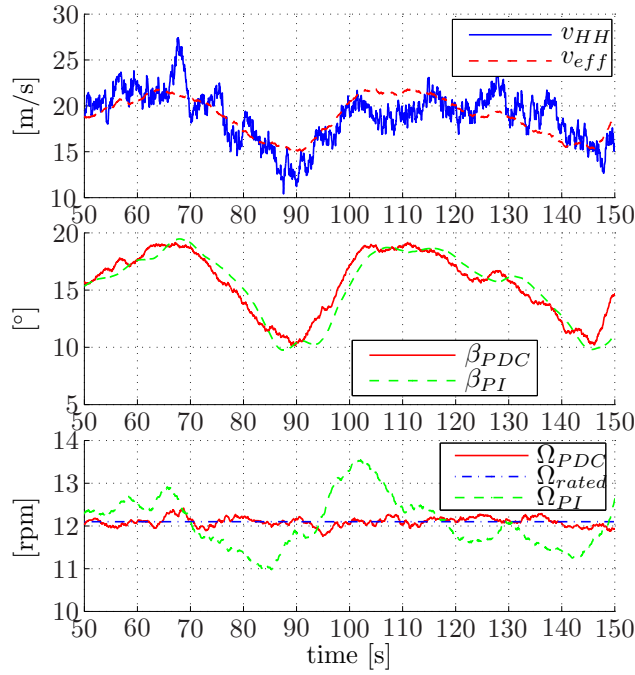
Figure 84. Comparison of conventional and PDC control strategy (turbulent wind field). v_{HH} is the hub height wind speed

Table 16. Standard deviation of signals from figure 84

	PI	PDC	PDC/PI
$\sigma(\Omega)$ / [rpm]	0.42	0.09	21%
$\sigma(M_{yT})$ / [MNm]	12.8	8.72	68%
$\sigma(\dot{\beta})$ / [deg/s]	0.60	0.47	78%

Robustness

A weaker performance of the PDC than the conventional PI controller is possible, if there are errors which are not included in the simulation, e.g.

- inaccurate measurements of the wind speed

- wrong calculation of the effective wind speed

- incorrect static pitch curve

- errors in the model used

- invalidity of Taylor's frozen turbulence theorem

- wrong estimate of the shift time τ

Simulations with a varying parameter τ (figure 85) result in a wide range, where the performance results of the PDC remain superior to the PI control.

Table 17. Standard deviation of signals from simulation including WITLIS.

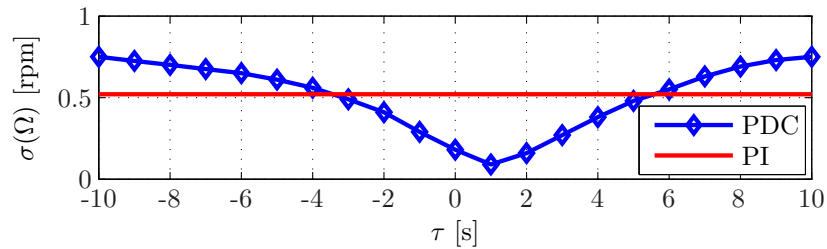|	PI	PDC	PDC/PI
$\sigma(\Omega)$ / [rpm]	0.48	0.17	35%
$\sigma(M_{yT})$ / [MNm]	15.1	11.8	87%
$\sigma(\dot{\beta})$ / [deg/s]	0.79	0.65	83%

Figure 85. Standard deviation of Ω subject to different prediction time shifts τ for PDC and PI control

Conclusions PDC

The proposed predictive disturbance compensation was presented as a new and powerful control strategy for wind turbine control in full load range. PDC has a guaranteed stability and implementation needs static pitch over wind speed information and one prediction time parameter only.

The performed simulations indicate a significant decrease in rotor speed variation and tower and blade loads without higher pitch actuator activity.

Further research concerns the other control objectives of table 13 as yaw control, speed control and individual pitch control by use of lidar measurements.

Notation

a	horizontal shear of the flow
$\mathbf{a}$	wind vector
d	disturbance
D	rotor diameter
EOG	extreme operating gust
h	hub height
M_{yT}	tower fore-aft bending moment
$\mathbf{p}$	vector point in space
P_{rated}	rated power output
PDC	predictive disturbance compensation
PI	proportional-integral (controller)
T_{X}	X% rising time
TI	turbulence intensity
u	control input
v_{eff}	effective wind speed
v_{HH}	hub height wind speed
v_{los}	line-of-sight wind speed
WITLIS	wind turbine lidar simulator
x_{SS}	steady state of variable x
y	system output
β	pitch angle
σ_X	standard deviation of a variable X
Σ	a model system or a subsystem, e.g. a wind turbine
Σ_{FB}	feedback controller
Σ_{DC}	disturbance compensation
τ	prediction time of a signal
Ω_{rated}	rated rotor speed

References

Boukhezzar B. and Siguerdidjane H. (2005) Nonlinear control of variable speed wind turbines without wind speed measurement. *Proc. of the 44th IEEE Conf. on Decision and Control and the European Control Conf.*, Seville

Catch the Wind (2009) Boosting power production. Catch the Wind, Inc. **1**:15 pp

IEC (2005) IEC 61400-12-1 Wind turbines - Design requirements. Int. Electrotechnical Commission

Jonkman B. J. (2009) TurbSim User's Guide. Technical Report NREL/TP-500-46198, **1.5**, 85 pp

Jonkman B. J., Butterfield S., Musial W., and Scott G. (2009) Definition of a 5-MW reference wind turbine for offshore system development. Technical Report NREL/TP-500-38060, **1**, 75 pp

Schlipf D. and Kühn M. (2008) Prospects of a collective pitch control by means of predictive disturbance compensation assisted by wind speed measurements. *DEWEC* **1**:4 pp

Selvam K., Kane S., van Wingerden J. W., van Engelen T., and Verhaegen M. (2009) Feedback-feedforward individual pitch control for wind turbine load reduction. *Int. J. Robust Nonlinear Control* **19**:72–91

9 Derivation of the mixing-layer height by remote sensing including RASS

Stefan Emeis
Institute for Meteorology and Climate Research,
Atmospheric Environmental Research Division (IMK-IFU),
Karlsruhe Institute of Technology, Garmish-Partenkirchen, Germany

9.1 Introduction

This chapter gives an overview of the derivation of mixing-layer height (MLH) by surface-based remote sensing instruments. Sometimes the terms mixed-layer height or mixing height are used as well for MLH, but we will stick here to the most common term mixing-layer height. The detection of the vertical layering of the atmospheric boundary layer (ABL) is one of the principal tasks of experimental boundary-layer research. We must distinguish between the mixing-layer height, MLH (see section 9.2) and the boundary-layer height, z_i (see section 9.3). The boundary-layer height is the height up to which the influence of the presence of the lower surface is detectable. The mixing-layer height is the height up to which atmospheric properties (such as wind speed and turbulence) or substances originating from the surface are dispersed by turbulent vertical mixing processes. The mixing-layer – if it is present at all – is a part of the ABL. Thus, the mixing-layer height is usually shallower than the boundary layer, but it fills the whole ABL in deep convective boundary layers.

The next section describes methods to detect the mixing-layer height, while section 9.3 briefly mentions methods to capture the boundary-layer height. Acoustic (see Chapter 16) and optical (see the majority of the preceding chapters) sounding techniques have got a broad coverage in throughout this volume. RASS techniques are quite unusual in the assessment of wind resources. Therefore, a subsection on technical details of this instrumentation has been added in section 9.2. A more complete survey of remote sensing instrumentation is given in Emeis (2010a) and an overview of applications of ground-based remote sensing is presented in Emeis (2010b).

9.2 Mixing-layer height

The mixing-layer height is the height up to which atmospheric properties or substances originating from the Earth's surface or formed within this layer are dispersed almost uniformly over the entire depth of this layer by turbulent vertical mixing processes. Therefore, the existence and the height of a mixing layer can either be analyzed from a detection of the presence of the mixing process, i.e. turbulence, or from the verification that a given conservative atmospheric variable is distributed evenly over a certain height range. The level of turbulence can for instance be derived from fluctuations of the wind components or from temperature fluctuations. Suitable conservative atmospheric variables for the identification of the mixing layer and its height are, e.g., potential temperature, specific humidity or aerosol particle concentrations.

The latest rather complete overview of methods to determine MLH from in-situ measurements and surface-based remote sensing had been given by Seibert et al. (2000). Since then considerable development has taken place, especially concerning the usage of surface-based remote sensing methods (see the review paper by Emeis et al. (2008)). This chapter will mainly follow this latter review.

Optical methods for MLH detection may be used to illustrate this recent progress.

Seibert et al. (2000) still classified lidar methods as expensive, not eye-save, with a high lowest range gate, limited range resolution, and sometimes subject to ambiguous interpretation. This has changed drastically in the last ten years when better lidars have been built and ceilometers have been discovered to be a nearly ideal boundary layer sounding instrument. Progress has been made in the field of acoustic sounding as well. Similarly, algorithms for the determination of MLH from vertical profiles of the acoustic backscatter intensity as described in Beyrich (1997) and Seibert et al. (2000) have been enhanced by using further variables available from sodar measurements such as the wind speed and the variance of the vertical velocity component (Asimakopoulos et al., 2004; Emeis and Türk, 2004). Such enhancements had been named as possible methods in Beyrich (1995) and Seibert et al. (2000) but obviously no example was available at that time.

A variety of different algorithms have been developed by which the MLH is derived from ground-based remote sensing data (see Table 18 for a short overview). We will mainly concentrate on acoustic and optical remote sensing because electro-magnetic remote sensing has too high lowest range gates for a good coverage of shallow MLH. The disadvantage of a too high lowest range gate can partly be circumvented by slantwise profiling or conical scanning if the assumption of horizontal homogeneity can be made.

Table 18. Overview of methods using ground-based remote sensing for the derivation of the mixing-layer height mentioned in this chapter (see right most column for section number).

| method	short description	section
acoustic ARE	analysis of acoustic backscatter intensity	9.2-sodar
acoustic HWS	analysis of wind speed profiles	9.2-sodar
acoustic VWV	analysis of vertical wind variance profiles	9.2-sodar
acoustic EARE	analysis of backscatter and vertical wind variance profiles	9.2-sodar
optical threshold	detection of a given backscatter intensity threshold	9.2-ceilometer
optical gradient	analysis of backscatter intensity profiles	9.2-ceilometer
optical idealized backscatter	analysis of backscatter intensity profiles	9.2-ceilometer
optical wavelet	analysis of backscatter intensity profiles	9.2-ceilometer
optical variance	analysis of backscatter intensity profiles	9.2-ceilometer
acoustic/electro-magnetic	RASS	9.2-RASS
acoustic/electro-magnetic	sodar-RASS and windprofiler-RASS	9.2-RASS
acoustic/electro-magnetic/in situ	sodar-RASS plus surface heat flux data	9.2-RASS
acoustic/electro-magnetic	sodar plus windprofiler	9.2-further techniques
acoustic/optical	sodar plus ceilometer	9.2-further techniques
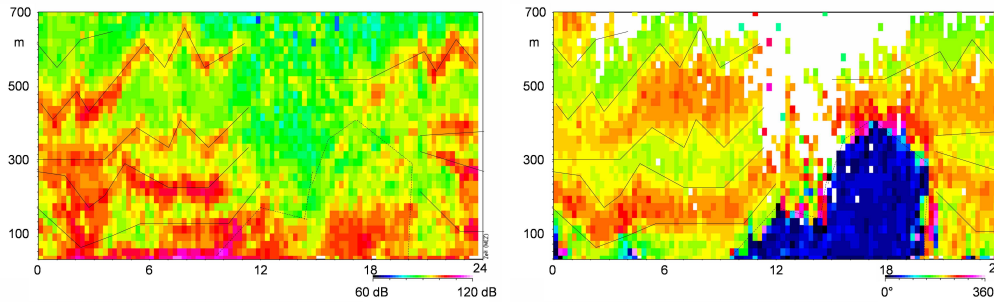
Figure 86. Sample time-height cross-section from acoustic sounding with a sodar. Left: acoustic backscatter intensity, right: horizontal wind direction. Thin black lines demark inversions.

Sodar

Acoustic methods either analyze the acoustic backscatter intensity, or, if Doppler shifts in the backscattered pulses can be analyzed, features of vertical profiles of the wind components and its variances as well. The acoustic backscatter intensity is proportional to small-scale fluctuations in atmospheric temperature (usually generated by turbulence) or by stronger vertical temperature gradients. The latter feature may be an indication for the presence of temperature inversions, which can often be found at the top of the mixing layer.

Beyrich (1997) listed possible analyses which can mainly be made from acoustic backscatter intensities measured by a sodar. Later, Asimakopoulos et al. (2004) summarized three different methods to derive MLH from sodar data: (1) the horizontal wind speed method (HWS), (2) the acoustic received echo method (ARE), and (3) the vertical wind variance method (VWV). We will mainly follow this classification here and finally add a fourth method, the enhanced ARE method (EARE).

Figure 86, showing an acoustic sounding taken in an Alpine valley, gives an impression what wealth of detailed vertical information can be derived from acoustic boundary-layer sounding. The left-hand frame displays the acoustic backscatter intensity and the right-hand frame the wind direction as time-height sections over one day (from midnight to midnight) and over a height range of 700 m. The depicted wintry situation from a day in January exhibits a multiple layering of the air in that valley due to the very stable thermal stratification of the valley air over a snow-covered valley floor. The multiple layering originated from an interlacing of down-valley (wind direction around 190°) and down-slope (wind direction around 230°) flows. The layers are separated by temperature inversions and each higher layer is potentially warmer than the next lower layer. They persisted nearly the whole day because no vertical mixing took place in the stably stratified valley atmosphere.

Acoustic received echo (ARE) method   The ARE method is the most basic method of determining MLH from acoustic remote sensing. Most of the methods listed in Beyrich (1997) belong to this method. The method does not require an analysis of the Doppler shift of the backscattered signals. The method makes use of the assumption that turbulence is larger in the mixing layer than in the atmosphere above, and that this turbulence is depicted in the intensity of the acoustic backscatter. MLH is analyzed either from the maximum negative slope or from the changing curvature of the vertical profile of the acoustic backscatter intensity or it is analyzed from the height where the backscatter intensity decreases below a certain pre-specified threshold value.

Horizontal wind speed (HWS) method   The HWS method requires the analysis of the Doppler shift of the backscattered acoustic signals. The algorithm is based on the analysis of the shape of hourly-averaged vertical wind speed profiles using the assumption that wind speed and wind direction are almost constant within the mixing layer but approach gradually towards the geostrophic values above the mixing layer. Beyrich (1997) listed this method in his Tab. 2 but did not discuss it further. The applicability of the method is probably limited to the well-developed convective boundary layers (CBL) due to the underlying assumptions. Such CBLs are often higher than the maximum range of a sodar. Even if the CBL height is within the range of the sodar the algorithm for the analysis of the Doppler shift often fails above the inversion topping of the CBL due to too low signal-to-noise ratios.

Vertical wind variance (VWV) method   The VWV method is also working only for CBLs. It is based on the vertical profile of the variance of the vertical velocity component σ_w. In a CBL σ_w reaches a maximum in a height az_i. Typical values for a are between 0.35 and 0.40. Thus, in principle, this is an extrapolation method. It has been tried for sodar measurements because it permits a detection of MLH up to heights which are 2.5 times above the limited maximum range (usually between 500 and 1000 m) of the sodar. Beyrich (1997) classified this method as not reliable.

Enhanced acoustic received echo (EARE) method   The EARE algorithm has been proposed by Emeis and Türk (2004) and Emeis et al. (2007). The method is an enhancement of the ARE method in two ways. Firstly, it includes further variables into the MLH algorithm that are available from Doppler-sodars. The benefits of the additional usage of the variance of the vertical velocity component have been demonstrated by Emeis and Türk (2004). Secondly, it determines not only MLH from sodar measurements but also the heights of additional lifted inversions. Especially in orographically complex terrain, the vertical structure of the ABL can be very complicated. Emeis et al. (2007) have shown that several persistent inversions one above the other which form in deep Alpine valleys can be detected from sodar measurements (Fig. 86).

EARE determines three different types of heights based on acoustic backscatter intensity and the variance of the vertical velocity component. Because the horizontal wind information above the inversion is not regularly available from sodar measurements, horizontal wind data have not been included into this scheme. In the following a letter "H" and an attached number will denote certain derived heights which are related to inversions and the MLH; while the variable z is used to denote the normal vertical coordinate. The EARE algorithm detects:

- the height ($H1$) of a turbulent layer characterised by high acoustic backscatter intensities $R(z)$ due to thermal fluctuations (therefore having a high variance of the vertical velocity component σ_w),

- several lifted inversions ($H2_n$) characterized by secondary maxima of acoustic backscatter due to a sharp increase of temperature with height and simultaneously low σ_w (like those depicted in the left-hand frame of Fig. 86), and

- the height of a surface-based stable layer ($H3$) characterised by high backscatter intensities due to a large mean vertical temperature gradient starting directly at the ground and having a low variance of the vertical velocity component.

The height $H1$ corresponds to a sharp decrease $\partial R/\partial z < DR_1$ of the acoustic backscatter intensity $R(z)$ below a threshold value R_c with height z usually indicating the top of a turbulent layer:

$$H1 = z, \quad \text{if} \quad (R(z) < R_c \quad \text{and} \quad R(z+1) < R(z) + zDR_1$$
$$\text{and} \quad R(z+2) < R(z) + 2zDR_1). \tag{152}$$

$R_c = 88$ dB and $DR_1 = -0.16$ dB m^{-1} have proven to be meaningful values in the above mentioned studies. R_c is somewhat arbitrary because the received acoustic backscatter intensities from a sodar cannot be absolutely calibrated. An absolute calibration would require the knowledge of temperature and humidity distributions along the sound paths for a precise calculation of the sound attenuation in the air. DR_1 is, at least for smaller vertical distances, independent from the absolute value of R_c. An application-dependent fine-tuning of R_c and DR_1 may be necessary.

Elevated inversions are diagnosed from secondary maxima of the backscatter intensity that are not related to high turbulence intensities. For elevated inversions increase in backscatter intensity below a certain height $z = H2$ and a decrease above is stipulated while the turbulence intensity is low:

$$H2_n = z, \quad \text{if} \quad (\partial R/\partial z|_{z+1} < -DR_2 \quad \text{and} \quad \partial R/\partial z|_{z-1} > DR_2$$
$$\text{and} \quad \sigma_w < 0.70 \text{ m s}^{-1}) \qquad (153)$$

for $n = 1, ..., N$. In Emeis et al. (2007) N was chosen to be five. A threshold value $DR_2 = 0.08$ dB m^{-1} has proven suitable. But again, an application-dependent tuning may be advisable.

The determination of the height of the stable surface layer $H3$ is started if the backscatter intensity in the lowest range gates is above 105 dB while σ_w is smaller than 0.3 m s^{-1}. The top of the stable layer $H3$ is at the height where either the backscatter intensity sinks below 105 dB or σ_w increases above 0.3 m s^{-1},

$$H3 = z, \text{ if } (R(z) > 105 \text{ dB and } R(z+1) < 105 \text{ dB and } \sigma_w(z) < 0.3\text{m s}^{-1}) \text{ or}$$
$$\text{if } (\sigma_w(z) < 0.3 \text{ m s}^{-1} \text{ and } \sigma_w(z+1) > 0.3 \text{ m s}^{-1} \text{ and } R(z) > 105 \text{ dB})(154)$$

The σ_w values used in Eqs. (153) and (154) have been determined by optimizing the automatic application of the detection algorithm. In doing so it turned out that no lifted inversions occurred with a variance σ_w higher than 0.7 m s^{-1} and that the variance σ_w in nocturnal stable surface layers was always below 0.3 m s^{-1}. The first σ_w threshold made it possible to distinguish between inversions and elevated layers of enhanced turbulence. The latter σ_w threshold made it possible to differentiate between nocturnal stable surface layers and daytime super-adiabatic surface layers although both types of surface layers yield more or less the same level of backscatter intensity. Finally MLH from the acoustic remote sensing is determined as the minimum of $H1$, $H2_1$, and $H3$:

$$\text{MLH}_{ac} = \min\left(H1, H2_1, H3\right). \qquad (155)$$

Ceilometer

Usually the aerosol content of the mixing layer is higher than in the atmospheric layer above, because the emission sources for aerosol are in most cases on the ground. Aerosol formation from precursors mainly takes place near the surface as well. Making the assumption that the vertical aerosol distribution adapts rapidly to the changing thermal structure of the boundary layer, MLH can be determined from the analysis of the vertical aerosol distribution. This also includes the assumption that the vertical aerosol distribution is not dominated by horizontally advected aerosol plumes or layers. The heights of the near surface aerosol layers ($H4_n$) can be analysed from the optical vertical backscatter profile obtained from optical remote sensing. Several methods have been developed, the most prominent of these being: (1) the threshold method, (2) the gradient or derivative method, (3) the idealised gradient method, (4) the wavelet method, and (5) the variance method.
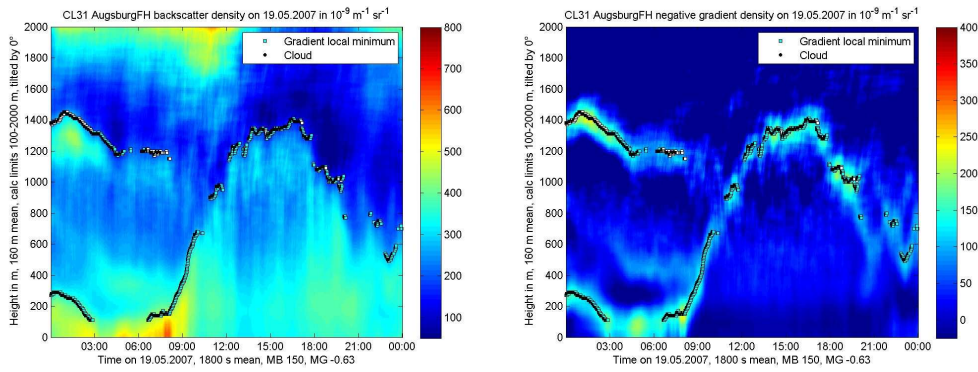
Figure 87. Sample time-height cross-section from optical sounding with a ceilometer. Left: optical backscatter intensity, right: vertical derivative of this backscatter intensity. Dots mark mixing-layer height derived from a gradient algorithm.

The application of optical remote sensing for MLH determination has focussed on the use of ceilometers in recent years. Ceilometers can be regarded as a small lidar. They are simpler and they have a much lower lowest range gate than lidars. For the detection of MLH below 150 to 200 m a ceilometer with one optical axis for the emitted and the received beam should be used. Due to the thin light beams the overlap of the emitted and received beam from a ceilometer with two parallel optical axes can be insufficient in this height range. Further on, Doppler shifts are not analyzed by ceilometers. Therefore, in contrast to acoustic remote sensing with Doppler-sodars, additional variables in addition to the backscatter intensity are not available from ceilometers for the design of determination schemes for MLH. Thus the schemes listed below all resemble to the ARE methods for acoustic remote sensing.

Figure 87 shows a sample measurement with a mono-axial ceilometer. The left-hand frame displays the optical backscatter intensity and the right-hand frame the negative vertical derivative of this intensity as time-height sections over one day (from midnight to midnight) and over a height range of 2000 m. The data was received on a clear day in spring and the vertical structure of the ABL was dominated by surface heating due to incoming solar radiation during daytime and radiative surface cooling during night-time. In the morning hours until about 0900 LST a shallow stable nocturnal surface layer with a depth of about 200 m and a residual layer with a depth of about 1200 to 1400 m can be distinguished. From 0900 LST onwards the evolution of a daytime convective boundary layer with a maximum depth of about 1400 m can be clearly seen. The dots in both frames of Fig. 87 indicate the mixing-layer height determined with the gradient method described below. The right-hand frame in Fig. 87 demonstrates that the analysed MLH values indeed coincide with maxima of the negative vertical gradient of the optical backscatter intensity.

Threshold method Melfi et al. (1985) and Boers et al. (1988) used simple signal threshold values, though this method suffers from the need to define them appropriately (Sicard et al., 2006). $H4$ is defined here as the height within the vertical profile of the optical backscatter intensity where the backscatter intensity first exceeds a given threshold when coming downward from the free unpolluted troposphere. The determination of several heights $H4_n$ would require the definition of several thresholds which probably cannot be done a priory to the analysis. Therefore this will always lead to a subjective analysis of MLH. The left-hand frame in Fig. 87 shows that the threshold value cannot be kept constant during the diurnal evolution of the boundary layer in order to get a result which is comparable to the one from the gradient method applied in Fig. 87.

Gradient or derivative methods Hayden et al. (1997) and Flamant et al. (1997) proposed to use the largest negative peak of the first derivative of the optical attenuated backscatter intensity ($B(z)$) for the detection of $H4$ from LIDAR data (height of gradient minimum $H4_{\mathrm{GM}}$):

$$H4_{\mathrm{GM}} = \min(\partial B(z)/\partial z). \qquad (156)$$

The right-hand frame of Fig. 87 demonstrates that this is a very meaningful assumption. Likewise Wulfmeyer (1999) used the first minimum of the slope to detect the top of a convective boundary layer from DIAL data. Münkel and Räsänen (2004) and Schäfer et al. (2004, 2005) applied the gradient method to ceilometer data. Menut et al. (1999) took the minimum of the second derivative of $B(z)$ as the indication for MLH:

$$H4_{\mathrm{IPM}} = \min(\partial^2 B(z)/\partial z^2). \qquad (157)$$

This method is called inflection point method (IPM). It usually gives slightly lower values for $H4$ than the gradient method in Eq. (156). A further approach was suggested by Senff et al. (1996). They looked for the largest negative gradient in the logarithm of the backscatter intensity (height of logarithmic gradient minimum $H4_{\mathrm{LGM}}$):

$$H4_{\mathrm{LGM}} = \min(\partial \ln B(z)/\partial z). \qquad (158)$$

This approach usually gives the largest value for $H4$. According to Sicard et al. (2006) $H4_{\mathrm{IPM}}$ from Eq. (157) is closest to the MLH derived from radiosonde ascents via the Richardson method. The other two algorithms in Eqs. (156) and (158) give slightly higher values.

In Emeis et al. (2007) the gradient method in Eq. (156) has been further refined and extended to enable the calculation of up to $n = 5$ lifted inversions. This algorithm, which has also been used for the MLH analysis shown in Fig. 87, is described in the following. Prior to the determination of gradient minima the overlap and range corrected attenuated backscatter profiles have to be averaged over time and height to suppress noise generated artefacts. Therefore the $H4$ values are determined in a two-step procedure. Between 140 and 500 m height sliding averaging is done over 15 min and a height interval Δh of 80 m. In the layer between 500 and 2000 m Δh for vertical averaging is extended to 160 m. Two additional parameters have been introduced to further reduce the number of false hits. The minimum accepted attenuated backscatter intensity B_{min} right below a lifted inversion is set to 200×10^{-9} m^{-1} srad^{-1} in the lower layer and 250×10^{-9} m^{-1} srad^{-1} in the upper layer. Additionally the vertical gradient value $\partial B/\partial z_{\mathrm{max}}$ of a lifted inversion must be more negative than 0.30×10^{-9} m^{-2} srad^{-1} in the lower layer and more negative than -0.60×10^{-9} m^{-2} srad^{-1} in the upper layer.

If $B(z)$ denotes the measured attenuated backscatter intensity in the height z above ground averaged over time and height and Δh is the height averaging interval, then the gradient $\partial B/\partial z$ in the height z is calculated as

$$\partial B/\partial z|_z = (B(z + \Delta h/2) - B(z - \Delta h/2))/\Delta h. \qquad (159)$$

A gradient minimum is characterized by a change of sign from minus to plus of the second derivative of $B(z)$. The height interval under examination is searched from bottom to top for these gradient minima $H4_n$.

The second derivative of $B(z)$ in the height z is

$$\partial^2 B/\partial z^2|_z = \left(\partial B/\partial z|_{z+\Delta h/2} - \partial B/\partial z|_{z-\Delta h/2}\right)/\Delta h. \qquad (160)$$

There is a gradient minimum $H4_n$ in the height z if the second derivative of $B(z)$ one range gate below z is not positive, if the second derivative of $B(z)$ in the height z is positive, and if the false hit conditions mentioned above are fulfilled:

$$H4_n = z, \qquad \text{if } \partial^2 B/\partial z^2|_{z-1} \leq 0 \text{ and } \partial^2 B/\partial z^2|_z > 0 \text{ and } B(z - \Delta h/2) \geq B_{\min}$$

$$\text{and } \partial B/\partial z|_z \leq \partial B/\partial z_{\max} \text{ for } n = 1, ..., 5. \tag{161}$$

The MLH from optical remote sensing is taken as the lowest height $H4_n$:

$$\text{MLH}_{op} = H4_1. \tag{162}$$

Idealised backscatter method A parallel development by Eresmaa et al. (2006) using an idealised backscatter profile, originally described by Steyn et al. (1999), is also an extension of the gradient method. MLH is not determined from the observed backscatter profile, but from an idealised backscatter profile fitted to the observed profile. The robustness of this technique is founded on utilising the whole backscatter profile rather than just the portion surrounding the top of the mixing layer. In this method an idealized backscattering profile $B_i(z)$ is fitted to measured profile by the formula

$$B_i(z) = ((B_m + B_u)/2 - (B_m - B_u)/2) \operatorname{erf}((z - h)/\Delta h) \tag{163}$$

where B_m is the mean mixing layer backscatter, B_u is the mean backscatter in air above the mixing layer and Δh is related to the thickness of the entrainment layer capping the ABL in convective conditions. Two new parameters $A1$ and $A2$ are defined so that $A1 = (B_m + B_u)/2$ and $A2 = (B_m - B_u)/2$. The value of $A1$ is kept constant during the fitting procedure. A good estimation of $A1$ based on an initial order-of-magnitude guess for the MLH is crucial for the quality of the result.

Wavelet method A Wavelet method has been developed for the automatic determination of mixing layer height from backscatter profiles of an LD-40 ceilometer by de Haij et al. (2006). Before that wavelet transforms have been applied in recent studies for MLH determination from LIDAR observations (Cohn and Angevine, 2000; Davis et al., 2000; Brooks, 2003; Wulfmeyer and Janjić, 2005). The most important advantage of wavelet methods is the decomposition of the signal in both altitude as well as vertical spatial scale of the structures in the backscatter signal.

The Wavelet algorithm in de Haij et al. (2006) is applied to the 10 minute averaged range and overlap corrected backscatter profile $B(z)$ within a vertical domain of 90–3000 m. For each averaged profile the top of two significant aerosol layers are detected in order to detect MLH as well as the top of a secondary aerosol layer, like e.g. an advected aerosol layer or the residual layer. This Wavelet MLH method uses the scale averaged power spectrum profile $W_B(z)$ of the wavelet transform with 24 dilations between 15 and 360 m and step size 15 m. The top of the first layer, $H4_1$, is detected at the first range gate at which the scale averaged power spectrum $W_B(z)$ shows a local maximum, exceeding a threshold value of 0.1. This threshold value is empirically chosen, based on the analysis of several cases with both well pronounced and less clearly pronounced mixing layer tops. $H4_2$ is optionally determined in the height range between $H4_1$ and the upper boundary of detection. A valid $H4_2$ is detected at the level with the strongest local maximum of $W_B(z)$ provided that this maximum is larger than the $W_B(z)$ of $H4_1$. MLH is set equal to $H4_1$.

However, problems with this method arise e.g. in case of multiple (well defined) aerosol layers, which renders the selection of the correct mixing layer top ambiguous. Furthermore, in spring and summer the detection of the MLH for deep (convective) boundary layers often fails. This is mostly due to the high variability of the aerosol backscatter signal with height which limits the range for MLH estimation in those conditions (de Haij et al., 2006).
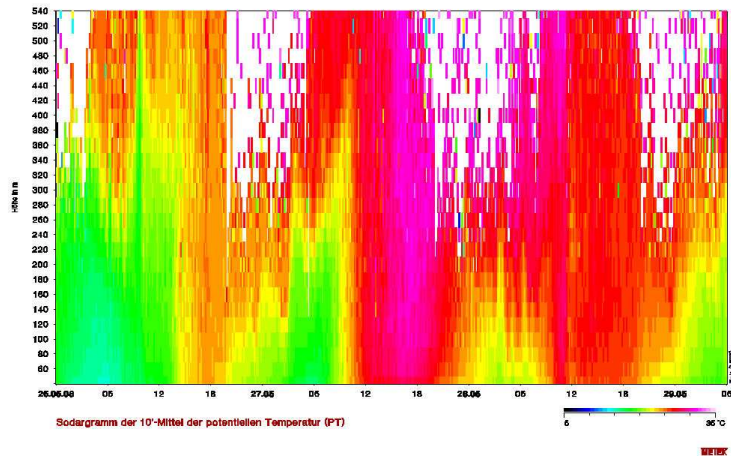
Figure 88. Sample time-height cross-section from a potential temperature sounding with RASS.

Variance method   At the top of the CBL we have entrainment of clear air masses from the free troposphere into the ABL. The entrainment process is temporarily variable and leads locally to considerable fluctuations in the aerosol concentration. Therefore the maximum in the vertical profile of the variance of the optical backscatter intensity can be an indicator for an entrainment layer on top of a CBL (Hooper and Eloranta, 1986; Piironen and Eloranta, 1995). The method is called variance centroid method in Menut et al. (1999). The variance method for the CBL height is also described in Lammert and Bösenberg (2006). Due to the assumptions made this method is suitable for daytime convective boundary layers only. An elucidating comparison between the gradient method and the variance method can be found in Martucci et al. (2004) although they used a Nd:YAG LIDAR at 532 nm instead of a ceilometer and thus suffered from a high lowest range gate in the order of 300 m.

RASS

The acoustic and optical methods for MLH determination, which have been described in the sections above, are all indirect methods that try to infer the mixing-layer height from other variables which usually adapt to the vertical structure of the ABL. The only direct and key variable for the analysis of the presence of a mixing layer is the vertical profile of virtual temperature. Temperature profiles can directly be measured with a radio-acoustic sounding system (RASS). Fig. 88 shows an example. We start here with a short description of the available RASS methods.

Instrumentation   A radio-acoustic sounding system (RASS) operates acoustic and electro-magnetic sounding simultaneously (Marshall et al., 1972). This instrument is able to detect acoustic shock fronts of the acoustic pulses and to determine their propagation speed from the Doppler shift of the backscattered electro-magnetic waves. This propagation speed is equal to the speed of sound which in turn is a known function of air temperature and humidity. To different types of RASS have been realised (Engelbart and Bange, 2002): a Bragg-RASS and a Doppler-RASS.

Bragg-(windprofiler) RASS   A Bragg-RASS (or windprofiler-RASS) is basically a windprofiler with an additional acoustic emitter. When the Bragg condition is fulfilled (Fig. 89), i.e. the wavelength of the sound waves λ_a is half the one of the electro-magnetic
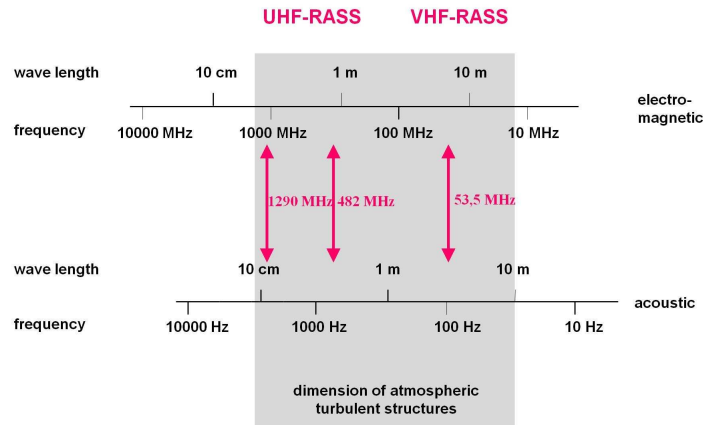
Figure 89. Bragg-related acoustic (below) and electro-magnetic (above) frequencies for RASS.

waves λ_e, then there is optimal backscatter of the electro-magnetic waves from the acoustic waves (Fig. 90). The electro-magnetic signal is emitted at a fixed frequency, but the emitted sound signal is a chirp signal with varying frequency f_a. From the sound wave length $\lambda_{a,B}$ at which optimal backscatter occurs the propagation speed of the sound signal can be determined via the following dispersion relation:

$$c_a = \lambda_{a,B} f_a / 2. \tag{164}$$

For a VHF windprofiler operating at 50 MHz a sound frequency of about 100 Hz is used, for a UHF windprofiler operating at 1 GHz a sound frequency around 2 kHz is most suitable to fulfil the Bragg condition. Because the attenuation of sound waves in the atmosphere is strongly frequency dependent, a UHF RASS can detect temperature profiles up to about 1.5 km height whereas a VHF RASS can observe temperature profiles throughout the troposphere.

Doppler-(sodar) RASS   A Doppler-RASS (or sodar-RASS) is a sodar with an additional electro-magnetic emitter and receiver (Fig. 91) operating at a frequency $f_{e,0}$. From the Doppler shift Δf_e of the electro-magnetic radiation which is backscattered at the density fluctuations caused by the sound waves the propagation speed c_a of the sound waves is determined:

$$c_a = -c\Delta f_e/(2f_{e,0}) \tag{165}$$

where c denotes the speed of light. A Doppler-RASS like a Bragg-RASS also emits a chirp sound signal in order to assure that the Bragg condition is optimally met due to the varying temperature over the entire height range.

The so determined propagation speed c_a is a sum of the speed of sound c_s and of the vertical movement of the air w within which the sound waves propagate:

$$c_a = c_s + w. \tag{166}$$

The vertical air speed component w can be determined separately from the Doppler shift of the backscattered electro-magnetic clear-air signal when operating a Bragg-RASS or from the Doppler shift of the backscattered acoustic signal when operating a Doppler-RASS. Using the definition of the acoustic temperature the height profile of c_s can then
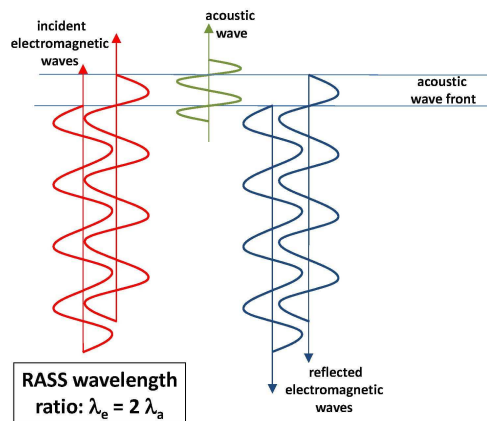
Figure 90. Bragg condition for RASS sounding.

Figure 91. Sodar-RASS. The acoustic antenna is in the middle, the electro-magnetic antennas to the left and right.

be converted in a height profile of the acoustic temperature T_a. For many purposes this acoustic temperature is a sufficiently accurate approximation of the virtual air temperature. The maximum range of a sodar-RASS is usually less than thousand metres so that such an instrument covers the lower part of the boundary layer. Due to the high vertical resolution and the low minimum range of about 30 to 40 m, which is comparable to the abilities of a sodar, a sodar-RASS is well suited for the detection of shallow nocturnal boundary layers.

Algorithms MLH can be determined from the lowest height where the vertical profile of potential temperature increases with height indicating stable thermal stratification of the air. The great advantage of RASS measurements is that the magnitude of stability (inversion strength) can be assessed quantitatively which is not possible from the acoustic

and optical sounding devices described before. Fig. 88 displays a time-height cross-section of potential temperature over three days starting at midnight for a height range of 540 m. On the afternoons of the second and the third day well-mixed boundary layers formed, which can be deduced from the vertically constant potential temperature. New surface layers form on the evenings of all three days at about 1800 LST. The depth of these new surface layers increase during the night to about 200 to 300 m. Above these nocturnal surface layers low-level jets (see below) form, indirectly visible from the white areas indicating missing data in Fig. 88. Stronger winds like those in low-level jets blow the sound pulses from the RASS out of the focus of the electro-magnetic antenna and hence lead to a failure of the temperature detection.

Ideally, thermal stratification of air should be analyzed from the virtual potential temperature ($\Theta_v = \Theta(1+0.609q)$, where q is specific humidity) in order to include the effects of the vertical moisture distribution on the atmospheric stability. Unfortunately, no active remote sensing device for the determination of high-resolution moisture profiles is available. Therefore, the acoustic potential temperature ($\Theta_a = \Theta(1 + 0.513q)$), which actually is the temperature that is delivered by a RASS, is often used as a substitute. This is sufficient for cold and dry environments, but somewhat underestimates the virtual potential temperature in humid and warm environments. In case of larger vertical moisture gradients and small vertical temperature gradients this can lead to a switch in stability from stable to unstable or vice versa.

Engelbart and Bange (2002) have analyzed the possible advantages of the deployment of two RASS instruments, a sodar-RASS and a high-UHF windprofiler-RASS, to derive boundary-layer parameters. With these instruments, in principle, MLH can either be determined from the temperature profiles or from the electro-magnetic backscatter intensity. The latter depends on temperature and moisture fluctuations in the atmosphere. The derivation of MLH from the temperature profile requires a good vertical resolution of the profile which is mainly available only from the sodar-RASS. But even if the inversion layer at the top of the boundary layer is thick enough, due to the high attenuation of sound waves in the atmosphere, also the 1290 MHz-windprofiler-RASS used by Engelbart and Bange (2002) can measure the temperature profile only up to about 1 km. Therefore, in the case of a deeper CBL, MLH was determined from a secondary maximum of the electro-magnetic backscatter intensity which marks the occurrence of the entrainment zone at the CBL top. Thus, with this instrument combination the whole diurnal cycle of MHL is ideally monitored by interpreting the temperature profile from the sodar-RASS at night-time and by analyzing the electro-magnetic backscatter intensity profile from the windprofiler-RASS during daytime.

Hennemuth and Kirtzel (2008) have recently developed a method that uses data from a sodar-RASS and surface heat flux data. MLH is primarily detected from the acoustic backscatter intensity received by the sodar part of the sodar-RASS and verified from the temperature profile obtained from the RASS part of the instrument. Surface heat flux data and statistical evaluations complement this rather complicated scheme. The surface heat flux is used to identify situations with unstable stratification. In this respect this observable takes over an analogous role as the σ_w in the EARE algorithm (see above). The results have been tested against radiosonde soundings. The coincidence was good in most cases except for a very low MLH at or even below the first range gate of the sodar and the RASS.

Further techniques

Beyrich and Görsdorf (1995) have reported on the simultaneous usage of a sodar and a wind profiler for the determination of MLH. For the sodar data the ARE method was used. From the wind profiler data MLH was likewise determined from the height of the elevated signal intensity maximum (Angevine et al., 1994; Grimsdell and Angevine, 1998; White et al., 1999). Good agreement between both algorithms was found for evolving

CBLs. The vertical ranges of the two instruments (50 to 800 m for the sodar and 200 to 3000 m for the wind profiler) allowed following the complete diurnal cycle of MLH.

Comparison of acoustic and optical MLH detection algorithms

There is an interesting difference between the schemes for the determination of MLH from acoustic and optical backscatter intensities which should be noted carefully. While the acoustic backscatter intensity itself is taken for the detection of $H1$ and $H3$ (see Eqs. (152) and (154)) and the first derivative of this backscatter intensity for the determination of $H2$ (see Eq. (153)), the first and the second derivative of the optical backscatter intensity (but not the optical backscatter intensity itself) is used to determine $H4$ (see Eq. (156)). This discrepancy in the processing of the two backscatter intensities is due to the different scattering processes for acoustic and optical waves: Acoustic waves are scattered at atmospheric refractivity gradients and thus at temperature gradients (Neff and Coulter, 1986) while optical waves are scattered at small particles. Therefore the optical backscatter intensity is proportional to the aerosol concentration itself. The MLH on the other hand, which we desire to derive from these backscatter intensities, is in both cases found in heights where we have vertical gradients of the temperature and of the aerosol concentration. Therefore, in principle, the vertical distribution of the acoustic backscatter intensity should look very much alike the vertical distribution of the vertical gradient of the optical backscatter intensity.

Simultaneous measurements with different remote sensing devices have mainly been made in order to evaluate one remote sensing method against the other (Devara et al., 1995). But one could also think of combining the results two or more remote sensing devices for determining the structure of the ABL. The analysis of the sodar data and the ceilometer data can be combined to one single piece of MLH information by forming the minimum from Eqs. (155) and (162):

$$\text{MLH} = \min\left(\text{MLH}_{\text{ac}}, \text{MLH}_{\text{op}}\right). \tag{167}$$

9.3   Boundary-layer height

Often, the boundary layer consists of more layers than just the mixing layer. For example, at night, a residual layer may persist over a newly formed near-surface stable surface layer. The deployment of sophisticated lidars (Bösenberg and Linné, 2002) may be a choice to detect such features as well as the combined deployment of a sodar and a ceilometer. Such a combination of parallel measurements of the vertical structure of the atmospheric boundary layer by a ceilometer and a sodar is described in Emeis and Schäfer (2006). Fig. 92, which is taken from this study, shows a daytime convective boundary layer, shallow nocturnal surface layers in the morning and the evening, and a residual layer above the nocturnal surface layers. The ceilometer detects the overall boundary layer height (blue triangles) whose height is partly modified by large-scale sinking motion in the anticyclone dominating the weather during the measurement period. Stable nocturnal surface layers with a depth of a few hundred metres can be detected underneath the black squares derived from the sodar soundings. The convective boundary layer during daytime fills the full depth of the boundary layer. This combination offers the same advantages as the combination of sodar and windprofiler presented in Beyrich and Görsdorf (1995). First results from a combined deployment of a RASS and a ceilometer are given in Emeis et al. (2009).

In such combined remote sensing measurements a sodar better detects the near-surface features such as nocturnal stable layers (a RASS instead of a sodar directly delivers the near-surface temperature profile) while the ceilometer is able to follow the diurnal variation of the daytime convective boundary layer and the top of the whole boundary layer. The residual layer then becomes visible as the layer between the new nocturnal
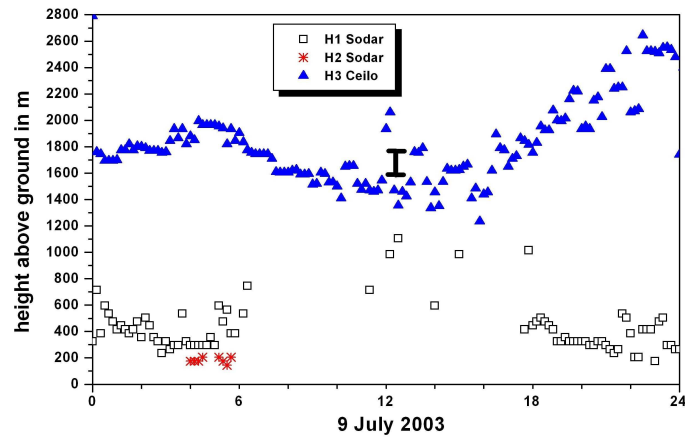
Figure 92. Combined sounding with a sodar (black squares and red asterisks) and a ceilometer (blue triangles) giving a complete view of the diurnal variation of the vertical structure of the ABL.

surface layer below and the top of the boundary layer above.

9.4   Summary

Wind resources depend on the large-scale weather conditions as well as on the local vertical structure of the atmospheric boundary layer. Ground-based remote sensing is now a viable technique to monitor the vertical structure of the atmospheric boundary layer. Three different techniques are presently available: acoustic sounding (sodars), optical sounding (lidars and ceilometers) and the combination of acoustic and electro-magnetic sounding (RASS). Direct detection of MLH from acoustic backscatter intensities is limited to the order of about 1 km due to the rather high attenuation of sound waves in the atmosphere. In contrast, optical remote sensing offers much larger height ranges of at least several kilometres, because the attenuation of light waves in the atmosphere is small unless there is fog, clouds or heavy precipitation. This now offers the possibility to introduce information on boundary layer structure such as mixing-layer height into the monitoring and description of wind resources.

Notation

a	factor of proportionality
$A1$	$(B_M + B_U)/2$
$A2$	$(B_M - B_U)/2$
ABL	atmospheric boundary layer
ARE	acoustic received echo (method)
$B_{\min}$	threshold value for $B(z)$
B_M	mixing-layer mean of $B(z)$
B_U	value of $B(z)$ above the mixing layer
$B(z)$	optical backscatter intensity
$B_i(z)$	idealized optical backscatter intensity
$\partial B/\partial z_{\max}$	threshold value for the vertical derivate of $B(z)$
c	speed of light
c_a	RASS speed of sound ($= c_s + w$)
c_s	true speed of sound
CBL	convective boundary layer
DR_1	threshold value for the vertical gradient of $R(z)$

DR_2	threshold value for the vertical gradient of $R(z)$
EARE	enhanced acoustic received echo (method)
f_a	acoustic frequency
f_e	electro-magnetic frequency
Hn	analysed height (n is a one-digit number)
$H4_{\mathrm{GM}}$	height of minimum of vertical gradient of $B(z)$
$H4_{\mathrm{IPM}}$	height of minimum of second vertical derivate of $B(z)$
$H4_{\mathrm{LGM}}$	height of minimum of logarithmic vertical gradient of $B(z)$
HWS	horizontal wind speed (method)
MLH	mixing-layer height
$\mathrm{MLH_{ac}}$	mixing-layer height from acoustic sounding
$\mathrm{MLH_{op}}$	mixing-layer height from optical sounding
q	specific humidity
R_c	threshold value for $R(z)$
$R(z)$	acoustic backscatter intensity
RASS	radio-acoustic sounding system
T_a	acoustic temperature
VWV	vertical wind variance (method)
w	vertical wind component
$W_B(z)$	scale averaged power spectrum profile
z	height above ground
z_i	boundary-layer height
Δf_e	Doppler shift of electro-magnetic frequency
Δh	height interval
Θ	potential temperature
Θ_a	acoustic potential temperature
Θ_v	virtual potential temperature
λ_a	wavelength of sound wave
$\lambda_{a,B}$	wavelength of sound wave fulfilling the Bragg condition
λ_e	wavelength of electro-magnetic wave
σ_w	standard deviation of the vertical wind component

References

Angevine W., White A. B., and Avery S. K. (1994) Boundary layer depth and entrainment zone characterization with a boundary layer profiler. *Bound.-Layer Meteorol.* **68**: 375–385

Asimakopoulos D. N., Helmis C. G., and Michopoulos J (2004) Evaluation of SODAR methods for the determination of the atmospheric boundary layer mixing height. *Meteorol. Atmos. Phys.* **85**: 85–92

Beyrich F. (1995) Mixing height estimation in the convective boundary layer using sodar data. *Bound.-Layer Meteorol.* **74**: 1–18

Beyrich F. (1997) Mixing height estimation from sodar data - a critical discussion. *Atmosph. Environ.* **31**: 3941–3954

Beyrich F. and Görsdorf U. (1995) Composing the diurnal cycle of mixing height from simultaneous SODAR and Wind profiler measurements. *Bound.-Layer Meteorol.* **76**: 387–394

Boers R., Spinhirne J. D., and Hart W. D. (1988) Lidar Observations of the Fine-Scale Variability of Marine Stratocumulus Clouds. *J. Appl. Meteorol.* **27**: 797–810

Bösenberg J. and Linné H. (2002) Laser remote sensing of the planetary boundary layer. *Meteorol. Z.* **11**: 233–240

Brooks I. M. (2003) Finding boundary layer top: application of a wavelet covariance transform to lidar backscatter profiles. *J. Atmos. Oceanic Technol.* **20**: 1092–1105

Cohn S. A. and Angevine W. M. (2000) Boundary Layer Height and Entrainment Zone Thickness Measured by Lidars and Wind-Profiling Radars. *J. Appl. Meteorol.* **39**: 1233–1247

Davis K. J., Gamage N., Hagelberg C. R., Kiemle C., Lenschow D. H., and Sullivan P. P. (2000) An objective method for deriving atmospheric structure from airborne lidar observations. *J. Atmos. Oceanic Technol.* **17**: 1455–1468

de Haij M., Wauben W., and Klein Baltink H. (2006) Determination of mixing layer height from ceilometer backscatter profiles. In: Slusser J. R., Schäfer K., Comerón A. (eds) Remote Sensing of Clouds and the Atmosphere XI. *Proc. SPIE* Vol 6362: paper 63620R.

Devara P. C. S., Ernest Ray P., Murthy B. S., Pandithurai G., Sharma S., and Vernekar K. G. (1995) Intercomparison of Nocturnal Lower-Atmospheric Structure Observed with LIDAR and SODAR Techniques at Pune, India. *J. Appl. Meteorol.* **34**: 1375–1383

Emeis S. (2010a) Measurement methods in atmospheric sciences. In situ and remote. Vol. 1 of Quantifying the Environment. Borntraeger, Stuttgart, in print.

Emeis S. (2010b) Surface-Based Remote Sensing of the Atmospheric Boundary Layer. Springer, Heidelberg etc., submitted.

Emeis S. and Schäfer K. (2006) Remote sensing methods to investigate boundary-layer structures relevant to air pollution in cities. *Bound.-Layer Meteorol.* **121**: 377–385

Emeis S. and Türk M. (2004) Frequency distributions of the mixing height over an urban area from SODAR data. *Meteorol. Z.* **13**: 361–367

Emeis S., Jahn C., Münkel C., Münsterer C., and Schäfer K (2007) Multiple atmospheric layering and mixing-layer height in the Inn valley observed by remote sensing. *Meteorol. Z.* **16**: 415–424

Emeis S., Schäfer K., and Münkel C (2008) Surface-based remote sensing of the mixing-layer height - a review. *Meteorol. Z.* **17**: 621–630

Emeis S., Schäfer K., and Münkel C (2009) Observation of the structure of the urban boundary layer with different ceilometers and validation by RASS data. *Meteorol. Z.* **18**: 149–154

Engelbart D. A. M. and Bange J. (2002) Determination of boundary-layer parameters using wind profiler/RASS and sodar/RASS in the frame of the LITFASS project. *Theor. Appl. Climatol.* **73**: 53–65

Eresmaa N., Karppinen A., Joffre S. M., Räsänen J., and Talvitie H. (2006) Mixing height determination by ceilometer. *Atmos. Chem. Phys.* **6**: 1485–1493

Flamant C., Pelon J., Flamant P. H., and Durand P. (1997) Lidar determination of the entrainement zone thickness at the top of the unstable marin atmospheric boundary-layer. *Bound.-Layer Meteorol.* **83**: 247–284

Grimsdell A. W. and Angevine W. M. (1998) Convective Boundary Layer Height Measurement with Wind Profilers and Comparison to Cloud Base. *J. Atmos. Oceanic Technol.* **15**: 1331–1338

Hayden K. L., Anlauf K. G., Hoff R. M., Strapp J. W., Bottenheim J. W., Wiebe H. A., Froude F. A., Martin J. B., Steyn D. G., and McKendry I. G. (1997) The Vertical Chemical and Meteorological Structure of the Boundary Layer in the Lower Fraser Valley during Pacific '93. *J. Atmos. Environ.* **31**: 2089–2105

Hennemuth B. and Kirtzel H.-J. (2008) Towards operational determination of boundary layer height using sodar/RASS soundings and surface heat flux data. *Meteorol. Z.* **17**: 283–296

Hooper W. P. and Eloranta E. (1986) Lidar measurements of wind in the planetary boundary layer: the method, accuracy and results from joint measurements with radiosonde and kytoon. *J. Clim. Appl. Meteorol.* **25**: 990–1001

Lammert A. and Bösenberg J. (2006) Determination of the Convective Boundary-Layer Height with Laser Remote Sensing. *Bound.-Layer Meteorol.* **119**: 159–170

Marshall J. M., Peterson A. M., and Barnes A. A. (1972) Combined radar-acoustic sounding system. *Appl. Opt.* **11**: 108–112

Martucci G., Srivastava M. K., Mitev V., Matthey R., Frioud M., and Richner H. (2004) Comparison of lidar methods to determine the Aerosol Mixed Layer top. In: Schäfer K., Comeron A., Carleer M., Picard R. H. (eds.): Remote Sensing of Clouds and the Atmosphere VIII. *Proc of SPIE* 5235: 447–456

Melfi S. H., Spinhirne J. D., Chou S. H., and Palm S. P. (1985) Lidar Observation of the Vertically Organized Convection in the Planetary Boundary Layer Over the Ocean. *J. Clim. Appl. Meteorol.* **24**: 806–821

Menut L., Flamant C., Pelon J., and Flamant P. H. (1999) Urban Boundary-Layer Height Determination from Lidar Measurements Over the Paris Area. *Appl. Opt.* **38**: 945–954

Münkel C. and Räsänen J. (2004) New optical concept for commercial lidar ceilometers scanning the boundary layer. *Proc. SPIE* Vol 5571: 364–374

Neff W. D. and Coulter R. L. (1986) Acoustic remote sensing. In: Lenschow D. H. (ed) Probing the Atmospheric Boundary Layer. Amer. Meteorol. Soc., Boston, MA, 201–239

Piironen A. K. and Eloranta E. W. (1995) Convective boundary layer depths and cloud geometrical properties obtained from volume imaging lidar data. *J. Geophys. Res.* **100**: 25569–25576

Schäfer K., Emeis S. M., Rauch A., Münkel C., and Vogt S. (2004) Determination of mixing-layer heights from ceilometer data. In: Schäfer K., Comeron A. T., Carleer M. R., Picard R. H., and Sifakis N. (eds.): Remote Sensing of Clouds and the Atmosphere IX. *Proc. SPIE* Vol 5571: 248–259

Schäfer K., Emeis S., Junkermann W., and Münkel C. (2005) Evaluation of mixing layer height monitoring by ceilometer with SODAR and microlight aircraft measurements. In: Schäfer K., Comeron A. T., Slusser J. R., Picard R. H., Carleer M. R., and Sifakis N. (eds) Remote Sensing of Clouds and the Atmosphere X. *Proc. SPIE* Vol 5979: 59791I-1–59791I-11

Seibert P., Beyrich F., Gryning S.-E., Joffre S., Rasmussen A., and Tercier P. (2000) Review and inter-comparison of operational methods for the determination of the mixing height. *Atmosph. Environ.* **34**: 1001-1-027

Senff C., Bösenberg J., Peters G., and Schaberl T. (1996) Remote Sesing of Turbulent Ozone Fluxes and the Ozone Budget in the Convective Boundary Layer with DIAL and Radar-RASS: A Case Study. *Contrib. Atmos. Phys.* **69**: 161–176

Sicard M., Pérez C., Rocadenbosch F., Baldasano J. M., and García-Vizcaino D. (2006) Mixed-Layer Depth Determination in the Barcelona Coastal Area From Regular Lidar Measurements: Methods, Results and Limitations. *Bound.-Layer Meteorol.* **119**: 135–157

Steyn D. G., Baldi M., and Hoff R. M. (1999) The detection of mixed layer depth and entrainment zone thickness from lidar backscatter profiles. *J. Atmos. Ocean Technol.* **16**: 953–959

White A. B., Senff C. J., and Banta R. M. (1999) A Comparison of Mixing Depths Observed by Ground-Based Wind Profilers and an Airborne Lidar. *J. Atmos. Oceanic Technol.* **16**: 584–590

Wulfmeyer V. (1999) Investigation of turbulent processes in the lower troposphere with water-vapor DIAL and Radar-RASS. *J. Atmos. Sci.* **56**: 1055–1076

Wulfmeyer V. and Janjić T. (2005) 24-h observations of the marine boundary layer using ship-borne NOAA High-Resolution Doppler Lidar. *J. Appl. Meteorol.* **44**: 1723–1744

10 Ground based passive microwave radiometry and temperature profiles

Fabio Scanzani[1,2]

[1]*Institute of Atmospheric Sciences and Climate CNR, Roma, Italy*
[2]*Tor Vergata University of Rome, Rome, Italy*

10.1 Introduction

The Earth's atmosphere is a layer of negligible thickness if compared to the Earth's diameter and is also, to a first approximation, transparent to electromagnetic radiation. Deviations from complete transparency are essential for life on Earth (e.g. importance of absorption of the ultraviolet radiation by ozone layer) and are the focus in the radiative physics of the atmosphere studies. At frequencies above 10 GHz, atmosphere continuously absorbs and emits electromagnetic radiation. The spectrum of this emitted radiation depends on a variety of atmospheric variables including temperature, water vapor concentration, and liquid water (e.g. clouds, rain and fog). Detecting and measuring the power of the thermal radiation emitted at certain frequencies allows to estimate some atmospheric parameters with very high spatial and temporal resolution.

The importance of the information that can be obtained from microwave observations of the atmosphere, is given in an excellent review article of the Environmental Research Laboratories of NOAA (Hogg et al., 1983): "... *Atmospheric observations form the essential base for almost all atmospheric research and services. Since the atmosphere is a variable three-dimensional fluid, these observations must be obtained in all three spatial dimensions. Ideally, such data sets should be continuous in both space and time; in practice, this has not been possible. Because existing observational systems use in situ instruments carried aloft by balloons, the National Weather Service has had to accept a compromise in which the data sets are neither continuous in time, nor continuous in space, but instead are taken once every 12 hours at stations spaced roughly 350 km apart across the United States. This system provides observations of upper air conditions that are suitable for identification and forecasting of synoptic scale phenomena such as cyclones and anti-cyclones (which have lifetimes of days and dimensions of 1000 km or more), but is not adequate for the observation and prediction of smaller scale, shorter lived phenomena such as thunderstorms, flash floods, etc. Other disadvantages of the existing system are that the profiles obtained are not usually vertical, and that significant man-hours per profile is required. ...*"

Hogg et al. (1983) also proposed an alternative observational network consisting of ground-based microwave systems upward-looking and satellite-borne, downward-looking radiometer systems. This network is envisioned to provide "profiles of wind, temperature, and to a lesser extent, humidity, continuously in time, in an unattended mode". In essence, the proposal integrates the capabilities of two complementary remote-sensing approaches to monitoring the atmosphere, one from below and the other from above. The retrieval of atmospheric parameters by passive remote sensing of thermal electromagnetic radiation at determinate frequencies is generally referred to as radiometry. A review of several radiometric techniques and the basics of the inversion algorithms to estimate the atmospheric temperature's profiles are here given.

10.2 Microwave radiometry fundamentals

Ground based radiometric measurements of lower tropospheric layers thermal emission, well known as ground-based passive radiometric sensing, has been successfully used in a variety of applications, including meteorological observations and weather and climate forecasting, air quality pollution forecasting, power energy plants design, geodesy and long-baseline interferometry, communications and satellite data validation, air-sea interaction, and fundamental atmospheric molecular physics study.

Radiometers can be operated continuously – on time scales of seconds to minutes – and unattended mode under almost all weather conditions to continuously measure the temperature profiles and temperature gradients (Troitsky et al., 1993; Westwater et al., 1998). The remote sensing measurements (e.g. radiometer, RASS, sodar, lidar, etc.) have characteristics that could be largely different from those taken by in situ instruments as radiosondes, tethered balloon or traditional sensors. Remote sensing measurements are representative of a volume (e.g. related to a radio antennas beam width or pulse length), whereas in situ measurements are usually only local point measurements. These differences must be considered in the comparison, interpretation and/or validation of data, and their use in models.

10.3 Upward-looking radiometric temperature profile measurements

The classical form of the radiative transfer theory describes the intensity of radiation propagating in a general class of medium which absorbs, emits, and scatters the radiation. The fundamental quantity measured by a radiometer is the radiant power, which is related to the specific intensity I_ν defined as the instantaneous radiant power that flows in a given point in the medium, per unit area, per unit-frequency interval at a specified frequency ν, and in a given direction per unit solid angle. As illustrated in Figure 93, its variation dI_ν at a point s along a elementary segment ds in the direction of propagation is obtained by considering the sources and sinks of the radiation in a elementary volume along that direction (in literature optical path) per unit solid angle.
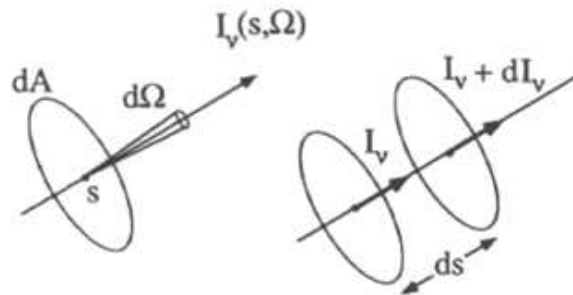

Figure 93. The specific intensity I_ν is the radiant energy flowing at each point in the medium per unit area normal to the flux, per unit solid angle, in the frequency range ν e $\nu + d\nu$. The variation of intensity with position is governed by an equation of transfer that takes into account the sinks and sources of radiation

This leads to a following balancing power differential form of the radiative transfer equation (RTE):

$$dI_\nu = -\alpha_\nu(s)I_\nu(s)ds + S_\nu(s)ds, \tag{168}$$

where $alpha_\nu(s)$ is the local absorption coefficient and $S_\nu(s)$ is a local contributive source term at point s, which respectively describe the loss and gain of energy along the direction

into the considered given elementary (Janssen, 1993).

The thermal radiation emitted from an ideal blackbody at a definite frequency ν, depends only on its thermodynamic temperature T: higher the temperature of the body more is its emission. Its radiance also called brightness $B_\nu(T)$ is given by the Planck's law:

$$B(T, \nu) = B_\nu(T) = \frac{2h\nu^3}{c^2} \frac{1}{\exp{(h\nu/kT)} - 1}, \tag{169}$$

where h is Planck's constant, k is Boltzmann's constant and c is the vacuum speed of light. The factor 2 in the numerator accounts for both polarizations according to the usual convention.

The related emission from a real body – often called grey body – at the same temperature is $A_\nu B_\nu(T)$ where A_ν is the fraction of incident energy absorbed from a certain direction. In the general theory, scattering into and from other directions can lead to both losses and gains to the intensity along a given propagation direction and can be taken into account in both the terms S_ν and α_ν. But if we assume a local thermodynamic equilibrium, so that each point into the elementary volume is characterized by the same temperature $T(s)$, the strict requirement of balance between the energy absorbed and emitted by any particular volume element leads to Kirchoff's law and for the S term we can suppose:

$$S_\nu(s, T) = [\alpha_\nu(s) (1 - A_\nu)] B_\nu(T). \tag{170}$$

For our application we will consider a no-scatter isotropic medium. In these hypothesis the source term $S_\nu(s, T)$ expresses only the locally generated contribution to the radiation, and the absorption coefficient $\alpha_\nu(s)$ becomes a local scalar characteristic of the medium that describes a true loss of energy from the radiation field into the medium. Moreover, for a perfectly reflecting or transmitting body, A_ν is equal to zero and incident energy can be assumed to be redirected or pass through the body without being absorbed. Under these hypotheses for an upward looking radiometer we can rewrite Eq. (170) as:

$$S_\nu(s, T) \triangleq \alpha_\nu(s) B_\nu(T), \tag{171}$$

where $B_\nu(T)$ is always given by Planck's function Eq. (169).

Operating in the microwave frequency range $\nu < 300$ GHz according to the Rayleigh-Jeans approximation of Planck's law by expanding the exponential term $\exp{(h\nu/kT)}$ and truncating to the second term of Eq. (169)

$$\left[\exp{(h\nu/kT)} = 1 + (h\nu/kT) + (h\nu/kT)^2 / 2! + ... \cong 1 + (h\nu/kT) \right],$$

we obtained for $B_\nu(T)$ a well approximated linear form (Figure 94):

$$B_\nu(T) \cong \frac{2k\nu^2}{c^2} T(s), \tag{172}$$

from which Eq. (171) becomes:

$$S_\nu(s) = \alpha_\nu(s) B_\nu(T) \cong \alpha_\nu(s) \frac{2k\nu^2}{c^2} T(s) \tag{173}$$

$B_\nu(T)$ is the surface brightness, which is the flow of energy across a unit area, per unit frequency, from a source viewed through free space in an element of solid angle. Since the brightness and the intensity have the same units (according to Figure 95) the two are locally equivalent in this case. It follows:

$$I_\nu(s) \equiv B_\nu(s) \cong \frac{2k\nu^2}{c^2} T(s), \tag{174}$$

in which I_ν is expressed as linear function of its relative thermodynamic temperature $T(s)$ as usually in the microwave frequency range formulation.

Substituting Eq. (173) form of $S_\nu(s)$ in Eq. (168) in the hypothesis of no scattering, in local thermodynamic equilibrium, plane horizontally stratified, perfectly transmitting
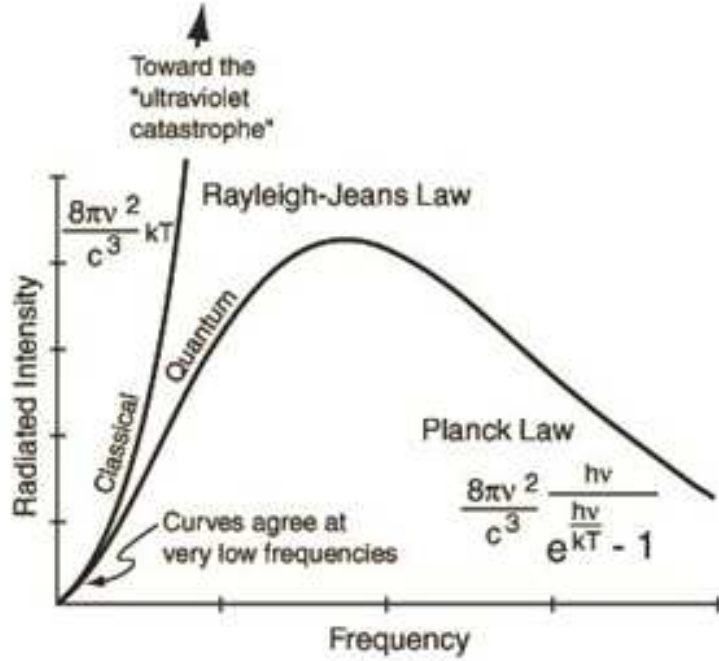
Figure 94. Rayleigh-Jeans' approximation assumed into the Planck'law

(or reflecting) atmosphere we obtain the following radiance power transfer differential equation:

$$dI_\nu = -\alpha_\nu(s)I_\nu(s)ds + \frac{2k\nu^2}{c^2}\alpha_\nu(s)T(s)ds. \tag{175}$$

Referring to the conventions reported in Figure 96(a), the previous differential equation provides the following integral solution:

$$I_\nu(0) = I_\nu(s_0)\exp\left(-\int_0^{s_0}\alpha_\nu(s')ds'\right) + \frac{2k\nu^2}{c^2}\int_0^{s_0}\alpha_\nu(s)T(s)\exp\left(-\int_0^{s_0}\alpha_\nu(s')ds'\right)ds. \tag{176}$$

If we define the integral function of the absorption $\alpha_\nu(s)$ along the path as optical depth $\tau_\nu(s)$

$$\tau_\nu(s) \triangleq \int_0^s \alpha_\nu(s')ds', \tag{177}$$

we can rewrite Eq. (176) in the following more readable form for the ground level measured value $I_\nu(0)$:

$$I_\nu(0) = I_\nu(s_0)\exp\left(-\tau_\nu(s_0)\right) + \frac{2k\nu^2}{c^2}\int_0^{s_0}\alpha_\nu(s)T(s)\exp\left(-\tau_\nu(s)ds\right)ds. \tag{178}$$

Substituting the equivalent formulation of $I_\nu(s)$ expressed in Eq. (174) we can rewrite Eq. (178) as a function of the brightness temperature $T_b(s)$:

$$T_b(0) = T_b(s_0)\exp\left(-\tau_\nu(s_0)\right) + \int_0^{s_0}T(s)\alpha_\nu(s)\exp\left(-\tau_\nu(s)\right)ds, \tag{179}$$

where $T_b(s_0)\exp\left(-\tau_\nu(s_0)\right)$ is the brightness temperature contribute to the atmosphere from cosmic background sources attenuated by the optical depth $\tau_\nu(s_0)$ existing between ground level and the point s_0.

Referring to polar axis system of the Figure 96(b), operating the substitution $ds = dz/(\cos\theta)$, where θ is angle off zenith axis of the radiometer's beam (for zenith $\theta = 0°$) and assuming z as the atmosphere layer's level, the measured ground level brightness
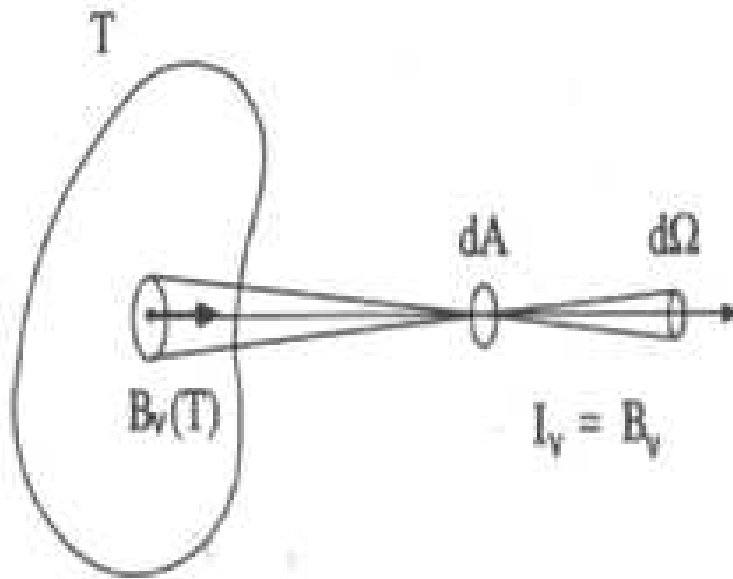
Figure 95. The surface brightness $B_\nu(T)$ of a blackbody emitter as viewed through free space in the solid-angle element $d\Omega$ produces a flow of energy given by the specific intensity $I_\nu \equiv B_\nu$
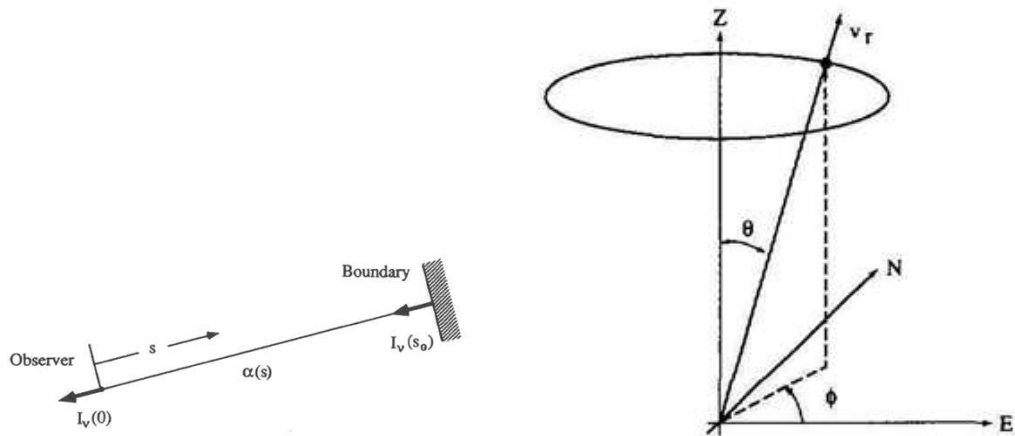

Figure 96. (a) Left: Conventions assumed into the integration of the RTE. (b) Right: Conventions assumed into the integration of the RTE

temperature for an upward looking radiometer expressed as function of frequency ν, and elevation angle θ it will become

$$T_b(0, \nu, \theta) \triangleq = T_b(\nu, \theta) = T_b(\infty) \exp\left(-\tau_\nu(\infty)\right) + \frac{1}{\cos\theta} \int_0^\infty T(z)\alpha_\nu(z) \exp\left(-\tau_\nu(z)\right) dz \tag{180}$$

with the optical depth at z-layer's quote :

$$\tau_\nu(z, \theta) = \frac{1}{\cos\theta} \int_0^z \alpha_\nu(z') dz'. \tag{181}$$

Assuming the cosmic background contribute $T_b(\infty) \exp(-\tau(\infty))$ as negligible for the effect of the opacity of the entire atmosphere, we can rewrite Eq. (180) at last as:

$$T_b(\nu, \theta) = \int_0^\infty T(z) \left(\frac{1}{\cos \theta} \alpha_\nu(z) \exp(-\tau_\nu(z, \theta)) \right) dz \qquad (182)$$

or:

$$T_b(\nu, \theta) = \int_0^\infty T(z) W(\nu, z, \theta) dz, \qquad (183)$$

in which the ground level measured brightness temperatures $T_b(\nu, \theta)$ is expressed as a convolution integral involving a temperature weighting function

$$W(\nu, z, \theta) \triangleq \frac{1}{\cos \theta} \alpha_\nu(z) \exp(-\tau_\nu(z, \theta)) \qquad (184)$$

(also defined kernel function) and the thermodynamic temperature profile $T(z)$. From a physical point of view the brightness temperature $T_b(\nu, \theta)$ of Eq. (183) can be considered a "weighted" average over the thermodynamic temperature of the atmosphere along the integration path[10]
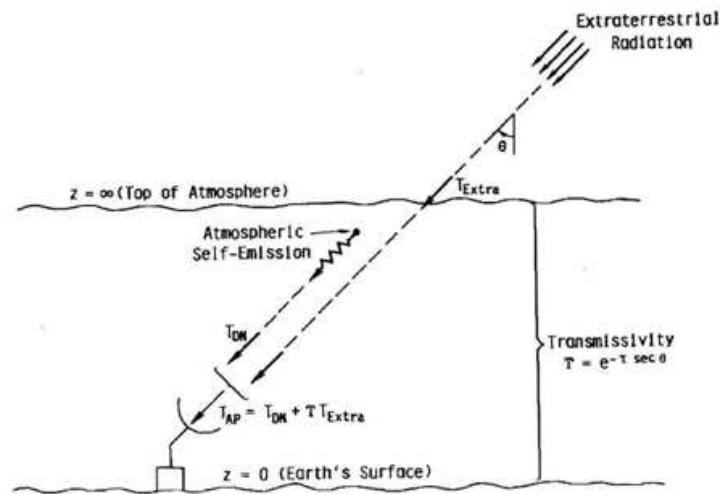

Figure 97. Brightness temperature also called apparent temperature that represents atmospheric radiation downwelling at angle θ measured by a radiometer

The integral Eq. (183) expresses the well known forward (or direct) problem: for a given weighting function $W(\nu, z, \theta)$. The atmospheric temperature's profile $T(z)$ can be computed by a measured ground level brightness temperature $T_b(\nu, \theta)$ using this equation.

In remote-sensing applications, we are concerned with the inverse problem in which $T_b(\nu, \theta)$ is generally measured by a radiometer at a discrete number of elevation angle θ^i (or at a discrete frequency ν^i or both) and the objective is to infer the atmospheric properties or simply to find a unknown function $T(z^i)$ that, when substituted in Eq. (182), will yield values of $T_b(\nu^i, \theta^i)$ approximately equal to the measured values. This is also known as the inverse problem and generally is more difficult to solve. A logic scheme of the two different procedures (direct and inverse) is shown in Figure 98.

Currently, there are three main absorption models that are widely used in these problems by the microwave propagation communities inside the recalled weighting function $W(\nu, z, \theta)$. A computer code has been developed and distributed of the microwave propagation model (MPM). More recently, Rosenkranz (1992) developed an improved absorption model that also is frequently used in the microwave propagation community. Another

---

[10]numerically is the integral sum of the elementary emission term $T(z)dz$ from each volume's element, attenuated by a factor $\exp(-\tau_\nu(z, \theta))$ (by the intervening medium as it travels toward the point of measurement), weighted by $\alpha_\nu(z)/\cos \theta$. It is of fundamental importance to notice the difference between this $T_b(\nu, \theta)$, also called apparent temperature T_{AP} (shown in Figure 97) sensed at ground level and a thermodynamic temperature profile $T(z)$ which remotely has originated it
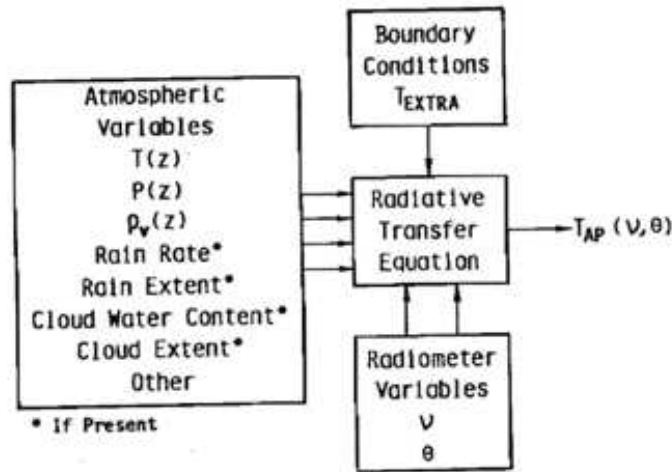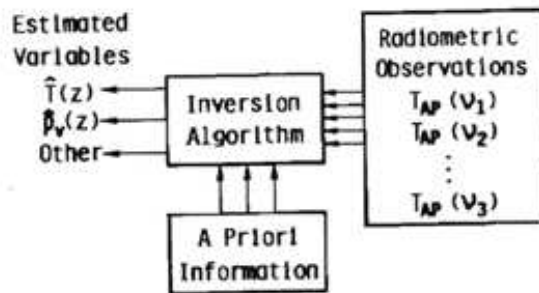
Figure 98. Schematics of the direct (a) and inverse (b) problem

model that is used extensively in the US climate research community is the line by line radiative transfer model.

10.4 Upward-looking angular scanning microwave radiometry

The spectrum of received radiation has seen to depend on a variety of atmospheric variables including temperature, water vapor concentration, and liquid water (i.e. rain, clouds and fog). Through the measure of his brightness temperature received it is possible to infer the atmospheric temperature profile $T(z)$ with a resolution that depends on the atmospheric absorption at the chosen frequencies. Therefore, the temperature weighting functions of upward-looking profiling radiometers above introduced in Eq. (183) have narrow peaks near the surface which decrease with altitude (see Figures 99(a) and (b)). In addition, sensitivity to oxygen is not degraded by radiation from the terrestrial surface. This allows accurate temperature profile retrievals with relatively high resolution in the boundary layer and lower troposphere, typically for level under 2 km.

The retrieval of atmospheric temperature's profile by passive measurement of brightness temperature $T_b(\nu, \theta)$ at one (or more) frequency and at various elevation angles is referred to as single (or multi) frequency angular scanning radiometry. For simplicity we will
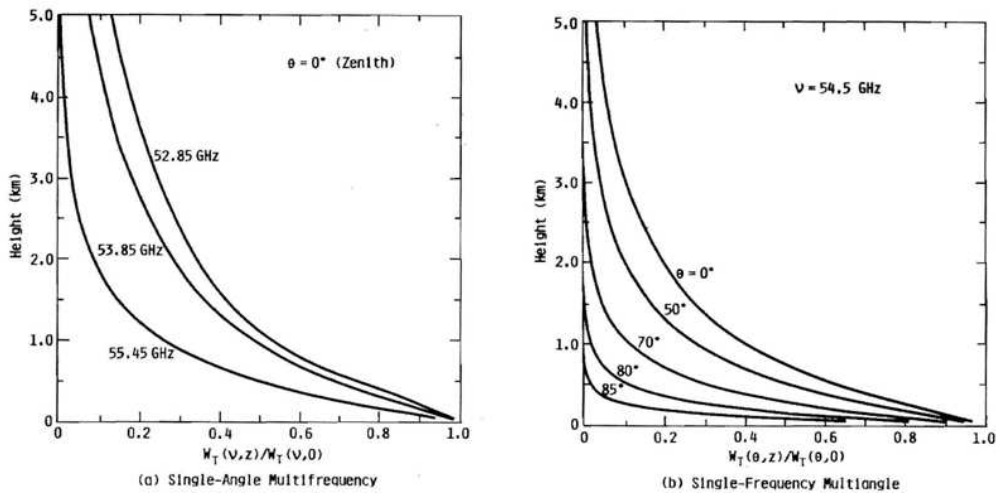
Figure 99. Normalized weighting functions

examine the single channel angular scanning typology but the conclusion are similar in the other cases.

The microwave atmospheric absorption (emission) in clear air and clouds, and the attenuation associated with rain in which individual contributions from water vapor, cloud liquid, rain, and oxygen are shown in Figure 100. A strong emission peak is present around 60 GHz due to oxygen absorption (emission), which dominates the contribution from all other constituents except rain. The strong emission $T_b(\nu)$ at frequencies near 60 GHz (see Figure 101) depending primarily on the concentration of molecular oxygen and layer's temperature. Moreover oxygen is well-mixed for altitudes below 80 km, its concentration is constant and well known so the only unknown associated with the high brightness emission near 60 GHz is atmospheric thermodynamic temperature.
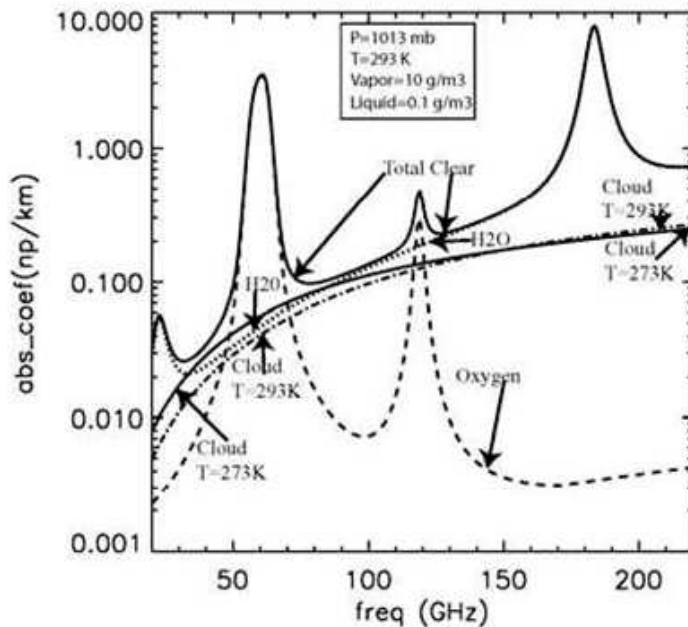

Figure 100. Atmospheric absorption normalized coefficient $\alpha_\nu(h)$ as frequency function notice the first narrow peaks at 60 Ghz
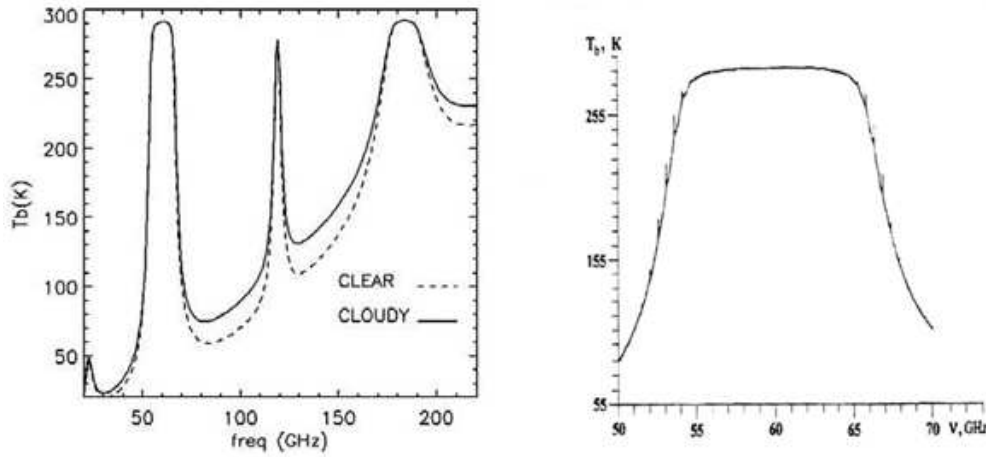
Figure 101. Spectral shape of the brightness temperature of atmospheric radio-emission, measured using ground based radiometric observation along the zenith direction in the oxygen absorption band at 60 Ghz

A ground-based radiometer looking upward detects the integrated emissions up to an heights which depends on the degree of absorption associated to the observation frequency. Frequencies in the immediate vicinity of the absorption peak (Figure 101) experience the largest attenuation, and only the lowest part of the atmosphere – in literature called skin depth – contributes to the signal detects by radiometer. The frequencies away from the peak, are less attenuated and radiation from higher layers in the atmosphere will contribute more to the measured signal deteriorating his noise ratio.

Askne and Westwater (1986); Troitsky (1986) described a multi-frequency (also called multi channel) passive microwave radiometer, which gave the possibility to measure temperature profiles in the troposphere (up to 10 km). But the height resolution in the lower troposphere is not good. A more simple technique for the microwave remote sensing of the boundary layer temperature is based on measuring of the brightness temperature of the atmosphere proper in the center of the oxygen absorption band. Troitsky et al. (1993) and Kadygrov and Pick (1998) described an angular scanning single-channel microwave radiometer centered proper on molecular oxygen band at 60 GHz. For our application we consider this second as case study.

As shown in Figure 101 at frequencies $\nu = 60$ Ghz we can suppose (with a good accuracy) an absorption coefficient independent with altitude h or $\alpha_\nu(h) = \alpha_\nu(0) =$constant and a skin depth around at $h = 300$ m. If we suppose that the skin depth equal to the boundary layer's height H_b at the zenith by integrating Eq. (181) follows:

$$\tau(H_b, \theta) = \frac{1}{\cos\theta} \int_0^{H_b} \alpha_\nu(z)dz = \frac{|\alpha_\nu(0)|(H_b - 0)}{\cos\theta} = \frac{|\alpha_\nu(0)300 \text{ m}|}{\cos 0} \triangleq 1, \qquad (185)$$

obtaining

$$|\alpha_\nu(0)| = |\alpha_\nu(h)| \triangleq \frac{1}{300 \text{ m}} \qquad (186)$$

and also:

$$H(\theta) \leq H_b = \frac{\cos\theta}{|\alpha_\nu(0)|} \triangleq \cos\theta 300 \text{ m} \qquad (187)$$

$$0 \leq H(\theta) \leq 300 \text{ m}. \qquad (188)$$

Thus, the remote temperature sensing is conducted by measurements of the brightness temperature at the different elevation angles $\theta = 0$–$90°$. In this case the depth of contributing radiation layer is a range from 0–300 m (Troitsky et al., 1993) in the hypothesis that the layers of an atmosphere which are above than 300 m will not influence the measure of $T_b^{\nu_0}(\theta)$.

More in general we can rewrite the Eqs. (182) and (183) of brightness temperature as function of the elevation angle θ and expressed by a defined integral function of $T(z)$ and Eq. (184) weighting function calculated at the frequency ν_0

$$T_b^{\nu_0}(\theta) = \int_0^H T(z)W^{\nu_0}(z,\theta)dz. \tag{189}$$

This is a Fredholm integral of the first kind and the superior limit of integration is finite and coincident with the limit of atmosphere's altitude sensed generally not more than $H_b = 2$ km. In this hypothesis we are supposing the layers of an atmosphere which are higher than 2 km do not influence $T_b^{\nu_0}(\theta)$ measurements.

The previous integral function Eq. (189) may be solved for an unknown temperature profile $T(z)$, given a set of measured radiometer brightness temperature data $T_b(\theta)$ at different elevation angles θ.

One of the first inversion alghorithm used was a variation of the Twomey-Tikhonov retrieval algorithm (Tikhonov and Arsenin, 1977) in form of generalized variation (Troitsky et al., 1993). Inversion techniques for upward-looking radiometers are generally based on the temperature climatology at the site that is typically derived from in situ radiosonde measurements. The inversion method use an initial-guess profile, usually derived from radiosonde observations or tethered balloon, and use temperature brightness measurements to correct this initial guess.

At this purpose instead of $T(z)$ the deviation from the restriction function can be minimized on the manifold of positively determined function (a class of normalized function). This method gives a good accuracy (about 0.5 K for accuracy of brightness temperature measurement better than 0.1 K) but sometimes results are not stable.

A more stable solution, having approximately the same accuracy, is given by a second method, which uses a variation of linear statistical retrieval (Turchin, 1967; Westwater et al., 1998). To implement this algorithm, it was constructed a covariance matrix which describes the brightness temperature differences at equally spaced zenith angles ranging from 0 to 90° with the in situ temperature. After having performed an eigenvector analysis on this covariance matrix a stable solution of the inverse problem is achieved. Other more modern frequently used method in radiometry include neural network inversion and Kalman filtering. A complete work on the most part of possible inversion methods is given in Janssen (1993).

10.5   Typical angular scanning temperature profile radiometer

A typical example of an angular scanning temperature profiler radiometer is shown in Figure 102 and was produced by the Russian scientific company ATTEX in cooperation with the Dutch company Kipp & Zonen: a polar regions version of the radiometer was realized in 2001 with improved vertical resolution and was called MTP-5P (P stands for polar). The MTP-5P has a microwave radiometer with the center frequency at about 60 GHz which measures the radio brightness temperature of the atmosphere with a high sensitivity (0.04 K at 1 s of integration time) at different discrete elevation angles. On the base of this discrete measurement, it is always possible to retrieve the discrete atmospheric temperature profile from the ground level around 5 m until to 600 m (instrument's intrinsic superior limit) with an accuracy 0.5 K at a vertical resolution at lower quotas of 10–20 m. The MTP-5P's electronics and parabolic antenna – beam aperture width of 0.5degrees – are housed into a thermostatic trailer (see Figure 103) whose temperature is controlled to within 5 K: over a year's time, the internal radiometer's receiver temperature should vary by less than 1 K.

Internal calibration of the instrument is achieved by sequentially switching between the antenna and one (or sometimes two) reference blackbodies (as current controlled resistive dummy). The complete radiometer's technical specifications are reported in Table 19.

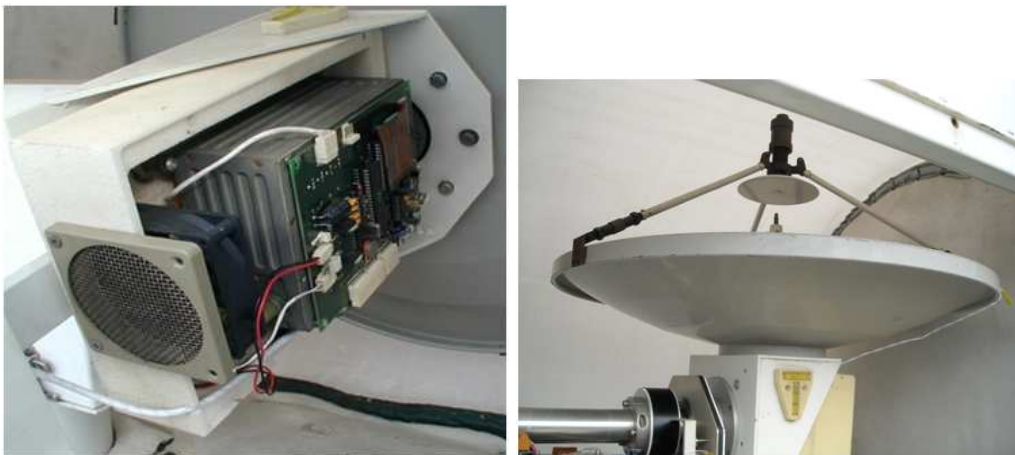Figure 102. Meteorological temperature profiler (polar version) MTP- 5P

Figure 103. (MTP5 radiometer - microwave receiver assembly (for courtesy concession of ISAC CNR, Rome, Italy

The brightness temperature data $T_b(\theta)$ for an angular scanning, MTP-5 radiometer has the previous integral form of Eq. (189) where atmospheric molecular oxygen absorption coefficient in weighted function $W^{\nu_0}(z,\theta)$ was calculated from Rosenkranz (1992) and upper limit of integration is $H = 1$ km. The statistical a priori database used for the setting up of the inversion process was a 2-year dataset of radiosonde's temperature profiles data from Russian upper air station network. In normal operation temperature profiles $T(z)$ are typically provided every 3 min.

Calibration factors require infrequent updating, perhaps once a year. External calibration procedures is necessary only in a long period maintenance's intervention and require a "tipping curves" (i.e. steering the antenna off-zenith by rotating the flat reflector to observe emission from a note source in a horizontal path) and/or radiative transfer calculations based on in situ comparison measurements (Figure 104).

10.6 Antarctica Dome C experimental site Radiometric measurements

In November 2002 a such MTP-5P radiometer was installed at the French-Italian Antarctic plateau station of Dome C (75°06'04" S, 123°20'52" E, altitude 3233 m) (Figure 104). The temperature profile measurements were provided from November 18 to December 17,

Table 19. MTP-5P Technical Specifications

Parameter	Value/characteristic
Microwave (passive) radiometer	Single frequency angular scanning
Altitude range [m]	0–600
Altitude resolution [m]:	
$0 < H < 50$	10
$75 < H < 100$	25
$100 < H < 600$	50
Accuracy of temperature profile [K or °C]	0.5
Central measurement frequency [GHz]	60.4
Antenna bean width (at 3dB) [deg.]	0.5
Receiver sensitivity [K]	0.04
Integration time [s]	1
Measurement cycle [s]	300 (minimum)
Operational temperature [°C]	−50–40
Calibration	Self calibrating (internal and external sources)
Dimensions [mm]	$900 \times 900 \times 870$

Figure 104. A recent maintenance intervention at the MTP5 radiometer – a microwave source for scanner alignment – (for courtesy concession of ISAC CNR Rome, Italy))

2002. The outside ground-based temperature range was −23.4°C– −45.7°C during the measurement period. The MTP-5P was installed at a height of 5 m above the Dome C surface and was in normal operational mode for all the period. Between November 18 and December 9 the data from the MTP-5P external in-situ temperature sensor were used for calibration. For the period December 9 to December 17 the data from the temperature sensor of a local meteorological station were used. Because of the strong influence of the radiation heating during the summer a shade-screen was installed in the near proximity of the instrument (Argentini et al., 2006).

One of the advantages of the MPT-5P is its continuity in acquiring data under all

meteorological conditions, which allows to obtain time series and time-height cross sections of temperature. The MTP-5P recorded continuous measurements of the atmospheric boundary layer temperature profiles above the Antarctic plateau for the first time and made possible to calculate some parameters of the temperature inversion such as the height of elevated inversion base, the inversion depth and temperature difference across the inversion.

Referring to Figure 105, as an example, the temperature time series between 0 and 240 m for 12 December 2002 at Dome C. The lower surface temperature is reached at 06:30 Local Time (LT). From 01:00 until 10:00 LT inversion conditions prevail, with a stronger inversion at 07:00 LT. Between 09:30 and 11:00 LT neutral conditions are observed in the transition between the stable and the convective boundary layer. A narrow convective boundary layer is observed between 10:30 LT and 17:00 LT. Inversion conditions are present after this moment. Figure 106 shows the temperature profile during stable (a) and (b), neutral (c), and unstable (d) thermal conditions for the same day. The lapse rate at 06:30 LT (Figure 106(b)) is about 2.5°C/100 m. In Figure 107 the temperature behavior (top part of the figure) and the temperature cross section (bottom figure) during all field experiment are given (Argentini et al., 2006).
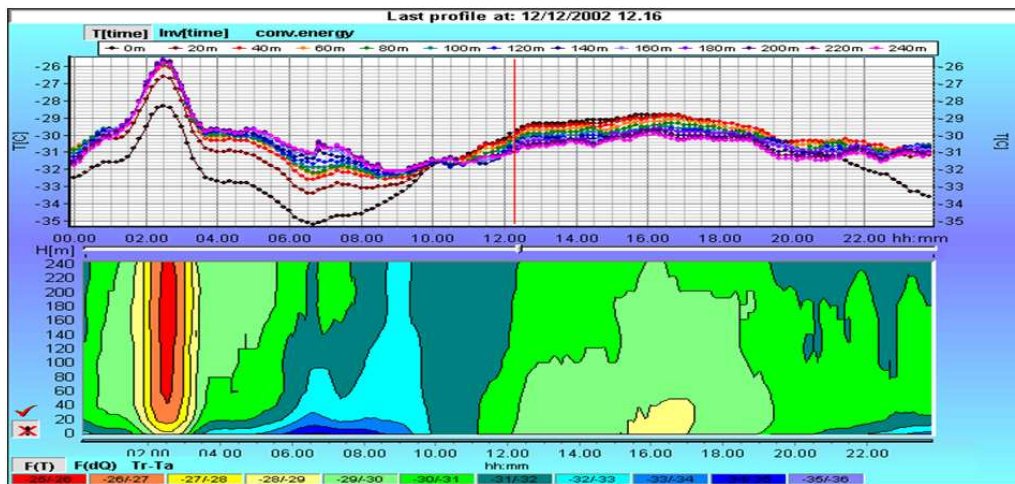

Figure 105. Temperature behaviour (top figure) and temperature cross section (bottom figure) during 12 December 2002

10.7 Summary

This chapter presents a general overview of physical fundamentals, measurement techniques and temperature profile retrieval methodology supported by a ground based microwave radiometry to derive meteorological temperature profiles. As case study is presented of a single channel multi angular scanning radiometer developed by Attex and Kipp&Zonen on request of the Italian ISAC CNR for the measure of the temperature profile in Antarctica.

From the concept of an ideal black body and Kickoff's law, it is known that the emission from a black body depends on its temperature and that the higher the temperature of the body, the more is its emission. The microwave energy emitted by the atmosphere, reflected from the surface, emitted from the surface, or transmitted from the subsurface can be recorded by a passive sensor a microwave radiometer.

In principle, temperature can be measured at any wavelength of the electromagnetic spectrum. Microwave radiometers measure brightness temperature whose values and variations at different frequencies can correlated with some atmosphere parameters. The atmosphere contains gaseous molecules, liquid and ice cloud particles. Microwave radiation
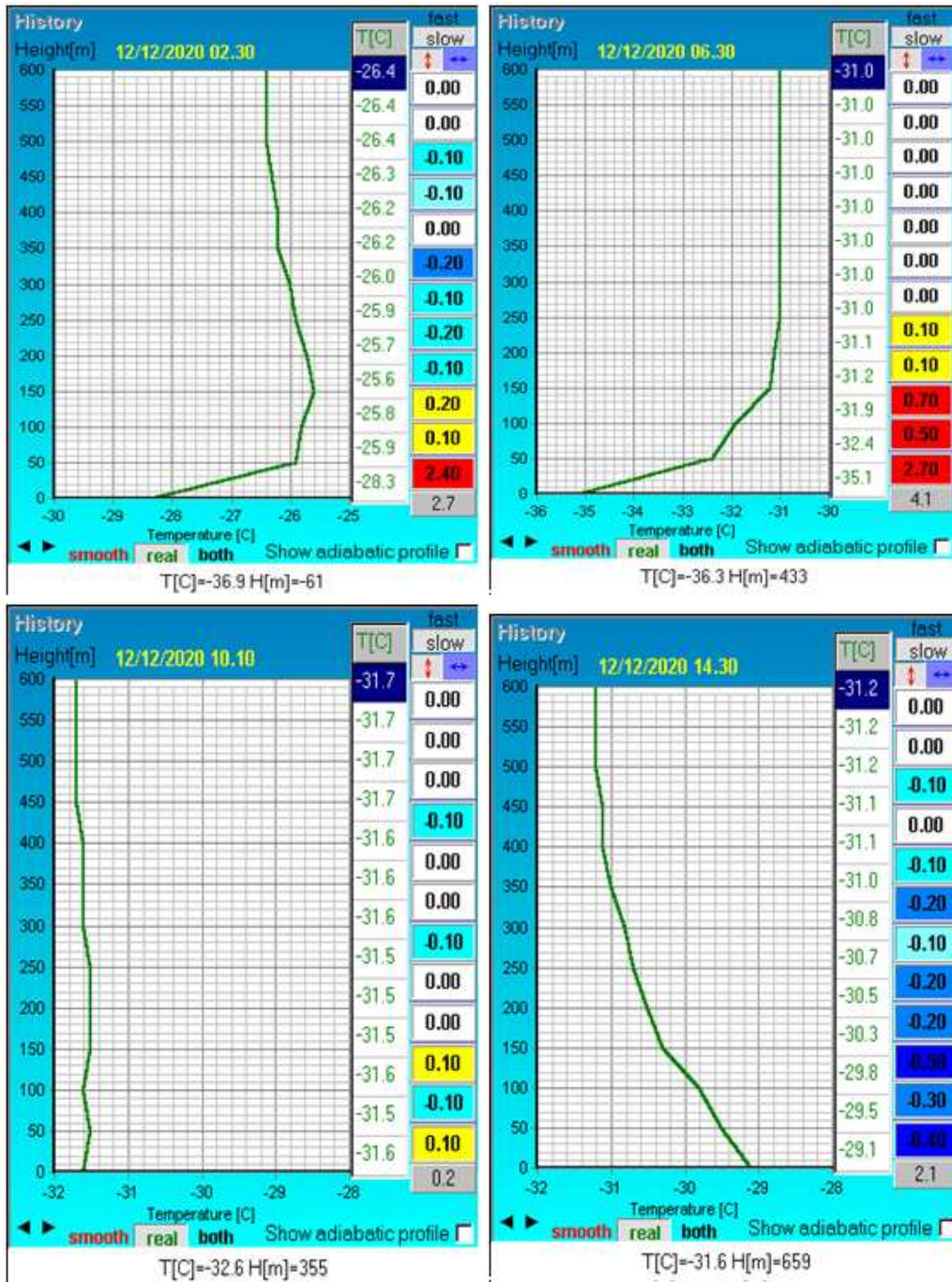
Figure 106. Temperature profiles in the first 250 me. The diurnal evolution of temperature is shown during (a)–(b) stable (c) neutral and (d) unstable conditions. The observation time is given at the top of each graph

from the atmosphere mostly is due to the absorption and scattering of gaseous molecules of molecular oxygen. For a well-mixed gas such as molecular oxygen, whose fractional concentration is independent of altitude below 80 km and the radiation contains information primarily on atmospheric temperature. In the case of atmospheric temperature profiling, advantage is taken of several properties of oxygen molecules, which comprise 23% of the mass of the Earth.s atmosphere. Moreover, molecular oxygen molecules radiate (and absorb) at a number of discrete frequencies between 50 and 70 GHz. These spectral lines are a consequence of rules of quantum mechanics which only allow oxy-
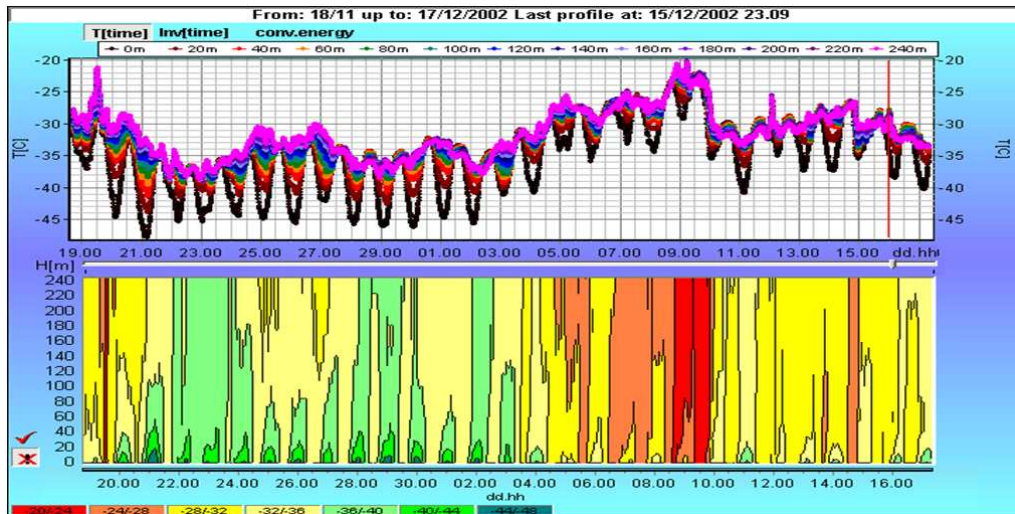
Figure 107. Temperature behaviour (top figure) and temperature cross section (bottom figure) during the all field experiment (18 November 2002 to 15 December 2002)

gen molecules to have particular rotational energy states. Furthermore, since the oxygen molecules are in thermodynamic equilibrium with the local environment, this means that if we can measure the strength of the thermal emission from the oxygen molecules, then we can deduce the physical temperature of the molecules that produced this emission. The oxygen absorption is strong enough that the effective distance that emission is seen is of the order of a few kilometers, depending on the frequency.

Radiometer measurements are inexpensive compared to the cost of remote sensing system, and it can provide all-time observations in both cloudy and clear air situations. However, using radiometer measurements can have specific difficulties:

- the measured brightness temperature is proportional to cumulative emission from various layers

- both scattering and absorption contribute to the measured radiation, which is governed by an integral - differential Radiative transfer equation

- the relation between brightness temperature and the atmospheric parameters is non-linear

To take advantage of continued improvements in radiometric techniques, it is important to provide such quality measurements with algorithms to calculate brightness temperature given the state of the atmosphere. Techniques to derive meteorological information from radiation measurements are generally based on numerically solving the radiative transfer equation (Tikhonov and Arsenin, 1977). For mildly nonlinear problems, a perturbation form of the RTE is frequently used as the basis of subsequent iteration. Microwave temperature profiling radiometers have been designed primarily for downward viewing from a satellite. However, upward-looking instruments can provide useful high-temporal-resolution information about temperature structure at the low troposphere and atmospheric boundary layer.

Two techniques are mostly used for microwave temperature profiling. First is well-known method used a zenith-viewing multi channel radiometer with frequencies of 53–58 GHz in the wings of the O_2 absorption band. It can measure temperature profile of the lower troposphere (up to about 5 km) (Troitsky, 1986). For good accuracy it is needed to have additional measurement channels for measurement of water vapor and cloud liquid (ordinary it is channels with the frequencies 23.8 GHz and 30 or 35 GHz). Multi channel method without scanning had a low vertical resolution at the lowest part of the ABL (about 300 m).

Second method (our discussed case study) is based on using of an angular-scanning single-channel radiometer with the central frequency of 60 GHz. This method and the instrument were proposed by Troitsky et al. (1993) and discussed in detail by Kadygrov and Pick (1998) and Westwater et al. (1999).

Due to the large atmospheric absorption by molecular oxygen at 60 GHz, angular-scanning method has some advantages for ABL temperature profiling over the multi channel method (Kadygrov et al., 2004a) summarized below:

- it can really to operate in all weather conditions: the measurements do not depends on changes of water vapor density or on the presence of fog or low clouds

- there is no need for calibration in the artificial microwave target

- better vertical resolution in the lower 300 m

- the bandwidth of the receiver is very wide which provides a high sensitivity of the receiver (about 0.04 K at 1 s integration time);

- instrument has a small sizes, is very portable, can provide reliable automated continuous profiling from a variety of sites and relatively small cost

However single-channel angular-scanning method, how we have seen, has its limitations in altitude measurement. It can measures only from the ground level up to 1000 m.

Notation

A_ν	fraction of incident energy absorbed from a direction
$B_\nu(T)$	brightness
c	vacuum speed of light
dI_ν	variation of specific intensity
ds	elementary segment in the direction of propagation
$d\Omega$	solid angle element
h	Planck's constant
	altitude
H_b	boundary-layer height
I_ν	specific intensity
k	Boltzmann's constant
MPM	microwave propagation model
RTE	radiative transfer equation
s	point in space
$S_\nu(s)$	local contributive source term at point s
T	temperature
T_{AP}	apparent temperature
$T_b(s)$	Brightness temperature
$W(\nu, z, \theta)$	temperature weighting function
z	layer level in the atmosphere
$\alpha_\nu(s)$	local absorption coefficient
θ	angle off zenith axis of the radiometer's beam
ν	frequency
$\tau_\nu(s)$	optical depth

References

Argentini S., Dargaud G., Pietroni I., Viola A., Mastrantonio G., Conidi A., Petenko I., and Pellegrini A. (2006) Behaviour of the temperature and inversion layer depth and strength at Dome C Antartica during the 2004–2006 field experiment. *Proc. of the 13th International symp. for the advancement of Bound.-layer Remote Sens.*, Garmish-Partenkirchen

Askne J. I. H., and Westwater E. R. (1986) A review of ground-based remote sensing of temperature and moisture by passive microwave radiometry. *IEEE Trans. Geosci. Remote Sens.* **24**:340–352

Hewison T. J., Cimini D., Martin L., Gaffard C., and Nash J. (2006) Validating clear air absorption model using ground-based microwave radiometers and vice-versa. *Meteorol. Z.* **15**:27–36

Kadygrov E. and Pick D. R. (1998) The potential for temperature retrieval from an angular-scanning single-channel microwave radiometer and some comparison with in situ observations. *Meteorol. Appl.* **5**:393–404

Kadygrov E., Koldaev A. V., Viazankin A. S., Argentini S., Viola A., and Mastrantonio G. (2004) First experience in monitoring the Temperature Profile over the Antarctic Plateau. Specialist meeting on Microwave Radiometry and Remote Sensing Application, Rome

Kadygrov E., Khaikin M., Miller E., Shaposhnikov A., and Troitsky A. (2004) Advanced atmospheric boundary layer temperature profiling with MTP-5HE microwave system. CAO Moskow region Russia

Janssen M. A. (1993) An introduction to the passive microwave remote sensing of atmospheres. In: Atmospheric Remote Sensing by Microwave Radiometry. Wiley, Interscience

Hogg D. C., Decker M. T., Guirand F. O., Eamshaw K. B., Merrit D. A., Moran K. P., Sweezy W. B., Stranch R. G., Westwater E. R., and Little C. G. (1983) An automatic profiler of the temperature, wind and humidity in the troposphere. *J. Clim. Appl. Meteorol.* **22**:807–831

Naumov A. P., Osharina N. N., and Trotsky A. V. (1999) Ground based microwave thermal sounding of the atmosphere *Radiophys. Quantum Elec.* **42**(1)

Rosenkranz P. W. (1992) Absorption of microwave by atmospheric gases. Atmospheric remote sensing by microwave radiometry, M. Janssen (ed). Wiley, Interscience

Troitsky A. V. (1986) Remote definition of the atmosphere temperature from spectral radiometric measurements in the line $\lambda = 5$ mm. *Izv. Vuzov Radiophysics* **XXIX**:878–886

Troitsky A. V., Gajkovich K. P., Gromov V. D., Kadygrov E. N., and Kosov A. S. (1993) Thermal sounding of the atmospheric boundary layer in the oxygen absorption band center at 60 GHz. *IEEE Trans. Geosci. Remote Sens.* **31**:116–120

Tikhonov A. N. and Arsenin V. Y. (1977) Solutions of III - Posed Problems. V. H. Winston and Sons, Washington

Turchin V. F. (1967) *J. Calc. Math. Mathematical Phys.* **102**, N3:In Russian

Ulaby F. T., Moore R. K., and Fung A. K. (1986) Microwave Remote Sensing: Active and Passive, from Theory to Applications - Vol III, chap 17-1.2

Westwater E. R. (1993) Ground-based microwave remote sensing of meteorological variables, Chapter 4 in atmospheric remote sensing by microwave radiometry, Janssen M. (ed). John Wiley & Sons, 145–213

Westwater E. R., Han Y., Irisov V. G., Ye V., Leuskiy V., Yu G., Trokhimovski G., Fairall C. W., and Yessup A. T. (1998) Air-sea and boundary-layer temperatures measured by a scanning 60-Ghz radiometer. Recent results. *Radio Sci.* **33**:291–302

Westwater E. R., Han Y., Irisov V. G., Leuskiy V., Kadygrov E. N., and Viazankin S. A. (1999) Remote sensing of boundary layer temperature profiles by a scanning 5-mm microwave radiometer and RASS: comparison experiments. *J. Atmos. Ocean. Tech.* **16**:805–818

11   SAR for wind energy

Merete Badger[1], Charlotte B. Hasager[1], Donald Thompson[2], and Frank Monaldo[2]
[1] *Wind Energy Division, Risø DTU, Roskilde, Denmark*
[2] *The Johns Hopkins University, Applied Physics Laboratory, USA*

11.1   Introduction

Modern, purpose-built wind sensors such as scatterometers and radiometers typically provide global wind products resampled to 0.25° latitude and longitude (∼25 km at mid-latitudes). A coastal mask is applied to avoid mixed land-ocean pixels and coastal areas are therefore neglected. Scatterometer and radiometer products offer daily global coverage and are very useful for large-scale wind monitoring and weather forecasting. To resolve mesoscale wind variability associated with e.g. weather fronts, hurricanes, gap flows, or barrier jets more detailed spatial information is needed. Synthetic Aperture Radar (SAR) measurements are high-resolution observations of the Earth surface. Although no SAR sensor has been designed specifically for wind mapping, it has become clear that the data are very suitable for high-resolution wind retrievals over the ocean including near-shore areas. In contrast to optical sensors, radar sensors are independent of sunlight such that measurements may be obtained both day and night. A further advantage is the ability of microwaves to penetrate clouds and light rain. In the following, we review techniques for mapping of ocean wind fields from SAR in a historical context. We then focus on different applications in meteorology and wind energy where high-resolution ocean wind fields are useful. Recent advances and issues that remain to be solved are addressed for each of these applications. Finally, we discuss the potential of two newly launched SAR sensors and the future perspectives of SAR sensing of ocean winds.

11.2   Background

A SAR is an active microwave sensor capable of imaging the amount of backscattered signal per unit area - the normalised radar cross section (NRCS). NRCS depends on the size and geometry of roughness elements on the scale of the radar wavelength at the Earth surface. Over a calm ocean surface, the returned NRCS is limited because radar pulses are reflected away from the SAR at an angle equal to the angle of incidence. As the wind picks up, roughness in the form of capillary and short-gravity waves is generated by the surface wind stress. The dominant scattering mechanism is then diffuse and known as Bragg scattering (Valenzuela, 1978). The relation of NRCS to the local wind speed and direction and to the radar viewing geometry forms the key principle in ocean wind retrievals from SAR. High-frequency radars (X- or Ku-band) are generally the most sensitive to small-scale waves generated by the instantaneous local wind. Lower-frequency SAR sensors (L-band) are more sensitive to longer-period surface waves that, because of their longer growth time, are not so sensitive to local wind fluctuations. For further discussion how the sea surface roughness affects NRCS, see e.g. Thompson (2004).

Remote sensing measurements of the ocean were first collected from space by the SEASAT satellite in 1978 from a variety of onboard sensors including a radar altimeter (Brown et al., 1981), scatterometer (Wentz et al., 1984), and passive microwave radiometer systems (Wentz et al., 1986). A SAR, also on board SEASAT, not only demonstrated

the ability to measure the ocean surface wind field, but also revealed the presence of surface and internal waves, current and temperature boundaries, and shoaling bathymetry (Holt, 2004). A consistent NRCS-to-wind relationship could not be established from the SEASAT SAR data due to calibration issues and the fact that it looked at only a single incident angle. However, an important observation was that wind-aligned rows created periodic variations of the surface roughness and thus the image brightness. Gerling (1986) applied Fast Fourier Transformation (FFT) to extract the orientation of linear features in SEASAT SAR imagery. Comparisons with the SEASAT scatterometer demonstrated that these features are aligned with the wind direction with a 180° ambiguity.

In 1991, the European Space Agency (ESA) launched ERS-1 – a C-band ($\sim$5 cm) SAR operating at vertical polarization in transmit and receive (C_{VV}). This mission was followed up by the nearly identical ERS-2 mission in 1995. ERS-1/2 SAR images covered a 100-km swath with a spatial resolution of 25 m. Due to the shorter wavelength of these sensors, compared to an L-band SAR, the sensitivity of NRCS to wind stress increased and wind signatures became more visible in the SAR imagery, especially at wind speeds less than 5 m s^{-1}. A renewed scientific interest emerged for the mapping of ocean wind fields from SAR.

The active microwave sensors aboard ERS-1/2 could also be operated as scatterometers with three antennae. Viewing of a given point at the surface from several different incidence and/or aspect angles allowed for unambiguous estimates of the wind speed and direction from a set of NRCS values at different aspect angles. Geophysical model functions (GMFs) were empirically developed to establish the wind-vector-to-backscatter relationship for the C-band scatterometer data. Scatterometer model functions have later proven to be suitable for SAR wind retrievals as well. SAR sensors operate with a single antenna and view each ground target from one angle only. As a consequence, several wind speed and direction pairs correspond to a given NRCS. The number of possible solutions may be reduced if a priori information about the wind direction is used to retrieve the wind speed.

A new era of SAR sensing began with the launch of Canadian RADARSAT-1 in 1995. RADARSAT-1 has ScanSAR capability and is by default operated with a swath width of 500 km and a spatial resolution of 75 m. The wider swath is very suitable for studying mesoscale meteorological phenomena at a resolution that is still far better than that of scatterometers and radiometers. RADARSAT-1 is designed mainly for ice monitoring and has a C-band SAR operating with horizontal polarization (C_{HH}). A major challenge related to ocean wind retrievals has been the modification of existing GMFs (developed for vertical polarization measurements of ERS-1/2) to fit the C_{HH} measurements from RADARSAT-1. Rather than the construction of completely new C-band GMF for use with RADARSAT-1, some researchers have assumed that the C-band HH-pol cross section, C_{HH} , is simply equal to C_{VV} times a function that describes the ratio $C_{\mathrm{HH}}/C_{\mathrm{VV}}$; the so-called polarization ratio. In general, this polarization ratio function should depend on the radar viewing geometry and the local wind vector. However, polarization ratio expressions proposed by Elfouhaily (1996), Thompson et al. (1998), and Vachon and Dobson (2000) over the past decade or so depend only on the radar incident angle and usually contain an adjustable parameter that can be tuned to fit the existing data. Recently, Mouche et al. (2005) proposed a more complete model for the C-band polarization ratio based on simultaneous measurements of C_{HH} and C_{VV} from an airborne radar.

Another ScanSAR sensor is ENVISAT launched by ESA in 2002. ENVISAT carries an advanced C-band SAR (ASAR) which may be operated in several different modes with co- or cross-polarization. The majority of ENVISAT's modes are suitable for ocean wind mapping. In ScanSAR mode, the ASAR sensor is capable of scanning in a 400 km wide swath with a spatial resolution of 100 m. A higher resolution over smaller areas may be achieved in the Stripmap mode. In recent years, the capacity of the SAR processing facilities has increased so that RADARSAT-1 and ENVISAT data are made available

for users in near-real-time; images can typically be downloaded via internet archives 1–3 hours after the data acquisition. This opportunity has opened up for operational SAR-based wind mapping.

A new C-band SAR sensor, RADARSAT-2 was launched in December 2007. This sensor is the first spaceborne C-band SAR to have fully polarimetric capabilities such that C_{VV}, C_{HH}, C_{VH}, and C_{HV} data can be acquired simultaneously. Polarimetric data have previously been collected from various airborne SAR missions and also from the three spaceborne systems ALOS PALSAR, TerraSAR-X, and COSMO SkyMed operating in L-band and X-band. ALOS was launched in 2006 by the Japanese Space Agency (JAXA) and TerraSAR-X was launched in 2007 by the German Aerospace Center (DLR). COSMO SkyMed is a constellation of four satellites launched in 2007, 2008, and 2010 by the Italian Space Agency (ASI). Altogether, the recent opportunity of using multipolarization and multifrequency SAR sensing is expected to provide new insight in oceanic and atmospheric processes including perhaps improving the retrieval of ocean wind fields.

11.3 Ocean wind retrievals from SAR

The most widely used GMFs for C-band SAR wind retrievals at low to moderate wind speeds are CMOD4 (Stoffelen and Anderson, 1997) and CMOD-IFR2 (Quilfen et al, 1998). These model functions are valid for wind speeds of 2–24 m s^{-1} and have a nominal accuracy of ± 2 m s^{-1}. A new model function, CMOD5, has been developed to improve the accuracy of wind retrievals at hurricane wind speeds (Hersbach, 2003). Generally, the empirical GMFs take the following form:

$$\sigma^0 = U^{\gamma(\theta)} A(\theta) \left[1 + B(\theta, U) + C(\theta, U) \cos 2\phi \right] \tag{190}$$

where σ^0 is the NRCS, U is wind speed at the height 10 m for a neutrally-stratified atmosphere, θ is the local incident angle, and ϕ is the wind direction with respect to the radar look direction. The coefficients A, B, C, and γ are functions of wind speed and the local incident angle. Empirical model functions rely on the assumption that wind speed increases logarithmically with height above the sea surface. This is normally true if the atmospheric boundary layer is neutrally stratified. Stable stratification would typically lead to an underestimation and unstable stratification to an overestimation of the 10-m wind speed. Deviations from the logarithmic wind profile are mostly found in near-shore areas where the atmospheric boundary layer may be influenced by the land. GMFs can thus be expected to perform better over the open ocean than in near-shore areas. Several parameters other than the surface wind vector or wind stress can affect the sea surface roughness and thus the NRCS. For example, mineral oil (Gade and Alpers, 1999; Espedal and Johannessen, 2000) or biogenic slicks (Espedal et al., 1996, 1998; Gade et al., 1998a,b) have a damping effect on Bragg waves. Other oceanographic processes including fronts and eddies (Lyzenga, 1991; Johannessen et al., 1996; Kudryavtsev et al., 2005; Johannessen et al., 2005), internal waves (Thompson et al., 1988; Hogan et al., 1996), long-period surface waves (Alpers et al., 1981; Hasselmann et al., 1985; Vachon et al., 2004), and bathymetry (Alpers and Hennings, 1984; Romeiser and Alpers, 1997) can also alter the NRCS. For each of these processes, it is the modulation of the surface wave spectrum due to the surface current field induced by the particular process that is responsible for the modulation of the NRCS. A convenient "rule of thumb" to estimate the sign of the NRCS modulation is that a positive gradient of this induced surface current (i.e. a current convergence) will increase the NRCS whereas a negative gradient (current divergence) will decrease the NRCS. The detailed character of the modulation, of course, is more complicated and depends on the radar frequency and local wind velocity among other things (see e.g. Thompson et al. (1988) and references contained therein).

The Johns Hopkins University Applied Physics Laboratory (JHU/APL) has developed the APL/NOAA SAR Wind Retrieval System (ANSWRS) that is currently being used for near real-time wind field retrievals at NOAA, JHU/APL, the Alaska SAR
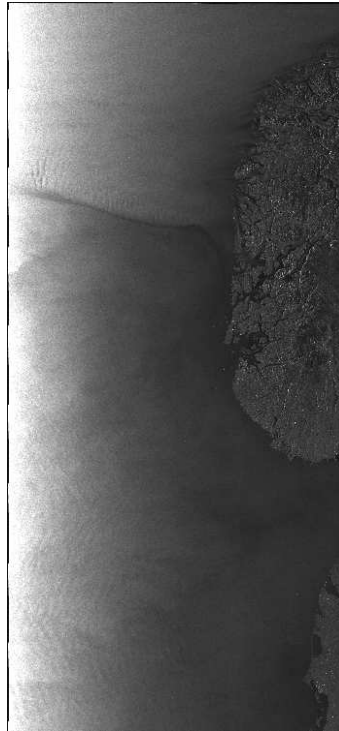
Figure 108. ENVISAT ASAR scene acquired over the North Sea on 30 October 2006

Facility (ASF), and Risø National Laboratory for Sustainable energy at the Technical University of Denmark (Risø DTU). To meet the requirements of processing in near real-time, the ANSWRS software produces high-resolution (< 1 km) wind speed fields initialized using wind directions determined by the Navy Operational Global Atmospheric Prediction System (NOGAPS) models. At present, we have an extensive database of SAR wind maps derived mainly from the SAR systems on the Canadian RADARSAT-1 and the European ENVISAT satellites. The wind maps in our database date back to the launch dates of RADARSAT-1 and ENVISAT and can be viewed at the web site: http://fermi.jhuapl.edu/sar/stormwatch/web_wind/. The maps in the database cover most areas of the globe, but are concentrated mainly in the Gulf of Alaska and coastal regions of continental US and Europe. Comparisons between the estimated wind speeds from these maps (mainly in the Gulf of Alaska and the US East coast) yield agreement with buoy measurements to within 1.76 m s^{-1} standard deviation (Monaldo et al., 2001) and with QuikSCAT wind speeds to within 1.25 m s^{-1} standard deviation (Monaldo et al., 2004).

Figure 108 shows an ENVISAT ASAR scene acquired over the North Sea on 30 October 2006. The scene is aligned according to the satellite orbit and shows a higher NRCS in near-range (left) compared to far-range (right). Several atmospheric features can be observed from the NRCS image. Dark streaks off the Norwegian coast indicate low-wind areas caused by shadowing from the land and a weather front is seen as an almost linear feature. Wave patterns are observed adjacent to this front and also towards the lower left image corner. The waves are most likely associated with atmospheric processes impacting the sea surface roughness. Their wavelength is several orders of magnitude larger than the Bragg wavelength. Figure 109 shows a wind field generated from the same ASAR image and mapped to geographical coordinates. The wind retrieval was initiated using wind directions from the NOGAPS model interpolated in time and space to match the satellite data. NOGAPS data are available at 6-hour intervals mapped to a 1° latitude/longitude grid. In this case, the model data capture very well the complex
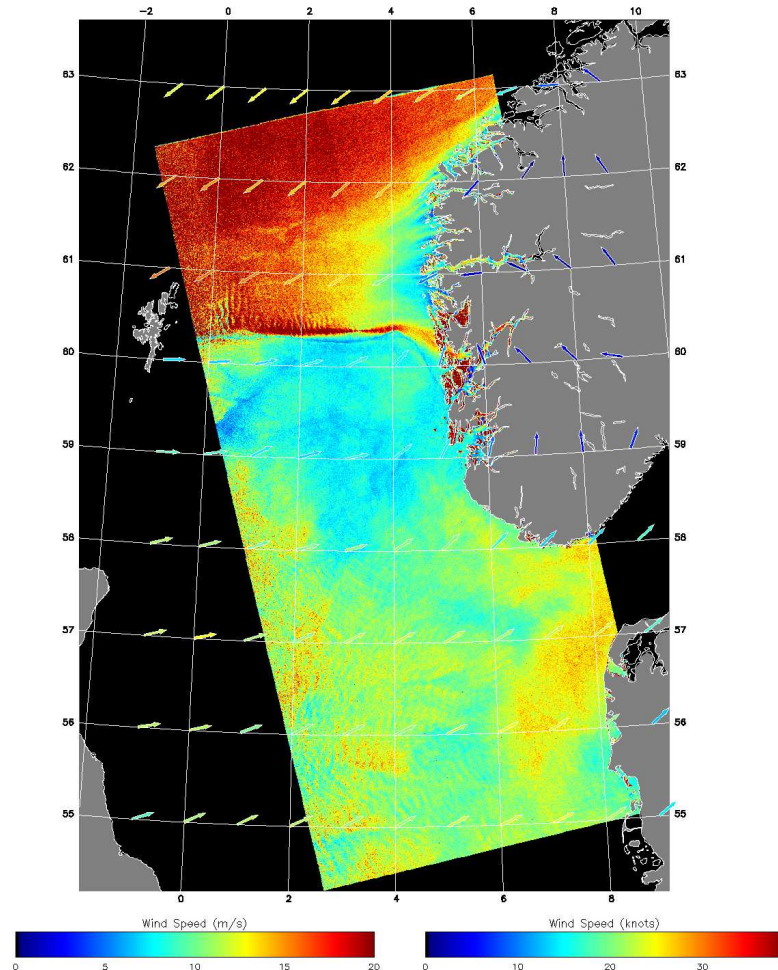
Figure 109. Wind field generated from the ENVISAT ASAR image in Figure 108 using the ANSWRS software from JHU/APL. Arrows indicate wind vectors from the NOGAPS model interpolated in time and space to match the satellite data. A weather front is captured by the satellite as well as the model data. There is a good overall agreement on wind speeds for this complex situation

wind pattern associated with a weather front. To the north of the front, strong winds are coming from the northeast. To the south of the front, winds are from the southwest and weaker. On the lee side of Norway, wind speeds are reduced significantly. Wind speeds around 5 m s^{-1} are found near the coastline. The wind speed increases to more than 15 m s^{-1} over a distance of 100 km offshore. There is an excellent overall agreement between the satellite and model wind speeds.

It is also possible to estimate the wind direction directly from km-scale streaks in the SAR imagery, aligned approximately with the wind direction. The streaks originate from atmospheric roll vortices and other phenomena impacting the sea surface. Different image analysis techniques such as FFT (Gerling, 1986; Vachon and Dobson, 1996; Lehner et al., 1998; Furevik et al., 2002) and wavelet transformation (Fichaux and Ranchin, 2002; Du et al., 2002) have been exploited to obtain the direction of wind streaks in SAR imagery with a 180° ambiguity. An advanced algorithm for wind direction retrieval, developed at GKSS Research Center in Germany, yields a wind speed and direction accuracy of 1.6 m s^{-1} and 20° (Horstmann et al., 2000, 2003; Koch, 2004). This method examines the change in intensity of the SAR image at various spatial scales. The wind direction retrievals are made at ~ 6-km scales and the wind speeds are usually computed on a 500-
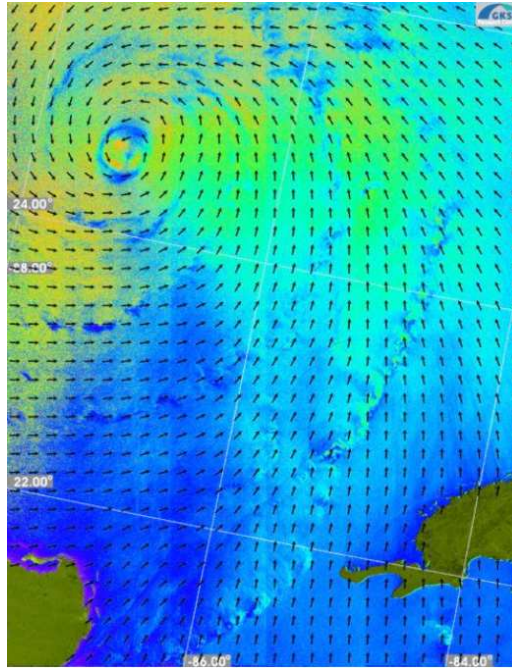
Figure 110. This image (provided by J. Horstmann from GKSS) shows the SAR wind vector retrieval over Hurricane Ivan in September 2004. The small arrows represent the SAR retrieved direction and the color indicates the extracted wind speed (dark blue ∼ 3 m s^{-1}; orange near the hurricane eye > 30 m s^{-1})

m pixel scale with wind directions interpolated down to the pixel location. Figure 110 shows an example of SAR wind vector retrieval over Hurricane Ivan in September 2004 where the wind direction was determined directly from features in the image (Horstmann et al., 2005).

Of course the two approaches for the determination of wind direction for use in SAR wind-speed retrievals have advantages and disadvantages. The use of model directions for the wind speed retrieval has the advantage that a dynamically consistent and unambiguous wind direction is always available. However, the direction associated with wind features at small spatial scales cannot be resolved by the numerical models. On the other hand, the use of linear features from the SAR image to infer direction has the inherent advantage that the entire wind vector (direction as well as magnitude) is obtained from the SAR image itself, independent of model estimates. The major disadvantage in this method lies in the fact that for a small fraction of cases, unique wind directions may not be found. In such cases, the directions must be interpolated from adjacent parts of the SAR image.

Finally, the possibility of obtaining wind directions from scatterometer data has been investigated (Monaldo et al., 2004; He et al., 2005). The method requires nearly simultaneous overpasses of a SAR and scatterometer, which becomes more practical with increasing latitudes. A solution to this time correlation issue may be a routine merging of the two data types (Monaldo and Beal, 2004). Estimation of the wind direction is among the largest sources of error in SAR wind speed retrievals. For offshore sites where high-quality meteorological data are available and used to provide the wind direction input, wind speeds may be retrieved with an standard deviation error as low as 1.1 m s^{-1} (Hasager et al., 2004, 2005, 2006; Christiansen et al., 2006).

11.4 Meteorological applications of SAR wind fields

The ocean wind fields shown in Figures 109 and 110 have already indicated how SAR imagery is valuable for meteorological applications such as weather prediction and hurricane monitoring. High-resolution SAR wind fields may also be used to provide measurements required in basic research efforts that are not available from other, more conventional instrumentation and sensors. An interesting example is to study the dynamics of coastal wind fields where terrain forcing can cause large gradients in the local wind over spatial scales on the order of a few kilometers or so. In the Gulf of Alaska, a combination of factors provides a nearly perfect location to study intense mesoscale meteorological phenomena. In addition to the meteorological forcing present in this region, excellent satellite coverage from polar-orbiting SAR satellites is available due to the high latitude. It is thus an excellent test bed for observing atmospheric phenomena with SAR.

Gap flows and barrier jets

Two specific examples of mesoscale meteorological phenomena that occur frequently in the Gulf and are readily observable using SAR are gap flows and barrier jets. Gap flows occur when cold continental air spills through gaps in the complex mountainous coastal terrain that forms the boundary of most of the Gulf. Barrier jets occur when stable atmospheric flow encounters a barrier in the local terrain from a high mountain ridge or wall for example (Parish, 1982). If the flow is sufficiently statically stable (i.e. resistant to vertical motion), it is blocked from crossing the barrier and as mass piles up along the upwind side of the barrier, a local, positive pressure gradient parallel to the terrain barrier is induced. The atmosphere adjusts to this gradient by deflecting the onshore flow to the left (northern hemisphere) and accelerating it along the pressure gradient. When the horizontal extent of the barrier is sufficiently large, the flow becomes rotationally trapped against the barrier by the Coriolis force (Chen and Smith, 1987; Bell and Bosart, 1988).

Figure 111 shows six barrier jets in the region between Mount Fairweather and Prince William Sound. It is immediately evident from the figure that very sharp offshore wind speed gradients are associated with these structures. This morphology is not consistent with the exponential wind speed increase predicted by classical barrier jet theory. However barrier jets similar to those seen in this figure have been previously observed by research aircraft and have long been part of the experience of local mariners in Alaska (Neiman et al., 2004). Having access to SAR images in this region has served to confirm and provide context to these previous observations. Of course, such observations of sharp gradients prompt one to seek understanding of the governing dynamics that cause these features to form. Once these dynamics are understood, further questions concerning forecasting the strength and shape of these phenomena naturally arise. Such questions have led to a project funded by the US National Science Foundation to study barrier jets in the Gulf of Alaska using SAR imagery (Winstead et al., 2006).

Flow model validation

A practical application of SAR wind fields in meteorology is the validation of mesoscale modeling over the ocean. Mesoscale models are widely used for operational prediction of atmospheric dispersion and also for wind resource assessment. The modeling of wind fields for a given domain is initiated with geostrophic wind and temperature profiles plus information about the terrain height and the surface roughness. Wind fields at different heights are typically modeled at a grid resolution of 5 km. The right-hand side of Figure 112 shows wind speeds for the height 70 m over the western part of the Baltic Sea predicted with the KAMM model using a geostrophic wind forcing of 10 m s−1 from the southeast. The spatial resolution is 2 km. Local effects of the land are clearly seen. For
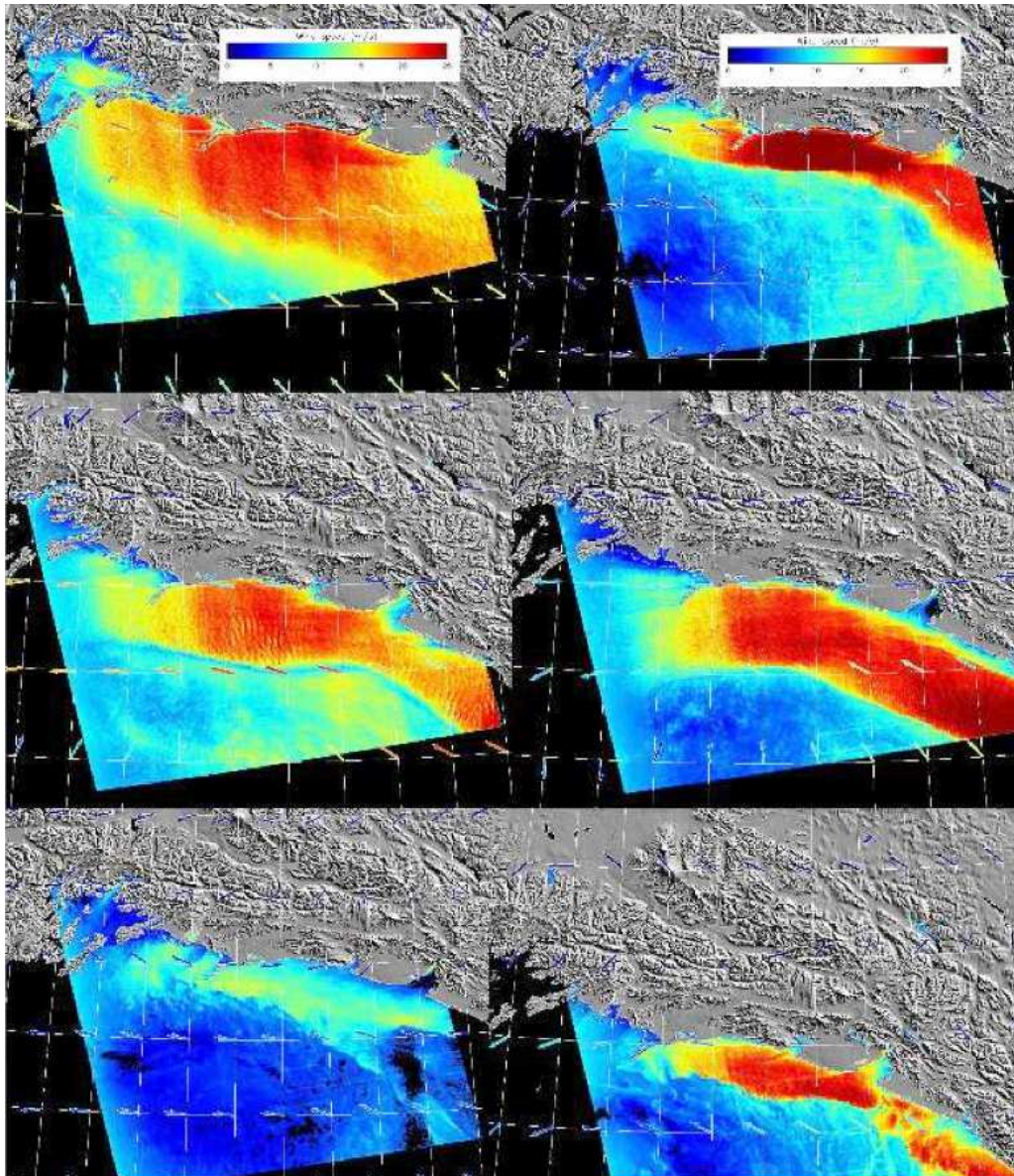
Figure 111. SAR-wind maps showing the wind structure of Barrier Jets around the region of Yakutat, AK. The collection dates are as follows (from left to right, top to bottom): 0311 UTC 30 May 1999, 0310 UTC 18 February 2000, 0306 UTC 4 September 2000, 0306 UTC 22 October 2000, and 0302 UTC 24 October 2001, and 0310 UTC 27 November 2001. All six images were collected by the RADARSAT-1 SAR

example, wind speeds are generally low on the lee side of Germany. Note also the very pronounced sheltering effect of the Danish and German islands. The best example is the small German island Rügen located around 11.2° east and 54.5° north. Other areas show an enhancement of the wind speed as the wind is forced between the different islands.

The left-hand side of Figure 112 shows a SAR wind field valid for a 10-m height. The SAR and the model wind fields cannot be compared quantitatively due to the difference in height and likely differences in the large scale forcing. However, it is interesting to compare the spatial variability of the wind speed, which is very similar for the two maps with identical color scaling. Work is in progress to model all the different wind situations that are found in our SAR data archive for Denmark and to quantify the differences between SAR and model wind fields. Ultimately, this analysis could provide valuable guidance for the improvement of mesoscale modeling results.
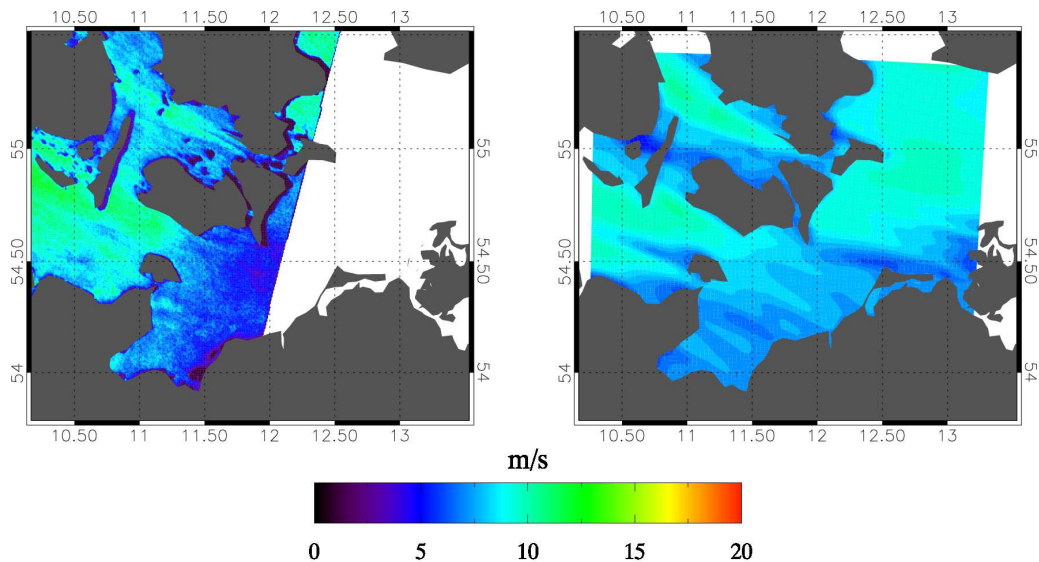
Figure 112. Ocean wind field over the western part of the Baltic Sea estimated from (left) an ENVISAT ASAR image acquired on 23 June 2004 at 09:46 UTC, and (right) the KAMM mesoscale model using a geostrophic wind forcing of 10 m s−1. The wind is directed from the southeast (∼ 120°). Wind variability caused by the terrain of Denmark and Germany is visible in both maps. Modified from Badger et al. (2006)

11.5 Wind energy applications of SAR wind fields

Prior to wind farm installation the best location within a given region needs to be identified. This is to ensure an optimal power production and economical benefit from the wind farm. The potential wind power production is closely related to the prevailing wind climate. Wind turbines were first established on land. Observations from meteorological masts within the region typically would be used to assess the wind climate. The landscape effects were of great importance for the wind resource as described in the European Wind Atlas (Troen and Petersen, 1989). This wind atlas method developed for wind resource assessment is a de facto standard today and it is used worldwide through the Wind Atlas Analysis and Applications Program (WAsP, www.wasp.dk) (Mortensen et al., 2005). Wind resource assessment is based on observations of wind speed and wind direction for a least one year and local scale maps of the area of interest. These maps should hold details on topography and obstacles as well as a general characterization of the roughness classes of the terrain. Wind resource assessment in the coastal region offshore – where most offshore wind farms are located or are in development – is challenging as coastal wind systems are complicated and ocean wind observations are sparse compared to land-based wind data.

Large wind farms cover areas of several square-kilometers. As an example, the Horns Rev I wind farm in the North Sea covers ∼ 25 km^2. This wind farm is located between 14 and 21 km offshore from the closest coastal point. Future wind farms will be located much further from the coast. At Horns Rev, a second wind farm (Horns Rev II) has just been installed (in 2009) approximately 26 to 31 km offshore. Thus the coverage needed in offshore wind resource analysis is roughly from 5 to 50 km offshore and with a spatial resolution that resolves variations in the wind climate at the 1–2 km grid scale. SAR images from ERS-1/2, Radarsat-1 and ENVISAT cover the coastal zone at the desired spatial resolution. The SAR data archives contain observations from many years (∼16, 11 and 5 years, respectively).

SAR-based wind statistics

Work was initiated in the EU WEMSAR project (2000–2003) to produce software for integration of SAR wind maps to standard wind resource mapping tools (e.g. WAsP). Further development has taken place within other projects and recently, cooperation between the institutions Risø DTU, JHU/APL, and GRAS A/S has resulted in the software Satellite-WAsP (S-WAsP) for SAR-based offshore wind resource assessment. In the following, we describe the key principles for treating a series of SAR-based wind maps and calculating wind resource statistics.

The collection of satellite SAR scenes for a given area of interest takes place at fixed times of the day. This introduces a bias in SAR-based wind climatologies. Another bias is associated with the relatively low number of available SAR samples compared to in situ measurements collected over e.g. 10-min intervals. A simulation study has been carried out to analyze the effect of these biases on statistical wind climate analyses (Barthelmie and Pryor, 2003; Pryor et al, 2004). The findings were relatively promising regarding estimates of the mean wind speed, which requires around 70 randomly sampled SAR images. To estimate the wind energy density, however, far more samples are needed (~ 2000). The conclusion of this work was that SAR-based wind resource estimations have a quality relevant in pre-feasibility studies. In other words, the SAR-based wind resource maps may be used as guide to site an offshore meteorological mast in a wind farm project. SAR-based wind resource maps provide quantification of relative wind resource variations in the spatial domain. In case offshore meteorological time series observations are already available, extrapolation using SAR-based wind statistics would be possible rather than erecting another meteorological mast nearby.

The software developed for SAR-based wind statistics takes care of several issues related to the nature of SAR-based wind maps. Firstly, grid cells upwind of the point of interest (any point in the selected domain) are averaged by a footprint-weighted function (Gash, 1986). Secondly, the samples available within each wind direction sector (bin) are used to calculate the Weibull shape and scale parameters. Finally, the fact that SAR-based wind mapping excludes winds below a certain threshold (2 m s−1) and above a certain threshold (24 m s−1) has made the choice of the maximum likelihood estimator relevant for Weibull fitting to SAR-based wind data (Nielsen et al., 2004; Hasager et al., 2007). Promising results on wind statistics based on ~ 100 SAR images were found by Christiansen et al. (2006) using a preliminary version of the S-WAsP software at Horns Rev in the North Sea.

Wind resource mapping for the Danish Seas

Wind resource mapping using a series of ENVISAT ASAR scenes acquired in wide swath mode (WSM) over the Danish seas has been performed. A total of 300 scenes were included in the study. Figure 113 (left) shows the number of overlapping samples. The orbital paths from ascending and descending frames are clearly visible. Most samples cover the inner Danish Seas whereas fewer cover the North Sea and the Baltic Sea. A first result on mean wind speed is shown in Figure 113 (right). The result shows much higher winds in the North Sea than in the inner Danish Seas. The very high mean wind speeds near the coast of Norway are likely caused by flow compression, as the wind is forced around the high-relief topography of southern Norway. For the near-coastal seas of Denmark and Sweden, the mean wind speed is seen to increase with distance offshore up to 50 km. It is possible to discern the orbital paths in the image but this artifact may be diminished or avoided in future image processing. The wind statistics are expected to improve in accuracy as our image archive continues to grow. The spatial coverage will be extended to include the entire North Sea, Baltic Sea, and Irish Sea as part of the project EU-NORSEWInD (2008–2012).

Wind resource assessment studies based on a relatively low number of SAR samples
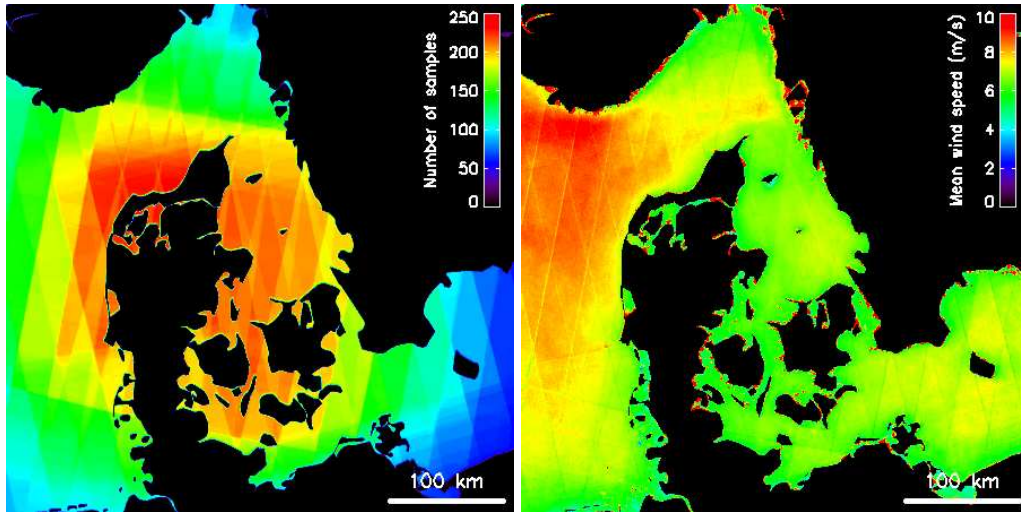
Figure 113. Left: Number of overlapping ENVISAT ASAR WSM images that are available for the Danish Seas. Right: Mean wind speed estimated from a total of 300 ENVISAT ASAR WSM satellite images covering the Danish seas

should take the directional distribution of the samples into account. This is particularly important in the vicinity of land where wind shadowing occurs. Our sampling strategy so far has simply been to collect as many random SAR samples as available from the image archives. Our ENVISAT ASAR image collection for the Danish seas contains several samples in each of 12 wind sectors. Figure 7 shows the directional distribution at Horns Rev, where the number of overlapping SAR scenes is 198 in total. Also shown is the directional distribution estimated from 7 years (1999–2006) of QuikSCAT data with 1–2 daily samples. Previous studies shave shown an excellent agreement between QuikSCAT and high-frequency in situ measurements of the wind direction (Hasager et al., 2007, 2008). The wind distribution from SAR and QuikSCAT data agree well for most wind sectors, except the SAR dataset underestimates the contribution from westerly winds and overestimates the contribution from easterly winds. The prevailing wind direction found from the SAR data is thus east whereas it should be southwest. This type of error is likely to diminish as more SAR samples are collected for the Danish Seas. Another way to cope with the wind distribution problem is to implement a weighting function according to higher-frequency observations such as in situ measurements, atmospheric models, or scatterometer data. For sites where thousands of SAR scenes are available in the image archives, the weighting could be performed during the initial image selection. This option is currently being investigated further.

Wind farm wake analysis

Wind resource assessment also includes an estimate on the wind reduction appearing within a wind farm – the so-called wind wake effect between wind turbines – or between wind farms in clusters. Typically, wind turbines and wind farms are located near each other to reduce the cost of cables from the turbines to the transform platform and from the transform to the electrical grid on land. The wind farm wake is characterized by lower wind speeds downstream of a wind turbine and higher turbulence level. Wind turbines in the wake of other turbines will thus produce less energy and suffer more tear due to the higher turbulence intensity.

Wind farm wake effects from two large offshore wind farms, Horns Rev wind farm in the North Sea and Nysted wind farm in the Baltic Sea, have been investigated from satellite and airborne SAR. The analysis showed – as expected – a significant reduction in wind
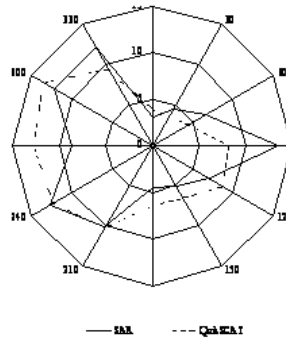
Figure 114. Directional distribution of winds at Horns Rev for a total of 198 overlapping SAR scenes (solid) and for QuikSCAT samples obtained 1–2 times daily for the period 1999–2006 (dashed)

speed downwind of the wind turbines. The magnitude of the wake near the wind farms was found to be similar to the wake effect predicted by state-of-the-art wake models and observed from meteorological masts. More surprisingly the study demonstrated that the wind farm wake may extend as far as 20 km downwind of a large offshore wind farm (Christiansen and Hasager, 2005, 2006). This is much longer than current wake models predict. Therefore the potential power production from wind farms in clusters may be more affected by wakes than it is assumed in general.

11.6 Future advances in ocean wind mapping from SAR

As already discussed in this chapter, two satellite SAR systems, RADARSAT-1 and EN-VISAT (both operating at C-band; ~ 5.3 GHz), are presently being used routinely to provide operational estimates of the near surface wind field at resolutions of ~ 500 m or so. In fact, the SAR on board ENVISAT, using its alternating polarization mode, is capable of transmitting vertically polarized radiation (V-pol) followed by horizontally polarized radiation (H-pol) on successive pulses, and collecting the reflected radiation in one of three distinct (user-defined) pairs: HH and VV, HH and HV, or VV and VH. New satellites have been launched with fully polarimetric transmit/receive SAR capability: ALOS (L-band; ~ 1.2 GHz), RADARSAT-2 (C-band~ 5.3 GHz), TerraSAR-X, and COSMO SkyMed (X-band; ~ 10 GHz). The ability to collect multi-polarization SAR imagery at three different frequencies represents a significant advance in SAR acquisition technology. Similar refinement in the interpretation and processing of data from these new SAR sensors is required in order to fully utilize this new technology for remote-sensing applications.

In order to extract geophysical information from the data collected by microwave sensors, it is clear that one must understand not only the scattering physics, but also surface wave hydrodynamics and the structure of the marine boundary layer. In particular, a method for characterizing the shape of the sea surface (the surface roughness) is necessary in order to properly apply the electromagnetic boundary conditions. Since these boundary conditions depend on the polarization state of the incident field, the scattering of electromagnetic radiation will be different for different polarization even for a smooth flat surface (Jackson, 1997). These differences generally become more pronounced as the surface roughness characteristics become more complicated. However, if scattering measurements from two (or more) polarization states are available, it should be possible to utilize the polarization-dependent differences in the scattering to improve the accuracy of the parameter extraction and perhaps even to separate wind-induced cross section

variations from those caused by oceanic processes such as internal waves or variable bathymetry (Ufermann and Romeiser, 1999).

Although much has been learned over the last years about the physics that governs microwave scattering from the ocean surface, there are still a number of outstanding problems that need to be addressed. In particular, the measured polarization ratios (HH/VV) of the backscattered cross section at moderate incidence angles for L-, C-, and X-band are larger than those predicted by the rough-surface scattering and surface spectral models commonly in use. At 45° incidence for example, the measured HH/VV ratio for a 10 m s^{-1} wind directed toward the radar is about -3 dB at X-band (Mazuko et al., 1986), about -5.0 dB or so at C-band (Mouche et al., 2005), and about -4 dB at L-band according to airborne E-SAR data from DLR acquired over the wind farm at Horns Rev, Denmark. Simple Bragg-based scattering models predict the HH/VV ratio to be about -9.5 dB; independent of radar frequency. Ratios predicted by composite-type scattering models that include the effects of long-wave tilt and hydrodynamic modulation yield frequency dependence and a somewhat large ratio (Romeiser et al., 1997), but the predicted polarization ratios remain significantly smaller than the measurement data.

Improved understanding of these discrepancies could yield significant improvement in the remote sensing of ocean processes, especially high wind events such as hurricanes. In particular, differences in the hurricane signatures observed by (roughly concurrent) SAR imagery collected by L-, C-, and X-band systems presently available could provide new insight into hurricane morphology and sea state as well as the rain rate since the influence of rain on the NRCS increases with increasing frequency. If such observations are collected at multiple polarizations, it may further be possible to estimate the foam or breaking wave coverage using techniques similar to those proposed by Kudryavtsev et al. (2003). Perspectives of mapping these properties of the ocean surface include not only an improved accuracy on ocean wind fields but also a possibility of using SAR-derived parameters for gas transfer parameterization and climate monitoring. Work by several international research groups is currently underway to begin to address these issues.

Acknowledgements

Notation

A	function of wind speed and local incident angle in a GMF
ANSWRS	APL/NOAA SAR wind retrieval system
ASAR	advanced C-band SAR
ASF	Alaska SAR facility
ASI	Italian Space Agency
B	function of wind speed and local incident angle in a GMF
C	function of wind speed and local incident angle in a GMF
C_{HH}	C-band SAR operating at horizontal polarization in transmit and receive
C_{HV}	C-band SAR operating at horizontal polarization in transmit and vertical in receive
C_{VH}	C-band SAR operating at vertical polarization in transmit and horizontal in receive
C_{VV}	C-band SAR operating at vertical polarization in transmit and receive
DLR	German Aerospace Center
ESA	European Space Agency
FFT	fast Fourier transformation

GMF	geophysical model function
H-pol	horizontally polarized radiation
JAXA	Japanese Space Agency
JHU/APL	Johns Hopkins University Applied Physics Laboratory
NCRCS	normalised radar cross section
NOAA	National Oceanic and Atmospheric Administration
NOGAPS	navy operational global atmospheric prediction system
Risø DTU	Risø National Laboratory for Sustainable Energy at the Technical University of Denmark
SAR	synthetic aperture radar
S-WAsP	satellite WAsP
U	wind speed at 10 m height
V-pol	vertically polarized radiation
WAsP	Wind Atlas Analysis and Application Program
WSM	wind swath mode
γ	function of wind speed and local incident angle in a GMF
θ	radar's local incident angle
σ^0	normalised radar cross section
ϕ	wind direction with respect to the radar look direction

References

Alpers W. R. and Hennings I. (1984) A theory of the imaging mechanism of underwater bottom topography by real and synthetic aperture radar. *J. Geophys. Res.* **89**:529–546

Alpers W. R., Ross D. B., and Rufenach C. L. (1981) On the detectability of ocean surface-waves by real and synthetic aperture radar. *J. Geophys. Res. Oceans* **86**:6481–6498

Badger J., Barthelmie R., Frandsen S., and Christiansen M. (2006) Mesoscale modelling for an offshore wind farm. *Proc. of the European Wind Energy Conf.*, Athens

Barthelmie R. J. and Pryor S. C. (2003) Can satellite sampling of offshore wind speeds realistically represent wind speed distributions. *J. Appl. Meteorol.* **42**:83–94

Bell G. D. and Bosart L. F. (1988) Appalachian Cold-Air Damming. *Mon. Wea. Rev.* **116**:137–161

Brown G. S., Stanley H. R., and Roy N. A. (1981) The Wind-Speed Measurement Capability of Space-borne Radar Altimeters. *IEEE J. Oceanic Eng.* **6**:59–63

Chen W. D. and Smith R. B. (1987) Blocking and Deflection of Air-Flow by the Alps. *Mon. Wea. Rev.* **115**:2578–2597

Christiansen M. B. and Hasager C. B. (2005) Wake effects of large offshore wind farms identified from satellite SAR. *Rem. Sens. Environ.* **8**:251–268

Christiansen M. B. and Hasager C. B. (2006) Using airborne and satellite SAR for wake mapping offshore. *Wind Energy* **9**:437–455

Christiansen M. B., Koch W., Horstmann J., and Hasager C. B. (2006) Wind resource assessment from C-band SAR. *Rem. Sens. Environ.* **105**:68–81

Du Y., Vachon P. W., and Wolfe J. (2002) Wind direction estimation from SAR images of the ocean using wavelet analysis. *Can. J. Rem. Sens.* **28**:498–509

Elfouhaily T. M. (1996) Modéle couple vent/vagues et son application à la télédétection par micro-onde de la surface de la mer. PhD thesis. University of Paris, Paris

Espedal H. A. and Johannessen O. M. (2000) Detection of oil spills near offshore installations using synthetic aperture radar (SAR). *Int. J. Rem. Sens.* **21**:2141–2144

Espedal H. A., Johannessen O. M., Johannessen J., Dano E., Lyzenga D. R., and Knulst J. (1998) COASTWATCH'95: ERS 1/2 SAR detection of natural film on the ocean surface. *J. Geophys. Res. Oceans* **103**:24969–24982

Espedal H. A., Johannessen O. M., and Knulst J. (1996) Satellite detection of natural films on the ocean surface. *Geophys. Res. Lett.* **23**:3151–3154

Fichaux N. and Ranchin T. (2002) Combined extraction of high spatial resolution wind speed and direction from SAR images: a new approach using wavelet transform. *Can. J. Rem. Sens.* **28**:510–516

Furevik B., Johannessen O., and Sandvik A. D. (2002) SAR-retrieved wind in polar regions - comparison with in situ data and atmospheric model output. *IEEE Trans. Geo. Rem. Sens.* **40**:1720–1732

Gade M. and Alpers W. (1999) Using ERS-2 SAR images for routine observation of marine pollution in European coastal waters. *Sci. Total Environ.* **237–238**:441–448

Gade M., Alpers W., Hühnerfuss H., Masuko H., and Kobayashi T. (1998) Maging of biogenic and anthropogenic ocean surface films by the multifrequency/multipolarization SIR-C/X-SAR. *J. Geophys. Res. Oceans* **103**:18851–18866

Gade M., Alpers W., Hühnerfuss H., Wismann V. R., and Lange P. A. (1998) On the reduction of the radar backscatter by oceanic surface films: scatterometer measurements and their theoretical interpretation. *Rem. Sens. Environ.* **66**:52–70

Gash J. H. C. (1986) A note on estimating the effect of a limited fetch on micrometeorological evaporation measurements. *Bound.-Layer Meteorol.* **35**:409–413

Gerling T. W. (1986) Structure of the surface wind field from the SEASAT SAR. *J. Geophys. Res.* **91**:2308–2320

Hasager C. B., Dellwik E., Nielsen M., and Furevik B. (2004) Validation of ERS-2 SAR offshore wind-speed maps in the North Sea. *Int. J. Rem. Sens.* **25**:3817–3841

Hasager C. B., Nielsen M., Astrup P., Barthelmie R. J., Dellwik E., Jensen N. O., Jørgensen B. H., Pryor S. C., Rathmann O., and Furevik B. (2005) Offshore wind resource estimation from satellite SAR wind field maps. *Wind Energy* **8**:403–419

Hasager C. B., Barthelmie R. J., Christiansen M. B., Nielsen M., and Pryor S. C. (2006) Quantifying offshore wind resources from satellite wind maps: study area the North Sea. *Wind Energy* **9**:63–74

Hasager C. B., Astrup P., Nielsen M., Christiansen M. B., Badger J., Nielsen P., Sørensen P. B., Barthelmie R. J., Pryor S. C., and Bergström, H. (2007) SAT-WIND final report. Risø-R-1586(EN). Risø National Laboratory, Roskilde

Hasager C. B., Peña A., Christiansen M. B., Astrup P., Nielsen M., Monaldo F., Thompson D., and Nielsen P. (2008) Remote sensing observation used in offshore wind energy. *IEEE J. Selected Topocs Appl. Earth Obs. Rem. Sens.* **1**:67–79

Hasselmann K., Raney R. K., Plant W. J., Alpers W., Shuchman R. A., Lyzenga D. R., Rufenach C. L., and Tucker M. J. (1985) Theory of synthetic aperture radar ocean imaging - a marsen view. *J. Geophys. Res. Oceans* **90**:4659–4686

He Y. J., Perrie W., Zou Q. P., and Vachon P. W. (2005) A new wind vector algorithm for C-band SAR. *IEEE Trans. Geo. Rem. Sens.* **43**:1453–1458

Hersbach H. (2003) CMOD5. An improved geophysical model function for ERS C-band scatterometry. Reading, UK: ECMWF Technical Memorandum 395, 50 pp

Hogan G. G., Chapman R. D., Watson G., and Thompson D. R. (1996) Observations of ship-generated internal waves in SAR images from Loch Linnhe, Scotland, and comparison with theory and in situ internal wave measurements. *IEEE Trans. Geo. Rem. Sens.* **34**:532–542

Holt B. (2004) AR imaging of the ocean surface. In Jackson C. R. and Apel J. R. (Eds.), Synthetic aperture radar marine user's manual. Washington, DC: U.S. Department of Commerce, National Oceanic and Atmospheric Administration

Horstmann J., koch W., Lehner S., and Tonboe R. (2000) Wind retrieval over the ocean using synthetic aperture radar with C-band HH polarization. *IEEE Trans. Geo. Rem. Sens.* **38**:2122–2131

Horstmann J., Schiller H., Schulz-Stellenfleth J., and Lehner S. (2003) Global wind speed retrieval from SAR. *IEEE Trans. Geo. Rem. Sens.* **41**:2277–2286

Horstmann J., Thompson D. R., Monaldo F., Iris S., and Graber H. C. (2005) Can synthetic aperture radars be used to estimate hurricane force winds? *Geophys. Res. Lett.* **32**, L22801, doi:10.1029/2005GL023992

Jackson J. D. (1997) Classical electrodynamics, John Wiley & Sons, 808 pp

Johannessen J., Shuchman R. A., Digranes G., Lyzenga D. R., Wackerman C., Johannessen O. M., and Vachon P. W. (1996) Coastal ocean fronts and eddies imaged with ERS 1 synthetic aperture radar. *J. Geophys. Res. Oceans* **101**:6651–6667

Johannessen J. A., Kudryavtsev V., Akimov D., Eldevik T., Winther N., and Chapron B. (2005) On radar imaging of current features: 2. Mesoscale eddy and current front detection. *J. Geophys. Res.* **110**, C07017, doi:10.1029/2004JC002802

Koch W. (2004) Directional analysis of SAR images aiming at wind direction. *IEEE Trans. Geo. Rem. Sens.* **42**:702–710

Kudryavtsev V., Hauser D., Caudal G., and Chapron B. (2003) A semiempirical model of the normalized radar cross-section of the sea surface - 1. Background model. *J. Geophys. Res.* **108(C3)**, 8054, doi:10.1029/2001JC001003

Kudryavtsev V., Akimov D., Johannessen J, and Chapron B. (2005) On radar imaging of current features: 1. Model and comparison with observations. *J. Geophys. Res.* **110**, C07016, doi:10.1029/2004JC002505

Lehner S., Horstmann J., Koch W., and Rosenthal W. (1998) Mesoscale wind measurements using recalibrated ERS SAR images. *J. Geophys. Res. Oceans* **103**:7847–7856

Lyzenga D. R. (1991) Interaction of Short Surface and Electromagnetic-Waves with Ocean Fronts. *J. Geophys. Res. Oceans* **96**:10765–10772

Masuko H., Okamoto K. I., Shimada M., and Niwa S. (1986) Measurement of Microwave Backscattering Signatures of the Ocean Surface Using X-Band and Ka-Band Airborne Scatterometers. *J. Geophys. Res. Oceans* **91**:3065–3083

Monaldo F. M. and Beal R. (2004) Wind speed and direction. In Jackson C. R. and Apel J. R. (Eds.), Synthetic aperture radar marine user's manual. Washington, DC: U.S. Department of Commerce, National Oceanic and Atmospheric Administration

Monaldo F. M., Thompson D. R., Beal R. C., Pichel W. G., and Clemente-Colon P. (2001) Comparison of SAR-derived wind speed with model predictions and ocean buoy measurements. *IEEE Trans. Geo. Rem. Sens.* **39**:2587–2600

Monaldo F. M., Thompson D. R., Pichel W. G., and Clemente-Colon P. (2004) A systematic comparison of QuikSCAT and SAR ocean surface wind speeds. *IEEE Trans. Geo. Rem. Sens.* **42**:283–291

Mortensen N. G., Heathfield D. N., Myllerup L., Landberg L., and Rathmann O. (2005) Wind Atlas Analysis and Application Program: WAsP 8 Help Facility. Risø National Laboratory, Roskilde

Mouche A. A., Hauser D., Daloze J. F., and Guerin C. (2005) Dual-polarization measurements at C-band over the ocean: Results from airborne radar observations and comparison with ENVISAT ASAR data. *IEEE Trans. Geo. Rem. Sens.* **43**:753–769

Neiman P. J., Persson P. O. G., Ralph F. M., Jorgensen D. P., White A. B., and Kingsmill D. E. (2004) Modification of fronts and precipitation by coastal blocking during an intense landfalling winter storm in southern California: Observations during CALJET. *Mon. Wea. Rev.* **132**:242–273

Nielsen M., Astrup P., Hasager C. B., Barthelmie R. J., and Pryor S. C. (2004) Satellite information for wind energy applications. Risø-R-1479(EN). Risø National Laboratory, Roskilde

Parish T. R. (1982) Barrier winds along the Sierra-Nevada mountains. *J. Appl. Meteorol.* **21**:925–930

Pryor S. C., Nielsen M., Barthelmie R. J., and Mann J. (2004) Can satellite sampling of offshore wind speeds realistically represent wind speed distributions? Part II Quantifying uncertainties associated with sampling strategy and distribution fitting methods. *J. Appl. Meteorol.* **43**:739–750

Quilfen Y., Chapron B., Elfouhaily T., Katsaros K., and Tournadre J. (1998) Observation of tropical cyclones by high-resolution scatterometry. *J. Geophys. Res. Oceans* **103**:7767–7786

Romeiser R. and Alpers W. (1997) An improved composite surface model for the radar backscattering cross section of the ocean surface. 2: Model response to surface roughness variations and the radar imaging of underwater bottom topography. *J. Geophys. Res. Oceans* **102**:25251–25267

Romeiser R., Alpers W., and Wismann V. (1997) An improved composite surface model for the radar backscattering cross section of the ocean surface.1: Theory of the model and optimization/validation by scatterometer data. *J. Geophys. Res. Oceans* **102**:25237–25250

Stoffelen A. and Anderson, D. L. T. (1997) Scatterometer data interpretation: Estimation and validation of the transfer fuction CMOD4. *J. Geophys. Res.* **102**:5767–5780

Thompson D., Elfouhaily T., and Chapron B. (1998) Polarization ratio for microwave backscattering from the ocean surface at low to moderate incidence angles. *Proc. Int. Geosci. Rem. Sens. Symp.*, Seattle

Thompson D. R.(1988) Calculation of Radar Backscatter Modulations from Internal Waves. *J. Geophys. Res. Oceans* **93**:12371–12380

Thompson D. R. (2004) Microwave scattering from the Sea. In Jackson C. R. and Apel J. R. (Eds.), Synthetic aperture radar marine user's manual. Washington, DC: U.S. Department of Commerce, National Oceanic and Atmospheric Administration

Thompson D. R., Gotwols B. L., and Sterner R. E. (1988) A comparison of measured surface-wave spectral modulations with predictions from a wave-current interaction-model. *J. Geophys. Res. Oceans* **93**:12339–12343

Troen I. and Petersen E. L. (1989) European wind atlas. Risø National Laboratory, Roskilde

Ufermann S. and Romeiser R. (1999) Numerical study on signatures of atmospheric convective cells in radar images of the ocean. *J. Geophys. Res. Oceans* **104**:25707–25719

Vachon P. W. and Dobson E. W. (1996) Validation of wind vector retrieval from ERS-1 SAR images over the ocean. *Glob. Atmos. Ocean Sys.* **5**:177–187

Vachon P. W. and Dobson E. W. (2000) Wind retrieval from RADARSAT SAR images: selection of a suitable C-band HH polarization wind retrieval model. *Can. J. Rem. Sens.* **26**:303–313

Vachon P. W., Monaldo F. M., Holt B., and Lehner S. (2004) Ocean surface waves and spectra. In Jackson C. R. and Apel J. R. (Eds.), Synthetic aperture radar marine user's manual. Washington, DC: U.S. Department of Commerce, National Oceanic and Atmospheric Administration

Valenzuela G. R. (1978) Theories for the interaction of electromagnetic and ocean waves – A review. *Bound.-Layer Meteorol.* **13**:61–85

Wentz F. J., Peteherych S., and Thomas L. A. (1984) A Model Function for Ocean Radar Cross-Sections at 14.6 Ghz. *J. Geophys. Res. Oceans* **89**:3689–3704

Wentz F. J., Mattox L. A., and Peteherych S. (1986) New Algorithms for Microwave Measurements of Ocean Winds – Applications to Seasat and the Special Sensor Microwave Imager. *J. Geophys. Res. Oceans* **91**:2289-2307

Winstead N. S., Colle B., Bond N., Young G., Olson J., Loescher K., Monaldo F., Thompson D., and Pichel W. (2006) Using SAR remote sensing, field observations, and models to better understand coastal flows in the Gulf of Alaska. *B. Am. Meteorol. Soc.* **87**:787–800